Universidade do Minho
Escola de Engenharia

Fabio Solarino

Analysis of retrofitting solutions to enhance the seismic behavior of masonry-to-timber connections in historical constructions

April 2022

Analysis of retrofitting solutions to enhance the seismic behavior of masonry-to-timber connections in historical constructions
Fabio Solarino
UMinho | 2022

This work was financed by the Portuguese Foundation for Science and Technology (FCT) through the PhD grant SFR/BD/131652/2017, co funded by the European Social Fund (FSE) through the Operational Programme of the North Region, who are strongly acknowledged. They provided the necessary financial support for the successful development of the research work and the writing of this document.

UNIVERSITÀ DI PISA

FCT Fundação para a Ciência e a Tecnologia

Universidade do Minho
Escola de Engenharia

Fabio Solarino

Analysis of retrofitting solutions to enhance the seismic behavior of masonry-to-timber connections in historical constructions

Doctoral Thesis
Doctoral in Civil Engineering

Work conducted under supervision of
Professor Daniel V. Oliveira
and
Professor Linda Giresini

April 2022

ACKNOWLEDGEMENTS

Such a work could not have been possible without the support of my supervisors. Prof. Daniel V. Oliveira is strongly acknowledged for all exciting meeting (in presence and in videoconference) necessary for giving the correct directions, driving me through the development of the thesis in unique, friendly, and motivating conversations. Even if he was not supposed to be my official supervisor at the initial stage, he welcomed me with open arms making me feel like at home. A super big thank also goes to prof. Linda Giresini, not only my supervisor, but also my mentor, since the end of my master studies. Her contribution not only provided the necessary knowledge for the thesis work, but also led me to a higher level within the research and the job communities. I thank her for the quick replies and comments, as well as for having faith in me.

To Dr. Susana Moreira. Her thesis inspired this research work. Thanks not only for sharing the experimental data but also for the support and for interesting and creative discussions.

A special thanks to the Secretariat of the Doctoral program in Civil Engineering at the University of Minho, in particular to Mariana, who has always provided the necessary support, documentation, information, immediately, with patience and kindness, even under the pressure of strict deadlines.

I also want to express my gratitude to “my” Claudia who has always believed in me, sustaining, and supporting me even during hard times and during my periods abroad. Thanks for giving me a lovely welcome after every back flight and thanks for letting me stay down-to-earth.

The development of the thesis could not have been possible without the vital support and the close relationship with my colleagues and friends in Guimarães who are kindly acknowledged. Thank you, Alberto, Antonio R., Antonio M., Niqui, Gianpaolo, Pia, Rafa, Meera, Xinyu, Leslie, Telma, Chandan, Abide, Elizabeth, Maria J., Reza, Federico, Francesco, Daniele, Alessandro, Alban, Jennifer, Lidia, Nicola, the “Sachsters” and everyone else who contributed to make the time spent in Portugal nice, lovely and peaceful.

Finally, I would like to thank, acknowledge and dedicate this thesis to my family and my friends in Italy who have always been available for me and who followed this “never-ending” doctoral program sharing my anxiety and stress.

A special thanks also to Michael, with whom I have been sharing every important education phase: school diploma, bachelor, master, and now PhD, too. Thank you, I hope to keep sharing important future life stages with you.

STATEMENT OF INTEGRITY

I hereby declare having conducted this academic work with integrity. I confirm that I have not used plagiarism or any form of undue use of information or falsification of results along the process leading to its elaboration.

I further declare that I have fully acknowledged the Code of Ethical Conduct of the University of Minho.

Análise de soluções de reforço para melhoria do comportamento sísmico de ligações de alvenaria a madeira em construções históricas

RESUMO

A modelação e interpretação de soluções de reforço em edifícios sismicamente vulneráveis é uma tarefa complexa e incerta, mas fundamental para compreender a sua influência no desempenho sísmico global e local de edifícios. Os edifícios históricos são vulneráveis a sismos, especialmente ao desenvolvimento de mecanismos locais para fora do plano. Esta tendência é devida à debilidade das ligações parede-parede e parede-diafragma horizontal (W-D), essencialmente concebidas para cargas gravíticas.

A análise global de edifícios de alvenaria não reforçada é convencionalmente realizada negligenciando as propriedades não lineares das ligações estruturais, enquanto a análise local é habitualmente realizada através de modelos de ligação simplificados, conduzindo possivelmente a resultados muito conservativos. Nesta tese estuda-se a influência das ligações W-D através de análises numéricas avançadas de um edifício de referência, com base numa revisão bibliográfica abrangente e dados experimentais disponíveis. Os modelos numéricos histéricos, calibrados com base em curvas experimentais cíclicas, conseguem reproduzir adequadamente as curvas força-deslocamento envolventes, a degradação de força e a capacidade de dissipação de energia. A análise global é realizada através de análises estáticas e dinâmicas não-lineares, capazes de incluir ligações W-D, obtendo-se a capacidade global do edifício e os correspondentes padrões de dano. Por outro lado, a análise local, baseada no princípio dos trabalhos virtuais, é aplicada como um procedimento eficiente, rápido e simples para a avaliação das ligações W-D reforçadas. Uma abordagem mais avançada, baseada na estabilidade dinâmica de blocos rígidos é ainda adotada para realçar os possíveis efeitos dinâmicos de mecanismos de colapso para fora do plano, incluindo ligações W-D não lineares.

A solução da ligação reforçada em estudo revela ser uma solução eficaz e pouco invasiva, capaz de aumentar claramente a segurança sísmica de mecanismos de colapso para fora do plano. A avaliação baseada em deslocamentos, através da análise cinemática e considerando a possível amplificação dinâmica da carga sísmica, revela ser um procedimento de dimensionamento dos mais simples e básicos, capaz de fornecer o conhecimento necessário do estado atual a mesma e os parâmetros de dimensionamento da solução reforçada

Palavras-chave: edifícios de alvenaria não reforçada; engenharia sísmica; ligações parede-diafragma horizontal; modelação numérica; reforço de ligações.

Analysis of retrofitting solutions to enhance the seismic behavior of masonry-to-timber connections in historical constructions

ABSTRACT

The modelling and interpretation of retrofitting solutions in seismically vulnerable buildings is complex and uncertain but fundamental for understanding their actual influence in the global and local seismic performance of buildings. Historical buildings are frequently prone to earthquakes, especially developing out of plane local mechanisms of structural elements. This tendency is due to weak wall-to-wall and wall-to-horizontal diaphragm (WD) connections, mainly solely designed for gravitational loads.

Global analysis of unreinforced masonry buildings is conventionally carried out neglecting the nonlinear properties of structural connections, while local analysis is commonly performed through simplified connection models, possibly leading to overconservative results.

In this thesis, the influence of WD connections is studied through simplified and advanced numerical analyses on a benchmark building, on the bases of a comprehensive literature review and available experimental data. Hysteretic numerical models, calibrated upon cyclic experimental curves, carefully fit the force-displacement backbone curves, the strength degradation and the energy dissipation capacity. Global analysis is performed through nonlinear-static and nonlinear dynamic analyses, capable of including WD connections, and providing the overall capacity of the building and the corresponding damage pattern. On the other hand, local analysis, based on the virtual work principle, is applied as an efficient, rapid and simple procedure for the assessment of existing and strengthened WD connections. A more advanced approach, based on the dynamic stability of rigid block is further adopted to better highlight the possible dynamic effects of out-of-plane mechanisms including nonlinear WD connections.

The strengthened solution under study reveals to be a prominent and low-invasive solution capable of strongly increasing the seismic safety index of out-of-plane mechanisms. Displacement-based assessment, through kinematic analysis, accounting for possible dynamic amplification of the seismic load reveals to be one of the most simple and basic design procedures capable of providing the necessary knowledge of the current state and the design parameters of the strengthened solution.

Keywords: earthquake engineering; numerical modeling; strengthening connections; unreinforced masonry buildings; wall-to-diaphragm connections;.

TABLE OF CONTENTS

LIST OF TABLES

LIST OF FIGURES

CHAPTER 1

INTRODUCTION

Overview

In this opening chapter, a general overview of the thesis is given presenting the motivation that drove the research work, focus, and main goals to be attained. The research methodology is also shown considering the main tools used to reach the main objectives. The structure of the thesis is finally illustrated, briefly describing the content of each chapter.

1.1 Motivation

Historical buildings weakly resist to seismic actions mainly due to their poor material quality, irregular geometry and reduced strength-to-weight ratio (Lang and Bachmann 2003). Structural connections reveal to be fundamental for tying the walls together making the construction to behave like a box (Bothara and Brzev 2011). The structural connections enable a more convenient load transfer of the inertial forces to the foundation through seismically-resisting walls. Weak wall-to-wall (WW) or wall-to-horizontal diaphragm (WD) connections can involve large relative displacements among structural elements, sometimes leading to dangerous collapses. Local mechanisms, mainly involving partial overturning of walls out of their plane, should be prevented as a priority (Tomaževič 1999). To this aim, the strengthening of WD connections is one of the most promising retrofitting solutions, enabling global equilibrated mechanisms through sufficiently resistant and ductile components, necessary for a proper dissipation of seismic energy.

Only in Italy more than 5,800 urban centres exist counting about 6.9 million residential buildings made of unreinforced masonry (URM) walls (Istat 2004) and commonly built with timber floors and roofs. This building stock represents about 61.5% of the total number of buildings, 81.5% of which was built before 1991. Similar percentages are present in the rest of Europe (Figure 1.1), which is known to be a high seismic area, especially in the south-eastern area, such as Greece, Italy, Romania, but also south of Portugal, where stonework is the typical masonry in structural heritage buildings.

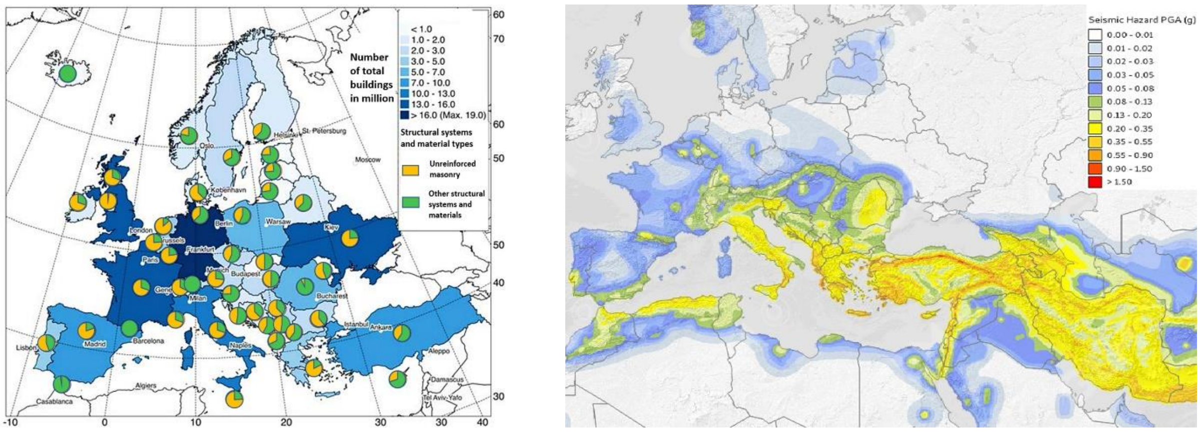

(a) (b)

Figure 1.1 (a) Distribution of URM buildings with respect to the total number of buildings; (b) Hazard map of the European and Middle-Eastern countries. Source: (Shabani, Kioumarsi, and Zucconi 2021).

Typical examples of weak WD connections consist in a timber beam partially embedded (or placed) into the masonry wall, and the pull-out resistance is solely based on friction (Emi

1856). During the last century, the increasing seismic culture and the relevant losses of human life and built heritage after earthquake events, motivated the development of strengthening solutions to enhance the seismic behavior of existing structures. Indeed, new masonry buildings address seismic engineer concepts since the early design stages; the same approach was not adopted for existing buildings, often constructed following the so-called “rule of thumb”.

Strengthening WD solutions often consist in steel ties and plates anchoring the beams to the wall or tying the parallel walls each other (Tomaževič 1999). Such a solution is often designed and verified through simple force-based procedures, suggested by code standards (ASCE 2017; C.S.LL.PP. 2019; FEMA 2006b). These formulations are, however, uncertain, and are not able to account for the dynamic interaction between the WD interface.

Conventional analysis of URM buildings allow for the presence of different types of diaphragms and walls, while WD connections are usually treated as full rigid links or simply neglected (Mendes 2012). Recently, few authors (Ferreira Freitas Araújo 2014; Ortega et al. 2018) developed simplified and advanced models accounting the influence of structural connections, thanks to the increasing technological development and the large availability of advanced tools.

Unfortunately, the actual behavior of WD connections is uncertain and too complex models are hardly accepted among practitioners and engineers. Strengthening solutions are, therefore designed based on the experience with no adequate analysis. This often leads to overestimated invasive and costly solutions, strongly impacting the original aspect and structure of the building.

The influence of the quality of WD connection in the seismic behavior of the overall building is crucial and should properly be studied. Finally, clear and simple guidelines are necessary for the adequate seismic assessment of WD connections in URM buildings, easily available among seismic engineers and practitioners. Moreover, a high number of existing buildings and monuments was built under absent seismic prescriptions and is still present in medium-high seismic risk areas (Menon and Magenes 2008; Polidoro 2010).

1.2 Objectives and methodology

The research work seeks to reach two main objectives: (i) understanding the influence of different types of WD connections, and (ii) developing design procedures capable to evaluate the WD connections in URM buildings in a simple and effective manner. The achievement of the overall goals requires the pursuing of the following detailed objectives:

- Acquiring a full knowledge about typical WD connections from the experimental and numerical point of view, as well as from design practice. A comprehensive state of art is carried out for this purpose, also considering current code standard guidelines;
- Sensitivity numerical analysis based on both global and local approaches capable of studying the influence of the connection quality on the overall system. Advanced detailed WD connection models are firstly developed based on available experimental data. Then, numerical studies are carried out on finite element, kinematic and rocking approaches;
- Development of the suggested design procedure for the seismic assessment of WD strengthened connections;

1.3 Thesis outline

The document is divided into six chapters. The first is an introductory chapter presenting the motivation that drove the research, the main objectives and the followed methodology. In chapter 2, a comprehensive state of the art discusses the role of WD connections in historical constructions, with the aim of understanding the current issues and the main gaps between experimental research, numerical tools, available standard codes and current practice. A model strategy of nonlinear WD connections useful for further static and dynamic nonlinear analyses is proposed in Chapter 3, while Chapter 4 is dedicated to a sensitivity analysis with the aim of understanding the influence of different WD connections through three different numerical approaches: (i) finite element analysis; (ii) kinematic analysis and (iii) dynamics of rigid block. An innovative design procedure is defined in Chapter 5. Conclusions and further works are finally presented in Chapter 6.

CHAPTER 2

THE ROLE OF WALL-DIAPHRAGM CONNECTIONS IN HISTORICAL CONSTRUCTIONS

Overview

This chapter presents a comprehensive state-of-the-art review of wall-to-horizontal diaphragm connections in historical constructions. The role of the structural connections in the seismic behavior of historical buildings is firstly presented, focusing on wall-to-horizontal diaphragm connections. The discussion is critically set upon typical adopted solutions, experimental, and numerical studies, taking into account the point of view of research, code standards and practice, in order to better understand the relationship between them and the missing gaps.

2.1 Introduction

Overturning of the perimeter out-of-plane (OOP) walls is considered the first-mode of failure and the last desirable in historical buildings (Brignola, Podestà, and Pampanin 2008; Rondelet 1802) cause of dramatic consequences, as shown in past seismic events in New Zealand (1931 M7.8 Hawke's Bay earthquake), California (1933 M6.4 Long Beach earthquake), San Francisco (1989 M6.9 Loma Prieta earthquake), Australia (1989 M5.6 Newcastle earthquake), or in Nepal (1988 M6.9 East Nepal earthquake) (Russell, Ingham, and Griffith 2006), among others. Old masonry buildings are most susceptible to seismic motions not only because they were built following the "rules of art", but also because of lacking anti-seismic criteria and poor quality of the materials (Menon and Magenes 2008).

Besides the in plane (IP) stiffness of the floor, the connection quality between floors and vertical elements strongly influences the seismic response of existing URM building. Without proper connections, the walls behave like a tall unrestrained cantilever vibrating laterally, highly vulnerable to flexural OOP action (Bothara and Brzev 2011; Lang and Bachmann 2003) Figure 2.1a. Moreover, diaphragms play a key role in the transmission of the seismic actions through the shear connections to the lateral resisting wall (Figure 2.1b).

(a)

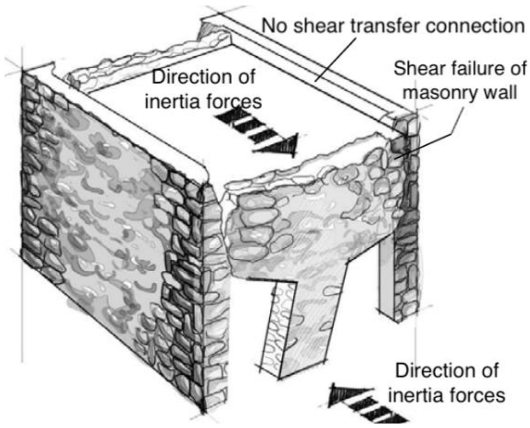

(b)

Figure 2.1 OOP failures of masonry walls due to the lack of wall-to-roof connections (Bothara and Brzev 2011): (a) collapse of a long wall in the 1988 East Nepal earthquake; (b) Inertia forces causing local failure mechanism.

Vertical seismic actions can also make the weak supports ineffective, causing the partial or total collapse of the structure. Effective solutions, together with the adoption of general seismic criteria, lower the vulnerability of the URM buildings ensuring the "box-behavior" and activating global equilibrated mechanisms (Tomaževič 1999) (Figure 2.2(a) On the other hand, inappropriate use of retrofit techniques can increase the seismic risk in existing constructions, as observed in failures during the 1997 Umbria-Marche earthquake (Figure 2.2(b)) where the increased seismic forces due to the new heavy roof caused the separation from the supporting walls.

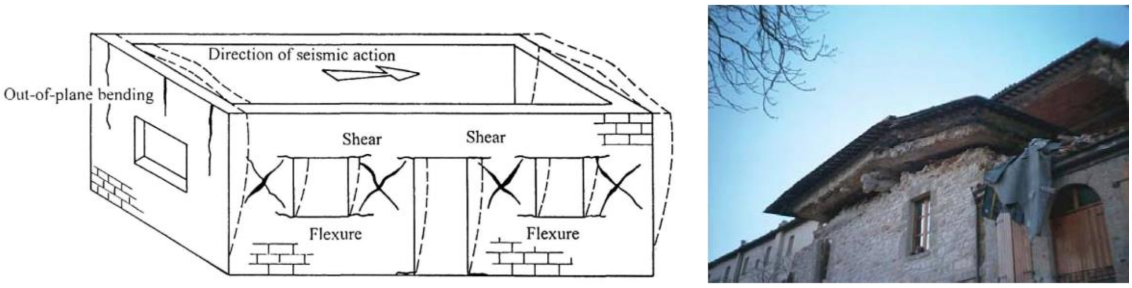

(a) (b)

Figure 2.2 URM buildings seismically damaged: (a) global damage pattern embraced by Tomaževič (1999)*; (b) stiff diaphragm disconnected from walls* (Brignola et al. 2008)*.*

Researchers mainly aim at understanding the global seismic behavior of the building neglecting the influence of connections, and strengthening solutions are suggested for the solely primary structural elements (Ismail and Ingham 2016; Scotta et al. 2018). The importance to account for OOP loading of the walls and to guarantee proper connections is highlighted in design codes and guidelines, yet it is not clear how to account for these effects in analytical models. Eurocode 8, part 3 (EC (Eurocode) 8 2005) gives general technical criteria specifically for masonry structures, for which inadequate connections between floors and walls or between roofs and walls should be improved and OOP horizontal thrusts against walls should be eliminated, but no assessment equations can be found to verify the quality of the current connections. The 2008 Italian code (C.S.LL.PP. 2009; DMI 2008) allows to perform kinematic analysis to assess local mechanisms of masonry structures constituted by macro-elements with a displacement-based approach. No suggestions can be found, however, on the value of stiffness of the connections between the OOP wall and the possible diaphragm. Circolare n. 26 (Presidenza del Consiglio dei Ministri 2011), aligned with NTC08, highlights the importance of reducing lacks in connections proposing the use of tie rods, external bounding and ring beams. It is worthy to notice that this code only mentions some connection details for existing constructions (e.g. use of steel elements to anchor the timber beam to the masonry wall al floor level) without giving clear guidelines on how to account for them in the numerical models. Few details and recommendations can be found in NTC2018 (DMI 2018) suggesting mechanical or injected anchor elements to increase the pull-out resistance. However, no analytical formulation is indicated for the design and assessment of those connections.

2.2 Typical wall diaphragm connections

Investigating the actual type and characteristics of the connections between vertical and horizontal structures is a complex but fundamental task, influencing the accuracy of assessment models to evaluate the building vulnerability and to design the optimum strengthening solution. Moreover, details are not on sight and no drawings are available for ancient buildings. Post-earthquake surveys from the inside are often risky.

The great variability of connections mainly relies on the typology of structural elements (single, multi-leaf or cavity walls, columns, floors, roofs, arches and vaults), and on their materials (bricks, stone, timber, steel and reinforced concrete), but similarities can be found among construction systems in different countries worldwide. Either one- or two-way timber floors are typically used in masonry buildings, while timber truss is the most common type of roofing system. Traditional examples of connection details are summarized and discussed below. A brief description about construction details typically found in older URM buildings in the USA was given by Lin and LaFave (Lin and LaFave 2012), citing the Architectural Graphic Standards (Ramsey and Sleeper 1932) and the I.T.B Company (Company 1923), indicating some methods by which wooden floor joists were connected to brick masonry walls. Suggestions about how to perform proper connections were also summarized by Cestari and Lucchio (2001) or Russel et al. (2006), who analyzed different construction typologies in Italy and other countries all over the world.

Certain rudimentary arrangements of stones or bricks could serve as corbel support for the joist as shown in Figure 2.3, providing a flat and stable support for the timber beams (Alberti 1452; Maresta 2018; Milizia 1785; Scali 2011). The simplest and oldest practice was to fix the joist directly in a slot inside the wall for a depth equal to the same thickness of the wall or to the half, for thin or thick walls respectively (Scamozzi 1615; Valadier 1831). Other authors indicated a fixing depth of 0.25-0.30 m according to the masonry walls thickness; for considerable timber sections and for walls with a thickness of more than 0.50 m, Emi (1856) suggested 0.32-0-33 m depth.

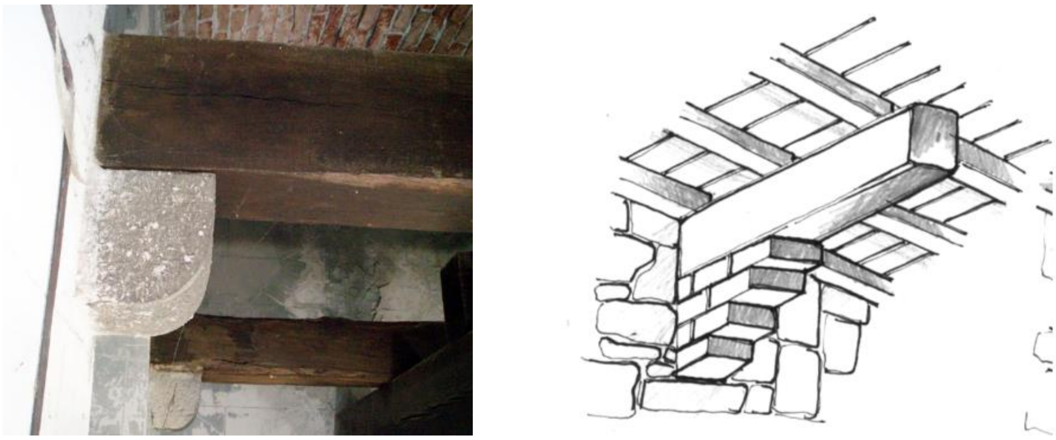

(a) (b)

Figure 2.3 Timber beams on corbels: (a) Connection detail inside Castello d'Albertis, Genova, Italy (Maresta 2018)*; (b) example of bricks arranged as corbels to support timber beams* (Scali 2011)*.*

The beam was simply supported by the walls, commonly constructed around the beam itself, either tightly filling with masonry the recessed support or by using weak grout to fill an oversized rectangular cavity housing the support for the beams (Bruneau 1994). Historical treatises proposed solutions to avoid the decay of headpieces of the timber beams infixed in the masonry, such as, leaving a gap between the timber and the masonry allowing airing (Alberti 1452; Emi 1856), sometimes including a hole on the outer wall covered with a grid (Pareto and Sacheri 1889). Formenti (1893), Donghi (1923) and Chevalley (1924) suggested to form a box around the headpiece through air bricks or insert hardwood or stone brackets under the headpieces of the floor beams. Further solutions comprised timber wall-plate (0.12-0.15 m thick) fixed in 3/4 or in the entire thickness of the wall linked to the joists through mortise and tenon joint type (Breymann 1880). Another way to better distribute the load on the wall was the adoption of wrought timber beams as shown in Figure 2.4a. The peripheral beam could also be supported on stone corbels to avoid reduction of wall thickness of upper floor (Figure 2.4c). Timber struts were often adopted to reduce the span (Figure 2.4d).

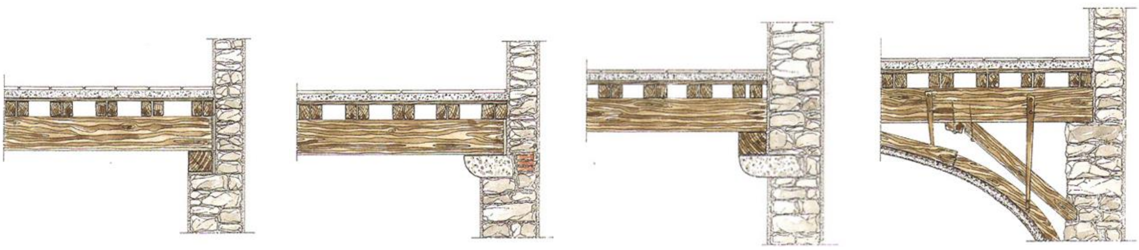

(a) (b) (c) (d)

Figure 2.4 Examples of typical floor-to-wall connections (Maresta 2018)*.*

Common New Zealand URM constructions built up until the 1931 Napier earthquake were typically cavity walls, with no rubble fill, supposed to be linked with steel ties. Details of such buildings were described by Russel et al. (2006) highlighting that the floor/roof diaphragms were just carried from the inner wythe of the cavity wall without any proper connection to the outer wall. Moreover, the gables in the upper end part of the walls were highly vulnerable because of the complete absence of effective connection with timber members.

All the above-mentioned solutions are mainly friction-based providing poor or absent linkage between the structural elements, causing weak load transmission. Sometimes, the reduced thickness at upper story led the timber floor system to simply bearing on the top of the lower wall with no embedment at all. Later solutions, studied by Lin and LaFave (2012) and Peralta et al. (Peralta, Bracci, and Hueste 2004), provided the use of iron straps to anchor timber joists or main beams to the masonry perpendicularly or in parallel (Figure 2.5a). Typical fish-tail iron anchors, where the strap was nailed to the timber joist and infixed into a pocket created in the masonry, in the other end, were shown by Cóias (2007) and used to link the new timber headpiece in place of the degraded one (Figure 2.6a). Post-1755 Lisbon earthquake Pombalino buildings presented a much complex detailing if compared to other constructions of the same period: the timber floor joist would be connected to a top and bottom timber wall-plates embedded in the masonry wall, through carefully done cross lap joints and the use of nails (Appleton 2003). Metal straps were nailed to the timber joists and going through or into the wall. Effective floor to wall connection could be obtained making use of a 1 m long steel bar anchored to the masonry fixed diagonally to the timber joists in contact with it. The bar was usually embedded in the timber joists covered by the timber plank (Figure 2.5b).

It was common to cover large span using timber roof because of the availability of the material and easy manufacturing. A good rule to improve the mechanical characteristic of its connection to the masonry was to use steel strap infixed inside the wall and connected to the bottom horizontal member (Figure 2.5c). The steel strap could also be fixed to a bended bar which was used also to improve the connection between the chain and the rafter. A timber truss seated on a concrete padstone was shown in NZSEE, part C8 (NZSEE 2016).

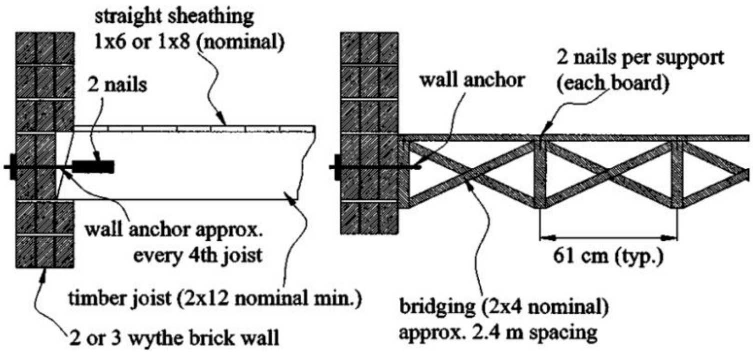

(a)

(b) (c)

Figure 2.5 Metal anchorages between timber beams and masonry wall: (a) connections between the parallel or perpendicular joist and the wall (Peralta et al. 2004)*; (b) diagonal bar embedded into the transversal joists* (Appleton 2003)*; (c) roof-to-wall connection* (Cóias 2007).

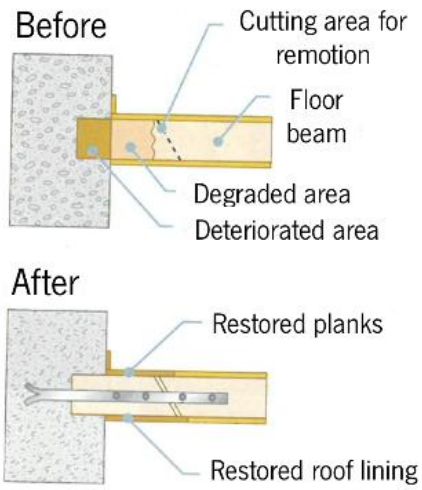

(a) (b)

Figure 2.6 Timber to masonry anchors (Cóias 2007)*: (a) Replacement of degraded timber joist headpiece; (b) iron strip from the inside.*

The use of horizontal metal tie-bars is common in heritage buildings to control the horizontal thrust exerted by vaults and arches or by wooden truss roof, but it is also one of the simplest and widespread solution on new and retrofitted constructions ensuring the box-type behavior connecting the walls at floor levels (Calderini et al. 2016; Spina, Ramundo, and Mandara 2005; Tomaževič, Lutman, and Weiss 1996). Metal tie-rods in the pre-industrial age were forged steel bars in pseudo-circular or quadrangular sections anchored to the bearing structure and inserted with minimum tensile action. Usually, anchor plates or simply bars, forced into the eye-end of the tie rod with the help of metal wedges, restrained the bar, acting on the outer surface of the wall.

A typical Mediterranean early 20th century floor, known as *jack arch system* (Figure 2.7), comprised iron beams supporting shallow brick masonry arches (Bothara and Brzev 2011). Here the metal beams were simply infixed in masonry slots and, sometimes, steel bars were present to reduce horizontal forces.

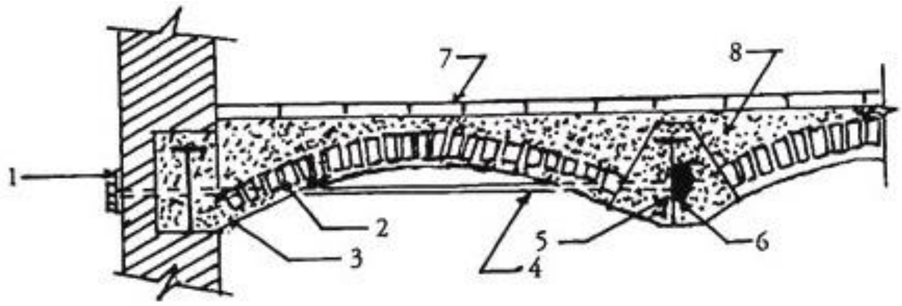

Figure 2.7 . Jack arch roof: 1. M.S. plate 10 mm thick; 2. Brick arch; 3 Plaster; 4. M.S. Tie rod; 5. R.S.J.; 6. Cement concrete; 7. Flooring; 8. Lime concrete (Bothara and Brzev 2011).

The arrival of reinforced concrete (RC) almost totally substituted masonry as main structural material for constructions, the latter being used merely for infill walls or non-structural components, such as partitions or aesthetic façades. The presence of RC bond-beams (tie beams) in newly masonry buildings at floor levels allowed the requested connection between the slab (usually made of RC) and the walls. This allowed the transfer of horizontal forces from the floor to the cross walls and improved the IP rigidity of horizontal floor diaphragms (Tomaževič 1999).

Among the general technical criteria for a successful strengthening of masonry buildings in seismic areas, there is proper geometrical layout of structural walls, their sufficient load bearing capacity, regularity and symmetry, adequate foundation capable to transfer loads to the soil. In addition, it is well recognized that the walls should be adequately tied and connected to each other, and the floors should be well anchored to the walls preventing OOP collapses (Tomaževič 1999). The latter criterion provides the structural continuity between different components and improves the capability of the building to dissipate energy through the introduction of newer ductile elements, which can improve the seismic response. In addition, not only the joist slipping is avoided, but anchoring the diaphragm to the wall prevents hammering, typical in historical constructions where the vertical and horizontal elements natural frequencies are uncoupled. Moreover, the selected solutions should be simple and economic, experimentally characterized and should fulfil the basic requirements of restoration and conservation of cultural heritage (in the case of historical monuments) (Andreini et al. 2013; de Falco, Giresini, and Sassu 2013).

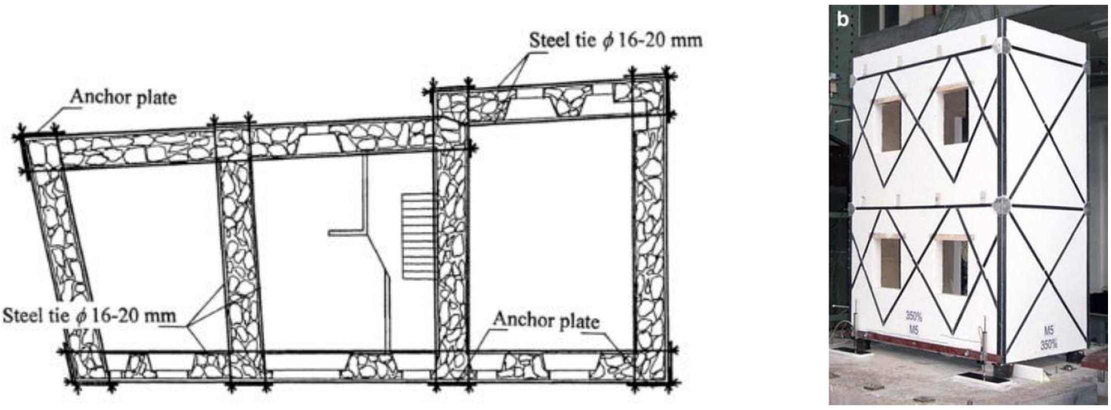

(a) (b)

Figure 2.8 Tying URM walls for a seismic reinforcement: (a) steel tie rods retrofitting (Tomaževič 1999)*; (b) CFRP laminates retrofitting* (Tomaževič, Klemenc, and Weiss 2009)*.*

The use of metal tie-bars is a very simple and widespread intervention technique for the seismic upgrade of the URM building improving its structural integrity (Tomaževič et al. 1996), useful both for semi-rigid and flexible floors such as vaults (Giresini et al. 2017). Typically, 16-22 mm diameter reinforcing steel slightly prestressed bars are placed at the floor levels on each side of the walls, anchored at the ends to steel anchor bars or plate (Figure 2.8a). However, as highlighted by Tomaževič (2009), typing the walls is sometimes not sufficient for providing adequate structural integrity, and existing wooden floor structures should be strengthened, anchored and connected with masonry walls. Furthermore, the prestressed force must be conceived, designed and executed carefully: despite the masonry shear force increases with the compression level, the pre-tension induces alterations in the equilibrium of the structure and modifies the tension state of the masonry (Appleton 2003). Recent suggestions for tying the masonry walls include the possibility to replace the steel ties with reinforced polymer laminates (Figure 2.8b), significantly improving the resistance and the lateral capacity, confining the building with vertically and horizontally placed strips (Alecci et al. 2017; Alecci, Briccoli Bati, and Ranocchiai 2009, 2014; Tomaževič 2011). For the latter solutions, precautions must be undertaken to face the great difference in strength and deformability between traditional masonry and innovative polymer, adopting compatible technologies for the bond and the anchoring system.

One of the firs solutions used to improve the connection of the joists to the wall makes use of iron straps nailed to the timber joist and fixed into or through the wall, anchoring on the exterior face with simple iron bar, squared, star shaped, or circular plates (Cóias 2007), as shown in Figure 2.9a. Figure 2.9b illustrates a strengthening solution proposed by Tomaževič (1999) with double steel anchors aligned with the axis of the floor joist avoiding eccentricity.

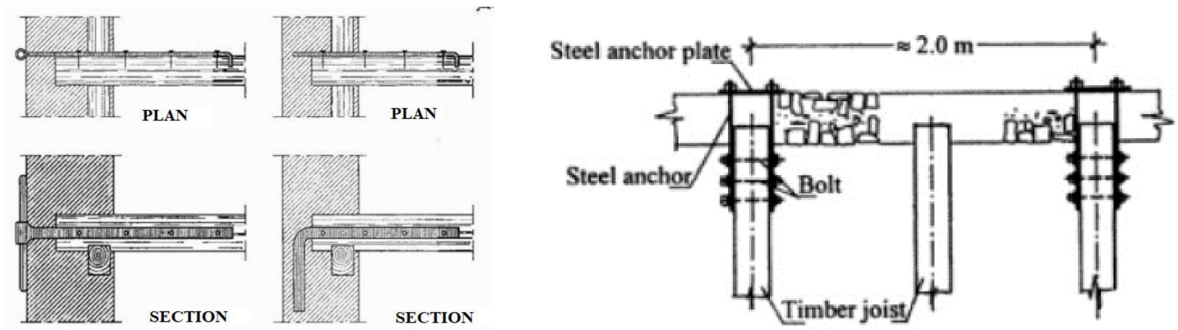

(a) (b)

Figure 2.9 Wall-to-floor strengthening solutions: (a) wrought iron straps (Cóias 2007); (b) double anchor system (Tomaževič 1999).

Blaikie and Spurr (Blaikie and Spurr 1992) described some retrofitting practices adopted after the 1931 Hawke's Bay earthquake, in New Zealand. Many of them include the installation of wall-floor and wall-roof connections, mainly through bolt anchors, used in conjunction with a steel bearing plate located on the exterior of the building and a bolted connection on the timber diaphragm joist, usually interconnecting a steel angle plate (Figure 2.10a). The bolted connections increase the shear resistance and improve the pull-out behavior of the solution. Newer interventions, studied by Moreira (2015) contemplate hinges at both ends of the anchor allowing for a diagonal fixing of the tie directly from the top of the floor (Figure 2.11), reducing the eccentricity and acquiring a more cost-effective solution. Cóias (2007) proposed different strengthening solutions including injection anchors, where the grout injection controls the bond behavior between the steel tie and the surrounded masonry. Such a solution (Figure 2.10b) requires access only from one side of the wall, facilitating the possible interventions on the façade or party walls. The connection to the timber joist is usually ensured by a bolted steel angle.

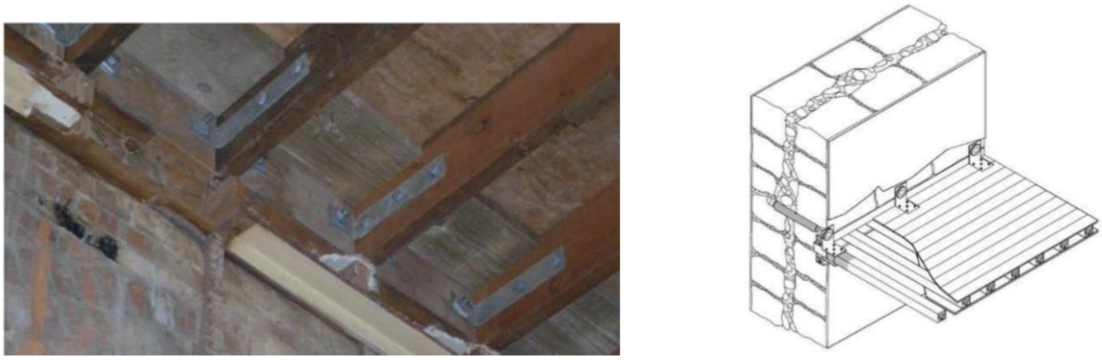

(a) (b)

Figure 2.10 Wall-to-diaphragm bolt anchorages: steel rods bolted to steel angles (Blaikie and Spurr 1992); (b) Strengthening solution with injected anchors proposed for Pombalino buildings (Cóias 2007).

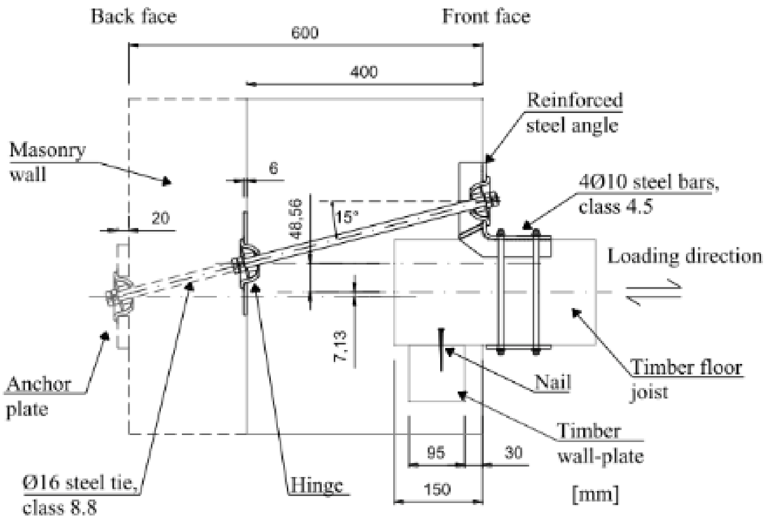

Figure 2.11. Innovative solution studied by Moreira (2015).

With respect to traditional steel anchors, dissipative passive systems may be integrated to improve the energy dissipation capability of the connections and may be based on the plasticity of the steel or on friction (NIKER 2010; Paganoni, D'Ayala, and D'Ayala 2010).

Horizontal diaphragm action on floors or roofs is usually very poor in existing URM buildings because of the high flexibility of the diaphragm in comparison with the lateral resistant masonry walls. To increase their IP stiffness, timber floors or roofs are often replaced by RC or precast slabs with perimeter bond-beams similarly to the modern masonry constructions where the RC ring beams provide the connection between the RC slab and the wall so that the structural system performs as a monolithic unit during an earthquake. If the bond-beams are not completely embedded in the masonry, the slabs should be adequately anchored to the walls as shown by Tomaževič (1999) (see Figure 2.12). However, using RC slabs and ring beams should be considered as the last option as the increasing mass could lead to unfavourable high seismic inertia forces, which can cause OOP modes and produce torsional effects.

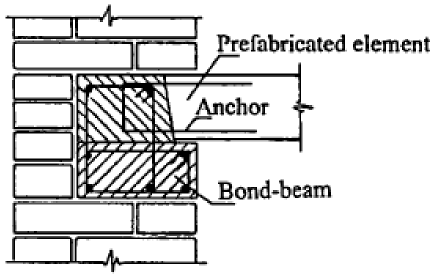

Figure 2.12 Connection between new RC bond beam and existing floor (Tomaževič 1999).

Effective solutions can be achieved by overlapping a second timber deck anchored to the existing one and providing proper connections between the joists and the walls, with or without steel tie rods (Senaldi et al. 2014; Valluzzi et al. 2013).

The ring beam also increases the IP stiffness of the floor behaving as diaphragm chords (International Code Council 2009) (Figure 2.13a) whose force can be computed considering the system considering the system (chords + diaphragm) as an I-beam under bending and shear in the direction of the earthquake (Figure 2.13b). Solutions shown in Figure 2.9 Figure 2.10 Figure 2.11 are not usually able to perform as a diaphragm chord element, as they were designed mainly for the prevention of the shear and axial failure caused by IP and OOP forces, respectively. A chord strengthening solution is proposed by Hsiao and Tezcan (Hsiao and Tezcan 2012) on the basis of FEMA (FEMA 1992). The retrofitting strategy considers the strengthening of the shear and axial connections between wood diaphragms and URM bearing walls, maintaining the original figure of the historic building (Figure 2.14).

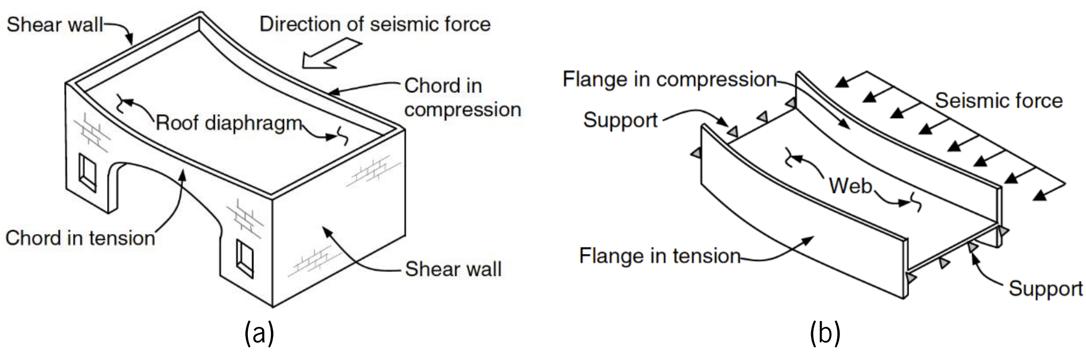

Figure 2.13 Chords and diaphragm corresponding to flanges and web (Hsiao and Tezcan 2012).

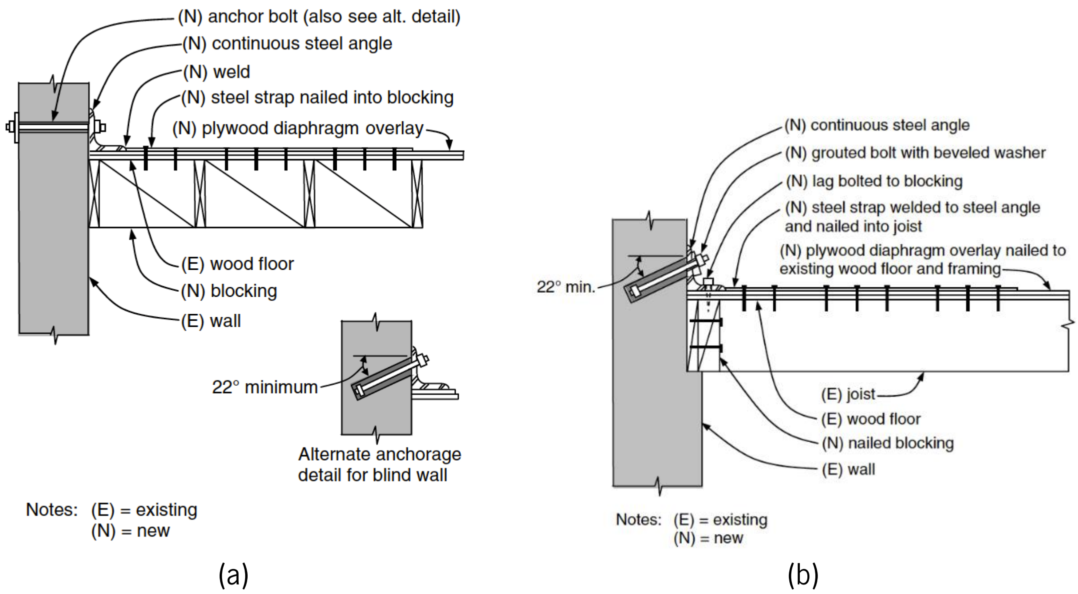

Figure 2.14 Chord strengthening connections (Hsiao and Tezcan 2012): (a) OOP bolted connection parallel to wall; (b) injected connection with joists perpendicular to the wall.

A seismic strengthening solution applied on an old and damaged church timber roof structure is shown in (Figure 2.15a). The main aim was to increase the diaphragm behavior without destroying the original inner aspect of the church. The solution included the replacement of old timber with new timber beams and the insertion of a stell truss. Particular attention was given to the connection of beams to the perimeter walls (Figure 2.15b). A lattice girder lying along the bearing walls functions as lower tie beam.

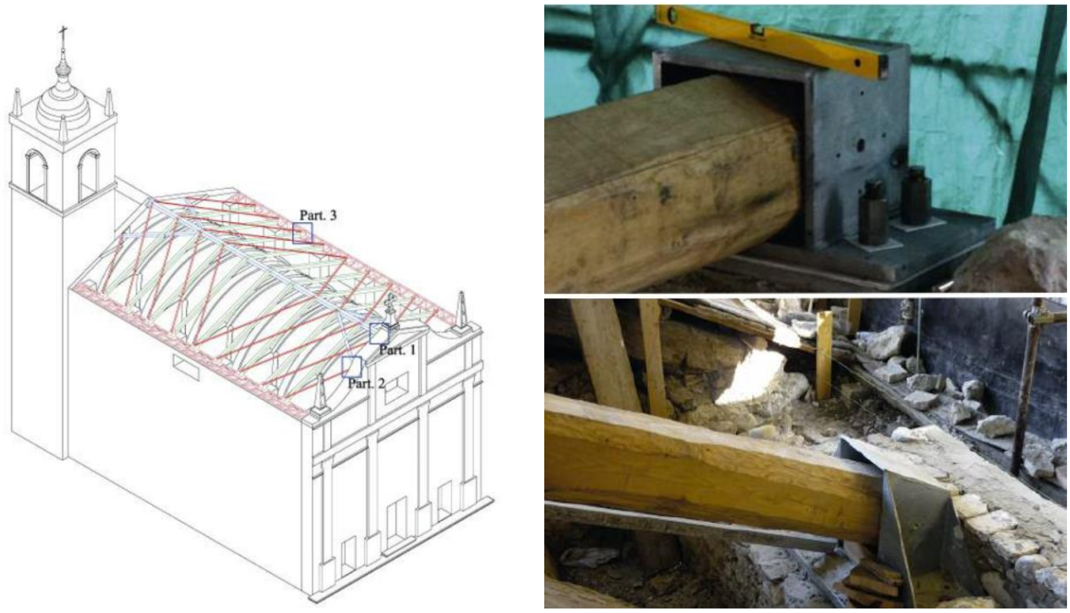

(a) (b)

Figure 2.15 Seismic strengthening of a monumental building timber roof (Quagliarini et al. 2014): (a) Drawing of the new truss system; (b) details of timber beam-to-wall links.

Figure 2.16 shows a solution called "Perimetro Forte" (strong perimeter), where steel anchors are injected to the perimeter walls and bolted to the floor in special steel clamps (LECA 2021). Reinforcing bars are seated onto the clamps longitudinally to the walls, and a reinforced cementitious slab of minimum 6 cm is laid over and anchored to the existing floor through steel bolted connectors. Such solution can be easily installed over a steel or RC floor achieving a reasonable weight-to-stifness ratio.

Figure 2.16 Strengthening solution recently developed by Leca Laterlite S.P.A. (LECA 2021)

2.3 Experimental studies

Various experimental researchers have been dedicated to the study of the global behavior of URM buildings, e.g. (Magenes, Penna, and Galasco 2010), or to characterize the solely timber floor/roof or IP/OOP walls, not paying much attention to the connection between vertical and horizontal components. Not only it is essential to understand the shear and pull-out behavior of the connection, but it is also important to study the influence of the links on the overall global system. Moreover, even if retrofitting solutions comprise newly material, this is not true for the existing ones, which should be experimentally characterized.

2.3.1 Shake table tests

An experimental investigation on the dynamic behavior of reduced-scale URM buildings, including OOP walls with flexible diaphragms, was conducted by Costley and Abrams (Costley and Abrams 1996), where a steel bars framed system was developed to reflect a timber diaphragm flexible enough to have a natural frequency well separated (≤ 1/3) from that of the equivalent masonry structure with a rigid diaphragm. The steel beams were pinned at their ends to the shear walls (IP walls) making use of washers and long steel box sections (Figure 2.17a), while the floor system was tied to the transverse walls through bolted threated rods and anchor plates set in the inner and outer faces of the wall (Figure 2.17b). Test results showed that substantial strength and deformation capacity still existed after the walls cracked during the experiments, indicating residual ductility within the structure. It was suggested the story drift to define different performance levels for URM buildings in performance-based design approaches.

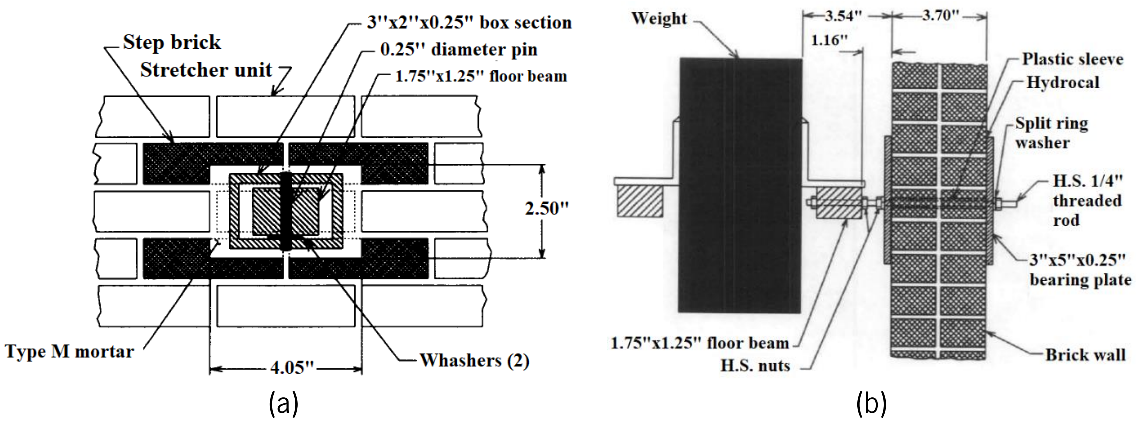

Figure 2.17 Shake table tests on reduced-scale URM building (Costley and Abrams 1996): (a) front view of floor beam-to-IP wall connection;(b) section of floor beam-to OOP wall connection.

Bothara et al. (Bothara, Dhakal, and Mander 2010) and Magenes et al. (Magenes et al. 2010) performed shake table tests on half-scale and full-scale brick and stone masonry buildings, respectively, with conventional timber floor and roof, representative of existing URM dwellings. The incremental dynamic motions in both experimental campaigns indicated OOP response of portions of the walls perpendicular to the shaking direction, especially in top story zones, in agreement with observations on similar buildings stroke by real seismic events.

A shake table experimental program carried out at EUCENTRE aimed at studying the effectiveness of improved wall-to-floor and wall-to-roof connections through comparison with the unreinforced homologous prototype (Magenes et al. 2014; Senaldi et al. 2014). Strengthening interventions included, among the others, the activation of steel tie-rods; the use of L-shaped steel beams at floor levels bolted to external steel plates; the adoption of steel through bars connected to the perimeter masonry walls and embedded into a lightweight RC slab cast above the existing floor; reinforced masonry ring beams employed at roof level. As shown in Figure 2.18, the applied strengthening techniques have clearly improved the behavior of the buildings activating IP mechanism of lateral resisting walls, typical of effective box-type buildings. However, from global experiments, the detailed mechanical characteristic of the connections was difficult to identify, therefore, local tests were needed. Further numerical analyses were recommended to evaluate different scenarios through calibrated models.

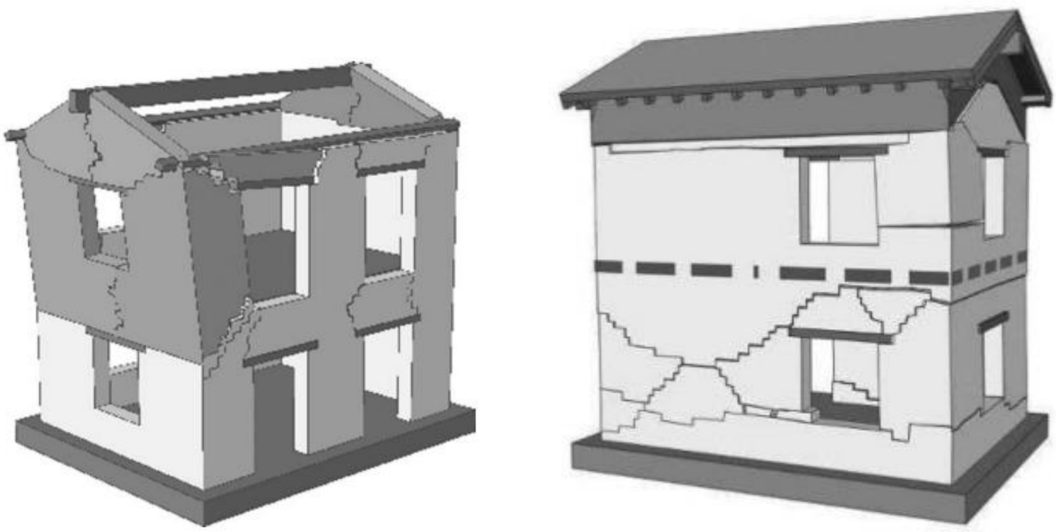

(a) (b)

Figure 2.18 Shake table tests on full-scale URM buildings performed at EUCENTRE (Magenes et al. 2014): (a) illustration of OOP mechanism on unreinforced building under nominal PGA of 0.4 g; (b) illustration of shear failure modes on reinforced prototype under nominal PGA of 0.7 g.

Three-leaf URM building models have been studied by Vintzileou et al (2015) through half-scale shake table tests. After initial shake, the damaged model was retrofitted (the timber floor was stiffened and accurately linked to the wall, reinforced through hydraulic lime based grout injections) to study the effect of widely applied intervention techniques. The wall-to-floor reinforcement was made by connecting the stiffened deck to the masonry with stell plates and grouted bar bolted each other. The selected scheme of interventions was very efficient, and it made the model able to sustain strong input motion, relying on the injections to enhance the OOP resistance of the external masonry leaf and its mechanical properties.

Dazio (2008) investigated the effect of different top and bottom boundary conditions ranging from fully fixed to simply supported, on the OOP behavior of the URM brick wall, applying different levels of initial axial load and varying the wall slenderness. Shaking table test results showed that boundary conditions could have larger effect on the lateral stability of a URM wall then its slenderness, and it was observed that simply supported walls could reach higher displacement capacity in comparison to the restrained one.

Simsir et al (2004) performed a shake table test set-up to investigate the response of OOP wall component as an integral part of the building system, where the floor mass was supported on the walls by means of a pin connection, while timber diaphragm (floor or roof) was simulated using different steel profiles connected to the walls through almost perfect pin connections. Mid-height collapses of the wall resulted only for low level of axial load and significant mass of the wall, corresponding to upper floors in real buildings. The authors measured peak accelerations values at the top and mid-height of the wall up to 4.5 times the peak base accelerations. In this study, the influence of adjacent IP walls and the deformability of the diaphragm-to-wall connection are neglected.

2.3.2 Wall-diaphragm anchor test

Accurate accounting for the connections into the numerical model requires their mechanical static and dynamic characterization and this is not usually obtained or addressed after shake table test on building or local wall scale. Detail-scale experiments (pull-out or shear tests) can be useful to address this problem aiming at force-displacement curves of existing or improved/repaired prototype connections.

In New Zealand the dynamic behavior of two types or URM walls anchors was performed by Jacks and Beattie (Jacks and Beattie 1990). Both through-bolt and epoxied-in anchors were investigated through pull-out tests. From the dynamic and static tests of the through-bolt anchors, no pull-out failure of the URM panel was observed even under high load levels (96 kN of dynamic and 200 kN of static loads) indicating the effectiveness of the practice for anchoring URM walls. From the static tests of the epoxied-in anchors, the anchorage failure was related to the crack occurred across the full width of the test panels.

Lin and LaFave (Lin and LaFave 2012) conducted static monotonic, as well as static and dynamic cyclic tests on two different types of typical brick wall to wood diaphragm connection specimens, with and without nailed strap anchors (Figure 2.19a). The authors considered the contribution of friction and of strap anchors nails loaded in shear separately and together. A value of friction coefficient was suggested as the average measured, well compared with historically published values. The behavior under dynamic cyclic loading was more brittle than behavior under monotonic or quasi-static cyclic loading, for the case of connections with nails and friction (Figure 2.19b). Results obtained from those tests can be used to calibrate nonlinear finite element models of these types of connections.

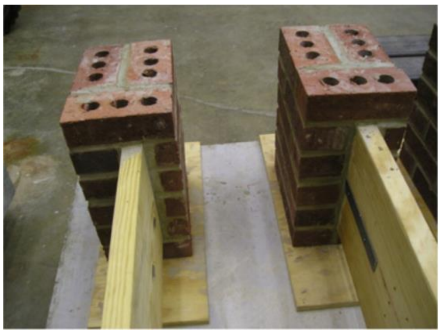

(a)

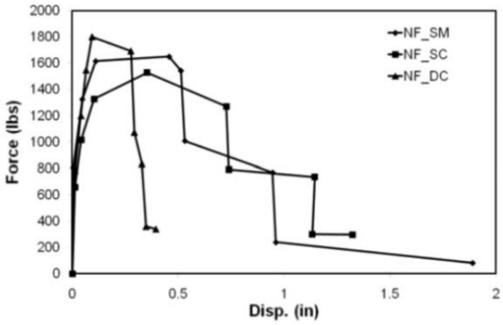

(b)

Figure 2.19 Experimental campaign performed by Lin and LaFave (2012): (a) test specimens of wall-diaphragm connections; (b) experimental curves. NF: nails and friction, SM: static monotonic, SC: static cyclic, DC: dynamic cyclic.

Campbell et al. (2012) studied typical existing wall-diaphragm anchor plate connections, extracted post-earthquake by sorting through the demolition debris from URM buildings damaged in the 2010 M7.1 Darfield (Christchurch) earthquake. The connections consisted of long, roughly 25mm diameter rod, with a rectangular or circular steel plate (about 5mm thick) attached to the wall end that is about 5mm wide x 450 mm long and fastened to the rod and positioned either inside the brick wall or in the center of a masonry pier or wall (Figure 2.20a). The authors established at least seven plausible failure modes associated with the wall-diaphragm anchor plate connections that were axially loaded to rupture (Figure 2.20b) (A Punching shear failure of masonry; B. Yield or rupture of connector rod; C. Rupture at join between connector rod and joist plate; D. Splitting of joist or stringer; E. Failure of fixing at joist plate; F. Splitting or fracture of anchor plate; G. Yield or rupture at threaded nut), based on 2010/11 Canterbury earthquake sequence damage observations and on a small amount of anchor samples tested (only six anchor plate connections). A lower 5th percentile characteristic ultimate tensile strength of 63.9kN was suggested for connections having anchor plates of approximately 200 mm diameter and connector rods of approximately 17 mm diameter. For degraded connections a 5th percentile characteristic ultimate stress of 269.5 MPa was recommended, but further testing to be undertaken was suggested to increase the test dataset.

Karim et al (2013) studied experimentally the WD connection focusing on the failure of the timber joist bolted connection. They recommended a set of design equations to assess the strength of the connection related to the minimum strength value that will govern the capacity of the whole connections. This procedure could quantitatively and quickly assess the performance level of wall-diaphragm connection, which could be reinforced, if necessary.

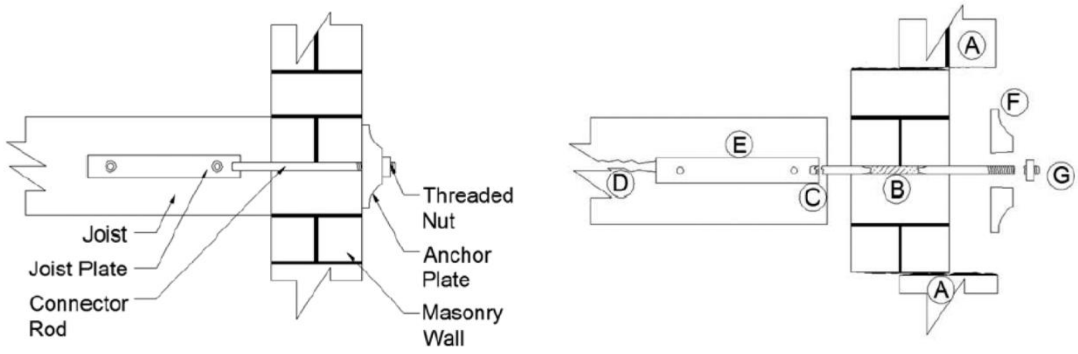

(a) (b)

Figure 2.20 Typical New Zealand wall-diaphragm anchor plate connections (2012): (a) connection assembly; (b) location of failure modes.

Moreira (2015) carried out an experimental campaign on both un-strengthened and strengthened wall-to-floor connections typical of late 19th century in Lisbon. The strengthened connection relied on anchoring the timber floor to the masonry wall through the use of steel tie-rods with anchor plates. Hinges at both ends reduced the bending force induced by the timber beam to the anchor, diagonally infixed into the masonry (Figure 2.10b). Both quasi-static monotonic and cyclic pull-out tests were carried out. In all unstrengthened specimens monotonic tests were performed and the two nails connecting the joists to the wall-plate failed causing clear sliding (Figure 2.21a,b) and the capacity was highly influenced by the rotation of the joist. For the strengthened connections, yielding of the steel angle, crushing and shearing of the timber was observed (Figure 2.21d), and the tensile capacity of the connections was approximately 19 times greater than the one of the unstrengthened ones and the ultimate displacements were much larger by comparison. However, a decrease in ductility could be observed due to increase of the elastic limit and cyclic tests degradation (Figure 2.21c,e). A retrofit design proposal was recommended for design at component level and future works are necessary to establish hysteretic rules useful to implement the connection as an element in numerical models of whole buildings.

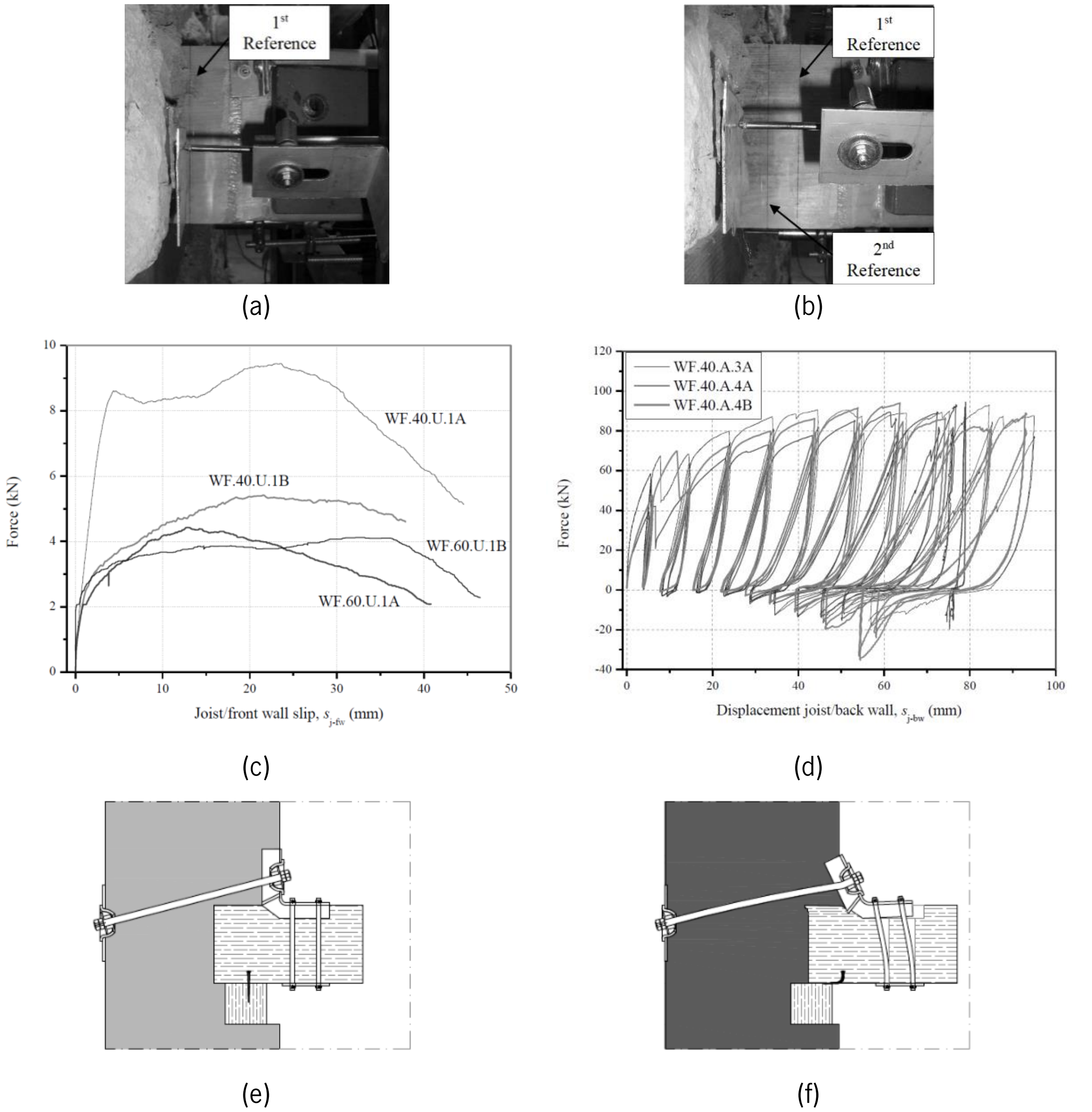

Figure 2.21 Experimental campaign performed by Moreira (2015): (a) and (b) sliding of the timber joist caused by failing of nails before and after; (c) monotonic force-displacement curve of unstrengthened specimen; (d) cyclic curves for strengthened tests. (e) and (f) deformation of pulled-out strengthened specimen before and after; Curve label: WF.TT.S.NL: where WF:wall-to-floor connection, TT: wall thickness, S: Unstrengthened (U) or Strengthened (A) configuration, NL: sample number;

Ismail (2016) tested 40 grouted/epoxied anchors for pull-out-capacity (POC) of which 30 were installed in salvaged heritage material assemblages and 10 in-situ at a heritage URM building. Two types of anchors were considered in this study: (1) helically shaped stainless steel 10 mm anchors; and (2) self-cutting stainless steel anchors with 12 mm diameter. The author investigated the influence of embedment length, installation quality, anchor location, condition of masonry and condition of substrate materials on anchor performance. The highest probability of failure during an earthquake is associated to the failure of anchor-diaphragm connection and thus limits the achievable POC of the wall to diaphragm anchorage system. However, this type of failure was observed to be reasonably ductile.

A consistent experimental campaign (almost 400 specimens) was undertaken by Dizhur et al. (2016) on adhesive anchor connections between unreinforced clay brick URM walls and roof or floor diaphragms. No conical masonry failure surface was observed in any of the tests.

Cementitious grout was a suitable anchor adhesive and 16 mm anchor rod diameter was considered to be the optimum rod size for the POC of the adhesive anchor. Low overburden weight negatively influences the POC and accurate installation process is critical to achieving adequate POC. The authors proposed a design equation of the POC of adhesive anchors considering relevant parameters and based on the concrete breakout strength of an anchor in tension as proposed by Fuchs et al. (1995). No strength reduction factor is required, except when ultra-weak masonry, or particularly low overburden loads, are encountered.

Recently, Dizhur et al (2018) undertook experimental tests on original vintage wall-to diaphragm plate anchor connections installed in an URM buildings, built in 1913. Two different types of anchorages between the masonry anchor and the timber diaphragm were studied: (i) metal connector directly fixed to the timber joist through a bolted joist plate (Figure 2.22a), and (ii) connections making use of timber blocking (vertical or horizontal timber elements interconnected between the joists) (Figure 2.22c). Failure modes and force- displacement curves were provided for the plate anchor, while ultimate capacity was established for the timber blocking systems with different configurations (Figure 2.22b, d). Among the main outcomes from the experimental campaign results, authors highlighted that timber joist splitting was the most commonly observed failure mode for joist plate anchor connections. While positioning the timber blocking horizontally allowed the highest performance to be achieved. Finally, when a small washer was used, timber bearing failure was observed in timber blocking systems.

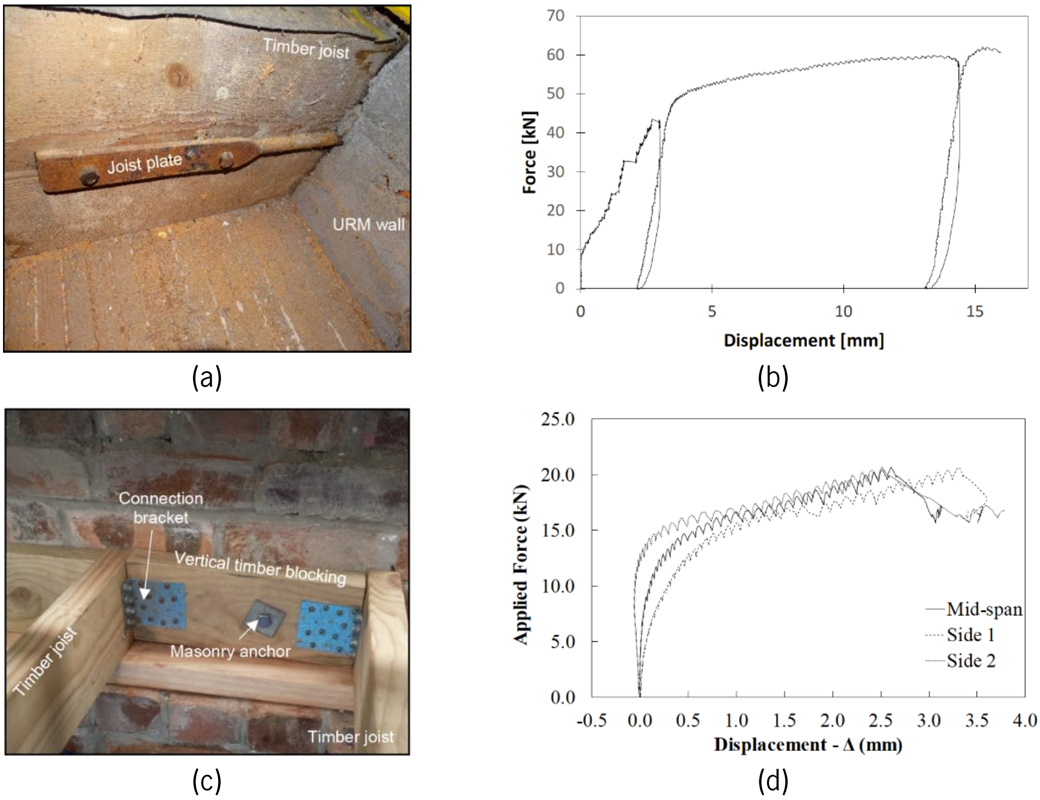

Figure 2.22 Wall-to-diaphragm experimental tests by Dizhur et al (2018) : (a) joist plate connection; (b) joist plate connection exhibiting anchor rod rupture; (c) timber blocking connection; (d) vertical timber blocking connection exhibiting screw withdrawal.

2.4 Numerical studies and code standards

Basically, an existing URM building can ben seismically assessed comparing its capacity (C) to the seismic demand (D) through the following inequality:

$$\boldsymbol{C} > \boldsymbol{D} \tag{2.1}$$

Different definitions of both the capacity and the demand lead to several approaches, which can be mainly grouped into two big families: force- based approaches (FBA), and displacement-based-approaches (DBA) (Casapulla, Giresini, and Lourenço 2017; Ferreira, Costa, and Costa 2015; Sorrentino et al. 2017). Energy-based-approaches (EBA) were also recently proposed by Sorrentino et al. (2017) and Giresini (2016) as a promising tool, but still less conservative procedure for assess the seismic response of local OOP masonry walls, if compared to current code verifications. A considerable number of modelling techniques have been developed for the seismic analysis and assessment of URM constructions in a building scale (e.g. de Felice et al. 2017; Penna 2015) and local scale (i.e. OOP mechanism) (e.g. Ferreira et al. 2015; Sorrentino et al. 2017), but only few included the behavior of the connections between vertical and horizontal members interfaces (e.g. Ewing and Kariotis 1981; Landi, Gabellieri, and Diotallevi

2015; Simsir et al. 2004). Moreover, authors often considered the connection assuming simplified hypothesis (i.e. perfect hinges or linear elastic springs), neglecting the cyclic nonlinear behavior, typical for many typologies of links and reducing the number of the degrees of complexity of the dynamic problem.

The most common modelling techniques comprise rigid block approaches, numerical finite elements models (FEM), and distinct (or discrete) elements models (DEM). For rigid block approaches, the capacity can be computed through static or kinematic analysis, while the demand is usually derived from the displacement response spectrum, based on the period of the equivalent SDOF system. When NLTH analysis is used, however, the demand can be related to the PGA or other Intensity Measures (IMs) of the ground motion leading to a certain level of damage or collapse. Static pushover and dynamic analysis with time step integration under artificial or real accelerograms are common tools when FEM or DEM techniques are adopted (Lemos 2007; Pantò et al. 2017). For the former analysis the capacity can be defined as the peak of the response curve, while for the latter the maximum response value in terms of acceleration can be considered. It must be noted that FBA are preferred by practitioners as simple and direct methods, in spite of high conservative results, while DBA appears to be adequate for cracked walls falling into the nonlinear range (Sorrentino et al. 2017).

2.4.1 Global scale approaches

Priestly (1985) proposed a DBA for the assessment of URM buildings, for which the author identified a seismic-load path: the earthquake excitation at the footing was filtered by the IP response of shear walls and floor diaphragms and reached OOP walls (Figure 2.23). The acceleration capacity was based on an “equal energy” criterion, while the acceleration demand was based on the height of the building, ratio of the period of the floor and shear walls. The analyses produced expected results, but assumptions were made, such as that the walls were properly connected to floor and roof (even if generally this was not the case).

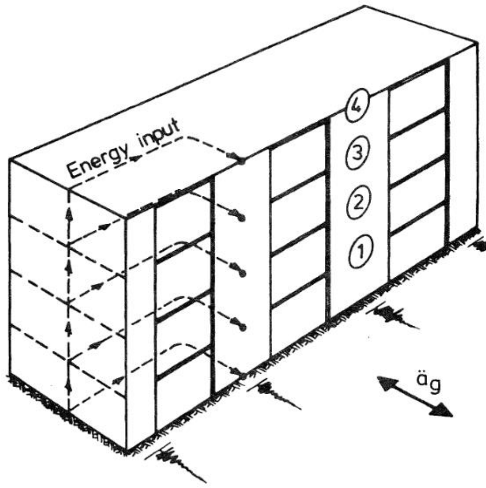

Figure 2.23 Seismic load path in URM according to Priestly (1985).

The influence of the floor on the seismic response of URM structures was studied by Tena-Colunga and Abrams (1996) through discrete MDOF dynamic models, based on linear masonry behavior and flexible and linear diaphragms (elastic springs). Mainly two structures served as case-study (Figure 2.24), and result demonstrated that, in some cases, diaphragm and shear-wall accelerations can increase with the flexibility of the diaphragm. Moreover, torsional forces could reduce considerably as diaphragm flexibility increased. Finally, the authors stated that the period of vibration of systems with flexible diaphragms could be underestimated if calculated through approximate expressions prescribed in current seismic codes.

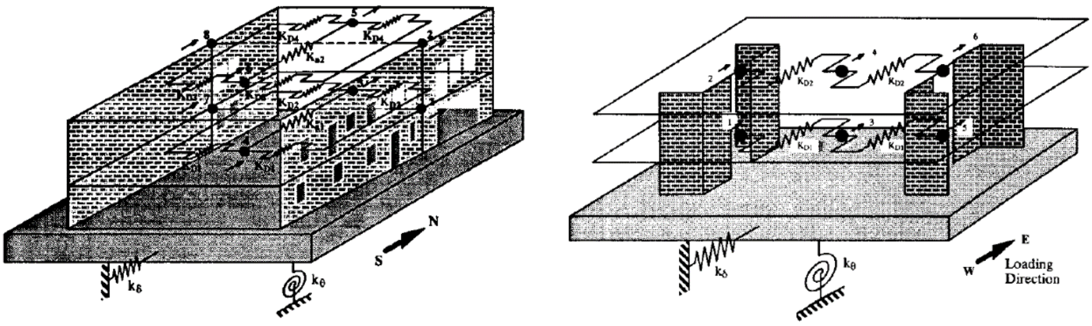

(a) (b)

Figure 2.24 Modelling of buildings through discrete dynamic models by Tena-Colunga and Abrams (1996): (a) firehouse; (b) office building.

An unconventional procedure for the simulation of the OOP dynamic behavior of URM buildings, considering the stiffness of the roof, was performed by Costa (2012), where the local mechanisms were modelled as kinematic chains of masonry portions (normally assumed as infinitely rigid bodies) whose nonlinear behavior is concentrated at the contact regions (Figure 2.25). the author considered a Coulomb-type sliding friction law and energy dissipation through the restitution coefficient at the impacts. Springs simulated the IP stiffness of the horizontal diaphragm. Lumped mass located at the ridge and top spreader beams represented the roof mass. Similarities of the method can be found in the modelling technique used by Oliveira et al (2002) based on DEM method for the interpretation of the post-seismic damage in URM structures. This methodology was adopted to simulate the experimental behavior of a full scale URM unstrengthened building tested at EUCENTRE (described in Section 2.3.1), for which elastic springs were placed at the top of each roof pitch (with a stiffness of 1.49 MN/m defined according to results obtained by Brignola et al (2008). The adopted numerical approach allowed simulating the experimental failure mode with sufficient accuracy, but further studies were suggested to obtain an adequate and suitable method for the simulation of the OOP behavior of masonry walls. As highlighted by Ferreira et al (2015), the main advantages of such methodology rely on the time efficiency and the mechanical parameters (using only geometric parameters, mass, friction coefficient and restitution coefficient), while the predefinition of the formed local mechanisms need further analysis or judgement to define a realist overturning mechanism, setting the limits and the drawback of the method.

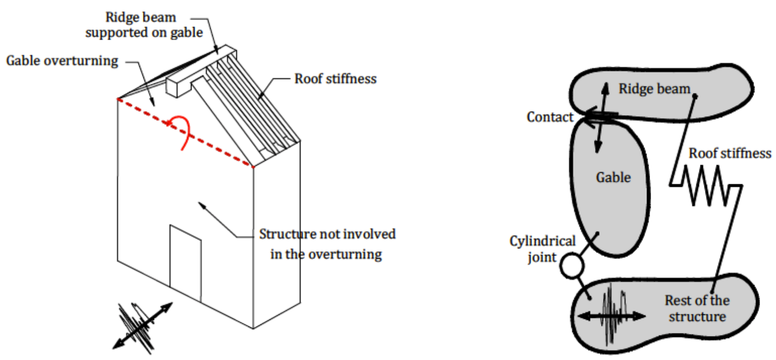

Figure 2.25 Schematic representation of the equivalent Multi-body dynamics-based approach (Costa 2012).

Ortega et al (2018) developed a parametric study through a detailed FEM and pushover analyses aiming at the evaluation and quantification of the influence of the type of diaphragm in the seismic behavior of vernacular buildings (Figure 2.26a). Among the different parameters that have been analysed, the connection between the timber beams and the walls, and the connection between the timber deck and the masonry were studied, considering different embedment and connection conditions. Results clearly showed the important increase in seismic resistance of the building if proper connections were adopted (i.e. timber beams fully embedded inside the whole thickness of the wall, and cross-board sheathing infixed in the walls), see Figure 2.26b, avoiding the prematurely cone failure on the masonry and a better redistribution of the forces to the IP walls. The adoption of rigid diaphragms with low levels of connections between the timber beams and the walls resulted to be ineffective. Besides FE approaches is rarely adopted from practitioners for masonry constructions, several examples demonstrate its capabilities also for large complex structures (Formisano, Ciccone, and Mele 2017). Nonlinear mechanical characteristics of the masonry and flexibility of the floor are few of the important parameters playing a crucial role on the vulnerability index, usually obtained through pushover analyses (Clementi et al. 2016, 2018). Because of the local behavior of structural elements, frequently observed in historical buildings due to the poor connections between each other, timber roofs of floors are often neglected as structural elements (included only as additional masses on top of the walls) (Formisano et al. 2018). When a good quality of the connection may be justified, the diaphragm timber beams can be included in the global 3d model, but the connection is usually perfect (acceptable only for properly retrofitted connections or new buildings).

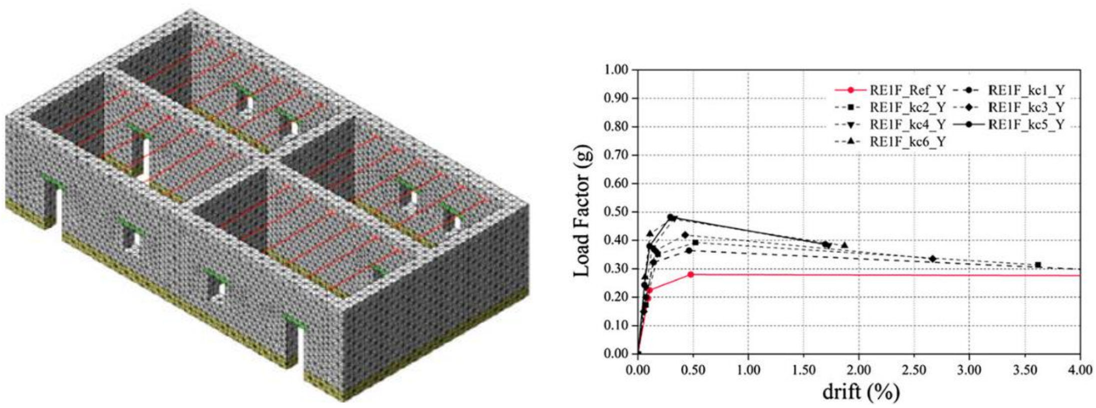

(a) (b)

Figure 2.26 Detailed FEM developed by Ortega et al (2018) in order to evaluate the influence of beam-to-wall connection: (a) one of the three case study buildings; (b) positive influence of proper beams-to-walls connections. Labels: RE1F: one-floor rammed earth building; Ref: reference model with no diaphragm, kc1,2,3,4,5,6: beams-to-wall connection increasing quality (from 0 to full thickness embedment). Y: load direction.

Senaldi et al (2014) simulated the experimental results by using an Equivalent Frame (EF) approach implemented in the program TREMURI (Lagomarsino et al. 2013). The macro-element model (Figure 2.27a) allowed for the shear-sliding damage evolution and rocking mechanism, with toe-crushing effect. Nonlinear beam elements have been introduced to account for the presence of the RC ring beam and of the wall to diaphragm connections at floor level. Pushover curves were compared to the experimental resistance curve, showing well similarities (Figure 2.27b). The equivalent frame modelling may be considered as a simplified approach, preferred by professional, for a first conservative approach for the seismic assessment of existing URM buildings. This approach, however, is not recommended for buildings with irregular opening patterns, high flexible floors and poor wall-to-floor and wall-to-connection (Quagliarini, Maracchini, and Clementi 2017).

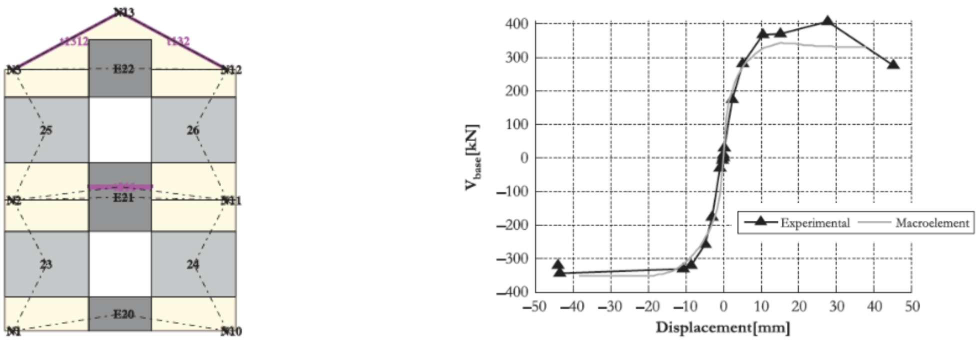

(a) (b)

Figure 2.27 Experimental model implemented in TREMURI program (2014): (a) geometry of the model; (b) experimental vs. numerical pushover curves.

A simplilfied modeling approach was presented based on three dimensional discrete elements as an extension of a plane macro-element (Pantò et al. 2016). The proposed approach lies in between the more complex, computationally cumbersome and more detailed nonlinear FE method and the classical limit approach and shows the capability of simulating the nonlinear response of monumental structures. The dynamic behavior of the structural connections is not usually taken into account.

2.4.2 Local scale approaches

Cross et al. (1994) provided a useful tool for the design of seismic retrofit details developing a FEM that accounts for friction and impact behavior at the diaphragm-to-wall interface. The effectiveness of the model was demonstrated through comparison to some MDOF systems and applying this approach to a historic brick building shaken during the Loma Prieta 1989 earthquake.

The influence of strengthening techniques (e.g., insertion of tie-rods, of rigid diaphragms, etc) was studied by Giuffrè (1994) through a rigid-body limit analysis on a comparative basis. The safety check was given between the maximum horizontal load multipliers causing OOP mechanisms, and an expected PGA normalized to gravity. A response spectrum for the bilinear non-dissipative model was proposed allowing to evaluate the maximum displacement expected as function of the PGA and several parameters concerning the static strength of the model to horizontal forces. On the same bases, D'Ayala and Speranza (2003) developed a simple but realistic mechanical model, based on post-earth-quake damage observations, capable of handling a large number of buildings and performing statical analysis. The model allowed to consider the influence of seismic strengthening (insertion of ring beams and ties), proving their efficiency, especially for slender vulnerable buildings. Several load factor equations were giver for each over-turning mechanisms (e.g. Figure 2.28) without and with the presence of strengthening devices (for which the arch effect was taken into account), and implem ented in the FaMIVE (Failure Mechanism Identification and Vulnerability Evaluation) procedure for the online evaluation of a façade or building seismic vulnerability.

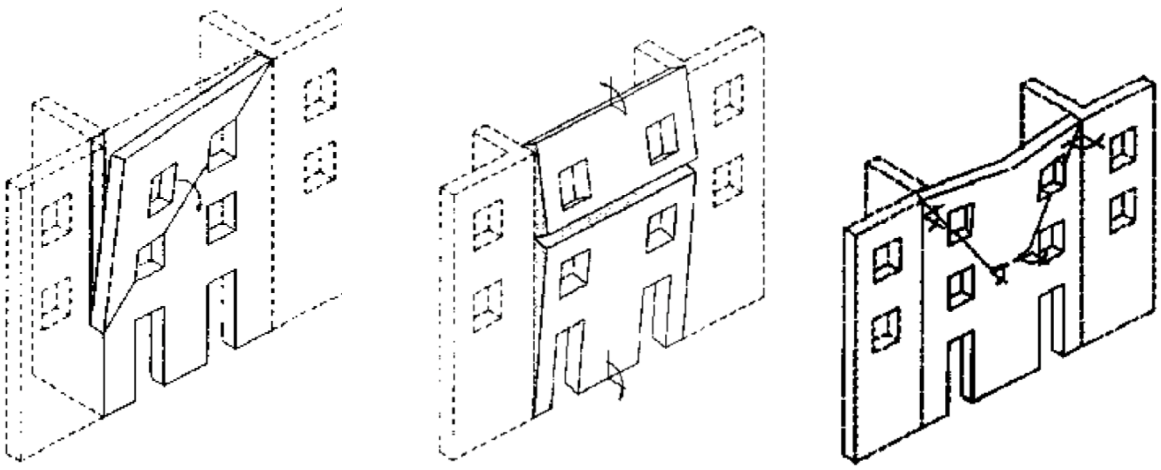

(a) (b) (c)

Figure 2.28 Mechanisms for overturning failures studied by D'Ayala and Speranza (2003)

Lawrence and Marshall (2000) proposed a new approach for the design of masonry OOP panels based on the knowledge of the likely crack lines, through application of virtual work principles. A design equation was given for different boundary conditions (the top of the masonry panel was considered either free or simply supported) and results were compared with several tests available in literature providing closer estimates with low variability. The method also allowed for the presence of door and window openings.

A two-degree-of-freedom model was introduced by Simsir et al (2004) as an assemblage of two rigid bars interconnected by rotational springs, simulating the cracked wall tested experimentally. The connection on the top was modelled as elastic spring representing the stiffness of the IP wall and the diaphragm connected in series (Figure 2.29b). The authors also compared a SDOF (Figure 2.29a) to a MDOF (Figure 2.29c) model to study the influence of OOP bending caused by cracks at the bed joints. The SDOF model seemed to be inaccurate if compared to MDOF, as could not capture higher mode response observed experimentally (i.e. it could not model the formation of the mid-height wall crack as shown in the experimental test result in Figure 2.29d, while the two-degree-of-freedom model revealed to be a simple and efficient tool for the evaluation of the seismic vulnerability of OOP walls showing sufficient experimental validation.

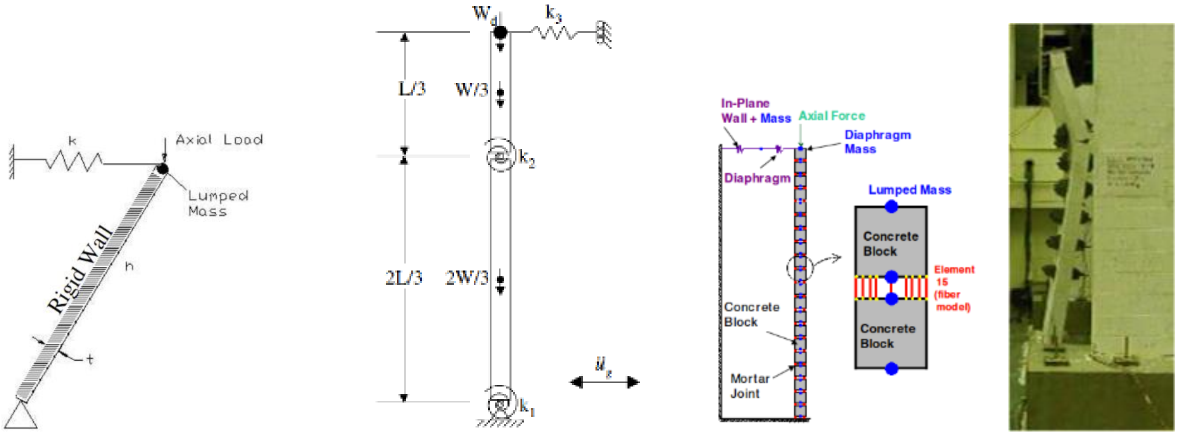

(a) (b) (c) (d)

Figure 2.29 Numerical and experimental studies carried out by Simsir et al (2004): (a) SDOF model; (b) 2DOF model; (c) MDOF model; (d) damaged specimen after tests.

When a monolithic behavior is a reliable assumption for the walls in OOP, they can be regarded as rigid blocks, and possible reliable approaches can be rocking and kinematic dynamics analysis simulating the local behavior.

Basis on rocking blocks can be found on the pioneering work of Housner (1963), who considered the motion of a SDOF free rigid block, a rigid prism with longitudinal rectangular cross section, rocking about the two corners O and O' (Figure 2.30a) subjected to free vibrations, constant and sinusoidal acceleration, and earthquake motion. Important contribution was given by Aslam et al. (1980) who considered the rocking vibrations of the free rigid block under ground motions through a computer program. Considering the rotation θ (> 0 if counter-clockwise) as a Lagrangian coordinate, the equation of motion takes the from: The energy dissipation is accounted for through the "restitution coefficient" $e_H = 1 - \frac{3}{2}\sin^2(\alpha)$, where α is the arctangent of the thickness to height ratio and is valid for slender and rectangular blocks. Giresini et al. (2018, 2016) modified the equation of motion to consider the influence of possible roof mass, thrust and horizontal restraint through single or bed spring with stiffness K, or K', respectively, simulating a tie-rod, a flexible diaphragm or transverse walls (Figure 2.30b). Comparison with experimental results demonstrated the accuracy of the method, contrary to the non-linear kinematic approach suggested by the Italian code for OOP mechanism. An improvement of the approach was performed by AlShawa et al. (2019) who considered the plasticity of tie rod. The model is used to investigate the response to variations of wall geometry and tie characteristics. The most relevant parameter was the steel strength, whereas other characteristics play minor roles allowing to recommend reduced values for pre-tensioning forces.

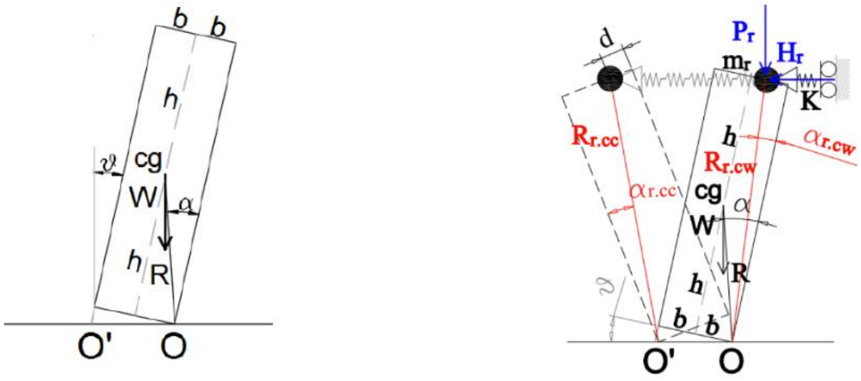

Figure 2.30 Rocking rigid block: (a) Housner free block model; (b) restrained rocking block (Giresini et al. 2016).

In cases when the degree of freedom cannot be assimilated to one (flexural bending failure modes), a MDOF dynamics could be a more realistic representation. Studies on 2DOF system consisting of two blocks, one placed on the top of other, and free to rock without sliding (Figure 2.31a), were developed by Psycharis (1990), who derived the equation of motion for each mode of vibration and analysed the redistribution of kinetic energy of the system in the blocks. Kounadis and Papadopoulos (2016) extended the study to a 3DOF system (Figure 2.31b), neglecting sliding, aiming at assessing the overturning instability with or without impact either between blocks or between the lower block and the ground.

All possible configuration patterns that may lead to rocking instability through an escaped motion were properly discussed. None of the latter studies took into consideration lateral boundary conditions. Landi et al. (2015) simulated the behavior of slender facades of URM buildings with flexible diaphragms subjected to OOP bending by means of a 2DOF model assembled as two rigid bodies connected by an intermediate hinge and restrained at the top by a spring (Figure 2.32a), while the damping has been modelled through the introduction of the coefficient of restitution.

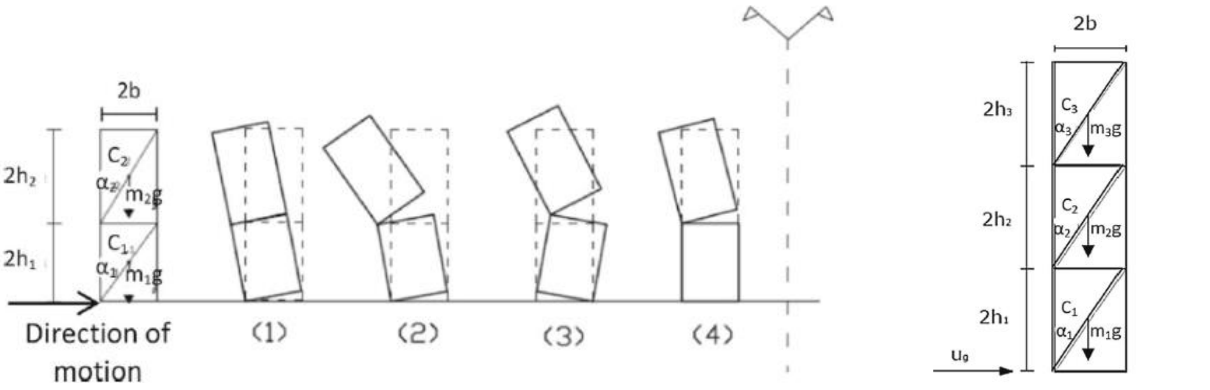

(a) (b)

Figure 2.31 MDOF configurations of rigid blocks (Kounadis and Papadopoulos 2016): (a) 2 DOF system with 4+4 possible configurations; (b) 3DOF system.

The calibrated model was used for parametric analyses (Figure 2.32b) and compared to simple models confirming its effectiveness. NLTH analyses of a set of walls subjected to recorded ground motions have been performed in order to compare the response of the simply supported wall with that of the restrained wall. Four different geometric conditions described by four corresponding sets of equations were studied, and the results compared to a simple 1DOF model, showing that with the increase of the spring stiffness, the response of the 2DOF model tended to reproduce well the response of the 1DOF model.

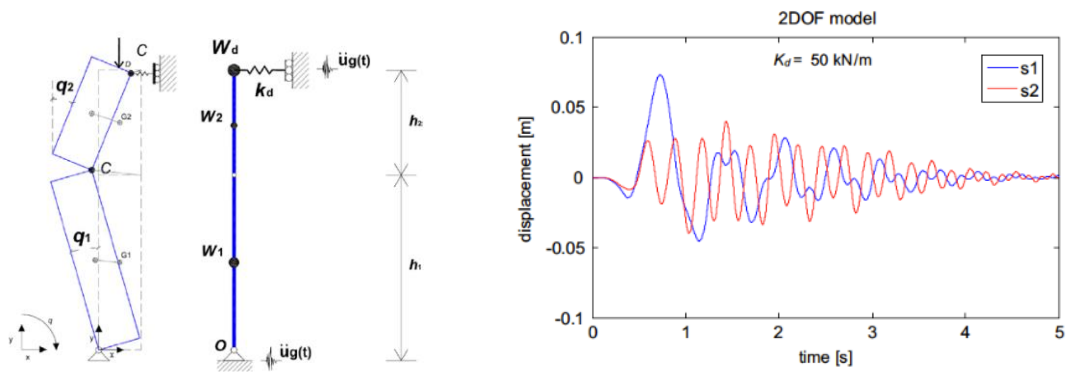

(a) (b)

Figure 2.32 2DOF model analysis of the wall in OOP bending (Landi et al. 2015): (a) illustration of the model; (b) mid-height (s1) and top (s2) displacements results for $K_d = 50kN/m$.

On the contrary, with the decrease of the spring stiffness, the top displacement increased and tended to be larger than the mid-height displacement.

A general settlement of the rocking procedure for the vulnerability of the OOP masonry wall, is still far from the professional practise. Currently for masonry structures, standard response spectra are used. A simple design method for assessing the maximum rocking displacement, using equivalent elastic characteristics and equivalent response spectrum was presented by Priestley et al. (1978)and compared to results from simulated seismic excitation of the model using an electro-hydraulic shake-table. Doherty et al (2002) presented a simplified linearized DB procedure based on a trilinear force-displacement relationship of the URM walls (Figure 2.33a). The authors considered both the free and simply supported condition on top (Figure 2.33b) and compared the procedure with NLTH analyses results and with quasi-static analysis showing that less scatter could be reached through DB approach rather than FB procedures. The selection of a proper substitute structure was recommended for each case and the secant stiffness was defined, which was found to correlate well with the predominant natural frequencies observed during experimental testing.

However, distinct differences were noted between rocking spectrum and the classic design response spectrum. Makris and Konstantinidis (2003) concluded that the rocking structures cannot be replaced by "equivalent" SDOF oscillators.

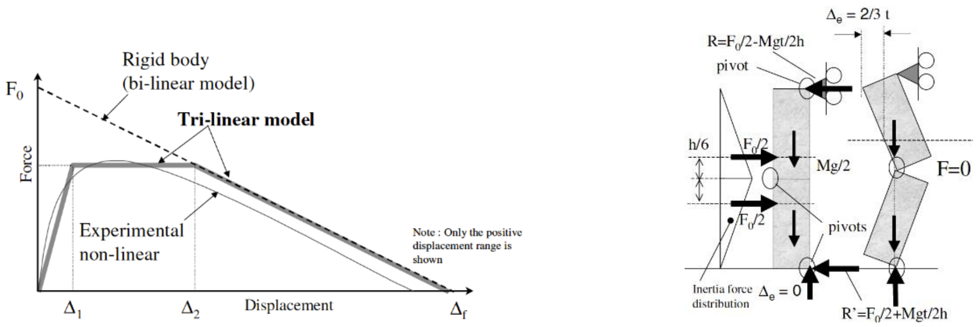

(a) (b)

Figure 2.33 Linearized DB approached proposed by Doherty et al. (2002): (a) force-displacement relationship of URM walls; (b) simply supported masonry wall on top.

2.4.3 Code standards

The seismic capacity of a local mechanism (i.e. OOP wall failure) can be assessed in terms of ultimate displacement through a non-linear kinematic analysis, considering forces given by possible restrains (steel tie rods, beam, etc) as recommended in the Italian code (C.S.LL.PP. 2019; DMI 2018), if the monolithic behavior of the block is reasonably assumed. This approach is based on the equilibrium limit analysis and allows for the calculation of the horizontal force which the structure is able to resist, during the evolution of the mechanism. This force-displacement curve can be transformed into the equivalent single Degree of Freedom (DOF) system capacity curve (Figure 2.34a) where the Ultimate Limit State (ULS) capacity, d_u^* is defined in terms of spectral displacement d^* and compared to the spectral seismic displacement demand, $S_{De}(T_s)$ based on the secant period, obtained from the capacity curve:

$$\boldsymbol{d_u^* \geq S_{De}(T_s)} \qquad 2.2$$

The Italian code standard also allows for the Damage Limit State (DLS) assessment through the following:

$$a_0^* \geq a_g S \qquad 2.3$$

Where s accounts for the type of soil and geographic conditions, while a_g is the reference acceleration for the specific geographic coordinates, and a_0^* is the spectral acceleration that activates the mechanism (Figure 2.34a). Moreover, the normative was found to be too conservative for some case studies (Giresini 2016b). On the bases of recent research works (Degli Abbati, Cattari, and Lagomarsino 2018; Degli Abbati and Lagomarsino 2017; Lagomarsino 2014) the new Italian standard (DMI 2018) allows to consider the amplified floor Response Spectrum in case of local mechanisms placed at higher levels of the structure. The seismic demand is defined in terms of overdamped elastic Acceleration Displacement Response spectrum (ADRS), to be compared to the multi-linear capacity curve, accounting for the initial dynamic elastic response (Figure 2.34b).

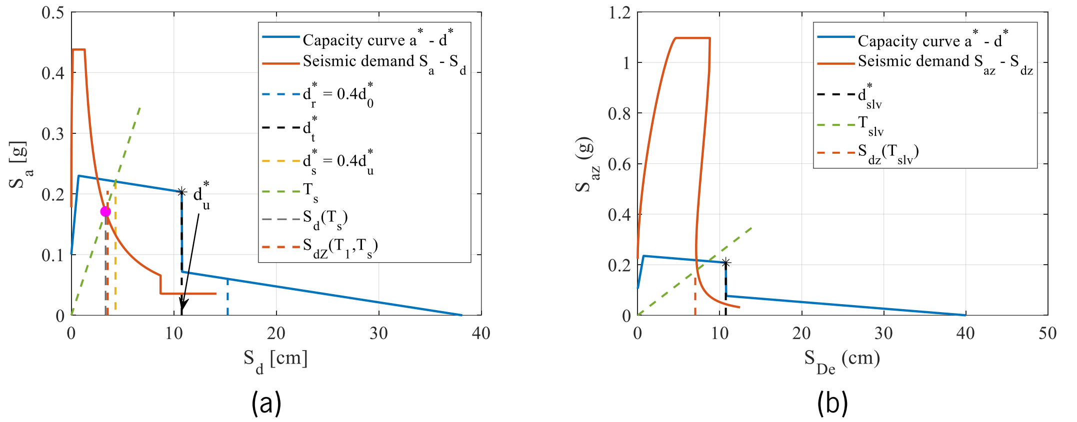

Figure 2.34 ULS assessment through the kinematic approach of a masonry wall restrained by a elastic-perfectly plastic spring on top, according to Italian code: (a) NTC2008 (C.S.LL.PP. 2009); (b) NTC2018 (DMI 2018).

The previous standard (C.S.LL.PP. 2009) considers the amplification assessing simplified expressions, (e.g. C8A.4.12 for ULS),

$$d_u^* \geq S_{DZ}(T_1, T_s) = S_{De}(T_1) \cdot \psi(Z) \cdot \gamma \frac{\left(\frac{T_s}{T_1}\right)^2}{\sqrt{\left(1 - \frac{T_s}{T_1}\right)^2 + 0.02\frac{T_s}{T_1}}} \qquad 2.4$$

Where S_{De} is the elastic displacement response spectrum; T_1 is the period of the first mode shape of the structure in the interested direction: $\psi(\boldsymbol{Z})$ is the normalized mode shape assumed as Z/H, where Z is the level of the locale mechanism, while H is the total height of the structure; γ is the coefficient of modal participation and can be assumed as $3N/(2N+1)$, where N is the number of floors of the building. The spectral demand based on floor spectra may be significantly higher if compared to the previous guideline.

The evaluation of load factors through the kinematic method of limit analysis was recently updated by using rigid-block modelling. An original criterion to account for the frictional resistance in the rocking-sliding failures of URM walls was proposed to assess their in-plane and out-of-plane behavior (C. Casapulla; L. U. Argiento 2018). This criterion was validated and applied e.g. to the analysis of the local failure of masonry corners accounting for the role of thrusting timber roofs (Casapulla et al. 2018).

If compared to FBA, DBA provide a more rational means of determining seismic design actions for unreinforced masonry walls, avoiding inevitable material mechanical characterization (Ferreira et al. 2015). The limitation of such formulations relies on the quantification of the displacement limit parameters which are calibrated based only on experimental data.

FEMA 547 (FEMA 2006b) addresses inadequate or missing wall-to-diaphragm tie deficiencies suggesting the use of tension and shear ties. Such anchors should transfer OOP inertial loads perpendicular to the face of the masonry back into the diaphragm or shear loads from the diaphragm into the wall where they are resisted by IP action. For tension anchors the use of through bolt anchored to an external steel plate and welded to an internal steel strap, nailed to the joists and timber blockings is suggested in the case of connections with joists parallel to wall. On the other hand, a steel angle connection is suggested for connections where joists are perpendicular to the wall. Adhesive anchors are also recommended for aesthetic reasons giving details of the connection procedure and material to use. A threaded rod is commonly suggested as ATSM A36 all-thread rod, relatively ductile material with high strength capacity. As highlighted from the guideline, holes need to be drilled with a rotary drill with the percussion setting turned off to limit vibration into the wall. The use of a diamond tipped blade is suggested. Eccentricity issues, together with other aspects are discussed and some examples are shown of different types of anchorages.

The ASCE/SEI 41-13 guidelines (American Society of Civil Engineers (ASCE) 2013) covers both analysis for the evaluation of existing buildings and design of retrofit measures. Tier 3 systematic procedure is suggested as the most reliable and complete, for with the analysis must include the entire structural system. Four analysis procedures are proposed: linear static procedure (LSP), linear dynamic procedure (LDP), nonlinear static procedure (NSP), or nonlinear dynamic procedure (NDP). Adoption of linear procedures is limited to regular and simple buildings, while nonlinear procedures are encouraged to account for non linearities, usually present in existing constructions. The guidelines set forth analysis requirement in 7.2.11.1 regarding the OOP wall anchorage to diaphragms. Walls shall be anchored to diaphragms at horizontal distances not exceeding $8\,ft$ $(2.44\,m)$ and anchorage shall positively transmit the seismic forces generated into the OOP wall to the diaphragm:

$$\boldsymbol{F_p = 0.4\,S_{XS}\,K_a\,K_h\,\chi\,W_p} \tag{2.5}$$

where $\boldsymbol{S_{XS}}$ is the spectral response acceleration for the selected hazard level and damping, adjusted for the site class; K_a is a factor accounting for the flexibility of the floor (not exceeding 2.0), for different Structural Performance Level (SPL); K_h is a factor accounting for the variation in force over the height when all diaphragms are rigid; χ is a factor accounting for different SPL and W_p is the weight of the wall tributary to the wall anchor. According to this standard the pull-out and shear strength of expansion anchors and adhesive anchors shall be verified by approved test procedures, while for other types of anchors, the lower-bound values for strengths with respect to pull-out, shear and combination of both shall be calculated according to approved building code and analysed as force-controlled action. The guideline refers to ACI (ACI 2008) TMS 402 and FEMA (FEMA 2009) for the design and analysis of anchors. New Zealand guidelines recently published (NZSEE 2016) allow for both force-based and displacement-based procedures for the assessment of existing retrofitted URM building. The evaluation is based on the value of the earthquake rating for the building expressed das %NBS (Percentage of new building standard as assessed by application of these guidelines) obtained by dividing the calculated ultimate seismic capacity of the component by the ULS seismic demand with the following expression:

$$\%\boldsymbol{NBS} = \frac{\boldsymbol{Capacity}}{\boldsymbol{Demand}}\boldsymbol{x100} \tag{2.6}$$

A building is defined as earthquake risk building (ERB) if < 67% NBS. These standards define the probable capacity of diaphragm to wall connections as the lowest among 7 different failure modes. These latter failure modes are based on damage observations during 2010/11 Canterbury earthquake sequence and on studies conducted by Campbell et al. (2012) (illustrated in Section 2.3). Probable failure mechanisms are also reported for adhesive anchorages, based on Canterbury earthquake sequence, too. These include, among the others: brick work cracking of the masonry in the proximity of the anchorages loaded in flexural tension; incorrect installation; bed-joint shear failure of the brick around its perimeter. Based on the above considerations, these standards provide tables in lieu of specific testing showing probable shear strength capacity and tension pull-out capacity for different anchorage details. The demand is calculated as the support reactions of the seismic inertial forces generated from the tributary OOP walls. Retrofitted connections are recommended to be stronger than the walls.

2.5 Conclusive remarks

This chapter presented a literature review on wall-to-horizontal diaphragm (WD) connections in URM buildings, considering the typical connections found in traditional buildings and the main solutions to enhance the seismic behavior of such connections. Both experimental and numerical research studies aimed at mechanically characterizing these connections are reported and discussed. This study reveals the necessity of accounting for wall-to-floor or wall-to-roof connections in the seismic analysis of existing URM buildings and stresses the need of simple but clear guidelines for their assessment and recommendations on their numerical modelling.

Considering the peculiarity of the connections, the calibration of numerical models based on experimental data is necessary for a reliable evaluation of the seismic capacity of historical constructions. Despite pull-out monotonic and cyclic tests on detailed connections for the axial and shear capacity are appropriate for this scope, they are costly and complex to set-up. Failure mechanisms and ultimate dynamic capacity can be assessed through shaking table test on building-scale and wall-scale specimens to understand the influence of the strengthening strategy on the original poor building.

Complex and detailed finite element models reveal to accurately simulate the global behavior of the URM building but they are hardly used from professionals who look for simpler procedure (equivalent frame or macro models). Uncertainties can be found on the definition of the mechanical characteristics of masonry elements and diaphragm are aether not-considered as structural elements or they are modelled as rigidly connected to the perimeter walls. From the literature review, it is clear how the structural nonlinearities are important, especially when dealing with connections. They affect the energy dissipation of the system, and therefore they influence the assessment of both global and local mechanisms. Pushover curves are widely used in the field of masonry constructions to evaluate the ultimate force/displacement capacity taking into account those nonlinearities. Non-linear time-his-tory analysis is also considered to be a valid tool able to better simulate the structural response under real seismic input. Selection of appropriate input motions, essential for predicting reliable results is, however, a topic requiring clearly further research.

Many code standards still indicate force-based approaches for the assessment of local failure mechanism and only few refer to displacement-based approaches, in many cases more reliable in presence of local URM wall mechanisms. Currently, kinematic analysis proposed in the Italian code is the only one recognized as completely reliable in European Standards, and it can be performed in nonlinear range. Indeed, no indications are given in EC8-3 (EN 1998-3 2005) about the analysis of local mechanisms.

Furthermore, the rocking approach considers the evolution of motion during time and dissipation properties at the plastic hinge around which the masonry wall rotates are not neglected. Limitations of such approach rely on the monolithic characteristic of the block, modelled as rigid, not always true for masonry walls or facades. However, improvements of the equation of motion have been done to account for the formation of an intermediate hinge, frequently developed during OOP bending of the walls horizontally restrained on top.

In literature, only few experimental data at connection level are available involving uncertainties on the seismic evaluation of the original or reinforced buildings. Common practise is to perform parametric analyses based on the calibrated model, in order to investigate a large set of the interesting parameters. This study reveals the necessity of clear and simple ready-to-use research-based procedures grounded on experimental and numerical approaches useful for professionals to assess existing wall-to-horizontal diaphragm connections and design strengthening solutions in historical constructions.

CHAPTER 3

MODELING OF WALL-TO-HORIZONTAL DIAPHRAGM CONNECTIONS

Overview

This chapter deals with the numerical simulation of wall-to-diaphragm connections, useful for a proper assessment of the connection and subsequent seismic evaluation of the building as a whole. The available experimental results are used to confirm and support the proposed analytical formulation and numerical modelling. The connection models here proposed are useful for being applied to conventional seismic assessment procedures and even to more advanced systems.

3.1 Experimental background

An accurate definition of nonlinear constitutive law valid for structural connections is only possible after proper numerical calibration of hysteretic models based upon experimental data. Only few experimental works were devoted to the detailed mechanical characterization of WD connections (Abdul Karim et al. 2013; Campbell et al. 2012; Jacks and Beattie 1990; Lin and LaFave 2012). The numerical development carried out herein was encouraged by the considerable experimental campaign done by Moreira (2015) on typical late 19th century

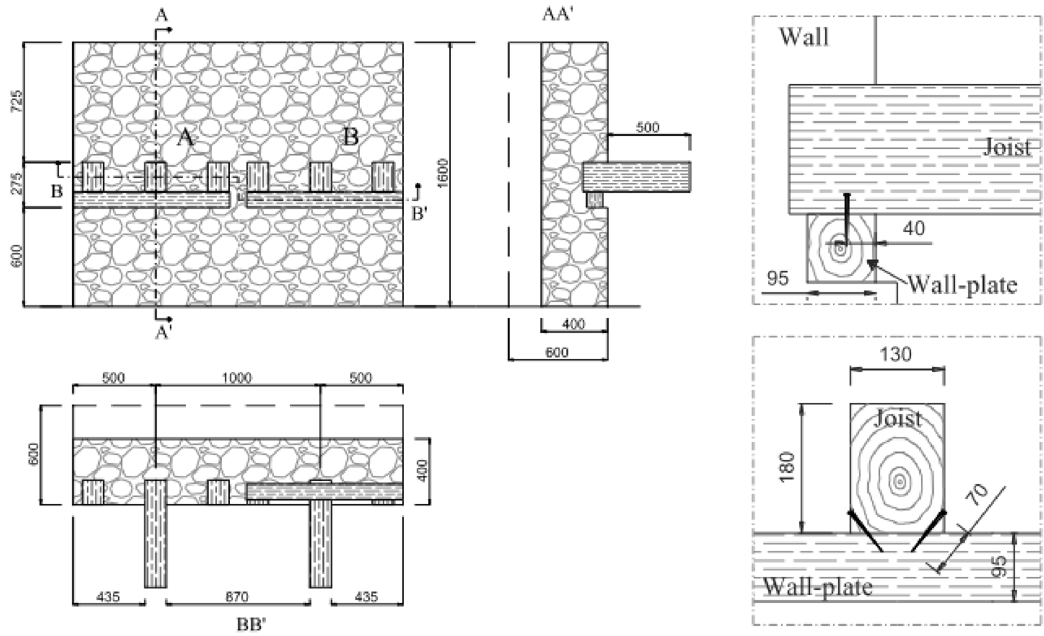

(a)

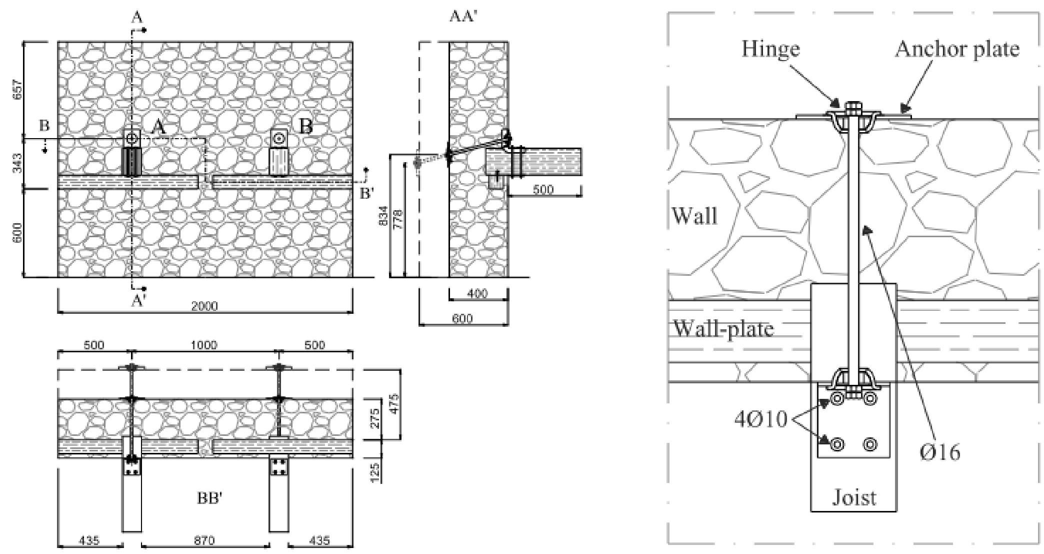

(b)

Figure 3.1 Drawings of WD connections experimentally tested by Moreira (2015)*: (a) unstrengthened configuration; (b) strengthened configuration.*

connections of Lisbon assets representative of weak existing WD connections and restrained configuration (Section 2.3). The experimental configurations are displayed in Figure 3.1.

A total of twenty quasi-static tests was carried out, twelve of which can be considered valid (Table 3.1). Two wall thickness values with different vertical stress levels were considered simulating connections at different floor levels. Strengthened configurations were tested in both monotonic and cyclic procedures, whilst only monotonic experimental curves are available for the unstrengthened configurations. It must be highlighted that every test was carried out on undamaged samples. The reinforced connection was seen to be promising for the seismic improvement of existing buildings, showing an increased strength of about 17 times with respect to the unstrengthened configurations. The experimental curves are shown in Figure 3.2 in terms of reaction force against joist slip (simply denoted as slip hereinafter), representative of the relative displacement between the wall and the timber joist.

Table 3.1 Summary of experimental tests developed by Moreira (2015)*; test are labelled using the following criterium: TT.R.NL, where TT is the wall thickness, R is the type of connection (U = unreinforced or A = reinforced), N is the number of the wall and L the location of the connection within the wall (Figure 3.1).*

floor level	stress level	wall thickness	connection type	monotonic	cyclic
upper level	0.2 MPa	40 cm	unstrengthened	40.U.1A 40.U.1B	-
			strengthened	40.A.1A	40.A.3A 40.A.4A 40.A.4B
lower level	0.4 MPa	60 cm	unstrengthened	60.U.1A 60.U.1B	-
			strengthened	60.A.1A	60.A.2B 60.A.3A 60.A.3B

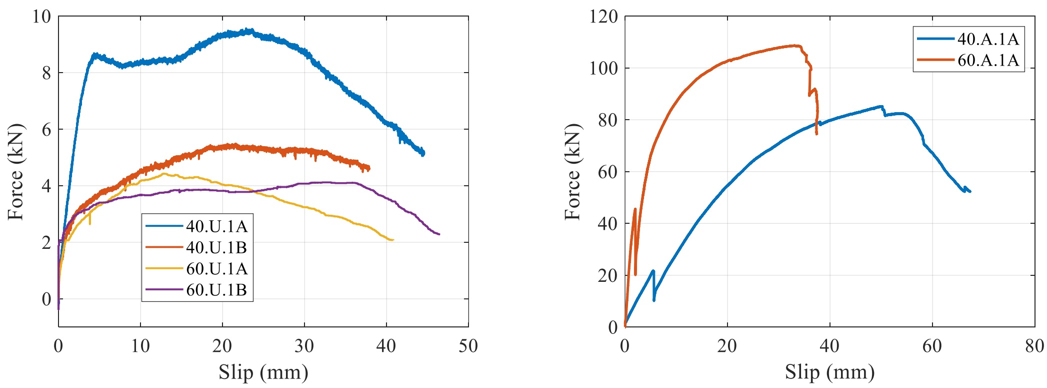

(a) (b)

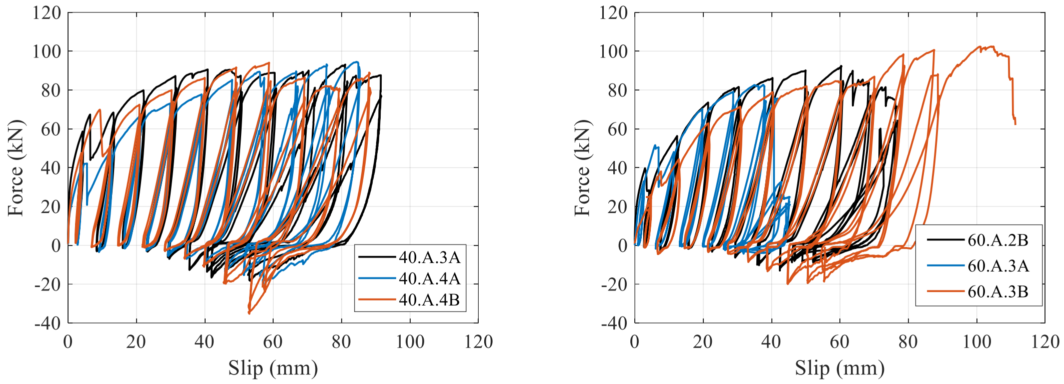

(c) (d)

Figure 3.2 WD force-slip experimental curves (Moreira 2015)*; (a) monotonic unstrengthened; (b) monotonic strengthened; (c) cyclic strengthened - upper level; (d) cyclic strengthened - lower level.*

Although the experimental campaign cannot be statistically representative of all the possible WD joints, a common trend was observed among the typologies of the connections. Figure 3.2a clearly shows that the 40.U.1A specimen is out of the average envelope. This was due to the considerable rotation of the beam during the pull-out test. Therefore, a vertical support under the timber joist was used to limit the rotation of the next specimen to test, 40.U.1B. Specimens with $60\ cm$ thick walls did not require the use of a support, since the rotation was minimal. For the remaining specimens, force-displacement curves are almost coincident. Indeed, there is not evident difference between lower and upper connections levels. For the specimen 60.U.1B, the acquisition system recorded only "noise" up to a force of $2\ kN$, possibly related with the small values measured. As a consequence, its mechanical characterization could not be possible.

Strengthened specimens were tested in both monotonic and cyclic load protocols (Figure 3.2b,c,d). The higher strength capacity of monotonic curve is physically justified by the damage accumulation within the cycles. Unfortunately, the results of 40.A.1A could not have been considered as corrupted by malfunction of data acquisition through LVTD. Among the cyclic curves, 60.A.3A resulted to have about half of the ultimate displacement capacity as the others and is not considered to be a reliable result for characterizing the connection.

Therefore, a total of eight experimental curves can be considered valid for analytical and numerical development, two of which for the unstrengthened specimen (monotonic), and six for the strengthened specimen (one monotonic and five cyclic), as summarized in Table 3.2.

Although it is well known that the vertical stress level may influence the behavior of some connections in terms of strength and axial displacement capacity, such experimental data reveal no evident difference, whether for the unstrengthened or the strengthened specimens.

Table 3.2 Valid experimental tests used for the numerical/analytical development.

connection type	**monotonic**	**cyclic**	**tot**
unstrengthened	40.U.1B 60.U.1A	-	2
strengthened	60.A.1A	40.A.3A 40.A.4A 40.A.4B 60.A.2B 60.A.3B	5
tot	3	5	7

Figure 3.4 supports this assumption as it shows that for strengthened samples the highest amount of energy is dissipated by failure modes associated to steel and timber elements, rather than masonry regardless of the stress level. Moreover, as also explained by Moreira (2015) the failure of the connection is governed by nails pull-out in unstrengthened connections and by bolted connection in strengthened connections (Figure 3.3), thus demonstrating the negligible influence of different stress levels and wall thickness.

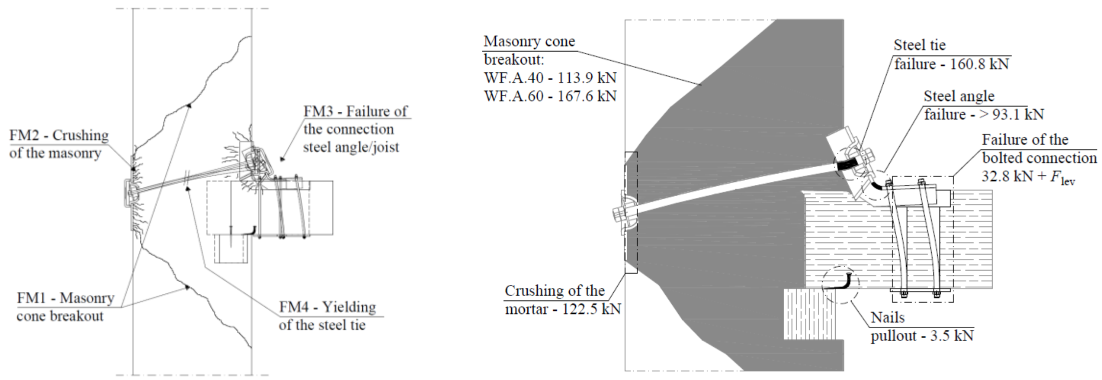

(a) (b)

Figure 3.3 (a) Failure mode definition: FM1: Conical masonry breakout; FM2: Masonry crushing below the anchor plates; FM3: Yielding of the tie rod; FM4: Failure of the bolted connection between the steel angle and the timber joist; (b) estimated capacity of each failure mode. (Retrieved from Moreira (2015)*).*

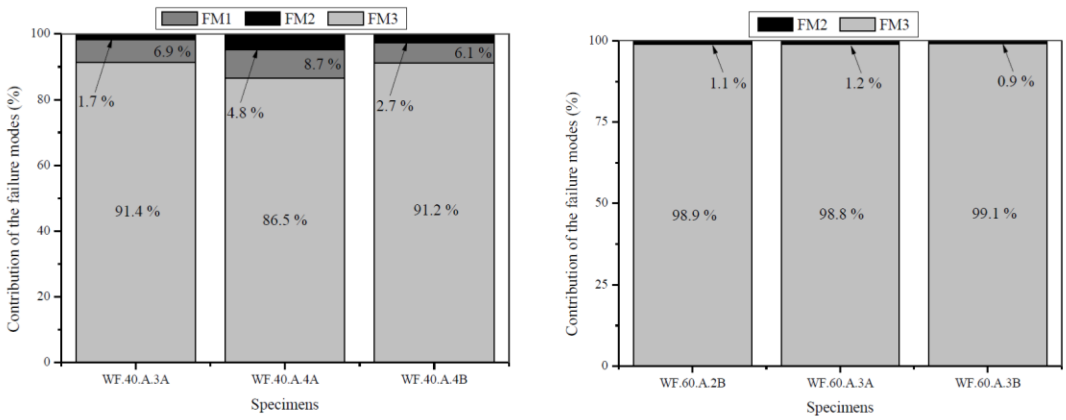

(a) (b)

Figure 3.4 Energy dissipated by each failure mode; (a) upper level specimens; (b) lower level specimens.(retrieved from Moreira 2015).

Based on these considerations, one single connection per type is defined and developed hereinafter. Furthermore, such connection models can be representative of a large variety of existing WD links that present similar characteristics.

3.2 Ideal bilinear curves

Within the framework of performance-based assessment procedures, suitable for highly nonlinear systems and currently used by practitioners for the increased computational capacity of calculators, bilinear curves can be constructed equivalent to the actual system in order to reflect the yielding limit and the ultimate displacement capacity, as well as the maximum resistance of the system.

Different criteria can be found in literature ((ASCE 2017; NTC2018; EC8-1 2004; Fema-445 2006)). They usually refer to the seismic capacity of the masonry buildings as a whole.

Aligned with multilinear simplification performed by Moreira (2015), the procedure adopted herein aims at defining simplified bilinear curves of both strengthened and unstrengthened structural WD connections of the type described in the previous section. The whole method can be summarized through the following steps:

1. Definition of the backbone curve;
2. Definition of the equivalent bilinear curve;
3. Definition of average bilinear curve;

For unstrengthened specimens, only monotonic curves are available, therefore step n.1 is not necessary, and it is possible to directly jump to step n.2. Moreover, as a single monotonic test is not representative of the behavior of the strengthened sample, this connection is characterized based only on cyclic curves. In this case, envelope curves are firstly built over each cyclic curve; a simplified bilinear curve is then computed based on the previously defined backbone; and the final equivalent bilinear curve is developed as the average of the previous bilinear curves.

3.2.1 Definition of the backbone curve

In case of cyclic experimental tests, the first step is to define multi-linear envelopes (also denoted as backbone curves). The methodology adopted here is the one suggested by ASCE/SEI 41-06 (ASCE 2007) allowing for strength degradation due to cyclic loading and giving more conservative results in comparison with the recently-published ASCE/SEI 41-17 (ASCE 2017).

The backbone curve is defined by multi-linear segments connecting the intersections between the first cycle curve for the i^{th} deformation level and the second cycle curve of the $(i-1)^{th}$ deformation level for all i levels (Figure 3.5).

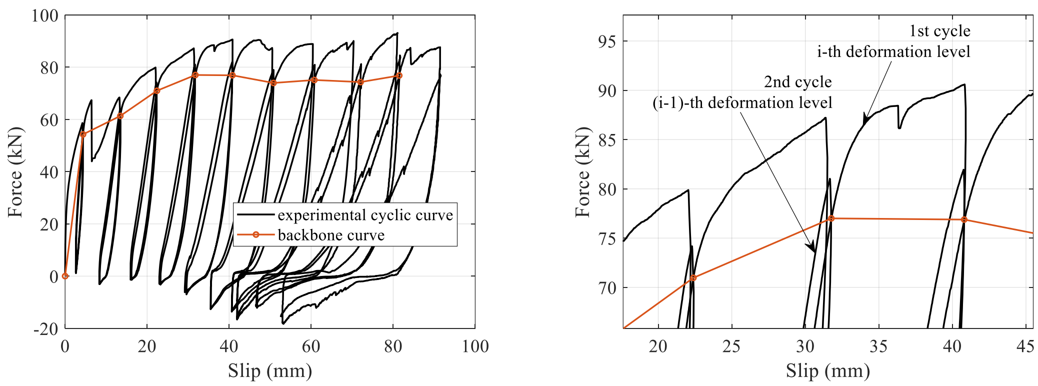

(a) (b)

Figure 3.5 Backbone curve definition according to ASCE/SEI 41-06 (ASCE 2007): (a) backbone curve over experimental cyclic curve; (b) backbone intersections.

It must be noted that according to the new ASCE/SEI 41-17 (ASCE 2017) the backbone curve is simply defined as the intersection of the peak displacement of the first cycle of the i^{th} deformation level, leading to a less conservative estimation with respect to the previous standard in terms of stiffness and strength, and thus is not considered in this work. Furthermore, the backbone curves according to ASCE/SEI 41-17 (similarly as done in previous ASCE/SEI 41-13) do not account for strength and stiffness degradation (Figure 3.6), aspect included in the considered ASCE/SEI 41-06 through the intersection of unloading branch with reloading of successive displacement level.

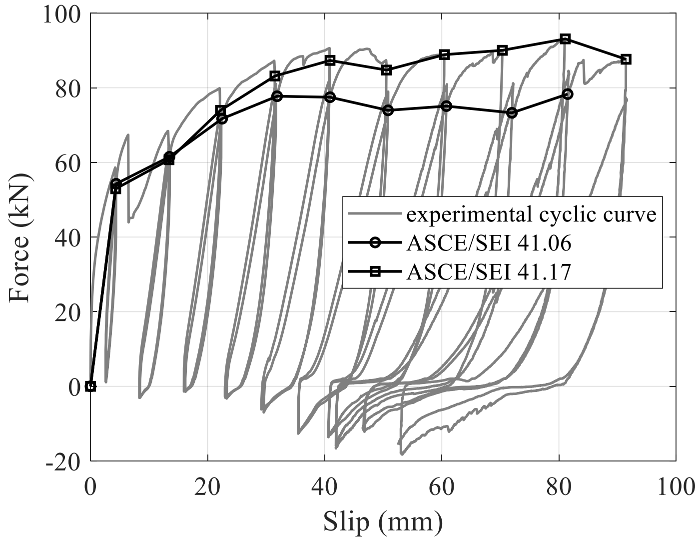

Figure 3.6 Comparison between definition criteria of backbone curves.

3.2.2 Definition of the equivalent bilinear curve

According to Tomaževič (1999) the bilinear curve corresponds to an elastic-perfectly plastic mechanical model expressed by an initial idealized elastic branch and successive horizontal branch connecting the elastic limit to the ultimate limit (Figure 3.7), and reads:

$$\boldsymbol{F(d)} = \begin{cases} \boldsymbol{k_e \cdot d}, & \boldsymbol{if} \quad \boldsymbol{0 \le d \le d_e} \\ \boldsymbol{F_u}, & \boldsymbol{if} \quad \boldsymbol{d_e \le d \le d_u} \end{cases} \qquad 3.1$$

where k_e is the effective stiffness, d_e is the elastic displacement, and d_u the ultimate displacement. The corresponding ultimate force F_u is evaluated by equating the energy dissipation capacity of the idealised curve to the experimental one:

$$\boldsymbol{F_u = k_e \cdot \left[d_{max} - \sqrt{d_{max}^2 - \frac{2 \cdot A_{env}}{k_e}} \right]} \qquad 3.2$$

where A_{env} is the area below the experimental envelope, and $\boldsymbol{d_{max}}$ is the maximum displacement attained in the experimental test. k_e is calculated as the ratio between the resistance and displacement at crack limit:

$$\boldsymbol{k_e = F_{cr}/d_{cr}} \qquad 3.3$$

where F_{cr} corresponds to the force at crack limit state equal to $0.7F_{max}$, as also suggested by the Italian code (DMI 2018) and by other code standards.

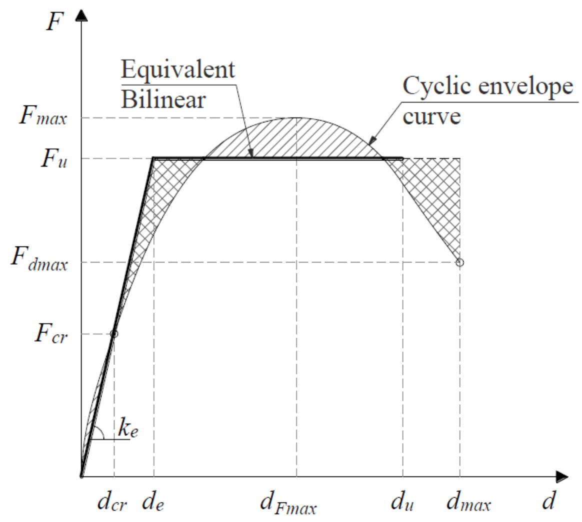

Figure 3.7 Definition of bilinear idealisation of experimental curve (retrieved from Moreira 2015).

3.2.3 Unstrengthened connection

Bilinearisation of unstrengthened specimen is solely based on two monotonic curves (40.U.1B and 60.U.1A) as only two are the reliable tests. The bilinear parameters are summarized in Table 3.3, and bilinear curves are shown in Figure 3.8. Note that ductility index is calculated as $\mu = d_u/d_e$.

Table 3.3 Ideal bilinear curves parameters for unstrengthened connection

	d_e [mm]	d_u [mm]	F_u [kN]	k_e [kN/mm]	μ [-]
40.U.1B	4.8	37.9	5.0	1.0	7.9
60.U.1A	3.3	26.6	3.6	1.1	8.1
average	4.0	32.2	4.3	1.1	7.9

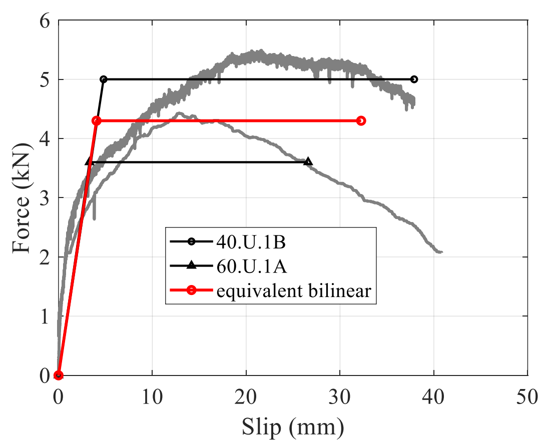

Figure 3.8 Bilinear idealisation of unstrengthened experimental curve.

3.2.4 Strengthened connection

For what concerns the strengthened connection, the backbone curves are firstly computed after each cyclic curve (Figure 3.9) according to ASCE/SEI 41-06 (2007) as illustrated in Section 3.2.1. Ideal bilinear parameters are summarized in Table 3.4.

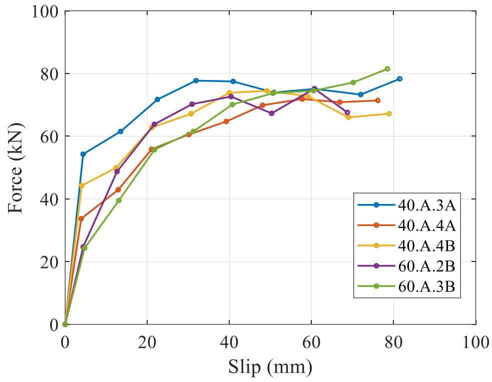

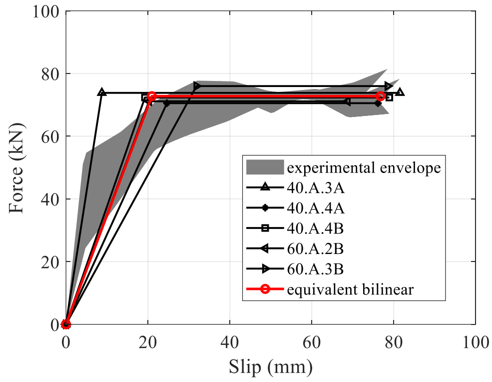

Figure 3.9 Bilinear idealisation of strengthened experimental curves: (a) backbone curves; (b) ideal bilinear curves.

Table 3.4 Ideal bilinear curves parameters for strengthened connections

	d_e	d_u	F_u	k_e	μ
	[mm]	[mm]	[kN]	[kN/mm]	[-]
40.A.3A	8.7	81.5	73.8	12.7	9.3
40.A.4A	24.6	76.1	70.5	5.2	3.1
40.A.4B	19.3	78.9	72.3	4.0	4.1
60.A.2B	20.3	68.7	71.1	4.5	3.4
60.A.3B	31.9	78.5	76.0	3.7	2.8
average	21.0	76.7	72.8	3.5	3.7

3.3 Hysteretic models

Although Finite Element (FE) analysis with homogeneous masonry elements is rarely performed by practitioners, the growing computational capabilities of calculators and continuous updating of material models, set forth the bases for larger range of users. Moreover, the FE modeling approach is widely used and common for the seismic vulnerability assessment among civil engineers. In addition, nowadays a large variety of softwares is equipped with simple graphical user interface facilitating modeling and analysis process, even for complex systems (Formisano et al. 2017). However, often simplified equivalent frame (Lagomarsino et al. 2013) or macro element (Pantò et al. 2016) models are preferable over more complicated approaches.

Whatever modeling approach, the nonlinear mechanical characteristics of masonry and the horizontal diaphragm flexibility play a crucial role on the seismic capacity of the building. Furthermore, depending on the quality of the WD connections, roofs or horizontal diaphragms are included or not within the model. When present, the connection is usually considered as perfect constraint; however, this assumption is solely acceptable for retrofitted connections or new buildings.

Examples of modeling hysteretical structural connections calibrated on experimental bases can be found for instance in (Collins et al. 2005; Isoda and Tesfamariam 2016; Rinaldin, Amadio, and Fragiacomo 2013) mainly for Cross Laminated Timber connections members. To the author's knowledge, no similar work has been done so far on WD connections in historical buildings. Araujo (2014) carried out a detailed FE model of timber wall-to-masonry injected anchors calibrated upon experimental tests. Accurate models are also possible, but not recommended on global analysis of entire buildings with large number of degrees of freedom for which the higher computational effort would be unacceptable.

On the bases of the experimental work done by Moreira (2015) and of the bilinear idealisation presented above, a simple yet versatile model of the WD connection is proposed, capable of reproducing the axial hysteretic law so to allow its implementation on global scale FE models.

Bearing in mind that no information is available about the shear or rotational behavior of the connection, the numerical model strategy only focuses on the axial behavior of the joint. Moreover, tests were only performed in pull-out and are only representative of tensile behavior, thus the axial-compression mode of the timber crushing to the masonry is uncertain and must be assumed.

The proposed model simulates the force-displacement behavior of the entire connection, from the timber joist end to the masonry surrounding the structural joint. Within a FE environment, this is possible through spring-like elements placed between the beam ends and the wall (Figure 3.10).

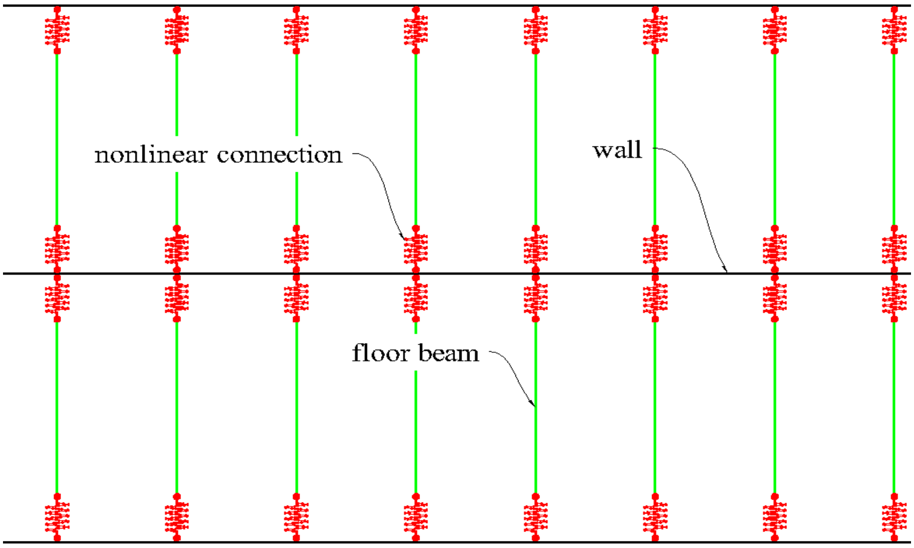

Figure 3.10 Nonlinear spring-like connection elements within a typical building floor plan.

Considering a local coordinate system with X axis parallel to the beam axis, and Z axis in vertical direction (Figure 3.11a), the nonlinear behavior is only represented along the axial X direction (Tx), while translational DOF in Y and Z (Ty and Tz, respectively) are simply assumed as rigid. Except for the torsional DOF, Rx, all the others (Ry and Rz) are free, forming a hinge-type constraint (Table 3.5). Such a connection is developed in OpenSees (McKenna et al. 2000) using a *ZeroLength* element, a non-geometrical finite element where two nodes at the same location are interconnected by a set of springs (Figure 3.11a), providing the force displacement relationship for a specified DOF. The nonlinear hysteretic model is simulated using *Pinching4* material model (Figure 3.11b) available in the OpenSees library and capable of degradation and pinching.

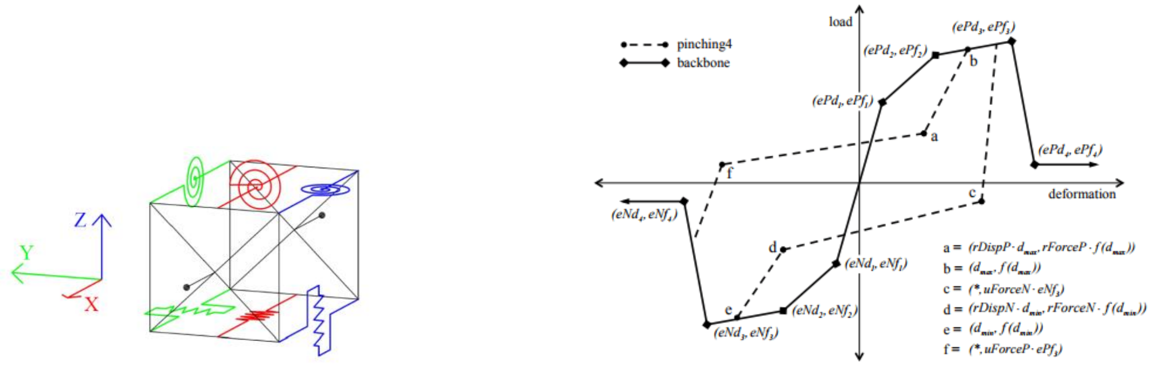

(a) (b)

Figure 3.11 WD connection model; (a) ZeroLength element DOF; (b) Pinching4 material model (Fmk and Nilinjan 2003).

Table 3.5 Characteristics of 3D ZeroLength DOF

DOF	T_X	T_Y	T_Z	R_x	R_Y	R_Z
Type	axial	shear	shear	torsional	bending	bending
Note	nonlinear	rigid	rigid	rigid	free	free

The finite element connection model is based on experimental data in such a way to better estimate:

- yielding limit;
- strength capacity;
- ultimate displacement capacity;
- energy dissipation capacity;

Four couples of coordinates define the backbone curve in the positive (tension) and negative (compression) direction, while cyclic degradation of strength and stiffness occurs in three ways: (i) unloading stiffness degradation; (ii) reloading stiffness degradation; (iii) strength degradation. Hysteretic rules, defining points a, b, c, d, e, f (Figure 3.11b) are governed by additional parameters (three per sign). Cyclic degradation is controlled by five parameters per type and can be based on deformation history or on energy. 39 parameters, summarized in Table 3.6, are necessary for a complete definition of the material model.

Table 3.6 Description of Pinching4 parameters

Parameter	**Description**
Backbone coordinates	
ePf1, ePf2, ePf3, ePf4	Forces of the positive backbone curve
ePd1, ePd2, ePd3, ePd4	Displacements of the positive backbone curve
eNf1, eNf2, eNf3, eNf4	Forces of the negative backbone curve
eNd1, eNd2, eNd3, eNd4	Displacements of the negative backbone curve
Hysteretic rules parameters	

rDispP, rDispN	Ratio of displacements at which reloading occurs to the maximum/minimum historic deformation
rForceP, rForceN	Ratio of the force at which reloading begins to the force corresponding to the maximum/minimum historic deformation
uForceP, uForceN	Ratio of the force at which unloading ends to the maximum/minimum force
Degradation parameters	
gK1, gK2, gK3, gK4, gKLim	unloading stiffness degradation parameters
gD1, gD2, gD3, gD4, gDLim	Reloading stiffness degradation parameters
gF1, gF2, gF3, gF4, gFLim	Strength degradation parameters
gE	Ratio of the maximum energy dissipated under cyclic loading to the energy dissipated under monotonic loading
dmgType	Type of damage: “cycle” or “energy”

The same basic equations describe deterioration in strength (F), unloading (K) and reloading (D) stiffness:

$$\boldsymbol{P_i = P_0 \cdot (1 - \delta P_i)} \qquad 3.4$$

where P_i is the generalized degrading variable at i^{th} state, P_0 is the generalized degrading variable at initial state, and δP_i is the value of the damage index at i^{th} state. In the general case where damage is a function of displacement history and energy accumulation (dmgType = “energy”), the damage index is computed as follows:

$$\boldsymbol{\delta P_i = \left(gP1 \cdot \left(\hat{d}_{max}\right)^{gP3} + gP2 \cdot \left(\frac{E_i}{E_m}\right)^{gP4}\right) \leq gPLim} \qquad 3.5$$

in which,

$$\boldsymbol{\hat{d}_{max} = max\left[\frac{d_{max,i}}{d_{u,p}}, \frac{d_{min,i}}{d_{u,n}}\right]} \qquad 3.6$$

$\boldsymbol{d_{max,i}}$ and $\boldsymbol{d_{min,i}}$ are the deformation demands that define the end of the reload cycle for increasing deformation demand in the positive and negative side, respectively; $\boldsymbol{d_{u,p}}$ and $\boldsymbol{d_{u,n}}$ are positive and negative deformations that define failure.

In Equation 3.5, $E_i = \int dE$ defined within the load history, whilst $E_m = gE \cdot \int dE$ is defined within the monotonic load history.

3.3.1 Unstrengthened connection model

The force-displacement numerical curve under cyclic load relative to the unstrengthened connection is shown in Figure 3.12a, compared to the experimental envelope as well as to the ideal bilinear curve. The total energy, simply computed as the integral of the force with respect to the slip, is also shown in Figure 3.12b.

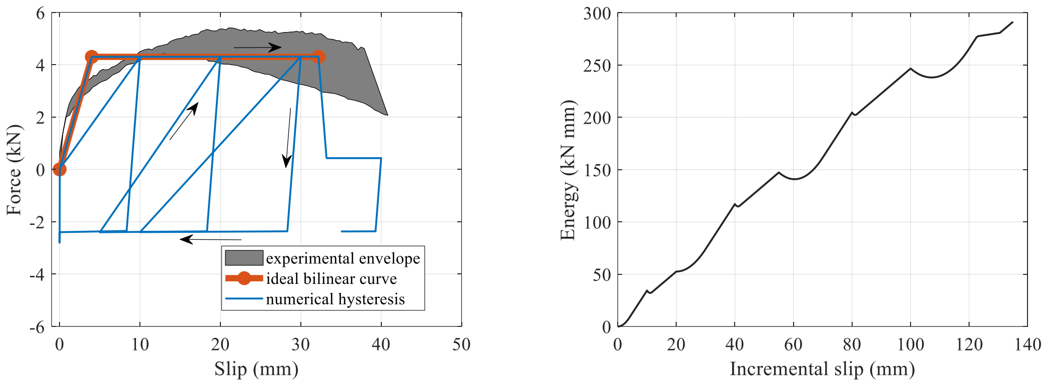

(a) (b)

Figure 3.12 Numerical hysteretic model of the unstrengthened WD connection; (a) comparison with experimental envelope and ideal bilinear curve; (b) total energy computation over the cycles.

Although no experimental evidence is available about the behavior of such a connection under cyclic loading, and although the load-displacement under compression is uncertain, it can be noted that the elastic limit in positive direction is governed by the yielding of the nails, while the rupture is controlled by the shear failure of the nails (Moreira 2015). The cyclic behavior can therefore be assumed to be partially governed by shear resistance of the nails and by the friction generated at beam-to-masonry interfaces. In principle, the frictional contribution could be analytically computed based on the vertical load N, transferred by the floor beams to the masonry wall. Indeed, timber joists are commonly infixed into a masonry slot leaving a small gap between the top of the beam and the masonry. The friction forces can, therefore, be computed as:

$$\boldsymbol{H_f = \mu \cdot N} \qquad 3.7$$

where μ is the friction coefficient depending on the contact materials surfaces. A value of $\mu = 0.2$ can be a conservative value based on timber-to-timber contact (Jaaranen and Fink 2020). This is justified by the presence of timber wall plates, placed along the walls for a better load distribution (Figure 3.1a).

The behavior in compression should simulate the rigid contact at timber-to-masonry interface. Within 3D solid finite elements modeling (Figure 3.11a), this is directly represented by the masonry blocks compression along the wall thickness, and the compression behavior can be simply assumed rigid. If shell elements are used (Figure 3.11b), a rigid compressive stiffness would directly activate the masonry bending out of its plane, possibly causing large deformations and convergence issues. In this latter case, the connection behavior in compression may be associated to the masonry compressive deformation along the thickness of the wall.

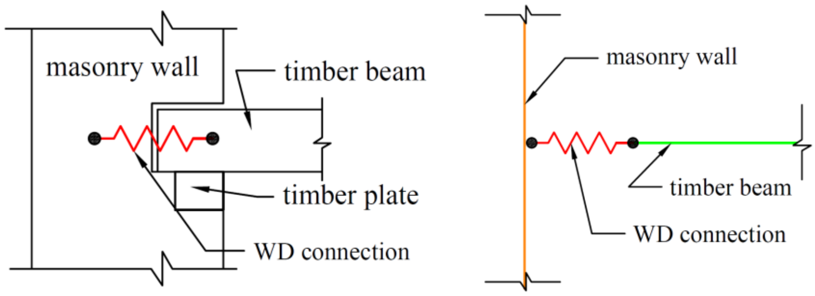

(a) (b)

Figure 3.13 Modeling of WD connection within FE environment; (a) solid finite elements; (b) shell elements.

Under these assumptions, connection model parameters are defined setting the following conditions:

- $K_{unloading} = 4 \cdot K_e$;
- $K_{compression} = E_m \cdot A_{beam}/t$ (E_m: masonry Young's modulus, A_{beam}: beam cross section, t: wall thickness;
- $F_{residual} = F_u/100$;
- $-F_u/2 < F < Fu$, if $d \geq 0$.

A comprehensive list of parameters defining the Pinching4 unstrengthened WD connection can be found in Table A 1 in Appendix 1. No degradation is accounted for such a connection.

3.3.2 Strengthened connection model

The numerical model of the strengthened connection is also developed on the bases of bilinear idealisation and experimental evidence. Indeed, hysteretic rules can be calibrated upon available experimental cycles. The numerical load-displacement hysteresis is shown in Figure 3.14, upon experimental envelope and equivalent bilinear curve. The total energy is also computed within cycles and is shown in Figure 3.13. Such a connection model is based on similar conditions set for unstrengthened connections. However, the frictional resistance can be neglected in this case as its contribution is very low with respect to the reinforcement system. This is controlled by hysteretic rules parameters. For the sake of simplicity and based on experiments, both strength and stiffness degradation are neglected.

Pinching4 parameters defining strengthened WD connection model are summarized in Table A 2 (Appendix 1).

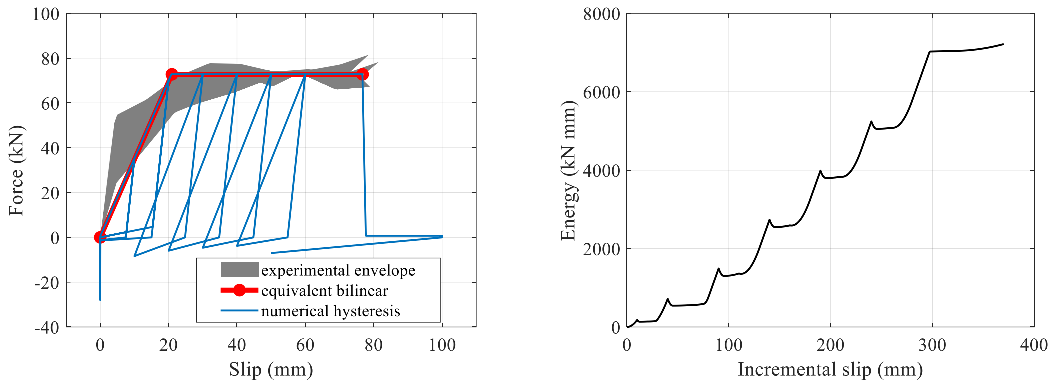

(a) (b)

Figure 3.14 Strengthened WD connection numerical hysteretic model; (a) comparison with experimental envelope and ideal bilinear curve; (b) total energy computation over the cycles.

The capabilities of the model are demonstrated in Figure 3.15 where the numerical model is calibrated upon 60.A.3B experimental sample (Figure 3.2d, Section 3.1). The accuracy of the model is shown in terms of force-slip hysteresis and total energy. The different values of total energy are highlighted especially at final cycles and can be justified by the linear reloading. Indeed, as shown in Figure 3.15a, the numerical reloading branch is basically a linear branch connecting the previous state to the backbone curve, in correspondence of the maximum deformation level attained. The experimental reloading branch presents, by contrast, a curvilinear shape, hard to capture numerically. For the detailed calibration of 60.A.3B sample only, and based on experimental curves, both unloading and reloading stiffness degradation is neglected, whereas strength degradation is considered to be proportional to energy ($gF1 = 0.0$; $gF2 = 0.7$; $fF3 = 0.0$; $gF4 = 0.8$; $gFlim = 0.9$; gE = 2)

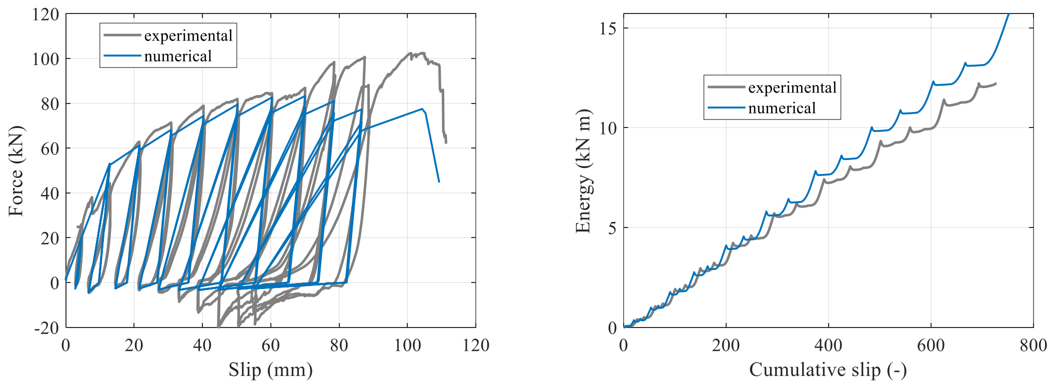

(a) (b)

Figure 3.15 Comparison between numerical and experimental 60.A.3B connection in terms of (a) hysteretic force-slip cure; (b) total energy within cycles.

It must be noted, however, that this behavior can be considered acceptable for the application on global FE models as such a connection hardly reaches high levels of stress and deformation over the yielding and failure limits. As a matter of fact, historical buildings under strong earthquakes, with retrofitted or strong WD connections have a box-like behavior, thus enabling structural elements to with simultaneous modes and allowing a proper distribution of seismic forces to the lateral resisting walls.

3.4 Conclusive remarks

In this chapter the modeling of wall-to-horizontal diaphragm (WD) connections was faced through simplified and advanced methods. Available experimental data set forth the bases for the following analytical and numerical studies. Conventionally, structural connections are not included into the model for the seismic vulnerability of the building. Eventually they are extremely simplified giving too conservative (or underestimated) results. When no experimental information is available about the nonlinear behavior of existing WD connections, their resistance can be estimated by analytical formulations, allowing force-based seismic assessment.

Following bilinearization criteria suggested by current Code standards, simplified elastic-perfectly plastic backbone curves were defined for two main WD connection configurations: (i) unstrengthened, and (ii) strengthened. Based on the same experimental data, the capability of advanced hysteretic model, developed in finite element environment, was demonstrated. Pinching4 hysteretic model was calibrated upon the experimental data capable of simulating the pull-out axial strength, yielding and ultimate limits, as well as the energy dissipation capacity. All the suggested models allows for implementing the WD connection into numerical models in order to study the influence of the quality of the connection over the global and local behavior of unreinforced masonry buildings. The study reported here highlighted the importance of experimental data for the proper simulation of structural connections, often one of the main uncertainties of the building under study.

CHAPTER 4

GLOBAL AND LOCAL SEISMIC ANALYSIS OF THE BUILDING PROTOTYPE

Overview

In this chapter the assessment of WD connections is faced in both global and local approaches making use of previously developed connection models. A global model of a four level URM building prototype is developed in a finite element environment, capable of introducing hysteretic models simulating the complex dynamic at wall-diaphragm interactions. Two different approaches are also proposed for studying the local OOP mechanisms of masonry walls, taking into account the influence of horizontal restraints: (i) kinematic approach based on virtual work principle; (ii) dynamic analysis of rigid bodies, also capable of taking into account dynamic effects.

4.1 Global analysis: finite element modeling

Structural analysis of historical constructions is often assessed through mathematical models capable of accounting for low tensile strength of masonry and high nonlinearity of the materials. Different approaches have been developed with different degree of complexity, such as equivalent frame models (Lagomarsino et al. 2013), macro element models (Pantò et al. 2016), continuum element models (Ortega et al. 2018; Scacco et al. 2019). The first approaches, namely equivalent frame and panel macro element models, are simplified and more versatile for their lower computational demand, even if they are recommended solely for regular building layouts (Aşıkoğlu et al. 2020). The latter can be an accurate numerical approach for the seismic vulnerability assessment through nonlinear static or nonlinear dynamic analysis. The fast technological development of the last decades in calculators and development of user-friendly FE softwares is encouraging the use of finite element programs by researchers and also by professionals.

4.1.1 Description of the prototype building

Within the aim of studying the influence of WD connections in historical constructions under seismic actions, a 4-storey URM building is analysed in FE environment through nonlinear static and nonlinear dynamic analyses. The prototype is a realistic made-up building (Figure 4.2) with floor plans, opening layout and material properties typical of common buildings of the Mediterranean basin, but that can also be found worldwide (Figure 4.1).

Figure 4.1 Typical 3- and 4-storey URM buildings of Italy [retrieved from (Donà et al. 2020)].

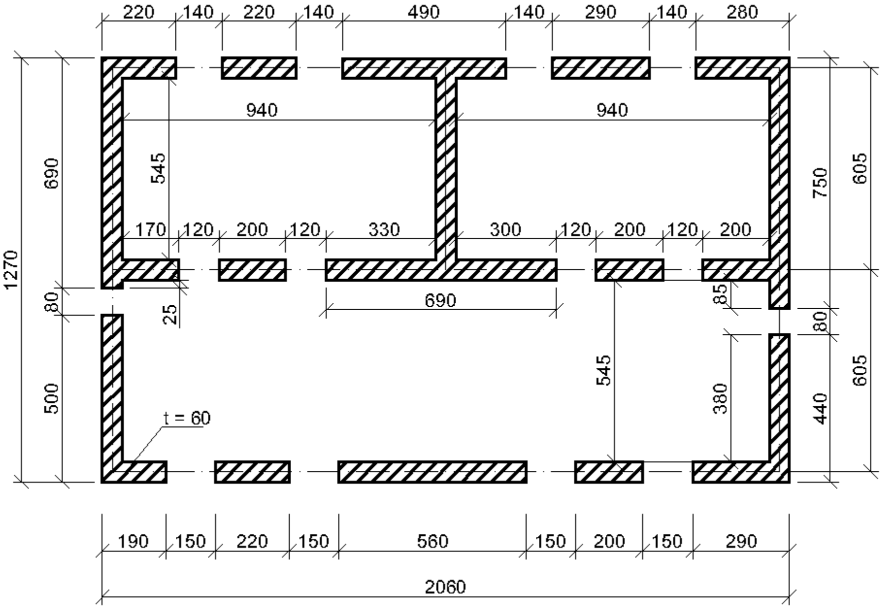

(a)

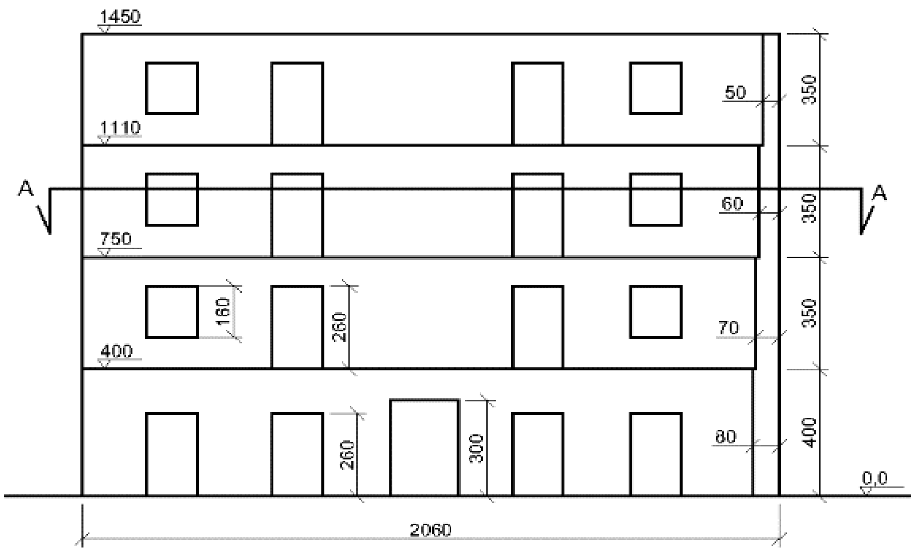

(b)

Figure 4.2 Prototype made-up building under study: (a) floor plan; (b) front view and wall thickness along the height (units in cm).

The building floor plan is $20.6 \times 12.70\, m^2$ and the floor height spacing is $3.5\, m$ unless the base level of $4.0\, m$, giving a total building height of $14.5\, m$. The wall plan layout is asymmetric in both directions with decreasing thickness along the height ($t = 80\, cm$; $70\, cm$; $60\, cm$; $50\, cm$, Figure 4.2b). A two-way timber floor is present with $160 \times 520\, mm^2$ main beam spanning $6050\, mm$ and spacing $1800\, mm$ (Figure 4.3).

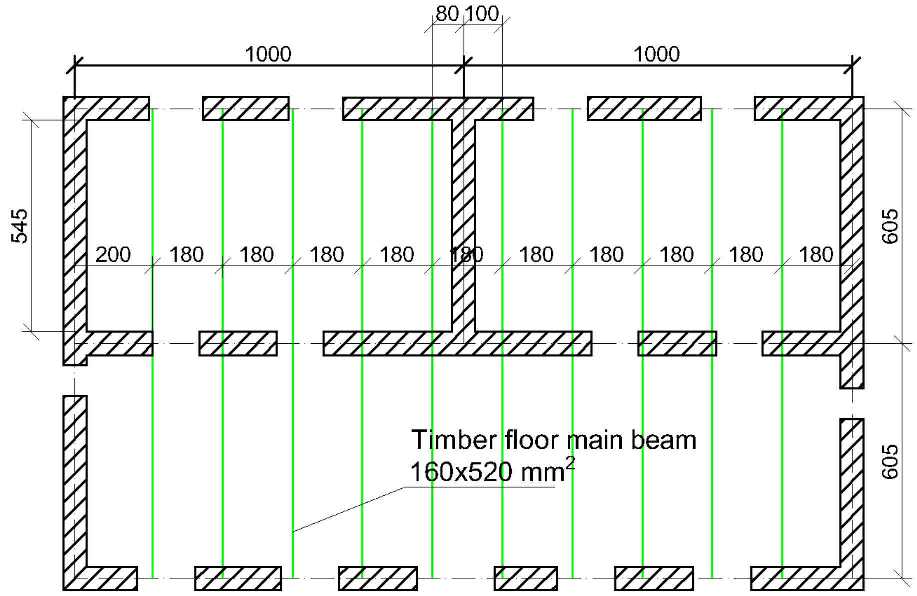

Figure 4.3 Timber floor beam layout (units in cm).

Timber lintels are present above the openings, having $10\ cm$ height and the same thickness of the corresponding wall.

The masonry of the building is double leaf rubble stone masonry, compatible with samples experimentally characterized by Moreira (2015). Mechanical properties are given based on axial compression and diagonal tests on masonry prisms, summarized in Table 4.1.

Table 4.1 Masonry mechanical properties

Young's modulus	**compressive strength**	**tensile strength**	**Poisson's ratio**	**density**
$\mathrm{E}\ [MPa]$	$\boldsymbol{f_c}\ [\boldsymbol{MPa}]$	$\boldsymbol{f_t}\ [\boldsymbol{MPa}]$	$\boldsymbol{\nu}\ [-]$	$\boldsymbol{\rho}\ [\boldsymbol{kg/m^3}]$
1187	1.7	0.14	0.2	1900

Timber properties are simply assumed based on standards, in particular, C22 timber class is selected according to Table 4.2 derived from UNI EN 338. The same timber is used for both timber floor beams and lintels above the openings.

Table 4.2 C22 timber mechanical properties [Derived from table 1 UNI-EN 338 (CEN 2009)].

mean elastic modulus	**mean shear modulus**	**bending strength**	**mean density**
$\boldsymbol{E_{0,mean}}[\mathbf{MPa}]$	$G_{mean}[\mathrm{MPa}]$	$\mathrm{f_{m,k}}\ [\mathrm{MPa}]$	$\rho_{\mathrm{mean}}[\mathrm{kg/m^3}]$
10000	630	1.7	410

4.1.2 Description of the FE model

The building under study is analysed using OpenSees (Pacific Earthquake Engineering Research Center (PEER) 2016), and the pre- and post-processing is performed in STKO

(Petracca, Candeloro, and Camata 2017). The masonry walls are modelled using a multi-layer shell formulation through ShellMITC4 element (Figure 4.4a), which is a four-node shell element based on the theory of mixed interpolation of tensorial component proposed by Dvorkin et al (Dvorkin, Pantuso, and Repetto 1995). The surface axis coincides with the axis of 60 cm wall, set as an average thickness along the height. The multi-layer element (Lu et al. 2015) is useful for representing wall sections having layers with different material characteristics and different thickness, such as concrete shear walls with reinforcement (Figure 4.4b). Such a tool is used here just to get additional integration points along the wall thickness; therefore each layer presents the same mechanical characteristic and thickness.

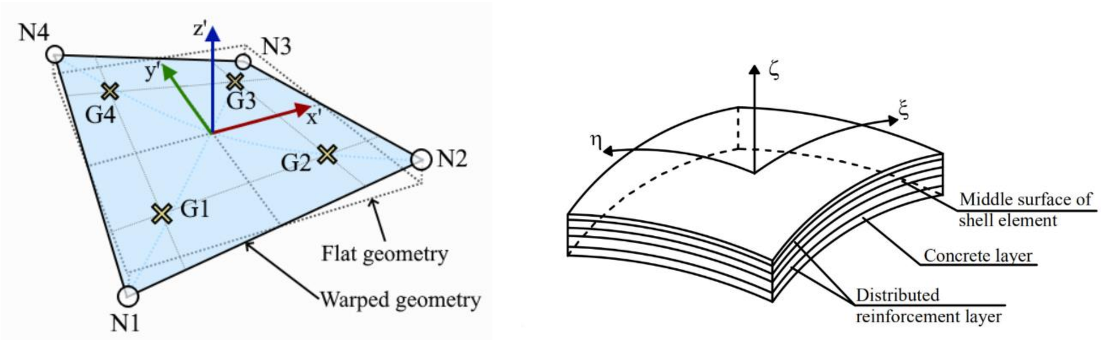

(a) (b)

Figure 4.4 (a) shellMITC4 element nodes and Gauss points; (b) layered shell section.

Five integration points are considered to be enough for a sufficient representation of out of plane stress state, obtaining a good cost/benefit compromise between using solid or shell elements.

Damage TC3D material model (Petracca, Pelà, et al. 2017; Petracca and Camata 2019) is adopted to simulate masonry based on tension/compression damage model on the bases of previous theories (Cervera, Oliver, and Faria 1995; Lubliner et al. 1989), capable of reproducing nonlinear response and to control the dilatancy. Both standard implicit (backward Euler) and mixed IMPLicit-Explicit (IMPL-EX) integration schemes can be selected. Tensile failure surface can be based on Rankine or Lubliner theory. Masonry nonlinear properties are summarized in Table 4.3 and are assumed based on literature and available experimental evidence.

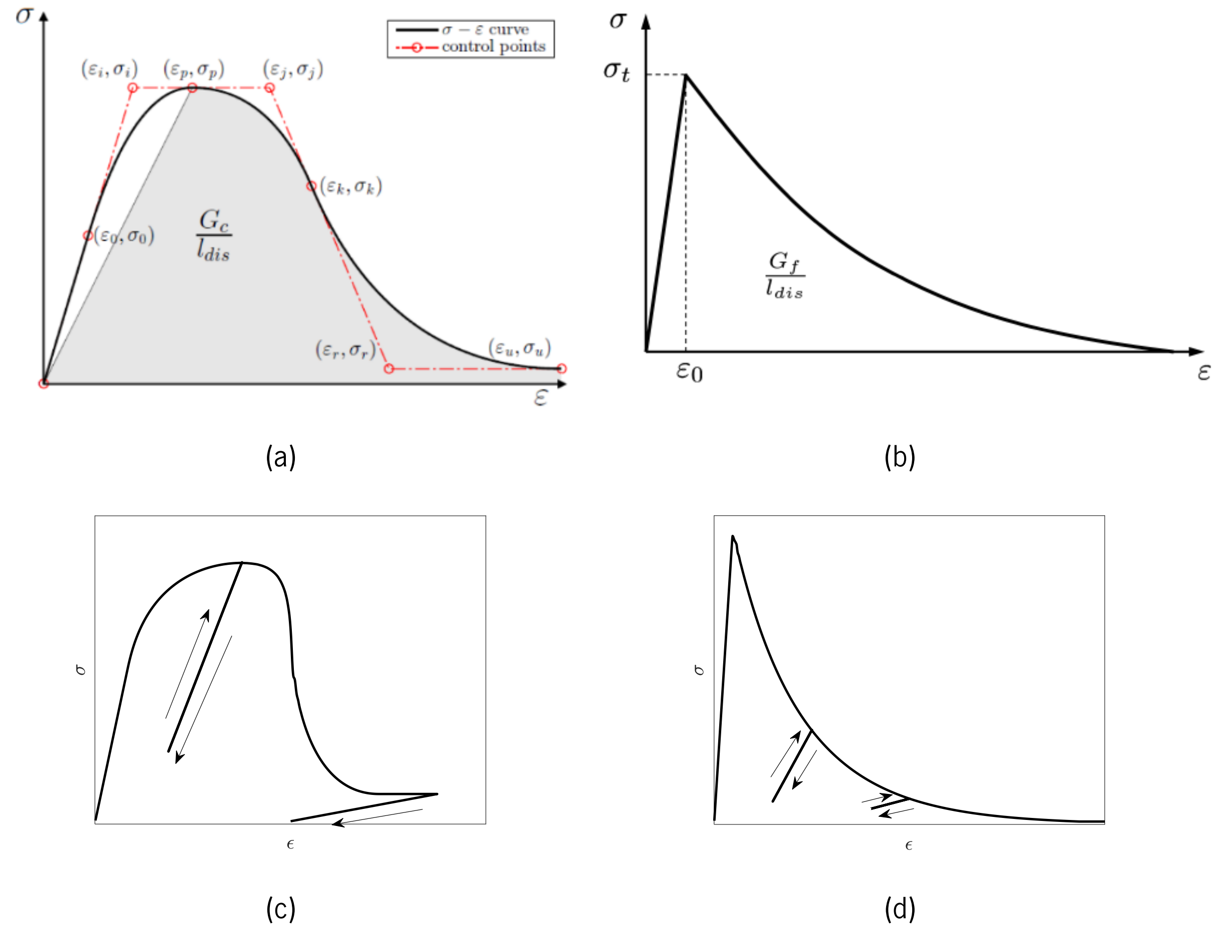

Figure 4.5 Damage TC3D material model used for masonry: (a) compressive uniaxial law; (b) tension uniaxial law; (c) compressive cyclic behavior; (d) tension cyclic behavior.

Indeed, the knowledge about parameters necessary for advanced nonlinear modelling strategies, such as tensile and compressive strength and tensile and compressive fracture energies is scarce.

Table 4.3 Nonlinear properties of the masonry model

tensile strength	**tensile fracture energy**	**compressive elastic limit**	**compressive strength**	**compressive fracture energy**
f_t $[MPa]$	$G_t[N\,mm/mm^2]$	f_{c0} $[MPa]$	f_c $[MPa]$	$G_c[N\,mm/mm^2]$
0.14	0.05	1.02	1.7	3.0

Therefore, it is commonly hard to experimentally reproduce the masonry behavior in tension, and recommended values are impossible for tensile strength. This mainly depends on unit properties, mortar properties, and workmanship quality and is usually very low ($0.10 < f_t < 0.20\ MPa$ (Lourenço 2009)), while tensile fracture energy G_t, ranges between 0.03 and

$0.05\ Nmm/mm^2$ (Van Der Pluijm 1992). According to the Model code 90 (CEB-FIP 1993), the compressive fracture energy can simply be computed as:

$$\boldsymbol{G_c = 1.6 \cdot f_c}; \qquad \text{if} \qquad \boldsymbol{f_c < 12\ MPa} \qquad 4.1$$

$G_c = 2.8 Nmm/mm^2$ is also a typical value. When compressive strength is not given, this can be derived from the elastic modulus as follows:

$$\boldsymbol{f_c = E/500} \qquad 4.2$$

In the considered model, compressive strength f_c, and tensile strength f_t, as well as Young's modulus E are set according to the compressive and shear tests on masonry prisms (Table 4.1) (Moreira 2015). Tensile fracture energy G_t is $0.05\ N\ mm/mm^2$ as recommended upper bound value for a better stability of the numerical model (Lourenço 2009). As for the fracture energy in compression, a value of $G_c = 3.0\ N\ mm/mm^2$ is calibrated upon the experimental compression envelope (Figure 4.6). Even if higher ductility is shown by experimental curves, higher values of fracture energy in compression are hardly achieved and not recommended in literature. Moreover, average envelope is solely built upon three tests, not sufficient for a reliable statistical representation of the results.

A masonry compressive elastic limit $f_{c0} = 0.6 \cdot f_c = 1.02\ MPa$ is set as properly fitting experimental curve. It is worth noting that, although the compression behavior of masonry sensitively influences the dynamic properties of the building, the most critical crack patterns are mainly caused by the low tensile strength, which is in turn the most important aspect for the overall building behavior.

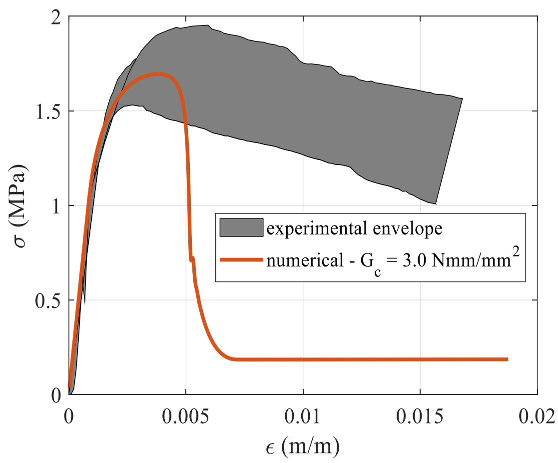

Figure 4.6 Comparison between numerical curve and experimental envelope

Tensile surface is based on Rankine theory, while an IMPL-EX integration scheme is used setting the behavior in tension and in compression partly based on damage and plasticity, causing residual strains after the unloading phase. The fracture energies are automatically regularized depending on the characteristic size of the element.

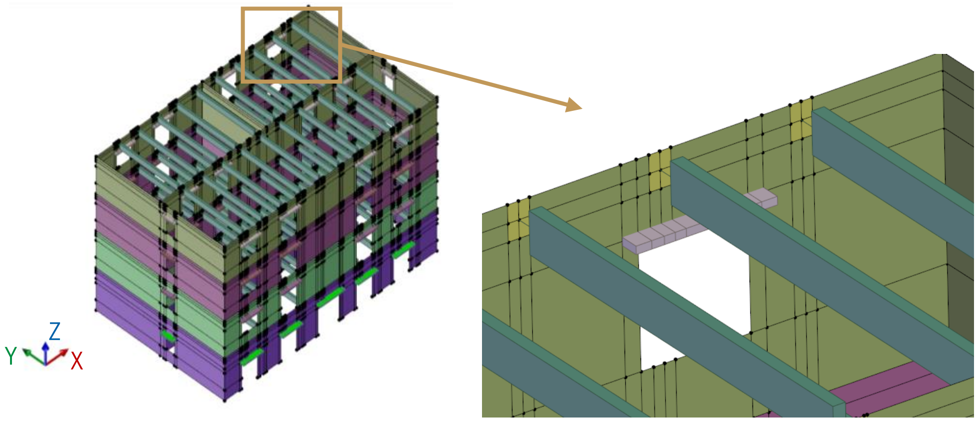

(a) (b)

Figure 4.7 FE model of the 4 level URM building prototype: (a) 3D view of the global building; (b) detail of WD connection and timber lintels above the openings.

Timber lintels, as well as timber floor beams are modelled using 3D elasticBeamColumn elements with elastic section. Timber lintels are embedded into the masonry (Figure 4.7b). A masonry portion (like that of timber beam section) at the WD interface is modelled as elastic for a better distribution of the load to the nonlinear surrounding masonry (Figure 4.7b). A comprehensive description of the WD connection modeling is presented in Section 3.3.

The base nodes are simply fixed, and the masonry self-weight is distributed over the wall surfaces while the floor load is linearly distributed over the beams.

4.1.3 Model configurations and types of analysis

Conventionally, there are two ways of modeling the horizontal diaphragms in a global FE model: (i) absence of the floor; (ii) presence of the floor beams fully attached to the masonry walls. The former approach is representative of poor friction-based WD connections, often present in historical constructions, whilst the second one simulates retrofitted or new building connections. Moreover, when the floor is present, both timber beams and timber planks can be modelled, or solely the main beams, depending on the stiffness of the timber deck. All these modeling approaches are often used to study the influence of diaphragm stiffness or are chosen by the engineer after careful personal judgment in function of the connection quality and floor layout.

Recalling that the scope of this work is to evaluate the influence of WD connections in the overall seismic response of the global building, and considering that the real behavior between the timber and the masonry lays between those two extreme boundaries, the same building prototype is modelled in four different configurations with increasing quality of WD connection: (1) no beams; (2) unstrengthened connections; (3) strengthened connections; (4); fully rigid connections (Figure 4.8).

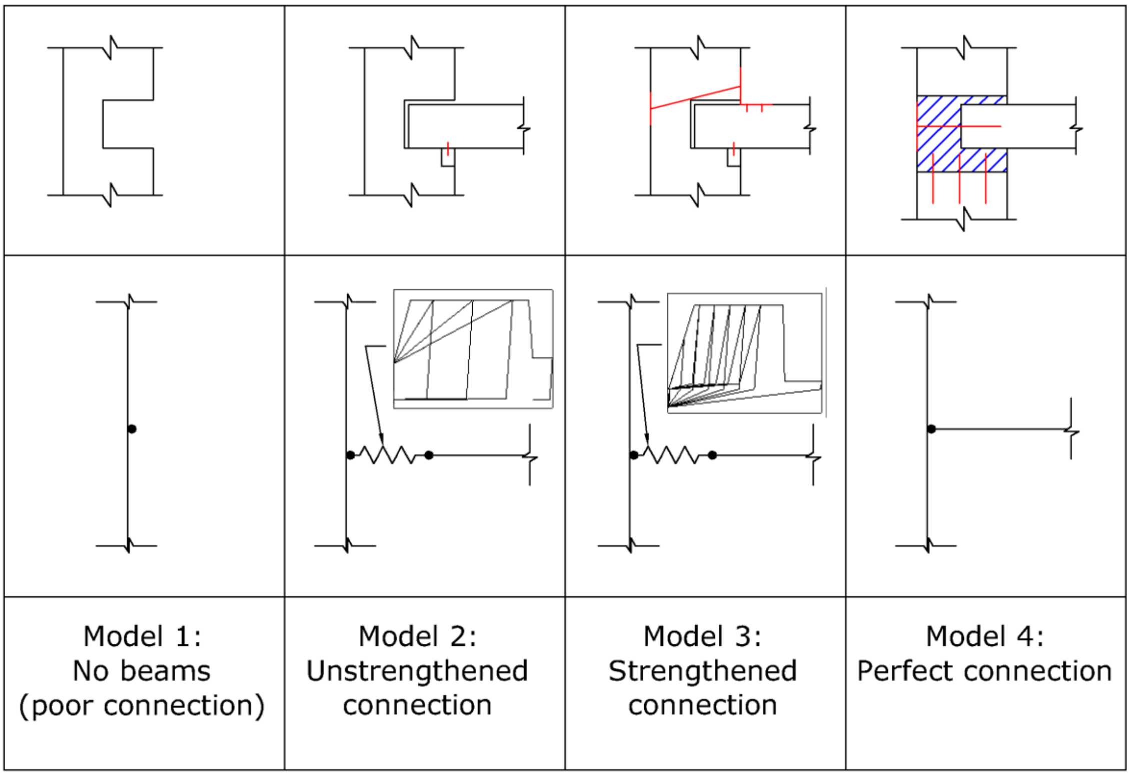

Figure 4.8 Model configurations: types of WD connections.

Model 1 considers fictitious beams (no stiffness) with the function of merely transferring the vertical load to the adjacent walls and simulates old buildings with very weak WD connections. In model 4 the link is modelled through a perfect kinematic constraint representative of new building WD connections. Models 2 and 3 are characterized by nonlinear WD connections, modelled as explained in detail in Section 3.3, placed between the beam end and the wall node. Those models are characterized by an intermediate behavior and should be representative of realistic unreinforced connection (Model 2) and strengthened connections (Model 3).

Modal (eigenvalue) analysis is firstly performed, followed by nonlinear static (pushover) analysis in order to estimate the capacity of the buildings in the Y-direction (parallel to the direction of the floor beams). Finally, an incremental dynamic analysis (IDA) is carried out under a scaled natural accelerogram capable of accounting for dynamic effects. The comparison between the pushover and IDA analyses is also presented.

The life-safety limit state seismic combination of loads is considered according to NTC2018:

$$\boldsymbol{E + G_1 + G_2 + P + \Psi_{21} \cdot Q_{K1} + \Psi_{22} \cdot Q_{K2}} + \cdots \qquad 4.3$$

where E is the seismic load, G_1 is the structural element self-weight, G_2 is the non-structural element self-weight, P is pre-tension and post-tension force, and Q_{Ki} is the i^{th}variable force. The floor load is simply computed as follows:

Timber floor structural distributed weight	$\boldsymbol{G_1}$	600	$\boldsymbol{N/m^2}$
Timber floor non-structural distributed weight	G_2	2360	N/m^2
Floor distributed live load	Q_K	2000	N/m^2
Seismic combination coefficient	Ψ_2	0.3	-

The total mass of the building is 1772 tons. The model comprises a total 11103 nodes and 22110 elements.

4.1.4 Modal analysis

Modal analysis (eigenvalue analysis) allows computing the building modal properties, once the vertical static analysis with gravitational loads is performed. The modal properties, such as vibration periods Ti, modal participation masses Mij, in each j^{th} direction, and mode shapes Φ_i, are summarized in Table 4.4. Although for all models the first mode is related to the translational mode in Y-direction (weakest direction), model 1 (unreinforced connections) presents rather higher period (T1 = 1.06 s) than the other models, with decreasing values of T from model 1 to 4. Models 2 and 3 exhibit very similar results, depicting slightly different modal participation masses; model 2, with unstrengthened WD connections, has lower values, as expected.

Table 4.4 Modal properties of modes with higher modal participation mass. For each model the value of the i^{th} period Ti, modal participation mass ratio in the j^{th} direction Mj, and the corresponding cumulative modal participation mass ratio CMj, are reported.

Model 1	Model 2	Model 3	Model 4
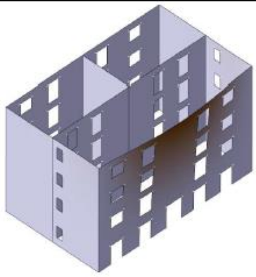	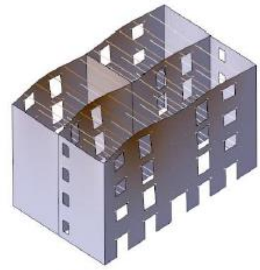	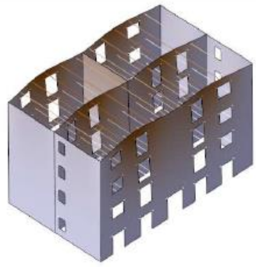	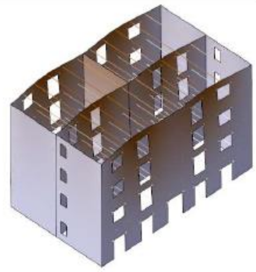
T1 = 1.06 s	T1 = 0.43 s	T1 = 0.43 s	T1 = 0.39 s
MY = 9.7 %	MY = 40.3 %	MY = 43.1 %	MY = 48.6 %
CMY = 9.7 %	CMY = 40.3 %	CMY = 43.1 %	CMY = 48.6 %
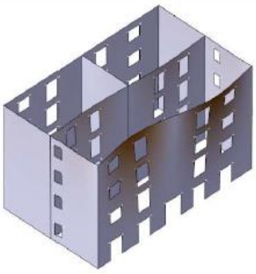	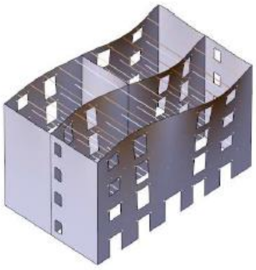	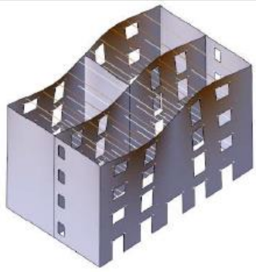	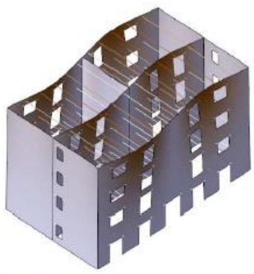
T3 = 0.45 s	T2 = 0.43 s	T2 = 0.42 s	T2 = 0.37 s
MRZ = 6.6 %	MRZ = 10.8 %	MRZ = 12.1 %	MRZ = 14.6 %
CMRZ = 6.8 %	CMRZ = 11.6 %	CMRZ = 12.1 %	CMRZ = 14.6 %
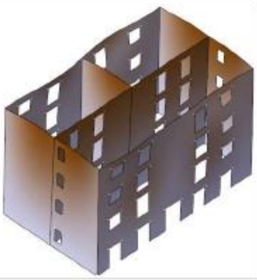	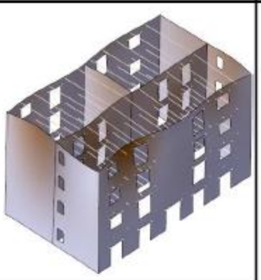	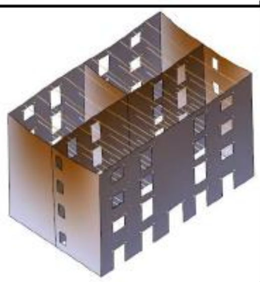	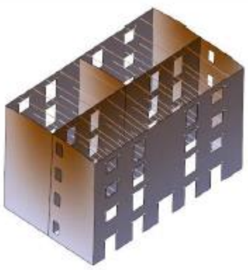
T12 = 0.24 s	T8 = 0.24 s	T5 = 0.24 s	T3 = 0.24 s
MX = 55.0 %	MX = 31.6 %	MX = 59.2 %	MX = 63.2 %
CMX = 58.3 %	CMX = 43.5 %	CMX = 60.4 %	CMX = 63.2 %
	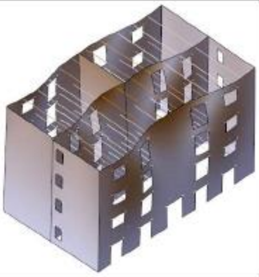	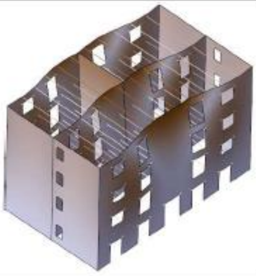	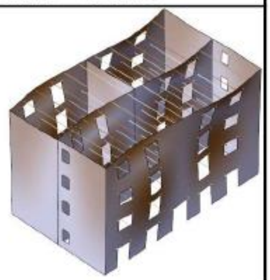
T16 = 0.21 s	T11 = 0.22 s	T7 = 0.22 s	T7 = 0.20 s
MY = 5.0 %	MY = 7.4 %	MY = 10.1 %	MY = 16.5 %
CMY = 60.7 %	CMY = 60.2 %	CMY = 62.5 %	CMY = 65.9 %

This may be due to the similar value of initial stiffness in tension and compression of unstrengthened and strengthened WD connections where the difference is mainly in the post-elastic force and displacement limits and not into the elastic behavior. The torsional RZ mode of each model corresponds to the 2nd mode except for model 1 in which it corresponds to the 3rd mode. The torsional mode has decreasing period of vibration with increasing WD connection stiffness (from model 1 to 4), as expected. The lower is the quality of the WD connection, the higher is the mode corresponding to translational X-direction. However, the same period T = 0.24 s corresponds to that mode of vibration, mainly because WD connections affect modes in Y-direction only (same direction of floor beams). Analysing the interesting translational Y-direction, a cumulative modal participation mass ratio $CMY \geq 60\%$ is only achieved in the 16th mode (T16 = 0.21 s) for model 1, 11th mode (T11 = 0.22 s) for model 2 and 7th mode for model 3 (T7 = 0.22 s) and 4 (T7 = 0.20 s).

4.1.5 Pushover analysis

A sensitivity analysis is performed through pushover analysis, that is a nonlinear static analysis aiming at simulating the structural seismic response after the application of incremental horizontal forces until collapse. Analysis can be conducted either in load control or in displacement control, as well as in event-by-event damage control (DeJong et al. 2009).The response of the structure is given by the so-called capacity curve given by the seismic coefficient α_H, (Equation 4.4) versus the horizontal displacement of the control node. The selection of a proper control node is not trivial, especially when flexible floors are present (Galasco, Lagomarsino, and Penna 2006).

$$\boldsymbol{\alpha_H}(\%) = -\frac{\sum \boldsymbol{horizontal\ base\, reaction\, forces}}{\boldsymbol{total\, weight\ of\ the\ structure}} \times \mathbf{100} \qquad 4.4$$

Moreover, the accuracy of the response is strongly dependent on a correct selection of the horizontal force distribution. Indeed, forces are commonly distributed proportional to the mass or to the modes. Even though the real dynamic behavior lays between these two boundaries, a mass-proportional distribution is considered here, as better describing the behavior of a building under extensive damage. Pushover displacement capacity is defined as the displacement corresponding to a reduction of 20% of the peak force.

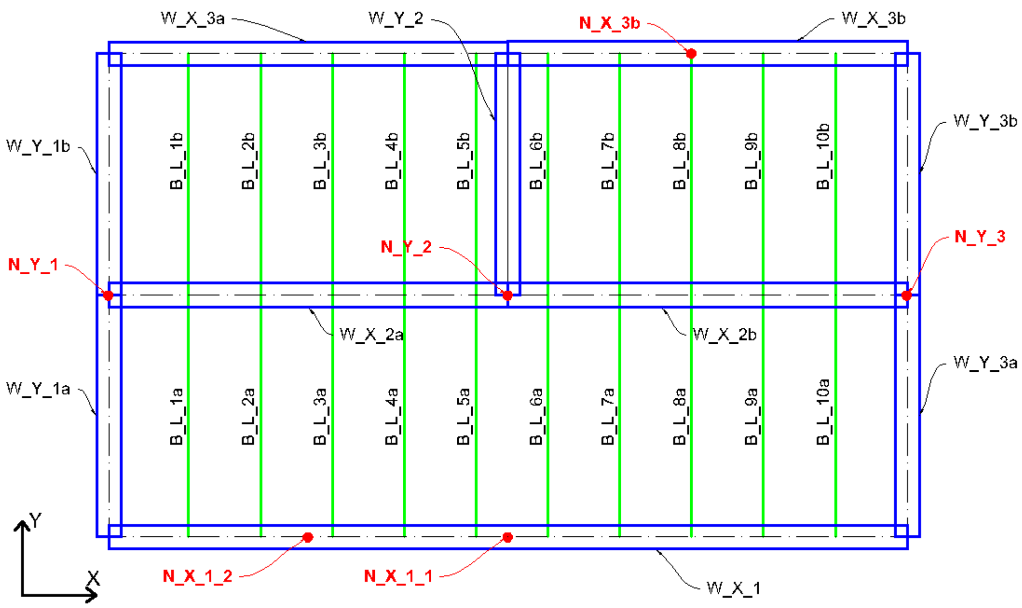

Figure 4.9 Building prototype element and control nodes labels: walls are labelled as W_D_nl, where W stands for wall, D is the direction of the wall axis, nl identifies the number of the wall; beams are labelled as B_L_nl, where B stands for beam, L is the floor level, and nl identifies the number of the beam.

The pushover analysis, which is a nonlinear static analysis, is carried out after vertical static analysis in which gravitational loads are applied. Pushover is later carried out in displacement control integrator setting a relatively small displacement increment of $\delta_u = 0.05\,mm$. The Newton algorithm is used with a convergence test on the norm of the displacement increment, setting a tolerance of 0.001 mm. The adaptive time-stepping analysis can be used in order to reduce or increase the displacement increment factor after no-convergence issues. The lateral loads, proportional to the mass, are linearly increased.

A preliminary pushover analysis is firstly computed for Model 1 and 4 in both positive and negative X and Y directions given the asymmetry of the structure, especially due to the presence of the internal W_Y_2 wall (Figure 4.9) contributing to increase asymmetry along the longitudinal W_X_2 wall. The pushover control nodes are selected where the maximum displacement at the top of the building is expected for that loading direction. Thus, N_Y_3 and N_Y_1 (Figure 4.9) are the control nodes for pushover in positive and negative X direction, respectively. When pushing to the Y direction, nodes N_X_1_1 and N_X_1_2 are selected for Model 1 and 4, respectively.

Pushover capacity in Y direction (both positive or negative) is clearly lower than capacity in X direction (Figure 4.10) in terms of strength and displacement for both Model 1 and 4. The failure mechanisms are investigated in terms of lateral displacement at peak strength capacity (Figure 4.11Figure 4.12). When forces act along the X direction, failure is mainly controlled by the OOP of lateral façades (W_Y_1 and W_Y_3, Figure 4.9), while the OOP mechanism of walls parallel to the X axis controls the pushover capacity along the Y direction. When no beams are present, that is for Model 1, failure is dominated by W_X_1 wall for both loading directions, while for Model 4 damage is better distributed among the other parallel walls. This can be justified as W_X_1 wall has a clearly lower restraint level, if compared to the rest of the walls, justifying its lower capacity. This is further evident for lack of diaphragm behavior (Figure 4.11c,d).

Although there is no evident difference between positive and negative Y direction for Model 4 (Figure 4.10b), Model 1 shows a lower capacity in the negative Y direction mainly because of the higher vulnerable OOP W_X_1 wall in the outward direction, compared to the inward direction.

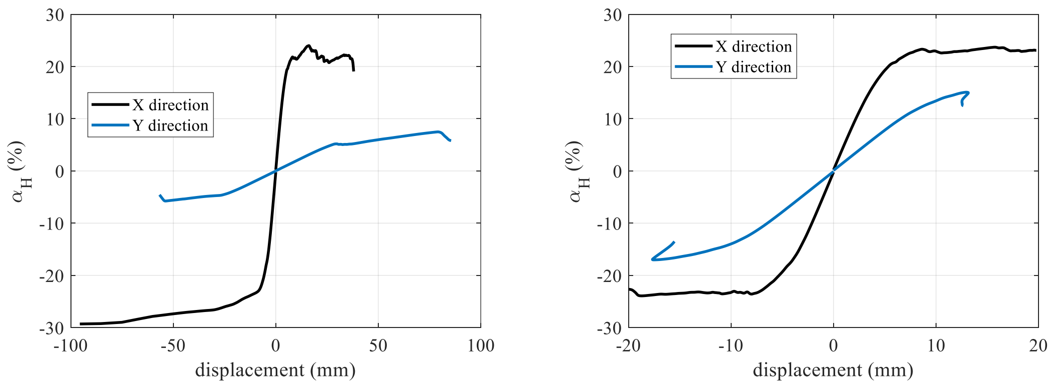

(a) (b)

Figure 4.10 Pushover curves in both positive and negative X and Y directions: (a) Model 1; (b) Model 4.

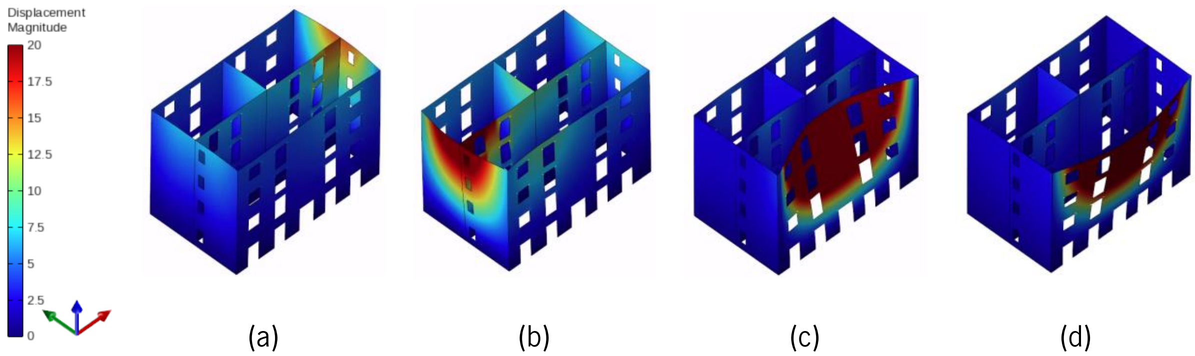

(a) (b) (c) (d)

Figure 4.11 Contour map of total lateral displacement at the peak strength capacity of Model 1: (a) +X dir.; (b) -X dir.; (c) +Y dir.; (d) -Y dir.

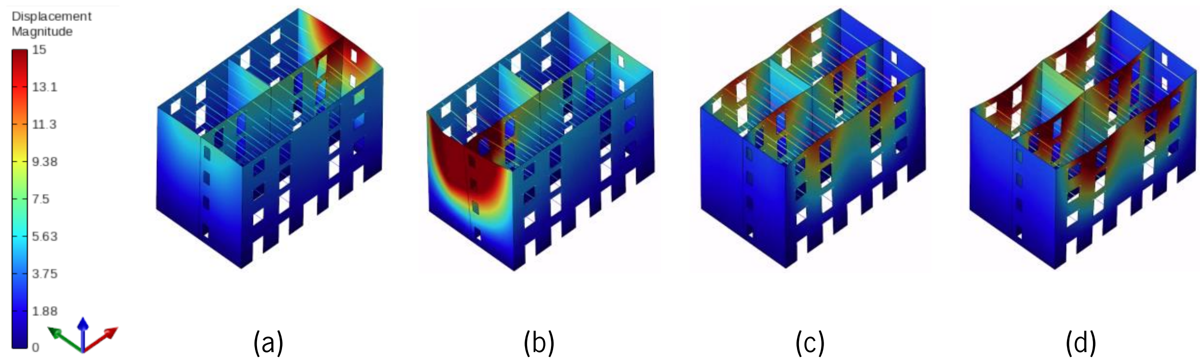

Figure 4.12 Contour map of total lateral displacement at the peak strength capacity of Model 4: (a) +X dir.; (b) -X dir.; (c) +Y dir.; (d) -Y dir.

This is due to the absence of the floor stiffness and to the weak wall to wall connections that could only rely on the poor masonry tensile strength. Therefore, the influence of the quality level of the WD connection on the overall behavior of the building is analysed in terms of force and displacement capacity with respect to the solely negative Y direction (parallel to timber floor beams axis direction) (Figure 4.7a), which corresponds to the weakest direction of the building. Actually, it is believed that Models 1 and 4 represent the boundaries of the real building which is more likely characterized by an intermediate behavior between the two.

Pushover analysis is, therefore, performed for each configuration loading in the negative Y direction. Different control nodes are selected at the top of the building (Figure 4.9) in order to show different displacements associated to different failure mechanisms. Node N_X_1_1 reflects the OOP displacement of the W_X_1 wall and it is placed at its mid-span. Node N_X_1_2 is placed at the same wall but at quarter span. Node N_Y_2 represents the IP displacement of W_Y_2 wall, whereas node N_X_3b reflects the OOP displacement of W_X_3b wall and is placed at mid-span. For a matter of clarity, the capacity curves are shown in the first quadrant, thus plotting the absolute value of both seismic coefficient and lateral displacement.

Figure 4.13 demonstrates that the selection of a proper control node is not obvious, as different results can be obtained with diverse control nodes. Indeed, pushover curves can be different in terms of stiffness, and displacement capacity, as well as displacement at peak strength. In particular, N_X_1_1 gives the curve with greatest displacement level for each model, apart from Model 4, in which this is obtained considering N_X_1_2 node.

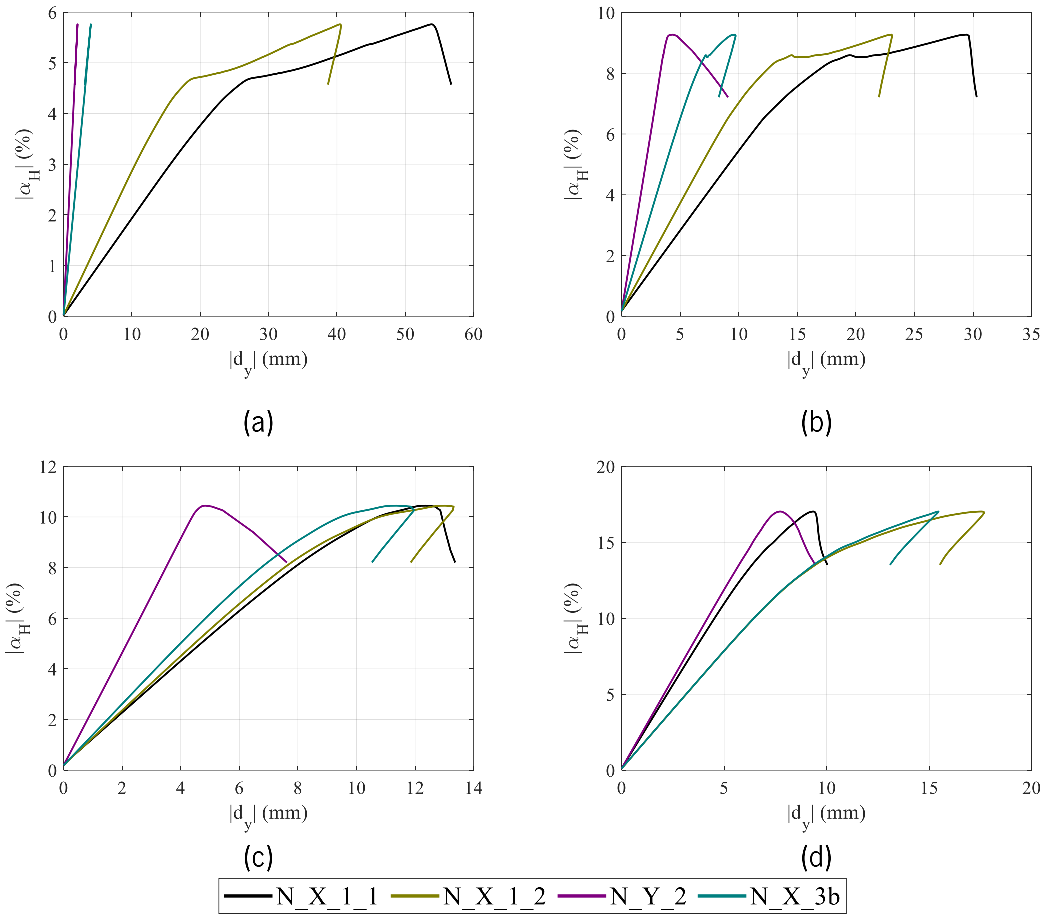

Figure 4.13 Pushover curves of each model configuration for negative Y displacement of different control nodes: (a) Model 1; (b) Model 2; (c) Model 3; (d) Model 4.

For Model 3, similar results are obtained using both nodes. The N_Y_2 node controlling the IP displacement of the central transversal wall W_Y_2 returns the pushover curve with the lower displacement level regardless of the Model, as expected. Moreover, in each model configuration, Nodes N_X_1_2 and N_X_3b, representing the OOP displacement of W_X_1 at the quarter span, and W_X_3b, show the so-called snap-back behavior in the post-peak phase. This can be explained by the sudden drop of resistance due to the failure of WW interface caused by high tensile stress level into the masonry. This is further confirmed by the damage pattern in terms of maximum tensile strain at peak strength shown in Figure 4.14.

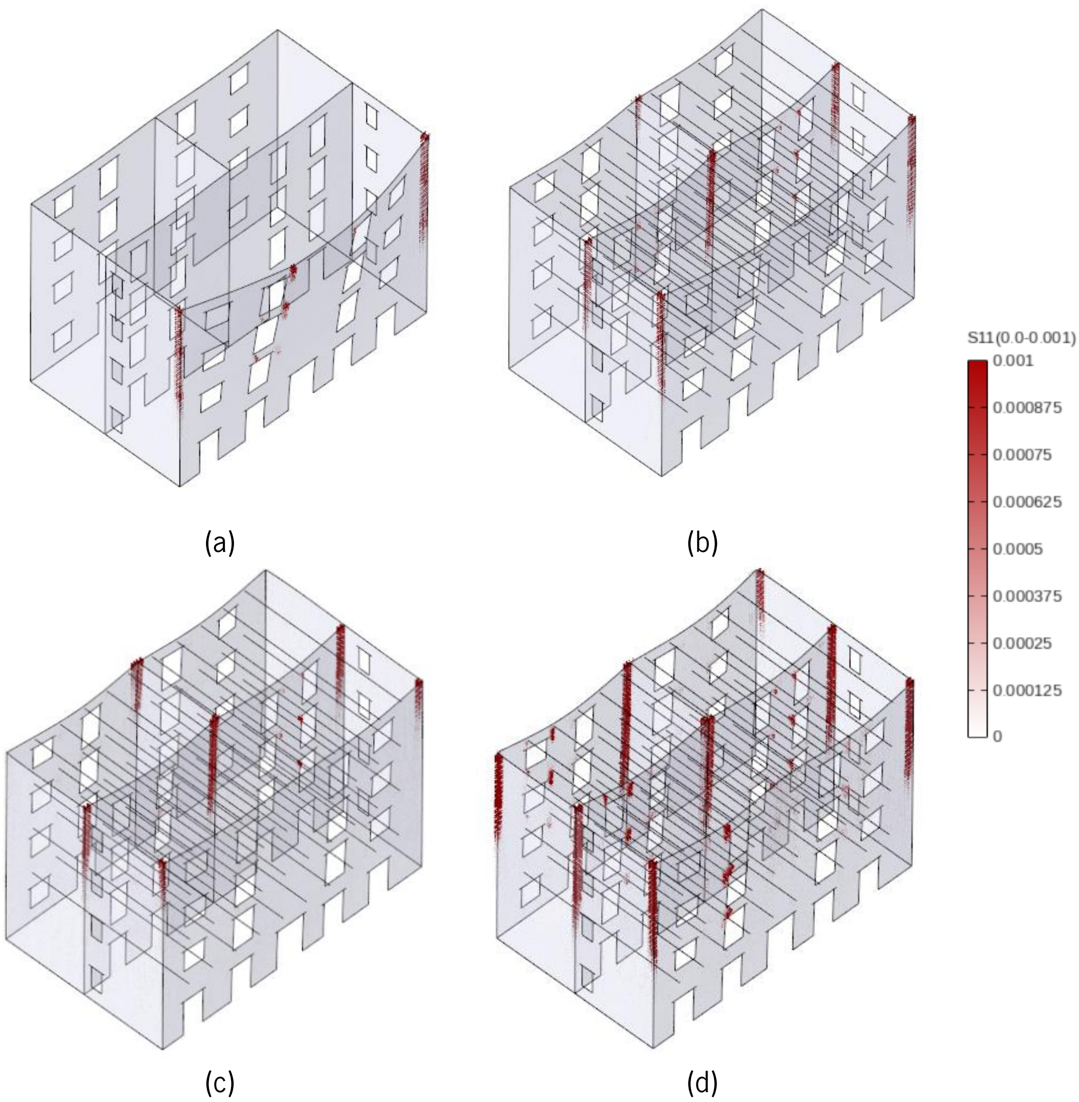

Figure 4.14 Principal tensile strains at the peak capacity of each model configuration for -Y pushover analysis: (a) Model 1; (b) Model 2; (c) Model 3; (d) Model 4.

As the level of the connection quality increases, the building responds in a more and more global manner. Indeed, if damage in Model 1 clearly refers to the OOP collapse of W_X_1 wall, Model 4 shows a more distributed damage along the vertical corners of all the walls. The failure mode is, however, associated to overturning of every OOP wall, highlighted by the vertical cracks. Further damage is also concentrated adjacent to the opening corners. Such a damage pattern is an index of building highly vulnerable to the local mechanisms that should be prevented prior to the strengthening of IP masonry walls.

Pushover curves obtained for the negative direction are compared for each model configuration selecting N_X_1_1 as the control node of Models 1,2,3, while N_X_1_2 for Model 4 and are shown in Figure 4.15. Models 1 and 4 behave in a considerably different way both in terms of strength displacement capacity, but also in terms of stiffness. Moreover, Models 2 and 3 are within those two boundaries, as expected. Despite Models 3 and 4 are characterized by good quality of WD connections, the rupture is more fragile than models 1 and 2, showing, in turn, a first crack limit followed by a plateau with less rigid branch. The collapse is characterized by a relatively higher then Models 3 and 4. In particular, Model 4 has a seismic coefficient peak by 17%, while models 2 and 3 reach a peak strength by about 10%.

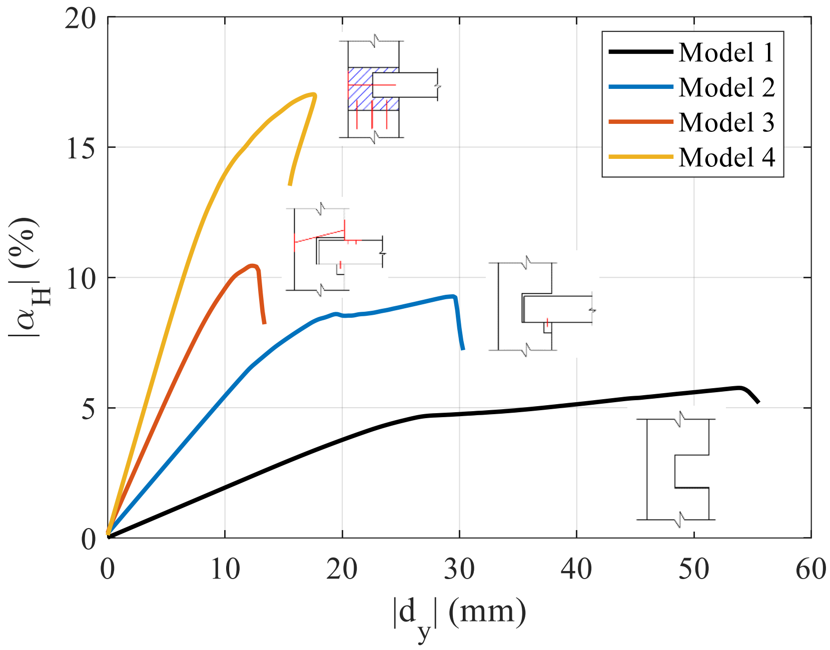

Figure 4.15 Influence of WD connection quality in terms of pushover curves in the interested -Y direction.

Model 1 has a very low resistance, with a value by about 6% of seismic coefficient (about 65% reduction with respect to Model4 and 43% reduction with respect to Model 3). Model 4 has the highest strength peak and is characterized by a ultimate displacement value greater than Model 3.

The behavior of nonlinear WD connection is analysed through the force-slip graphs shown in Figure 4.17 referred to Model 2 and 3. Such curves are produced selecting six WD connections at both ends of three different floor beams placed at the top of the building. Beams B_4_5a, B_4_6b and B_4_8b (Figure 4.16) are chosen as those having the most representative and vulnerable WD connections at their ends.

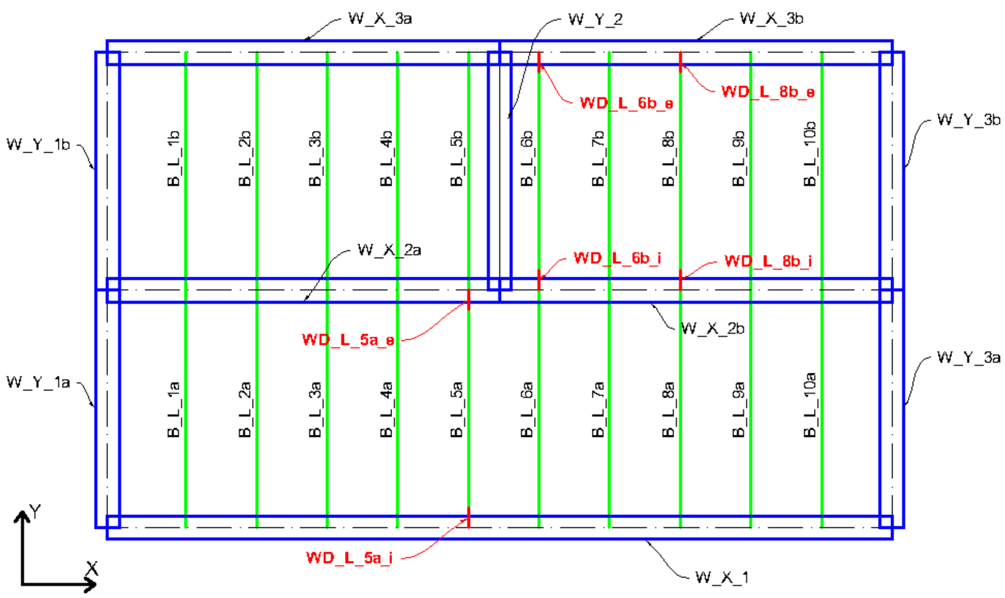

Figure 4.16 Building prototype element and WD connections labels: wall to diaphragm connections are labelled as WD_L_nl_i(e), where L stands for level; nl is the connection numbering (corresponding to the adjacent beam) and i or e pedix defines the side of the beam.

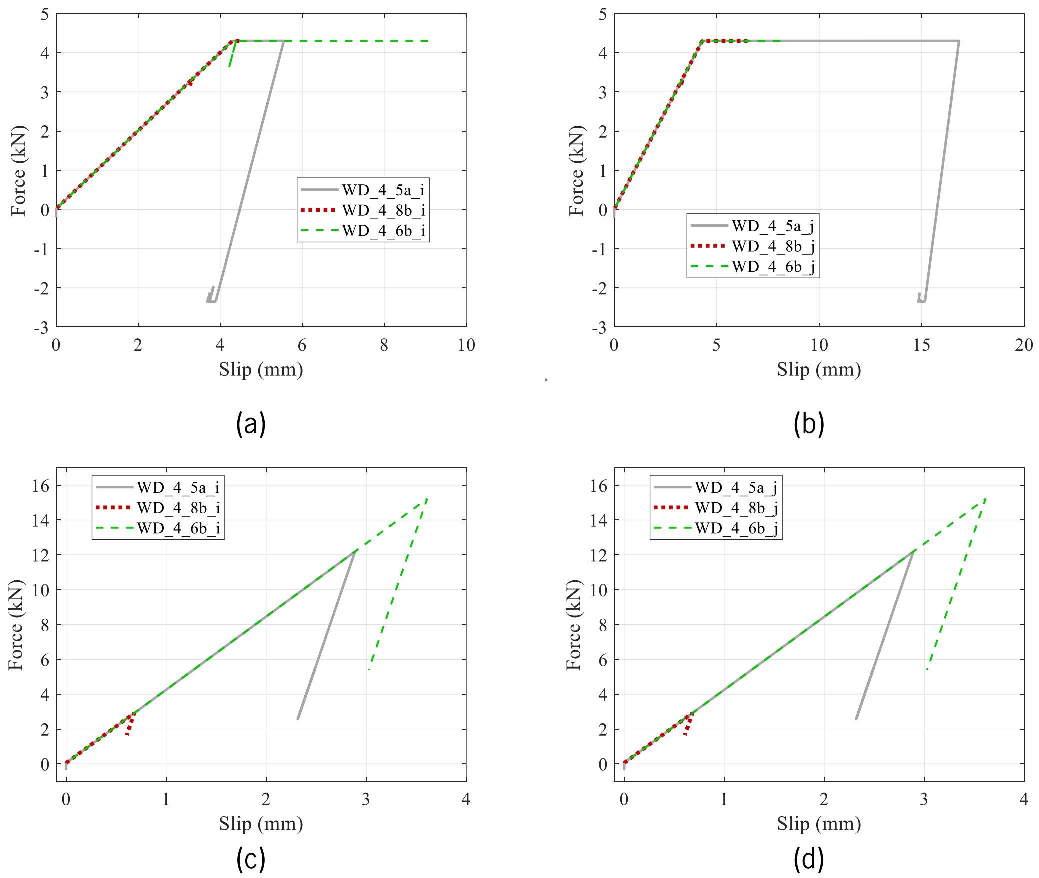

Figure 4.17 Force-Slip curves of nonlinear WD connections obtained from pushover analysis in -Y direction: (a) (b) Model 2; (c), (d) Model 3.

Although in no cases the failure of the connections occurs, all the selected connections in Model 2 undergo their elastic limits reaching 50% of the slip capacity of the unstrengthened connection (see WD_4_5a_j connection in Figure 4.17b). As demonstrated in Figure 4.17a,b the displacement level is not always the same in the two beam ends, while exactly the same strength level is obtained in both extremities, as expected. Model 3 (strengthened configuration) exhibits the same behavior in both beam ends, and the connections undergo higher force levels. All the selected connections, however, remain elastic, reaching rather lower displacement levels than unstrengthened model. The lower WD slip obtained for strengthened connections is clearly a positive sign of increased restraint level of the walls leading to a building with better box-type behavior.

4.1.6 Transient analysis

Every model configuration is successively analysed through Incremental Dynamic Analysis (IDA) that is dynamic nonlinear analysis under selected accelerogram, scaled up until the building collapse occurs. The accelerogram is extrapolated from Engineering strong motion database (Luzi et al. 2020) is a natural waveform referring to the 6.5 magnitude Norcia (PG, Italy) seismic event that stroke central Italy in October 2016, within the Amatrice-Norcia-Visso seismic sequence. The accelerogram is shown in Figure 4.18a and has a peak ground acceleration (PGA) of 0.44 g, while the elastic acceleration response spectra are shown in Figure 4.18b for 3% and 5% damping ratios. Despite the original waveform has a total duration of 15 s, a reduced strong motion duration is considered for the analysis as the period between 0.01% and 99% of the total Arias intensity energy, I_a (Figure 4.19). This is defined as the cumulative energy per unit weight absorbed by an infinite set of undamped single-degree-of-freedom oscillators at the end of an earthquake,

$$\boldsymbol{I_a = \frac{\pi}{2g}\int_0^{T_f} a_x^2(t)dt} \qquad 4.5$$

Trifunac and Brady (Trifunac and Brady 1975) actually suggest 5% and 95% values as thresholds defining the period of interest, that is the significant duration t_D, but a wider domain is considered herein in order not to neglect relevant portions of the strong motion. The accelerogram is finally filtered using SeismoSignal (Seismosoft 2001) also ensuring baseline correction.

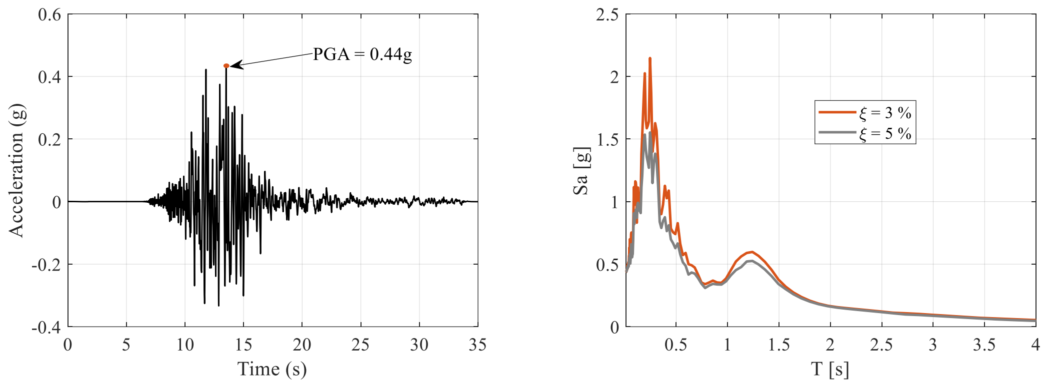

(c) (d)

Figure 4.18 Original natural accelerogram selected for dynamic analysis; (a) accelerogram time-hystory; (b) acceleration response spectra for 3% and 5% damping ratios.

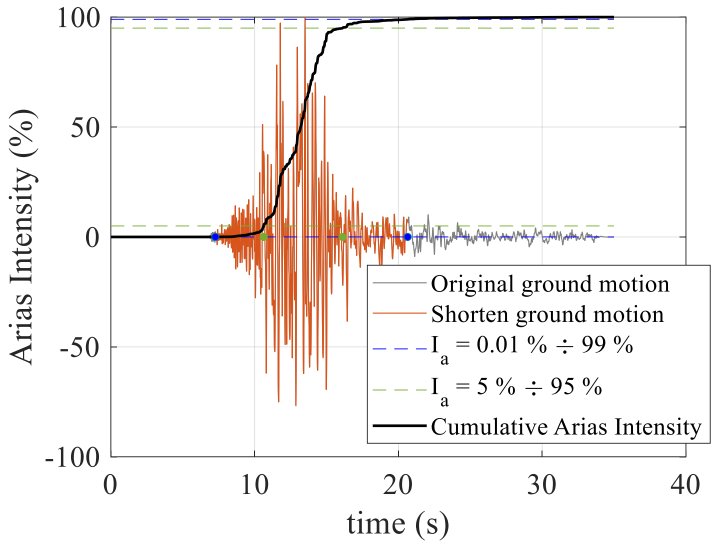

Figure 4.19 Reduced strong motion duration as the period between $T|_{0.05\% I_a} \leq T_{red} \leq T|_{99\% I_a}$

Considering the capacity obtained through preliminary static nonlinear analysis, the acceleration is scaled in such a way to have the following PGA values: [2.5% 5.0% 7.5% 10.0%] g. Each increment is carried out separately starting from the undamaged configuration, without accounting for damage history of previous steps.

A static analysis is firstly performed considering the gravitational loads. Afterwards, the transient analysis is carried out for the selected PGA increment level, under the Hilber-Hughes-Taylor (HHT) scheme with $\alpha = 0.9$, setting a linear algorithm, which was seen to perform well for dynamic analysis. It is worth noting that in OpenSees $\alpha = \alpha_{HHT} + 1$, where α_{HHT} is the value found in (Hilber, Hughes, and Taylor 1977), thus $\alpha = 1.0$ corresponds to the Newmark method. Such an integration method is an implicit scheme attempting to increase the amount of numerical damping without degrading the order of accuracy. Indeed, numerical damping is defined using Rayleigh damping approach in order to properly account for energy dissipation. The modes with significant participation mass in the interested Y direction are selected to properly define the frequency dominium of interest. In every model configuration the first mode is the first significative mode for the translational Y direction, while the last significant mode is defined as that corresponding to a cumulative participation mass in translational Y direction $CMY \geq 60\%$ (see Section 4.1.4). The damping matrix is, therefore, defined proportional to the mass and to the current stiffness matrix, and a value of damping ratio $\xi = 3\%$ is selected.

Similarly to the pushover analysis, the convergence is set based on the norm of the displacement increment defining a 0.001 mm tolerance. The linear algorithm is selected as it was seen to perform well within transient analysis.

The analysis time step Δt should be defined capable of accounting for the lowest significant period T_{fin}, with an error less than 5 % (Mendes and Lourenço 2010) according to the following equation:

$$\boldsymbol{\Delta t = \frac{1}{20} T_{fin}} \tag{4.6}$$

Given the lower significant period equal to $T_{fin} = 0.20s$, a value of $\Delta t \leq 0.01\, s$ should be selected. Considering the waveform time increment $\Delta t_{acc} = 0.005\, s$, this same value is chosen as analysis time step in order not to lose significant acceleration peaks.

Modal analysis, performed before and after dynamic analysis, allows an additional information about the damage level of the building after each PGA increment.

The total computational time necessary for each increment is of about 13 hours using a Windows-based machine with Intel Core i9-7900X 3.30 GHz CPU and 128 GB Memory RAM.

Results are condensed into displacement- or force-based dynamic envelope curves simply constructed as the envelope of the peak displacement of peak forces in the direction of interest. Figure 4.20 shows as an example, the envelope points extracted over the seismic coefficient hysteresis of Model 4 under 25% g ground motion. Such envelope curves are intended to be compared to pushover curves in negative Y direction, where higher level of damage is expected, thus only the negative displacement is considered for the selection of dynamic envelope peak forces and displacements.

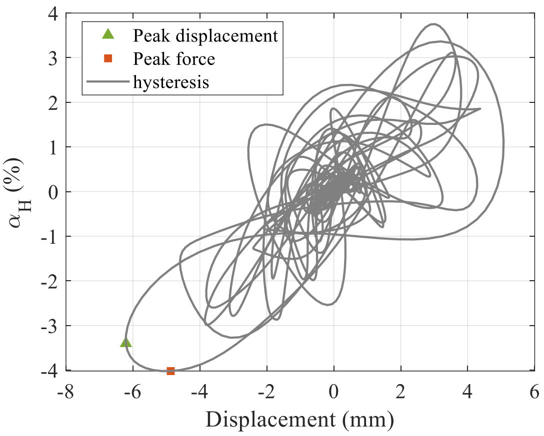

Figure 4.20 Definition of dynamic envelope curves over the seismic coefficient hysteresis; Model 4 under 25% g earthquake.

Control nodes are obviously the same selected for pushover curves, according to the criterium of node better representing the OOP of W_X_1 wall. Dynamic envelope curves are displayed in Figure 4.21 and compared to pushover curves for each model configuration.

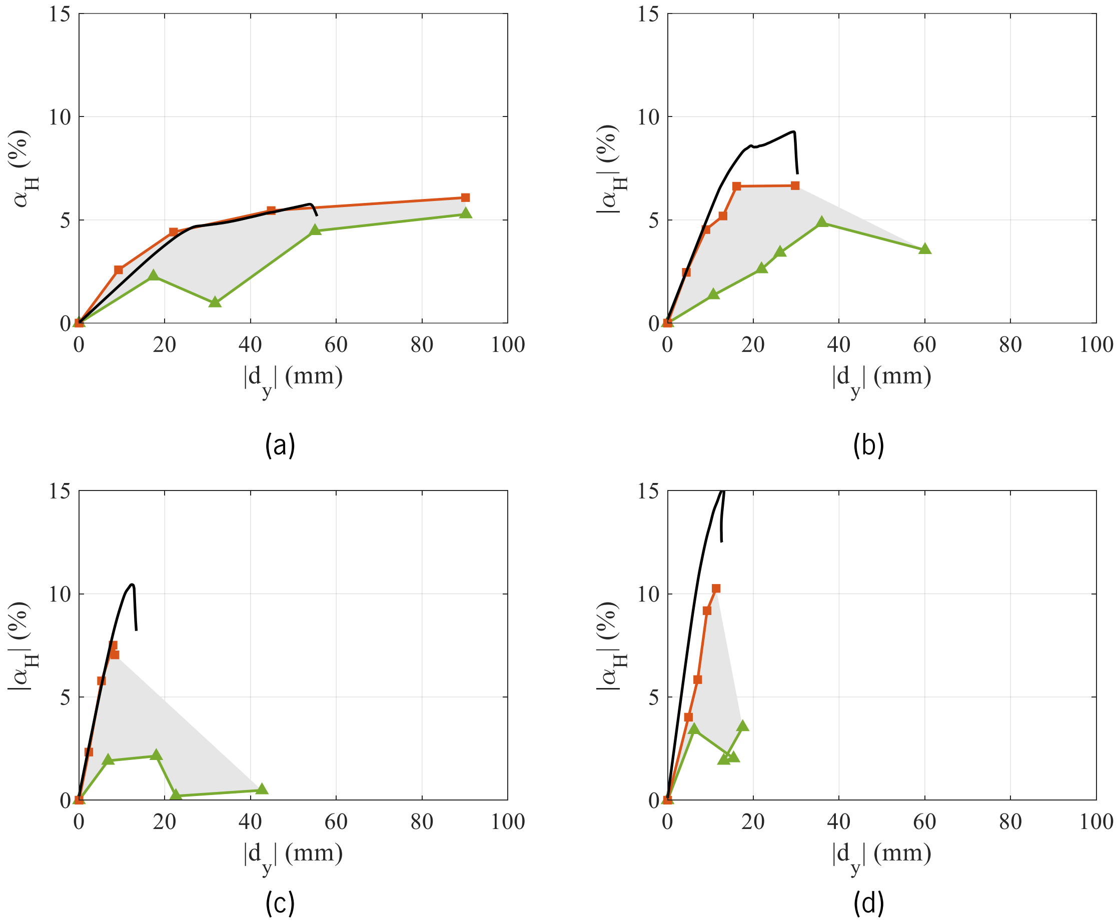

Figure 4.21 Dynamic envelope curves versus pushover curves: (a) Model 1; (b) Model 2; (c) Model 3; (d) Model 4.

Pushover capacity is clearly closer to the force-based dynamic envelope, in terms of stiffness, displacement and force capacity. Pushover force capacity is overestimated in Models 2,3 of about 40%, while in case of Model 4 pushover capacity overestimates initial stiffness and maximum force. A difference of 50% in terms of maximum force is obtained in this latter case. The high nonlinearity of the problem causes the displacement-based envelope curves to be very different from force-based curves. This is visible since the initial increments and is present in every model configuration.

Figure 4.22 shows the damage pattern of all model configurations at the peak force under the final 10% g earthquake. It seems evident that most of the damage is concentrated to wall-to-wall (WW) structural connections, regardless of the WD connection type. This is a clear index of possible formation of OOP mechanisms of the walls. The better quality of WD connection, however, increases the restraint level of W_X_1 wall, leading to a more distributed damage pattern as better shown in model 4 (Figure 4.22d). Damage is also localized at the corners of the openings.

With the aim of better understanding the damage history, it is possible to analyse the damage increment for every dynamic increment step, for each model (Figure 4.23). Model 1 shows a severe damage level even after the first 2.5% g increment. The rest of the model configurations undergoes moderate cracks after the 5.0% g increment. 7.5% g increment is likely to be the one responsible of partial collapses of walls portions regardless of the WD connection. Finally, the damage pattern obtained under 10.0% g increment is typical of ultimate limit state where the main failure mechanism is mainly associated to the OOP of the walls rather than the IP of transversal walls. Indeed, even if a perfect link at wall-diaphragm interface, the building is not able to perform as a well-connected box, probably because of the peculiarity of the geometry taken into account.

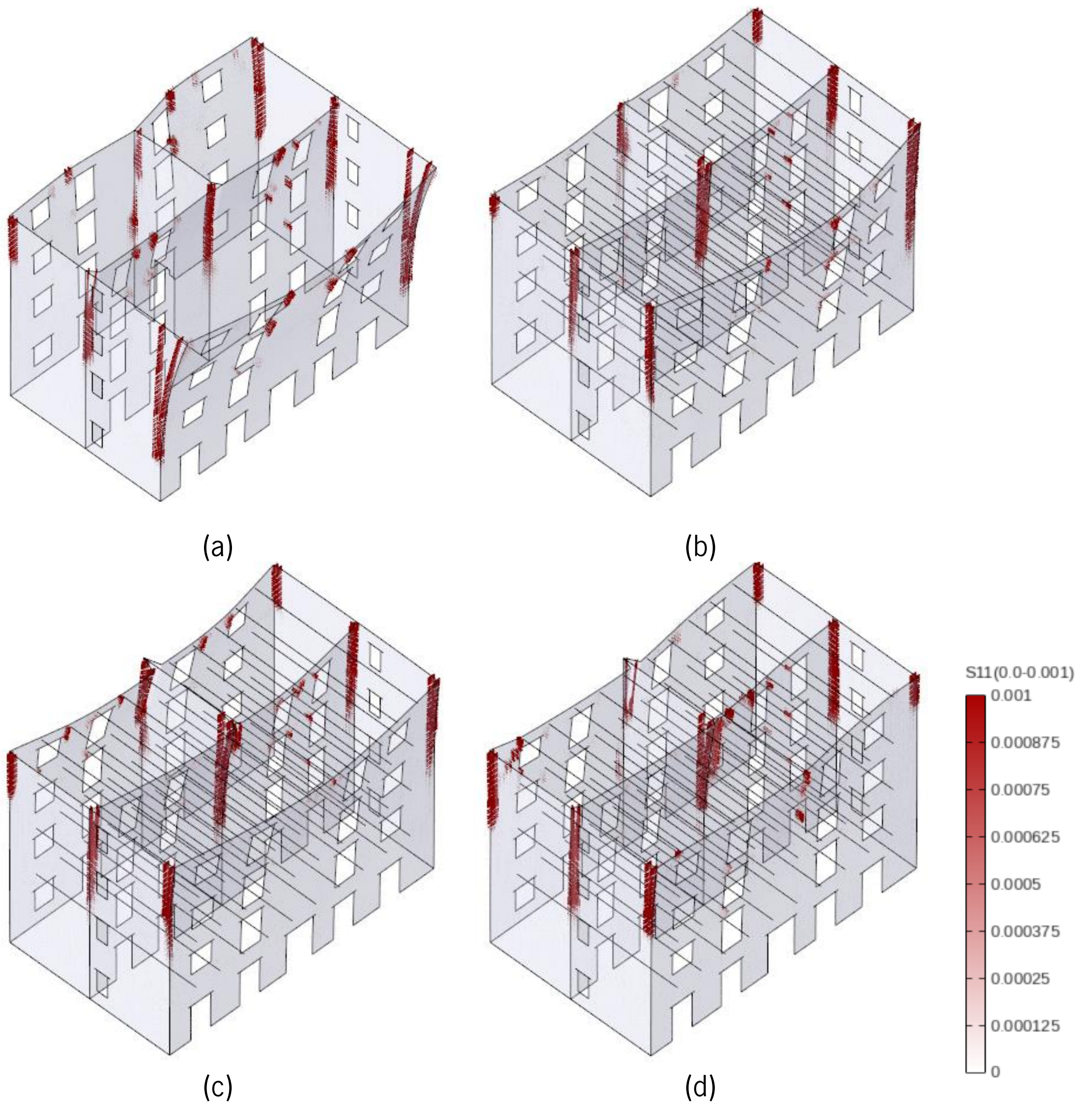

Figure 4.22 Principal tensile strains at the peak capacity of every model configuration for 10% g dynamic analysis: (a) Model 1; (b) Model 2; (c) Model 3; (d) Model 4.

The influence of WD connection quality is studied here in terms of force-based capacity and displacement time-history (Figure 4.24). A clear increase in terms of initial stiffness and peak strength is shown if the quality of the connection improves. Model 2 and 3 (unstrengthened and strengthened models, respectively, with nonlinear WD connections) show a quite similar behavior especially at the lower stage of the IDA, while Model 3 depicts a stiffer behavior reaching slightly higher strength peak. Similarly to pushover results, models 1 and 4 set the boundaries of the connection configurations, as expected. Allthough Model 4 capacity has a similar trend to model 3 curve, the former reaches 37% higher strength.

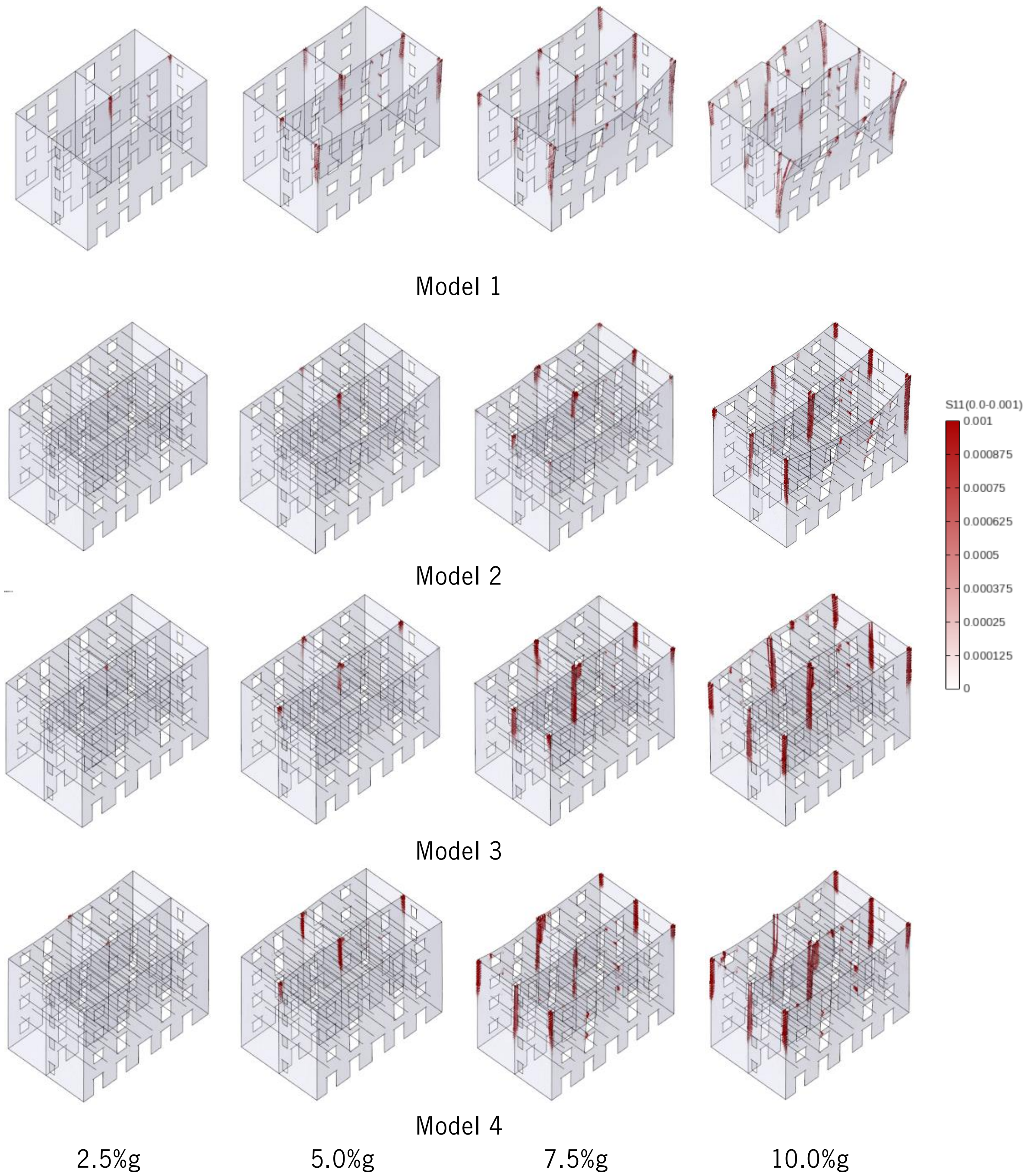

Figure 4.23 Incremental damage in terms of principal tensile strains at the peak capacity of every model configuration.

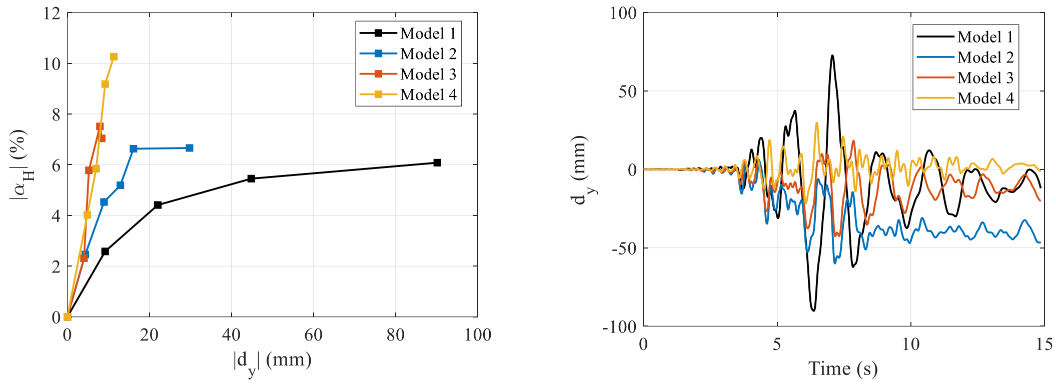

Figure 4.24 Influence of WD connection quality in terms of (a) dynamic force-based capacity and (b) displacement time-history.

It is worth noting that the lower constraint level at the diaphragm-to-wall interfaces leads to higher displacement peaks, index of possible wall OOP overturning. The displacement time-histories under ultimate 10% g earthquake are shown for N_X_1_1 node representing the mid-span OOP displacement at the top of W_X_1 façade. Every model, apart from Model 4, shows a clear residual displacement at the end of the analysis, due to the strong damage level under peak acceleration.

The dynamic effects of nonlinear WD connections are here analysed in terms of force-slip curves. These curves are constructed directly reading the forces and deformations into the ZeroLength elements (see Section 3.3).

WD_4_5a_i and j connections undergo higher level of relative beam-to-wall displacement and force for both Models 2 and 3 (Figure 4.25). Even though connections exhibit a substantial symmetric behavior for Model 2 response (Figure 4.25a,b), this is not true for Model 4 (Figure 4.25c,d), where WE_4_5a_i connection results in a higher peak force in compression (over 200 kN).

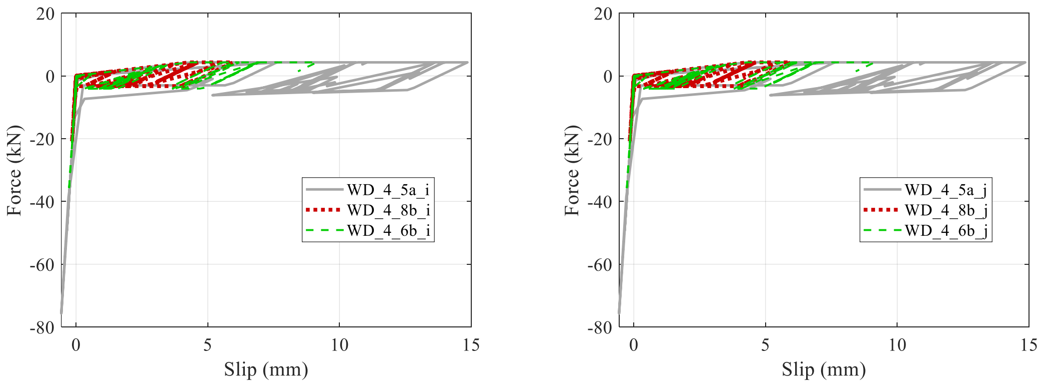

(a) (b)

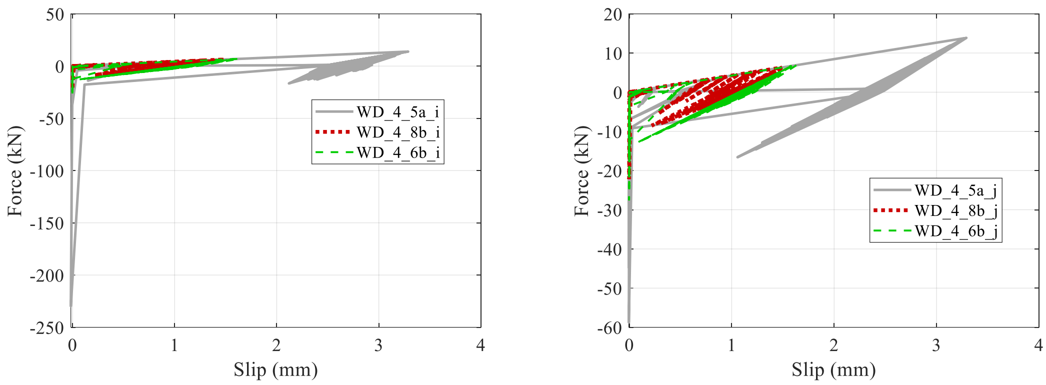

(c) (d)

Figure 4.25 Nonlinear WD connections Force-Slip hysteresis after dynamic analyses: (a) (b) Model 2; (c), (d) Model 3.

It can be noted how the WD connection is characterized by moderate nonlinear behavior even for low stress levels. This is given by the very low elastic limit set for the definition of Pinching4 hysteretical model and can be justified by the experimental evidences where unloading branches have higher slope with respect to reloading branches, even at lower forces.

Figure 4.26 demonstrates that the connection pull-out behavior (in tension) is basically symmetric in both beam sides for Model 2, whereas there is a slightly different behavior in Model 3, even if the same peak force and slip are obtained in the direction of interest.

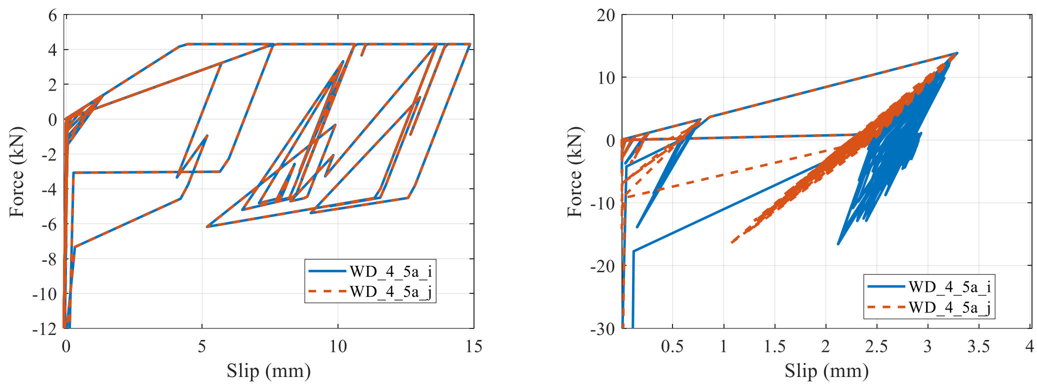

(a) (b)

Figure 4.26 WD_4_5a connection hysteresis at both beam ends: (a) Model 2 (b) Model 3.

The influence of WD connection is shown in terms of total energy, simply computed as the area within the force-slip hysteresis, for the solely WD_4_5a_i connection (Figure 4.27). The comparison between models 3 and 4 connection shows that the total energy is higher in model 3 only at lower cumulative slip. The considerably higher cumulative slip obtained in model 2 corresponds to higher total energy involved during the hysteresis (Figure 4.27b).

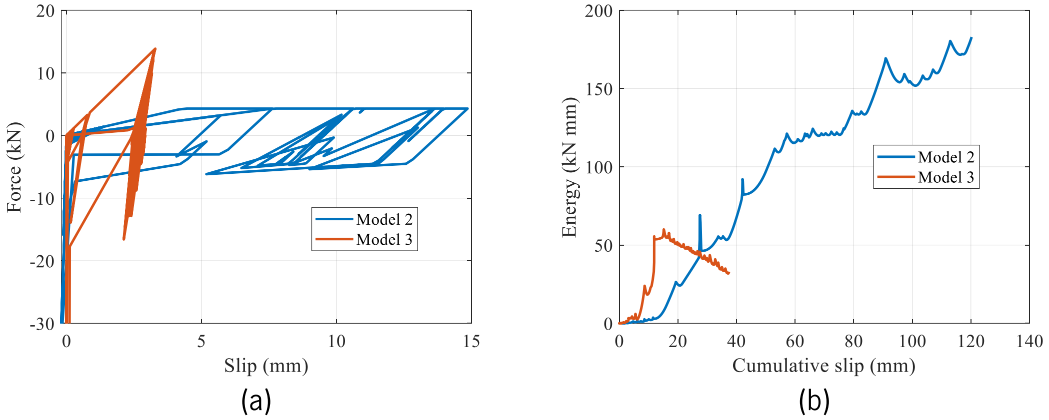

Figure 4.27 Influence of WD connection in terms of (a) force-slip hysteresis; and (b) total energy at the wall-diaphragm interface: WD_4_5a_i connection.

4.2 Local analysis: kinematic approach

Although global analysis is fundamental for the seismic capacity of the building as a whole, URM buildings are vulnerable to the formation of cracks and subsequent activation of dangerous local mechanisms, such as the out of plane (OOP) of entire walls or portions of them, the corner masonry detachment, as well as other complex masonry assembly mechanisms, particularly when WW and WD connections are poor, and should be detected with priority. Moreover, even though advanced tools are available for accurate analysis of rather large entire buildings, uncertainties given by poor information about material mechanical properties and structural connections may lead to uncertain results, making the computational effort not acceptable. On the other hand, the local analysis of the building, can be simply carried out through limit analysis based on the virtual work principle (VWP), also known as kinematic analysis, and can be easily performed on any worksheet to quickly gain important information about the most vulnerable walls where local damage is more likely to occur. Such an approach is recommended by the Italian code standards (C.S.LL.PP. 2019; DMI 2018) and can be performed for rigid-like block behavior of the masonry walls. The method is based on the following hypothesis:

- negligible masonry tensile strength;
- negligible sliding;
- infinite masonry compressive strength.

Such a method can consider the influence of eccentric overburden loads, asymmetric geometries, possible roof thrusts and the presence of ties or anchors. Recently, the contribution of frictional forces acting along the WW interface was considered (Casapulla et al. 2018). Furthermore, the seismic assessment should take into account the dynamic amplification due to the formation of the hinge at a certain level of the building, thanks to the recent development of floor spectra, included in the Italian code standards on the bases of research studies carried out by Degli Abbati et al. (Degli Abbati et al. 2018).

The geometry of the mechanism should be firstly assumed; secondly the seismic capacity can be assessed in terms of force (that is linear kinematic analysis) or displacement (that is nonlinear kinematic analysis, capable of evaluating the evolution of the horizontal force to which the mechanism is progressively able to resist until loss of equilibrium). The force-based verification is suggested for assessing both the Serviceability Limit State SLS (SLD in Italian), and the Life-safety Limit State LLS, through linear kinematic analysis (simplified q-factor approach), which is briefly summarized in the following steps:

1. Mechanism identification;
2. Evaluation of the load multiplier α_0;
3. Evaluation of the spectral acceleration [capacity] a_0;
4. Evaluation of the LLS peak acceleration [demand]:
    4.1. Peak ground acceleration $PGA(LLS)$; $(Z = 0)$
    4.2. Peak floor acceleration $PFA(Z)$; $(Z \neq 0)$
5. Evaluation of the Acceleration Safety Factor ASF;

On the other hand, the seismic assessment of local mechanisms under the LLS, through nonlinear kinematic analysis can be briefly summarized in the following steps:

1. Mechanism identification;
2. Evaluation of the evolution of the load multiplier with increasing displacement of a control point $\alpha = \alpha(d_C)$;
3. Transformation of the $\alpha - d_C$ curve into the $a - d$ capacity curve;
4. Evaluation of the Displacement Safety Factor DSF;

Linear and nonlinear kinematic analysis under the Life-safety Limit State (LLS) is applied here to the 4-level URM building prototype, described in Section 4.1.1. Seismic parameters (Table 4.5) are assumed for a building located in Norcia (PG, Italy), with Soil type B (Table 3.2.IV, (DMI 2018)), topographical category T1 (Table 3.2.III, NTC2018)).

Table 4.5 Life-safety Limit State (LLS) seismic parameters for the reference building.

description	symbol	value	unit
return period	RP	475	years
peak ground acceleration	a_g	0.255	g
spectral amplification factor	F_0	2.376	-
spectral reference period	T_c^*	0.335	s
soil factor	S	1.1358	-

Conventionally, failure mechanisms are selected based on experience gained from past earthquakes and now available in several catalogues or based on the expertise of the analyst. Many commercial softwares are also available performing optimization process in order to select the most vulnerable mechanisms. It is important to point out that local analysis should be performed prior to the global assessment, as also suggested by the Code (DMI 2018). Possible failure modes, occurring at the external facades of the prototype building, are selected as few of the most likely to activate local collapse (Figure 4.28). Indeed, damage pattern after pushover and nonlinear dynamic analyses performed for the most vulnerable direction (Figure 4.14 and Figure 4.22) show the high vulnerability of the building to local mechanisms activation, especially regarding the OOP overturning of masonry façades. The quality of WD connections influences both global and local analysis: by increasing the connection quality, the global and the local seismic capacities increase as the local mechanisms develop with restrained wall boundaries.

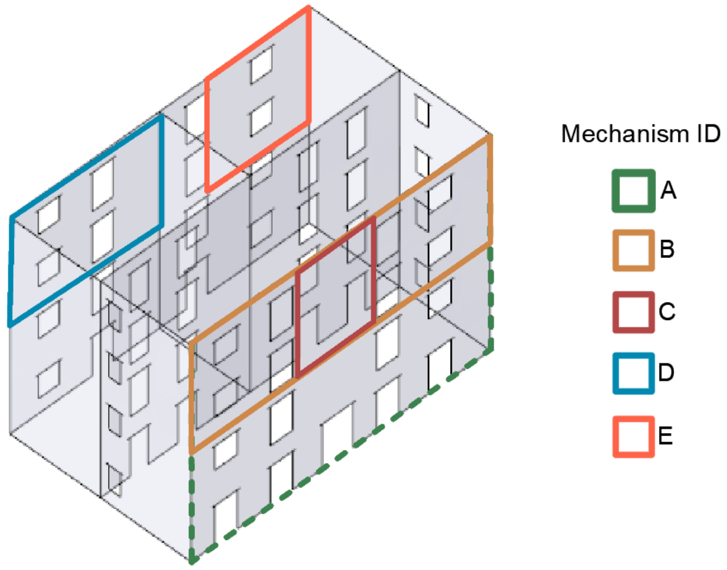

Figure 4.28 Selection of failure mechanisms for limit analysis.

Four different WD configurations (Figure 4.8, Section 4.1.3) with increasing quality are assumed, similarly as previously done in FEM analysis. Models 2 and 3 are considered with simply elastic-perfectly plastic WD connection behavior, based on the analytical formulations illustrated in Section 3.2.

4.2.1 Linear kinematic analysis

This approach allows for the seismic assessment of local mechanisms directly computing the seismic load multiplier α_0 (Equation C8.7.1.1, (C.S.LL.PP. 2019)):

$$\boldsymbol{\alpha_0} = \frac{\sum_{k=1}^{N} \boldsymbol{P_k \delta_{Py,k}} - \sum_{k=1}^{m} \boldsymbol{F_k \delta_{F,k}} + \boldsymbol{L_i}}{\sum_{k=1}^{N} (\boldsymbol{P_k} + \boldsymbol{Q_k}) \boldsymbol{\delta_{PQ_{x,k}}}} \qquad 4.7$$

where P_k denotes k^{th} vertical gravity force, while F_k refers to the k^{th} external (beneficial or detrimental) force, L_i is the total work done by internal forces, $\mathrm{Q_k}$ is related to any gravity force not directly acting to the block but inducing a horizontal seismic force to it, as not acting elsewhere. δ terms are the virtual horizontal or vertical displacements of the corresponding force. The virtual displacement $\delta_{F,k}$ corresponding to the k[th] external force F_k is projected in the same direction of the force and is positive if the contribution of the force is detrimental for the mechanism. The evolution of the capacity curve is not necessary at this stage, allowing to consider the nonlinearities using the equivalent building behavior factor q, usually assumed equal to 2.

The load multiplier α_0 is also known as the collapse multiplier and is associated to the minimum force necessary for the activation of the considered mechanism and can also be computed by the rotational equilibrium around the horizontal base hinge:

$$\boldsymbol{\alpha_0} = \frac{\boldsymbol{Stabilizing\ Moment}}{\boldsymbol{Destabilizing\ Moment}} \tag{4.8}$$

In the following calculations, self-weight terms are denoted with W_k terms, Q_K refer for overburden loads, while F_k denotes WD anchors, for the sake of clarity. Assuming the total work done by internal forces equal to zero, the generalized load multiplier calculated for this work reads:

$$\boldsymbol{\alpha_0} = \frac{\sum_{k=1}^{N}(\boldsymbol{W_k \delta_{Wy,k}} + \boldsymbol{Q_k \delta_{Qy,k}}) - \sum_{k=1}^{m} \boldsymbol{F_k \delta_{F,k}}}{\sum_{k=1}^{N}\left(\boldsymbol{W_k \delta_{W_{x,k}}} + \boldsymbol{Q_k \delta_{Q_{x,k}}}\right)} \tag{4.9}$$

Horizontal and vertical virtual displacements of a general point G_i where the i^{th} force is applied, can be defined as:

$$\boldsymbol{\delta_{x,i}} = \boldsymbol{y_i \delta_\theta}; \qquad \boldsymbol{\delta_{y,i}} = \boldsymbol{x_i \delta_\theta} \tag{4.10}$$

where y_i and x_i are the vertical and the horizontal distance of the point from the pivot, respectively (Figure 4.29), whereas δ_θ is the virtual rotation of the block. Given the beneficial effect of the contribution of the anchor forces, $\delta_{F,k} < 0$.

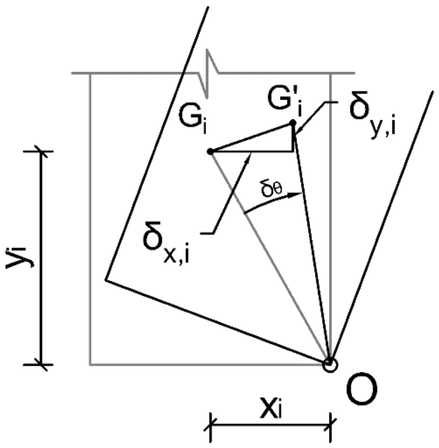

Figure 4.29 Definition of virtual displacements for the application of virtual work principle.

The corresponding spectral acceleration is calculated in function of modal mass participation factor e^*, and of the Confidence Factor CF (Equation C8.7.1.8 (C.S.LL.PP. 2019)):

$$\boldsymbol{a_0 = \frac{\alpha_0 g}{e^* CF}} \qquad 4.11$$

$$\boldsymbol{e^* = \frac{\left[\sum_{k=1}^{N} W_k \delta_{Wy,k} + Q_k \delta_{Qy,k}\right]^2}{\left[\sum_{k=1}^{N}(W_k + Q_k)\right]\left[\sum_{k=1}^{N} W_k\, \delta_{Wy,k}^2 + Q_k \delta_{Qy,k}^2\right]}} \qquad 4.12$$

For mechanisms taking place at the foundation level, the corresponding peak ground acceleration demand $PGA(LLS)$ can be directly obtained from the formulation of the elastic ground response spectrum for zero period $S_e(T = 0)$ given in Equations 3.2.2 (DMI 2018), depending on the site hazard, the soil factor S and reduced by the behavior factor q:

$$\boldsymbol{PGA(LLS) = \frac{a_g(LLS)S}{q}} \qquad 4.13$$

The Acceleration Safety Factor at the ground ASF_g is finally computed:

$$\boldsymbol{ASF_g = \frac{[capacity]}{[demand]} = \frac{a_0}{PGA(LLS)}} \qquad 4.14$$

Alternatively, when the mechanism takes place at certain building levels, it is possible to resort to the analytical simplified formulations of floor spectra (Equations C7.2.5÷10 (C.S.LL.PP. 2019)). Floor spectra consider a combination of all significant modes for the mechanism under study. The dynamic amplification depends on the dynamic properties of the whole structure and on ground spectral acceleration computed for the building modal periods. Therefore, modal analysis should be performed first.

The Peak Floor Acceleration at a certain Z level is given by Equation 4.15 and corresponds to the floor spectral value for zero period $S_{eZ}(T = 0)$:

$$\boldsymbol{PFA(LLS)} = \frac{\boldsymbol{a_z(Z)}}{\boldsymbol{q}} \tag{4.15}$$

where

$$\boldsymbol{a_z(Z)} = \sqrt{\sum \left(\boldsymbol{a_{z,k}(Z)}\right)^2} \tag{4.16}$$

in which $a_{z,k}(Z)$ is the contribution of the k[th] mode to the peak floor acceleration:

$$\boldsymbol{a_{z,k}(Z) = S_e(T_k, \xi_k)|\gamma_k \psi_k|\sqrt{(1 + 0.0004\xi_k^2)}} \tag{4.17}$$

It is worth highlighting that subscript k denotes values referred to the building, rather than to the mechanism. In Equation 4.17, $S_e(T_k, \xi_k)$ is the elastic ground response spectrum, evaluated for the equivalent period T_k, and equivalent viscous damping ξ_k of the building. $\gamma_k = \frac{3n}{2n+1}$ is the k[th] modal mass participation factor, in which n is the number of the floors, whereas $\psi_k(Z) = Z/H$ is the value of the k[th] modal shape at height Z and located at the coordinates of the mechanism under study.

The seismic assessment is finally performed computing the Acceleration Safety Factor at Z level ASF_Z:

$$\boldsymbol{ASF_Z} = \frac{\boldsymbol{[capacity]}}{\boldsymbol{[demand]}} = \frac{\boldsymbol{a_0}}{\boldsymbol{PFA(LLS)}} \tag{4.18}$$

In general, when no information about modal properties of the building is available, it is possible to estimate the first period of the building T_1 through simplified formulations. NTC2018 currently suggests the following expression (Equation 7.3.6 (DMI 2018)):

$$\boldsymbol{T_1 = 2\sqrt{(d)}} \tag{4.19}$$

solely function of the maximum elastic displacement d (metres) at the top of the building under seismic forces applied as horizontal forces. However, such a formulation needs the definition of a model and the analysis to be performed, therefore it is possible to use the previous formulation, still suggested by the corresponding Commentary to the code (Equation C7.3.2):

$$T_1 = 0.05H^{3/4} \qquad 4.20$$

Allowing to estimate the first period of vibration based on the total height of the building H. Unfortunately, URM buildings often present higher modes with significant modal participation mass in the interested direction and this assumption should be done with care.

The load multiplier capable of activating the mechanism is firstly computed for possible mechanisms highlighted in Figure 4.30 for all four models based on damage pattern obtained from transient analysis in the four configurations. It must be noted that in case of no data by global analysis, the adequate selection of possible mechanisms can be based on experiences, or suggested by literature (such as (Milano et al. 2009)), as well as automatically generated by more advanced algorithms (Grillanda, Valente, and Milani 2020). Many commercial softwares are nowadays available and developed within BIM ideology, such as (sismica s.r.l. 2018; Software 2021).

Notwithstanding the increasing quality of the connection, Models 2, 3 and 4 show similar out of the plane mechanisms that are likely to occur. All mechanisms are characterized by the OOP of entire walls or wall portions, encouraged by formation of vertical cracks especially at the WW interfaces. Recalling the terminology adopted for walls names in Figure 4.9, the complete absence of timber floor stiffness in Model 1 reveals the OOP vulnerability of the entire front façade W_X_1 (Figure 4.30a) (Mechanism A). Similarly, in Models 2,3 and 4 the formation of the hinge for the same façade is more likely to occur at a higher level. For this reasons, Mechanism A is only considered to be significant for Model 1, thus not evaluated for the remaining models. Mechanism B only considers the partial rotation of W_X_1 wall occurring at 2nd floor level. Mechanism C is defined as the central masonry wall portion of W_X_1 façade overturning around 2nd floor level hinge and likely to activate for vertical crack formation around the openings. Mechanisms D and E are selected onto W_X_3a and W_X_3b external walls. The former is the simple OOP overturning of the wall around the 2nd floor level and for the entire span defined by transversal walls, while the latter is a smaller portion defined up to the openings.

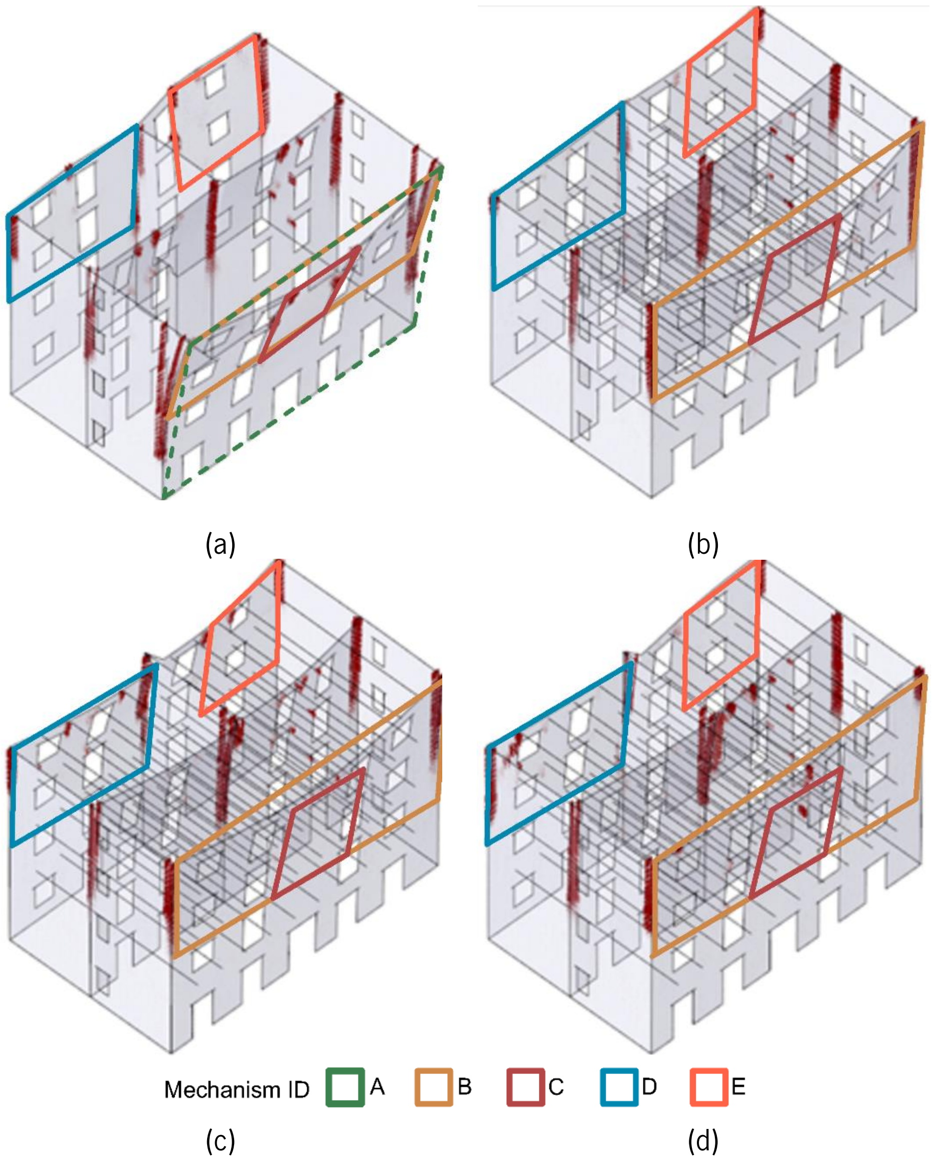

Figure 4.30 Possible failure mechanisms after nonlinear dynamic analysis: (a) Model 1; (b) Model 2; (c) Model 3; (d) Model 4.

The timber beams are assumed to be infixed into masonry for 30 cm and the corresponding load is therefore assumed acting 15 cm from the internal surface. Base hinge is simply set at the corner assuming no withdrawal due to masonry crashing. Considering the worst-case scenario, internal walls are assessed only considering the stabilizing force of one-side timber floor, that is that working in tension, neglecting the eventual benefit obtained by the opposite side working in compression. This can be justified by the complex dynamics of the system, possibly leading to wall tilting out-of-phase.

Both the equivalent damping coefficient of the building ξ_k and the damping coefficient of the mechanism ξ are assumed equal to 5%.

In general, it is possible to consider the nonlinearities of the whole building through increase of equivalent damping coefficient ξ_k and of the equivalent period T_k of the main building. These nonlinearities cause a reduction of the dynamic amplification at the floor level, reducing the acceleration demand of the local mechanism. Indications given by the Commentary of the code standard for masonry buildings recommend increment by about $50\% \div 100\%$ of T_k and equivalent damping ξ_k by about $10\% \div 20\%$ (Section C8.7.1.2.1.4 (C.S.LL.PP. 2019)). Given the aim of this work and for the sake of simplicity, the equivalent damping ratio is set to 5%, while no increase in the equivalent period is considered, keeping the results on the safe side.

The seismic assessment of Mechanism A occurring at the foundation level of Model 1 (no connections) is illustrated in Figure 4.31.

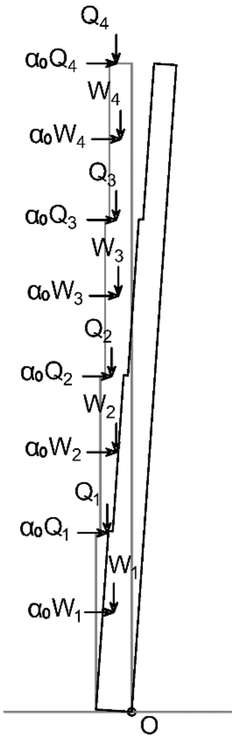

$$\boldsymbol{\alpha_o} = \frac{\sum_{k=1}^{4} W_k \delta_{W_{y,k}} + \sum_{k=1}^{4} Q_k \delta_{Q_{y,k}}}{\sum_{k=1}^{4} W_k \delta_{W_{x,k}} + \sum_{k=1}^{4} Q_k \delta_{Q_{x,k}}} = \mathbf{0.0482}$$

$$a_0 = \frac{\alpha_0}{e^* CF} g = 0.0625\, g$$

$$PGA(LLS) = \frac{a_g(LLS)S}{q} = 0.148\, g$$

$$ASF_g = \frac{a_0}{PGA(LLS)} = \frac{0.0325g}{0.148g} = \color{red}{0.423}$$

Figure 4.31 Linear kinematic analysis of Mechanism A – Model 1 (no connections), under the LLS.

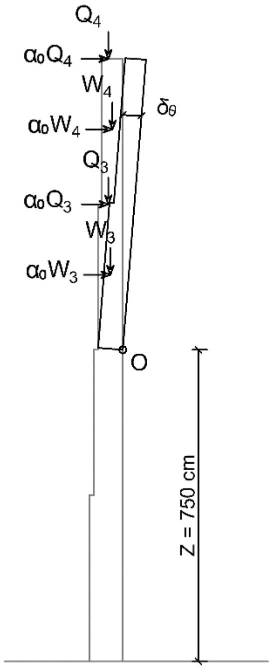

$$\alpha_o = \frac{\sum_{k=3}^{4} W_k \delta_{W_{y,k}} + \sum_{k=3}^{4} Q_k \delta_{Q_{y,k}}}{\sum_{k=3}^{4} W_k \delta_{W_{x,k}} + \sum_{k=3}^{4} Q_k \delta_{Q_{x,k}}} = 0.0764$$

$$a_0 = \frac{\alpha_0}{e^* CF} g = 0.0952g$$

$$S_e = a_g S \eta F_0, \qquad T_B < T_1 < T_C$$

$$a_{z,1}(Z) = S_e \, |\gamma_1 \psi_1| \sqrt{\left(1 + 0.0004\xi_1^2\right)} = 0.4837\ g$$

$$PFA(LLS) = \frac{a_{z,1}(Z)}{q} = 0.242\ g$$

$$ASF_Z = \frac{a_0}{PFA(LLS)} = \frac{0.0952\ g}{0.0838\ g} = 0.393$$

Figure 4.32 Load multiplier computation of mechanisms B – model 1 (no connections) assuming unavailable modal properties of the building.

The application of the same procedure is applied for the Mechanism B taking place at 7.5 m from the base, thus considering amplified floor spectrum. Given the peculiarity of the considered Model 1 (with no floor stiffness) kinematic analysis is performed considering two possible circumstances: (i) unavailable modal properties of the building (Figure 4.32); (ii) available modal properties of the building (Figure 4.33). When no modal analysis is performed, only the contribution of the first mode is considered, and the first period is estimated as $T_1 = 0.05H^{3/4} = 0.37s$. In this case the $ASF_Z = 0.393 < 1$ leading to a unverified safety condition. On the other hand, modal analysis provides modal properties (Section 4.1.4), assuming the contribution of the significant modes up to a cumulative modal participation mass in the Y-direction $Cum.My > 50\%$. Table 4.6 summarizes the modal properties of Model 1 in terms of period, percentage of the modal participation mass and percentage of the cumulative modal participation mass.

Table 4.6 Modal properties in the interested Y direction of Model 1.

Mode	$T[s]$	$My[\%]$	$Cum.My[\%]$
1	1.063	9.7	9.7
5	0.413	25.8	37.7
11	0.25	11.0	55.3

According to Table 4.6, the contribution of three modes should be taken into account. Indeed, considering only the first mode would give trivial results as representing less than 10% of the modal mass in the direction under study. The corresponding floor spectrum is therefore obtained through the combination of the contribution of each mode through Equation C7.2.5 (Figure 4.33):

$$\boldsymbol{S_{eZ}(T,\xi,Z)} = \sqrt{\sum \left(\boldsymbol{S_{eZ,k}(T,\xi,Z)}\right)^{2}} \qquad 4.21$$

where

$$\boldsymbol{S_{eZ,k}(T,\xi,z)} = \begin{cases} \dfrac{\boldsymbol{1.1\xi_k^{-0.5}\eta(\xi)a_{Z,k}(Z)}}{\boldsymbol{1+\left[1.1\xi_k^{-0.5}\eta(\xi)-1\right]\left(1-\dfrac{T}{aT_k}\right)^{1.6}}} & \langle \boldsymbol{T < aT_k} \rangle \\ \boldsymbol{1.1\xi_k^{-0.5}\eta(\xi)a_{Z,k}(Z)} & \langle \boldsymbol{aT_k \le T < bT_k} \rangle \\ \dfrac{\boldsymbol{1.1\xi_k^{-0.5}\eta(\xi)a_{Z,k}(Z)}}{\boldsymbol{1+\left[1.1\xi_k^{-0.5}\eta(\xi)-1\right]\left(\dfrac{T}{bT_k}-1\right)^{1.2}}} & \langle \boldsymbol{T \ge T_k} \rangle \end{cases} \qquad 4.22$$

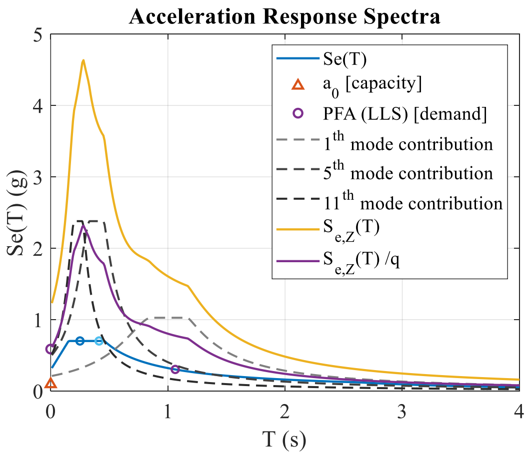

$$a_z(Z) = \sqrt{\sum \left(a_{z,k}(Z)\right)^2} = 1.18\ g$$

$$PFA(LLS) = \frac{a_Z(Z)}{q} = 0.588\ g$$

$$ASF_Z = \frac{a_0}{PFA(LLS)} = \frac{0.0847\ g}{0.203\ g} = 0.162$$

Figure 4.33 Linear kinematic analysis through amplified spectrum obtained after combination of significant modes: Mechanism B, Model 1.

The damping coefficient is assumed $\xi_k = 5\%$ for each considered mode (k=1,5,11).

This latter method results to a corresponding acceleration safety factor $ASF_Z = 0.162 < 1$, which is about 60% less than the safety factor obtained based on the first mode only, thus revealing that it is extremely important to account for higher modes when modal participation mass of the first mode is not sufficient to reach significant values. Therefore, in Model 1 all mechanisms occurring at higher level are assessed through the combination of the significant modes 1,5 and 11. Given the modal properties of Models 2,3, and 4, however, the first mode is assumed sufficient for a correct estimation of seismic demand. Furthermore, the latter models are evaluated considering a value of the first period estimated with the simplified formulation $T_1 = 0.05H^{3/4} = 0.37s$, rather than using the modal analysis results (not always available).

The main results of the LLS seismic assessment of all selected mechanisms are summarized in Table 4.7, where the high vulnerability of each mechanism is demonstrated by the low values of safety factors obtained, especially for those corresponding to higher level (about -65% less).

Table 4.7 Life-safety Limit State (LLS) seismic assessment of local mechanisms through linear kinematic analysis: Model 1.

Mechanism	$\alpha_0\,[-]$	$a_0[g]$	$PGA(LLS)$ or $PFA(LLS)[g]$	$ASF\,[-]$
A (base)	0.048	0.062	0.108	**0.423**
B (floor)	0.076	0.095	0.588	**0.162**
C (floor)	0.078	0.098	0.588	**0.166**
D (floor)	0.0688	0.085	0.588	**0.145**
E (floor)	0.070	0.087	0.588	**0.148**

The influence of any horizontal restraint (such as steel tie rods, or WD anchors) can be included in the linear kinematic procedure through T_k terms in the computation of the load multiplier α_0 (Equation 4.9). In this case the load multiplier α_0 can be considered as the collapse load multiplier, rather than the load multiplier necessary for the activation of the selected mechanism. Usually, Equation 4.9 can be inverted in order to evaluate the minimum design force necessary to avoid the wall collapse under a given seismic intensity. Seismic assessment of masonry walls restrained by existing anchors under LLS, can be carried out assuming the WD anchor force equal to:

$$\boldsymbol{T_{max} = n_b F_u} \qquad 4.23$$

where n_b is the number of beams taking part to the mechanism, while F_u is the maximum WD anchor resistance. For models 2 and 3 the maximum force is related to the ultimate force of the bilinear curves (Table 3.3 and Table 3.4), whereas, assuming a very good quality of connection in Model 4, the horizontal force can be related to the axial beam strength in tension:

$$\boldsymbol{F_{t,0,k} = A_b f_{t,0,k}} \qquad 4.24$$

where A_b is the beam cross section, and $f_{t,0,k}$ is the timber strength stress parallel to the grain. Table 4.8 summarizes the values of maximum force assumed for each Model configuration depending on the quality of the connection.

Table 4.8 Maximum values of WD connection force used for linear kinematic analysis for each Model configuration.

	Model 1	**Model 2**	**Model 3**	**Model 4**
connection quality	poor	unstrengthened	strengthened	perfect connection
$\boldsymbol{F_u}$	0.0 KN	$4.3\ kN$	$72.8\ kN$	$1081.6\ kN$

The calculus of the load multiplier and the corresponding seismic assessment of Mechanism B in Model 2 are shown in Figure 4.32.

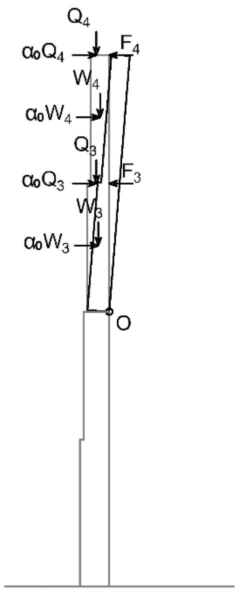

$$\boldsymbol{\alpha_o = \frac{\sum_{k=3}^{4} W_k \delta_{W_{y,k}} + \sum_{k=3}^{4} Q_k \delta_{Q_{y,k}} - \sum_{k=3}^{4} F_k \delta_{F_{x,k}}}{\sum_{k=3}^{4} W_k \delta_{W_{x,k}} + \sum_{k=3}^{4} Q_k \delta_{Q_{x,k}}} = 0.364}$$

$$\boldsymbol{a_0 = \frac{\alpha_0}{e^* CF} g = 0.453g}$$

$$\boldsymbol{S_e = a_g S \eta F_0, \qquad T_B < T_1 < T_C}$$

$$\boldsymbol{a_{z,1}(Z) = S_e\, |\gamma_1 \psi_1| \sqrt{\left(1 + 0.0004\xi_1^2\right)} = 0.484\ g}$$

$$\boldsymbol{PFA(LLS) = \frac{a_{z,1}(Z)}{q} = 0.242\ g}$$

$$\boldsymbol{ASF_Z = \frac{a_0}{PFA(LLS)} = \frac{0.4533\ g}{0.2419\ g} = 1.874}$$

Figure 4.34 Load multiplier computation of Mechanisms B – Model 2 (unstrengthened connections).

The same procedure is applied for all remaining mechanisms and models, and results are collected in Table 4.9. The vulnerability of the selected mechanisms clearly decreases with increasing of the connection quality. Moreover, the beneficial influence of the WD connection is visible even for poor existing connection (simulated through Model 2). Moreover, Models 3 and 4 results in very high safety factors, highlighting the beneficial effect of strengthening solutions.

Table 4.9 Life-safety Limit State (LLS) seismic assessment of local mechanisms through linear kinematic analysis: Models 2,3,4.

	Mechanism	α_0 [−]	$a_0[g]$	$PFA(LLS)[g]$	ASF [−]
Model 2	B	0.364	0.453	0.242	**1.874**
	C	0.352	0.442	0.242	**1.829**
	D	0.360	0.446	0.242	**1.846**
	E	0.266	0.326	0.242	**1.347**
Model 3	B	4.942	6.159	0.242	**25.463**
	C	4.723	5.935	0.242	**24.540**
	D	5.002	6.199	0.242	**25.633**
	E	3.419	4.190	0.242	**17.324**
Model 4	B	72.361	90.18	0.242	**372.86**
	C	69.090	86.832	0.242	**359.017**
	D	73.356	90.928	0.242	**375.953**
	E	49.858	61.099	0.242	**252.621**

4.2.2 Nonlinear kinematic analysis

The analysis of the mechanism can be assessed through a displacement-based procedure through nonlinear pseudo-static analysis, that is nonlinear kinematic approach. In this case the load multiplier α (Equation 4.9) should be evaluated for initial and varied configurations, too. Indeed, the $\alpha - d_C$ curve should properly represent the evolution of the mechanism, described by the displacement d_C of a freely defined control point C. Generally, α decreases progressively up to null value in correspondence with the ultimate displacement d_{C0}.

Once the reactive force-displacement curve (similar to the pushover curve) is obtained, the "capacity curve" of the local mechanism should be determined, referring to the equivalent SDOF system response. The corresponding acceleration-displacement curve $\mathrm{a} = \mathrm{a}(d)$ is then obtained from Equations 4.25 and 4.26.

$$\boldsymbol{a} = \frac{\boldsymbol{\alpha}(\boldsymbol{d_C})\ \boldsymbol{g}}{\boldsymbol{e}^*\ \boldsymbol{CF}} \tag{4.25}$$

$$\boldsymbol{d} = \boldsymbol{d_C} \frac{\sum_{k=1}^{n}(\boldsymbol{W_k} + \boldsymbol{Q_k})\boldsymbol{\delta}_{PQx,k}^2}{\boldsymbol{\delta}_{Cx}\sum_{k=1}^{n}(\boldsymbol{P_k} + \boldsymbol{Q_k})\boldsymbol{\delta}_{PQx,k}} \tag{4.26}$$

where δ_{Cx} is the horizontal virtual displacement of the control point evaluated starting from the initial undeformed configuration. Similarly, $\delta_{PQx,k}$ is the horizontal virtual displacement of the kth force (Equation 4.10). The initial branch of the previously defined capacity curve is basically vertical, based on the assumption of a rigid block perfectly connected until the activation of the mechanism.

To proceed with the seismic assessment of local mechanism in terms of performance, it is necessary to properly create the response spectrum. As previously done for the linear kinematic analysis (for which only the peak floor acceleration is necessary), the dynamic amplification given by mechanisms occurring at higher levels of the building can be taken into account through proper floor spectra. The seismic safety check under LLS is performed comparing the displacement capacity d_{LLS} to the displacement demand $S_D(T_{LLS})$ defined as the response spectral displacement corresponding to the period equivalent to the considered limit state T_{LLS} (secant period). The corresponding Displacement Safety Factor DSF reads:

$$\boldsymbol{DSF = \frac{d_{LLS}}{S_D(T_{LLS})}} \qquad 4.27$$

where the LLS equivalent period is defined by Equation [C.8.7.1.10] (C.S.LL.PP. 2019):

$$\boldsymbol{T_{LLS} = 1.68\pi\sqrt{\frac{d_{LLS}}{a(d_{LLS})}}} \qquad 4.28$$

The latter formulation results an updated formulation of the previous NTC2008 (DMI 2008) and is based on the Modified Acceleration-Displacement Response Spectrum method (MADRS), where the secant period through which the displacement demand is computed, is the intersection between capacity and overdamped spectrum, reduced by a proper reduction factor. This allows to consider the equivalent linear system not to vibrate over the period corresponding to the maximum displacement but to a reduced displacement, avoiding too conservative results. The OOP response is usually characterized by a reduction factor equal to 0.8, similarly as adopted by New Zealand Standard (NZSEE 2015), thus leading to the general formulation of the secant period for a given limit state:

$$\boldsymbol{T_{LS} = 2\pi\sqrt{\frac{0.8\, d_{LS}}{a(0.8\, d_{LS})}}} \qquad 4.29$$

Usually, the capacity curve ($a = a(d)$) is linearly decreasing (Figure 4.35) and the ultimate displacement capacity at the LLS is

$$\boldsymbol{d_{LLS} = 0.4 d_0} \qquad 4.30$$

It is possible to substitute Equation 4.30 into Equation 4.29 obtaining the proposed formulation given in the code (Equation 4.28) (see Figure 4.35).

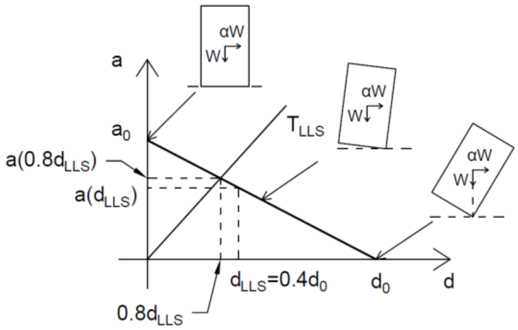

$$\boldsymbol{a(d) = a_0\left(1 - \frac{d}{d_0}\right)}$$

$$\boldsymbol{a_{LLS} = a(d_{LLS}) = a_0(1 - 0.4) = 0.6\, a_0}$$

$$\boldsymbol{a(0.8\, d_{LLS}) = \frac{0.68}{0.6} a_{LLS}}$$

$$\boldsymbol{T_{LLS} = 2\pi \sqrt{\frac{0.8\, d_{LLS}}{\frac{0.68}{0.6} a_{LLS}}} = 1.68\pi \sqrt{\frac{d_{LLS}}{a_{LLS}}}}$$

Figure 4.35 Formulation of the LLS secant period for simple overturning mechanism of free-standing walls.

When horizontal restraints are present, acting as beneficial resisting forces within the evolution of the mechanism, the capacity curve varies and it is commonly influenced by the increased stiffness and strength given by the tie or anchor, as well as by the increased ductility. The $a - d$ OOP capacity curve of a simple wall restrained by a steel tie rod on top is shown in Figure 4.36 for the matter of clarity. The ultimate displacement capacity d_{LLS} is defined as the minimum among:

- $0.4d_0$;
- Displacement corresponding to the failure of the possible restraint (tie, WD connections, etc.).

In cases where the response spectrum is based on site accelerograms (recorded by seismic stations and sensors) possibly giving the corresponding displacement response spectrum which is not necessarily increasing with increasing period T, the displacement demand of the mechanism under study under the LLS should be defined as the maximum value of the spectral displacement evaluated for periods within the interval $[T_0, T_{LLS}]$.

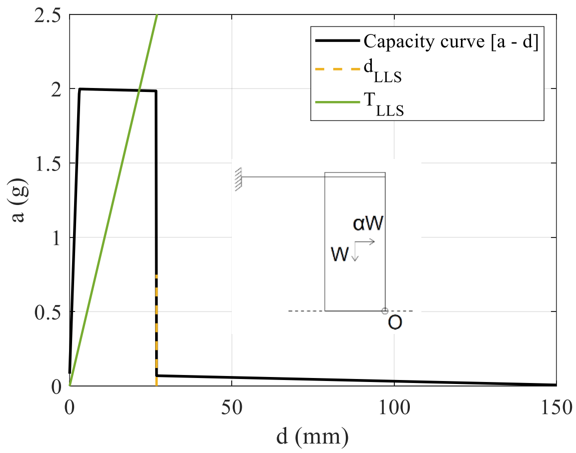

Figure 4.36 Capacity curve and secant period definition for masonry wall restrained by elasto-plastic tie-rod.

When the mechanism takes place at the foundation level, the seismic demand is directly retrieved by the elastic displacement spectrum $S_{De}(T)$ (§ 3.2.3.2.3 (DMI 2018)) calculated for the characteristics values of the period of corresponding limit state.

On the other hand, when the mechanism takes place at higher levels Z, amplified displacement floor spectra should be considered, obtained by acceleration floor spectra (Equation 4.21) multiplied by a factor of $T^2/4\pi^2$. Generally, the first significant mode for the considered mechanism should be sufficient for the computation of the corresponding floor spectrum.

Commonly for the LLS, assuming an increasing displacement spectrum with increasing period T, the seismic demand in terms of displacement reads:

$$\boldsymbol{S_D(LLS) = S_{eZ}(T_{LLS}, \xi, Z)\frac{T_{LLS}^2}{4\pi^4} \quad (\geq S_{eZ}(T_1, \xi, Z)\frac{b^2T_1^2}{4\pi^2}}, \text{ if } \boldsymbol{T_{LLS} > bT_1}) \qquad 4.31$$

The energy dissipation effects due to whole building nonlinearities, and due to the local mechanism nonlinearities, should be properly considered for adequate computation of the displacement seismic demand at the ultimate limit state. Indeed, the equivalent damping of the mechanism under the LLS can be generally assumed as $\xi = 8\%$.

Considering that the aim of this work is to study the influence of the connection over the global or local seismic analysis of a URM building, the most vulnerable mechanism in terms of ASF resulting from linear kinematic analysis (Section 4.2.1) of each model configuration is selected here in order to be assessed through the nonlinear kinematic method.

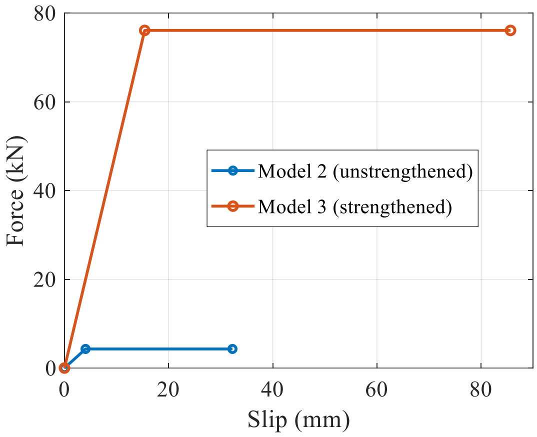

(a)

	d_e [mm]	d_u [mm]	F_u [kN]	K_e [kN/mm]
Model 2	4	32.2	4.3	1.1
Model 3	21	76.7	72.8	3.5
Model 4	78.6	78.6	1081.6	13.7

(b)

Figure 4.37 Elasto-plastic WD connections in Models 2 and 3 (Model 4 excluded for clarity): (a) force-displacement curves; (b) bilinear parameters (including Model 4).

Recalling that Model 1 simulates very poor WD connections, the corresponding mechanism is basically a free-standing block. Models 2 and 3 are characterized by elastic-perfectly plastic behavior (Figure 4.37), defined in Section 3.2 on available experimental bases and representing existing unstrengthened and strengthened WD connections, respectively. Model 4 simulates a very good connection and the WD Force-Slip behavior is associated to the axial stiffness and strength of the beams. The ultimate displacement coincides with the elastic displacement in this case, simulating the fragile rupture of the beam.

According to Table 4.7 and Table 4.9 one of the most vulnerable mechanisms among the performed selection is Mechanism E for each model. Indeed, in Model 1, both Mechanisms D and E have very similar safety factor, whereas Mechanism E is clearly the most vulnerable with respect to the other mechanisms, and for any model. It must be noted as only Model 1 (absent connections) results in highly vulnerable mechanism, reaching ASF < 1, while this is over the unity for the restrained models.

Nonlinear kinematic analysis is applied on Mechanism E for every model configuration. Given the mechanism taking place over the 2nd level, the corresponding floor spectrum is computed and the safety assessment check is performed both using the elastic spectrum and the floor spectrum (Figure 4.38). The first period of vibration T_1 is assumed based on the simplified formulation 4.22, while the control point d_C is assumed at the top of the building.

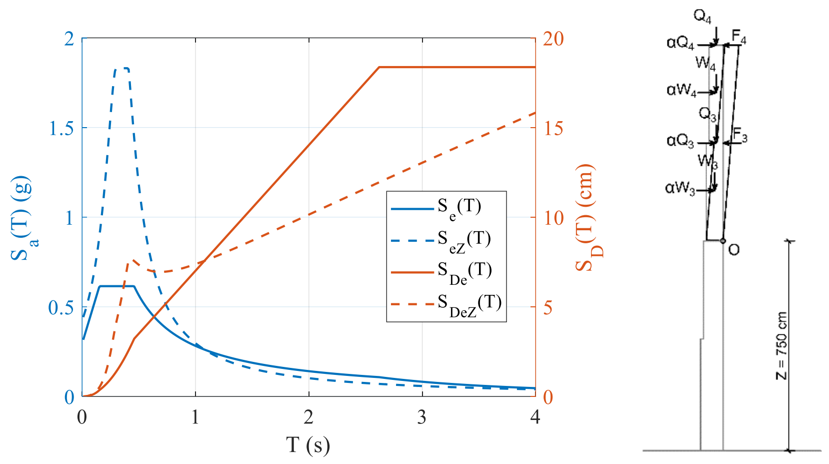

(a) (b)

Figure 4.38 (a) Ground and floor spectra in terms of acceleration and displacement; (b) geometry of the local mechanism and corresponding forces: Mechanism 4.

Results are graphically reported in Figure 4.39,Figure 4.40, Figure 4.41, and Figure 4.42, comparing side-by-side the safety assessment according to the elastic spectrum (a) and according to the floor spectrum (b) in M-ADRS format.

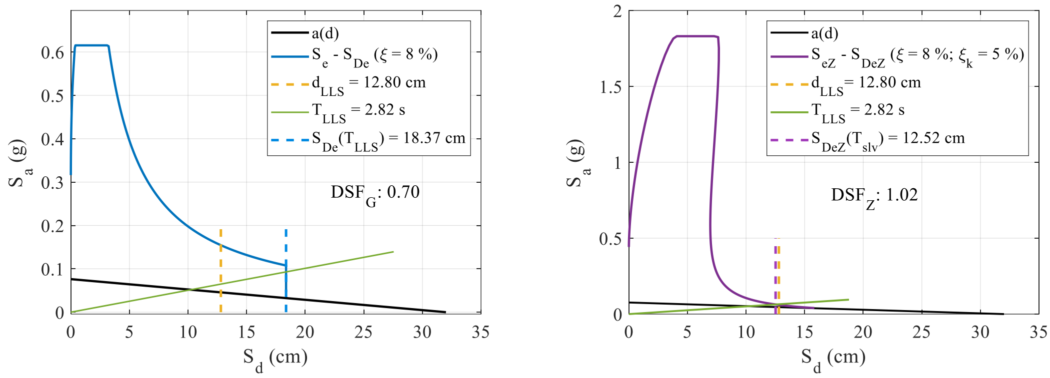

(a) (b)

Figure 4.39 Nonlinear kinematic analysis of Mechanism E, Model 1 (no connections): (a) ground response spectrum ;(b) floor response spectrum. M-ADRS format.

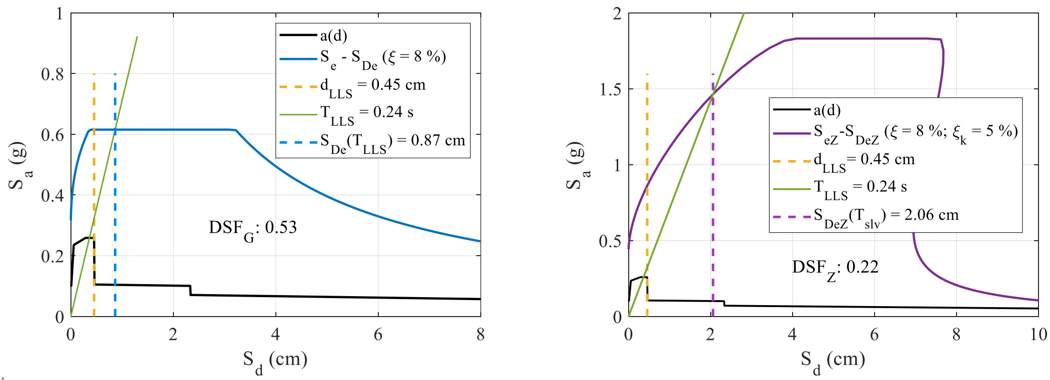

(a) (b)

Figure 4.40 Nonlinear kinematic analysis of Mechanism E, Model 2 (unstrengthened connections): (a) ground response spectrum; (b) floor response spectrum. M-ADRS format.

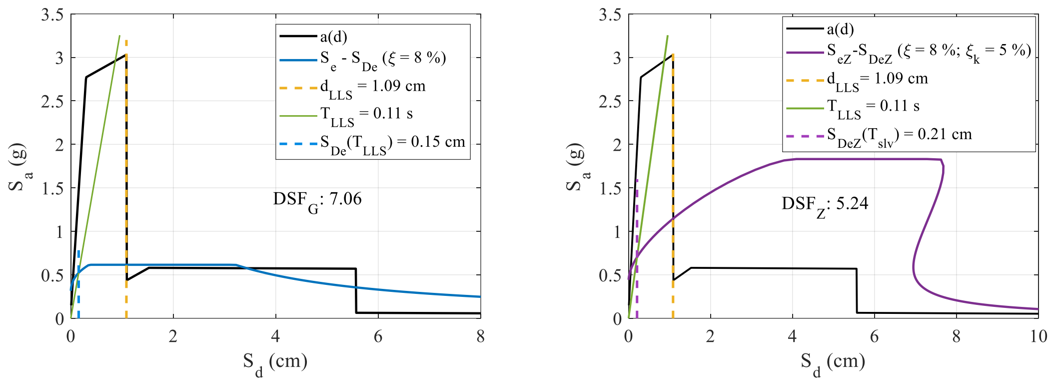

(a) (b)

Figure 4.41 Nonlinear kinematic analysis of Mechanism E, Model 3 (strengthened connections): (a) ground response spectrum; (b) floor response spectrum. M-ADRS format.

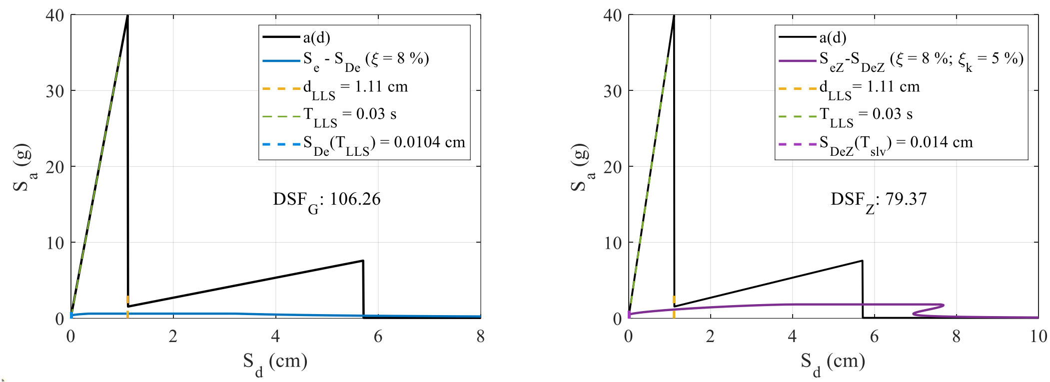

(a) (b)

Figure 4.42 Nonlinear kinematic analysis of Mechanism E, Model 4 (perfect connections): (a) ground response spectrum; (b) floor response spectrum. M-ADRS format.

Furthermore, the capacity curves $a = a(d)$ obtained for each model configuration are compared in Figure 4.43. Even though all capacity curves are shown for the complete evolution of the mechanism, from the undeformed configuration until zero value of acceleration, these should be interrupted when an abrupt change (>50%) in terms of acceleration occurs.

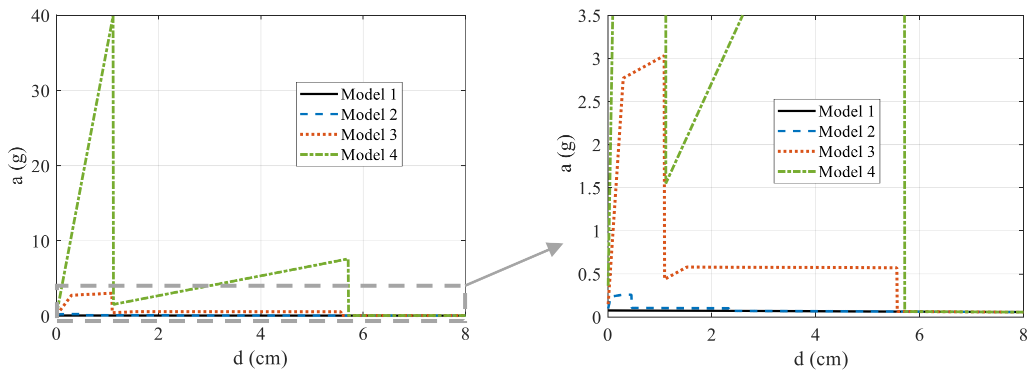

(a) (b)

Figure 4.43 Capacity curves of Mechanism E computed for each model configuration: (a) complete curves; (b) zoomed curves.

Results in terms of displacement capacity and displacement demand, as well as displacement safety factors are summarized in Table 4.10, calculated for both ground and floor spectra. The overall behavior of the connection improves if the quality of the connection improves. In particular, both Models 1 and 2 result to have vulnerable mechanisms, whereas for the strengthened configuration of Model 3, the safety factors are over the unity, reaching very high safety factors in case of Model 4, where the behavior is controlled by the highly stiff and resistant timber beam in tension.

Table 4.10 Life-safety Limit State (LLS) seismic assessment of local Mechanism E through non linear kinematic analysis: Models 1,2,3,4. DSF: Displacement Safety Factor.

Model	$\mathbf{d_{LLS}}$ [cm]	$\mathbf{S_{De}(T_{LLS})}$ [cm]	$\mathbf{S_{DeZ}(T_{LLS})}$ [cm]	$\mathbf{DSF_G}[-]$	$\mathbf{DSF_Z}[-]$
1	12.80	18.37	12.52	**0.70**	**1.02**
2	0.24	0.87	2.06	**0.53**	**0.22**
3	1.09	0.15	0.21	**7.06**	**5.24**
4	1.11	0.014	0.0104	**106.26**	**79.37**

The importance of performing the safety assessment according to the ground response spectrum even for local mechanisms taking place at a certain level, is highlighted for Models 1, where $DSF_G < DSF_Z$. Basically, accounting for the amplified demand spectrum not always leads to conservative results, especially for long secant periods resulting to high levels of displacements. However, given the lower values of DSF_Z for the rest of the models, floor spectra lead to amplified demand and corresponding reduced seismic factor, as expected.

The capacity curve of Model 1 (Figure 4.39a) is the conventional bilinear rigid-linearly decreasing curve characteristic for free-standing walls. When the WD connection stiffness and strength increase, the capacity of the corresponding mechanism is characterized by an initial linear elastic branch, with successive post-elastic phase until the failure of the connection on the 4th level occurs (Figure 4.43).

Results of safety factors obtained for Model 4 suggest that when a very good WD connection is assumed, the OOP mechanism of the restrained wall is not of primary importance, and global mechanisms should be further be analysed. Furthermore, the selection of more realistic mechanisms accounting for horizontal restraints along the height should also be considered as more likely to occur, in this case. It must be noted, however, that such a complex mechanisms usually leads to higher seismic load multiplier and should not be of concern.

When a performance-based procedure is adopted, results may highly differ from those obtained by force-based simplified methods. Indeed, based on nonlinear kinematic analysis, not only the safety requirements are not fulfilled by Model 2 (Table 4.10), but this is even more vulnerable than Model 1. Such a result highlights the importance of properly accounting for nonlinear WD connections in the seismic assessment of local mechanisms, as this is not possible using linear kinematic analysis (possibly leading to underestimated results). Indeed, the ASF computed for Mechanism E is > 1 for Model 2 (Table 4.9), while $DSF < 1$. The higher level of local mechanism vulnerability of Model 2 with respect to Model 1 can be justified by the definition of the displacement capacity as the minimum among $0.4d_0$ and $d_{failure}$ (abrupt decrease of resistance), when the horizontal restraint is considered. Commonly, the displacement corresponding to the failure of the anchor is << 0.4d_0, thus the displacement capacity is highly reduced with respect to the free-standing configuration.

4.3 Local analysis: rocking approach

4.3.1 Introduction

The seismic vulnerability of OOP masonry walls can be investigated through the rocking analysis, allowing for dynamic nonlinear time-history analysis of rigid blocks tilting at the base. Such a methodology requires the mechanism to be defined *a-priori* and is aligned with the kinematic approach, presented in Section 4.2 and widely spread among the research community and practitioners. The rocking analysis can be seen, in fact, as the natural improvement of the pseudo-static methodology as allows to account for complex dynamic effects, even when the maximum static capacity is attained. In the pioneering Housner's work (1963) rocking analysis was first systematized:

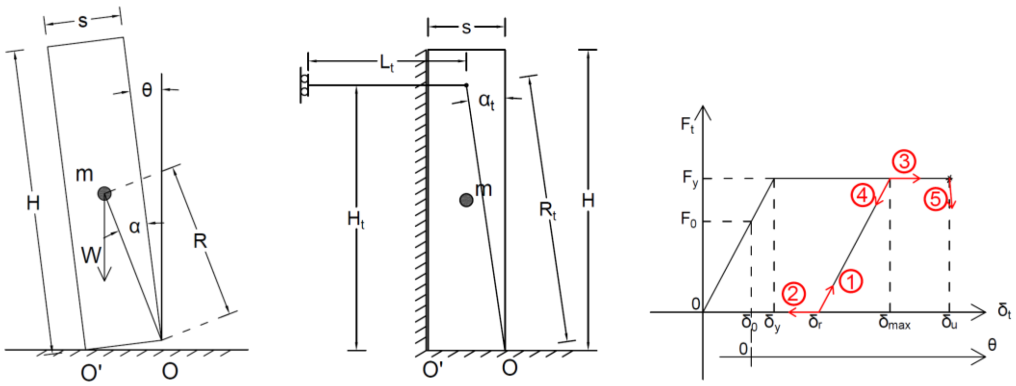

(a) (b) (c)

Figure 4.44 Free-standing (a); restrained rocking block (c). Elasto-plastic constitutive model assumed for the steel-tie rod.

Sliding and bouncing are commonly neglected, justified by experimental evidences (Lipscombe and Pellegrino 1993) for sufficiently slender blocks (i.e. $s/H \geq 5$), being s and H the wall thickness and height, respectively. Moreover, the energy is dissipated through a coefficient of restitution, solely function of the block geometry, $e_H = 1 - \frac{3}{2} sin^2(\alpha)$, where $\alpha = \tan^{-1} s/H$, valid for slender blocks Figure 4.44. The velocity reduction factor was experimentally calibrated to be about $90\ \%\, e_H$ for unreinforced masonry walls in one-sided motion (Sorrentino, AlShawa, and Decanini 2011).

Recently, the equation of motion was improved in order to account for different restraints and boundary conditions, such as the presence of horizontal diaphragms (Giresini and Sassu 2017), transverse walls, roof thrusts (Giresini et al. 2016) steel tie-rods (Mauro, de Felice, and DeJong 2015) or tendons (Aghagholizadeh and Makris 2018) and dissipative devices (Dimitrakopoulos and DeJong 2012; Giresini et al. 2021; Solarino, Giresini, and Oliveira 2020).

The influence of the horizontal restraints on the rocking motion mainly depends on their ultimate elongation and strength. Moreover, if one deals with historical anchors, the mechanical properties can be scattered, as shown by Calderini et al. (Calderini et al. 2016), mainly for tie-rods.

The tie-rods strongly reduce the mean values of maxima amplitude rotations, as demonstrated by Casapulla and Argiento (Casapulla and Argiento 2016) even for kinematic analysis. The effect of the change of aspect ratio of two walls of the same size was shown to be negligible for tied walls (AlShawa et al. 2019). The same occurred for walls restrained by tie-rods at different heights; the overall effect of tie-rod length (normalized to the wall thickness and variable between 4 and 20) as well as the normalized prestress (between 0 and 0.6) is limited. As for the influence of mechanical properties, the role of the elastic modulus and of the axial stiffness appeared to be negligible. The yielding strength is the most relevant parameter that influences the response, besides the brittle or ductile behavior of the tie-rod.

Although several studies are available in literature on the behavior of rocking masonry walls restrained by steel ties, possibly modelled as elasto-plastic, there is a lack of information about the influence of WD connections. The latter horizontal restraints can be simulated in a very similar way and the main outcomes obtained for steel tie rods can still be valid.

Based on this perspective and given the recent advances in high level programming language, this Section examines the influence of WD connections on the dynamic stability of restrained rocking walls simulating rigid-like OOP mechanisms. Actually, the recent Code Standard (DMI 2018) allows the seismic vulnerability assessment of local mechanisms through advanced computational tools, capable of simulating the activation of the mechanism and the dynamic response of the structure, such as macro-element and discrete-element approaches. Moreover, the mechanism can be also modelled as the group of rigid blocks constituting the kinematic chain and characterized by the same capacity curve described in Section 0. It is important to point out that the dynamic response of the mechanism is very sensitive to the selected accelerograms, thus the number of earthquakes should be sufficiently high (usually higher than those used for global dynamic analysis of buildings). A combination of natural accelerograms compatible to the response spectrum in terms of acceleration, using recording databases. The safety assessment after dynamic nonlinear analysis on the Life-safety Limit State can be performed by simply checking the maximum displacement attained by the wall with the ultimate displacement d_0 after which the equilibrium is loss. Moreover, the average of maxima displacements should be less than $0.4\, d_0$.

The influence of WD connection in the dynamic stability of Mechanism 4 previously analysed in Section 0 is studied here through non-linear transient analyses.

4.3.2 Dynamics of rigid blocks

Based on the leading formulation originally conceived by Housner (1963), the equation of motion of laterally restrained rigid blocks tilting around the base corners reads (Figure 4.44b):

$$\boldsymbol{I_0\ddot{\theta} + sgn(\theta) mgR\, sinA_\theta + T_t + T_L = m\ddot{u}_g R\, cosA_\theta} \qquad 4.32$$

The term in the right-hand side refers to the seismic excitation $m\ddot{u}_g$, which is the seismic effective force applied to the block of size R and slenderness α ($\tan^{-1}(s/H)$). The argument of the cosine is:

$$\boldsymbol{A_\theta = \alpha - sgn(\theta)} \qquad 4.33$$

The first term in the left-hand side of Equation 4.32 refers to the inertia force ($I_0 = 4/3\, m\, R^2$, polar inertia moment around the pivot point O), the second one relates to the self-weight $m\, g$ which acts as stabilizing term as long as the projection of the gravitational force falls into the wall thickness.

The term T_t of Equation 4.32 refers to the contribution given by the WD anchors, whose role is modelled as individual elasto-plastic horizontal restraint only acting for outward rotations ($\theta \geq 0$):

$$\boldsymbol{T_t = sgn(\theta)K\beta^2R^2 \cos A_{t,\theta}\left[\sin \alpha_t - \sin A_{t,\theta}\right]} \qquad 4.34$$

in which K is the spring stiffness, $A_{t,\theta} = \alpha_t - sgn(\theta)$, where α_t is a position angle dependent on the position coefficient $\beta = R_t/R$. Considering the axial stiffness of the beam $K_b \gg K$, the elongation strain ϵ can only be that of the WD connection. The WD anchor displacement depends on the rotation:

$$\boldsymbol{u_t = R_t\left[\sin \alpha_t - \sin A_{t,\theta}\right]} \qquad 4.35$$

Considering Equation 4.35, the potential energy V stored by the WD connection is:

$$\boldsymbol{V = \frac{1}{2}K(u_t)^2 = \frac{1}{2}K\left[R_t\left(\sin \alpha_t - \sin A_{t,\theta}\right)\right]^2} \qquad 4.36$$

The derivation of the potential energy with respect to the variable θ gives the elastic term T_t of Equation 4.34:

$$\boldsymbol{T_{t,e} = \frac{\partial V}{\partial \theta} = \left[sgn(\theta)KR_t\left(\sin \alpha_t - \sin A_{t,\theta}\right)\right]R_t \cos A_{t,\theta}} \qquad 4.37$$

The modelling of elasto-plastic phases of the WD connection depends on the connection elongation history or, equivalently, on its displacement from a reference value, δ_t. Five cases are distinguished as shown in Figure 4.44c: (1) from inactive to elastic, $\delta_t > \delta_r$; (2) from elastic to inactive, $\delta_t < \delta_r$; (3) from elastic to plastic, $\delta_t > \delta_{max}$; (4) from plastic to elastic, $\delta_t < \delta_{max}$; and (5) rupture, $\delta_t > \delta_u$.

Once yielding is attained, the spring exerts the constant force F_y . The term related to the tie contribution is then:

$$\boldsymbol{T_{t,p} = sgn(\theta)F_yR_t \cos A_{t,\theta}} \qquad 4.38$$

In summary, the complete equation of motion is given in Equation 4.32, where the T_t term assumes either the value expressed in Equation 4.37 or that of Equation 4.38. Alternatively, one of the two terms $T_{t,e}$ and $T_{t,p}$ is recalled by the code through a specific subroutine depending on the actual value of the tie-rod displacement δ_t.

The integration of the equation of motion is performed through a Matlab (MathWorks 2016) script through the ODE45, that is a built-in ordinary differential equation solver capable of solving nonstiff differential equation of medium order method.

The WD connection influence can be controlled through the following parameters: stiffness, yielding, ductility and strength associated to it.

T_L has a similar meaning but refers to the lateral walls modelled as elastic spring bed. Its contribution is different from zero only for inward rotations (spring bed in compression, Figure 4.44b). T_L is function of the rotation angle θ, the stiffness of the spring bed K_L , the effective height of the spring bed $\bar{h}$ and the block thickness s (Giresini and Sassu 2017):

$$\boldsymbol{T_L = sgn(\theta) K_L \bar{h} \left(A + \frac{B\bar{h}}{2} + \frac{C\overline{h^2}}{3} \right)} \qquad 4.39$$

where:

$$\boldsymbol{A = sgn(\theta) s^2 \sin\theta \cos\theta\, (1 - \cos\theta)}$$

$$\boldsymbol{B = s(\sin^2\theta \cos\theta - \cos^3\theta + \cos^2\theta)}$$

$$\boldsymbol{C = sgn(\theta) \sin\theta \cos^2\theta} \qquad 4.40$$

The stiffness of the spring bed K_L can be calculated as function of the horizontal elastic modulus of masonry E_L, effective transverse wall length L_{eff} and transverse wall thickness t_t as illustrated in Giresini and Sassu (Giresini and Sassu 2017).

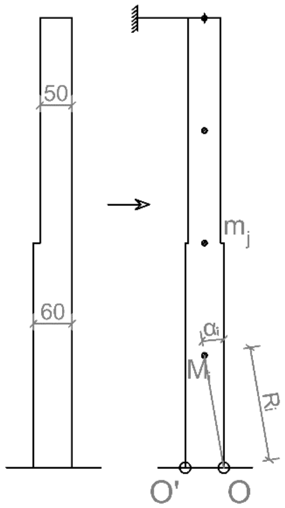

Figure 4.45 Simplification of the mechanism geometry for rocking analysis.

Although the selected Mechanism 4 is not characterized by perfect symmetry with respect to the vertical axis, the rocking analysis is carried out over a symmetric block, hypothesis justified also by the floor timber beams supported on both sides, thus reducing eccentricity. Moreover, previous studies showed that the influence of eccentric loads caused by overburden loads is negligible with respect to the slenderness of the block, as well as its dimension (known as scale factor). Considering this simplification, the cross section is slightly adapted (Figure 4.37) for the sake of a reduced computational effort.

When complex geometries are considered, and the mechanism basically consists of sub-blocks (such as walls of different levels with different thickness values), one of the first steps is to compute the moment of inertia of the whole geometry with respect to the axis of rotations, also including possible floor masses, corresponding to the floor loads (self-weight + live load). The moment of inertia of any solid can be directly computed using CAD softwares but when simple geometries are considered (such as parallelepipeds) this can be calculated analytically. Once the moment of inertia of each solid, about the centre of gravity, $I_{CM,i}$ is given, the total moment of inertia is simply given by the Huygens-Steiner's Theorem:

$$\boldsymbol{I_O = \sum_i \left(I_{CM,i} + M_i R_i^2\right) + \sum_j m_j R_j^2} \qquad 4.41$$

Where M_i is the mass of the i^{th} solid, R_i is the distance between the centre of gravity of the i^{th} solid and the rotation axis, while m_j and R_j are the j^{th} additional mass assumed lamped at a distance R_j from the rotation axis. Obviously, if vertical symmetry exists, $I_O = I_{O'}$ and the calculus of different radius vectors, as well as slenderness ratios is not necessary.

The analysed mechanism is assumed to be pre-activaved by the presence of vertical cracks. Moreover, in consistence with hysteretic models already used for nonlinear dynamic analysis of the global building, the behavior of the WD connection in compression is associated to the axial compression stiffness of the timber beams, $K_{comp} = E_b A_b / L_b$. In the same way as what done in Section 4.2, only the effect of one floor side is considered, keeping the results on the safe side.

Masonry masses M_i are assumed located at the centre of gravity of the i^{th} sub-block and the location is simply defined by the i^{th}radius vector R_i and slenderness ratio α_i. Equation 4.32 simply becomes:

$$\boldsymbol{I_0\ddot{\theta} + \sum_k sgn(\theta) m_k g R_k sinA_{\theta,k} + T_t + T_L = \sum_k m_k \ddot{u}_g R_k cosA_{\theta,k}} \qquad 4.42$$

Where the subscript k is extended to both i^{th} self-weight masses, and j^{th} overburden masses.

4.3.3 Input selection

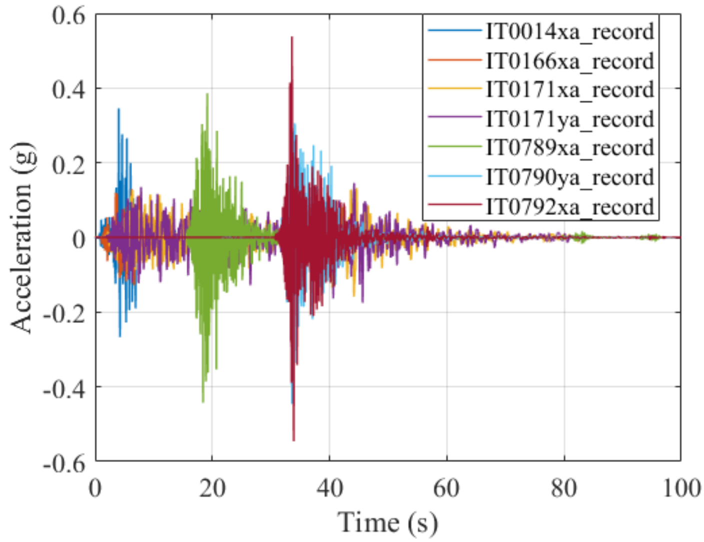

Figure 4.46 Acceleration time-histories of the selected waveforms.

Within the aim of this work a selection of 7 natural accelerograms is performed assuming the mechanism to be placed at the foundation level. The selection is carried out through Rexel program (Iervolino, Galasso, and Cosenza 2010) that allows to search for suites of waveforms, from different databases, such as the European Strong-motion Database (ESD) (Ambraseys et al. 2002), the Italian Accelerometric Archive (ITACA) (D'Amico et al. 2020), or the world strong motion database (SIMBAD) (Smerzini and Paolucci 2013) compatible to reference spectra being either user-defined or automatically generated according to Eurocode 8 and Italian seismic code (DMI 2008). The analysis carried out by Rexel and the corresponding parameters are shown in Figure 4.47. In particular, the accelerograms are selected and scaled in such a way that the average spectrum, S_m is compatible to the site-related elastic spectrum. This compliance is such that, for a range of periods of interest $[T_1, T_2]$, the average spectrum is within $[70\% S_e < S_m < 130\% S_e]$, where S_e is the elastic target spectrum obtained for $\xi = 5\%$.

The building is assumed located in Norcia (Perugia, Italy), on a B-site class, T1, topographic category, 50 years nominal life, II functional type. The 7 records refer to the LLS selecting as significant periods of interests $T = [0.2, 1.0]s$, according to the modal properties of the building (see Section 4.1.4).

In consistence with dynamic analysis performed over the global finite element model (Section 4.1.6), a reduced strong motion duration is considered as the period between 0.01% and 99% of the total Arias intensity energy, I_a (Equation 4.5).

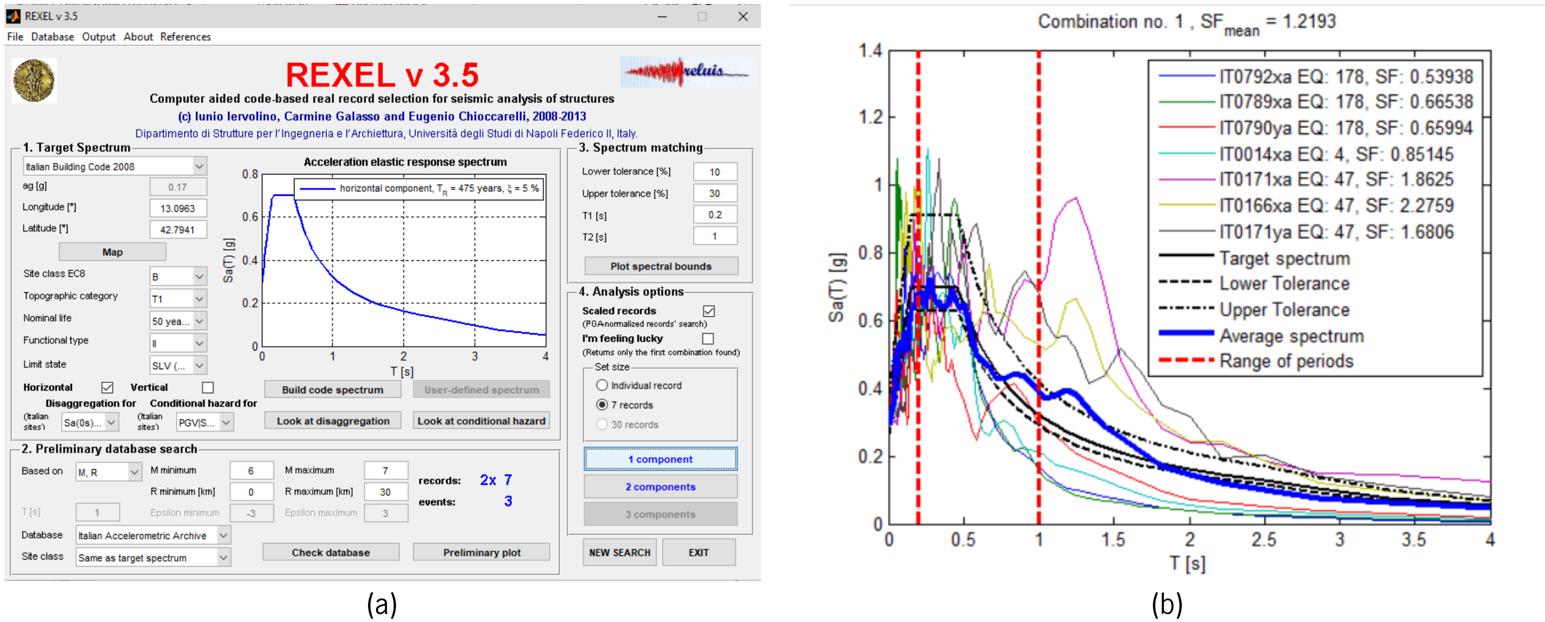

Figure 4.47 Selection of acceleration spectrum-compatible waveforms in Rexel V.3.5 (Iervolino et al. 2010): (a) Graphical user interface; (b) waveforms spectra.

Waveform ID	arthquake I	Station ID	Earthquake Name	Date	Mw	Fault Mechanism	Epicentral Distance [km	PGA_X [m/s^2]	PGA_Y [m/s^2]	PGV_X [m/s]	PGV_Y [m/s]	ID_X	ID_Y	Np_X	Np_Y
792	178	AQV	L'Aquila Mainshock		6.3	Normal	4.870	5.352	6.443	0.427	0.402	5.441	6.810	0.535	0.719
789	178	AQA	L'Aquila Mainshock	06/04/2009	6.3	Normal	4.634	4.339	3.947	0.267	0.319	9.317	7.892	0.460	1.120
790	178	AQG	L'Aquila Mainshock	06/04/2009	6.3	n/a	4.392	4.793	4.374	0.358	0.310	4.815	6.104	0.794	0.926
14	4	TLM1	FRIULI EARTHQUAKE 1ST SHOCK	06/05/1976	6.4	Thrust	21.721	3.390	3.090	0.222	0.301	6.501	8.053	0.535	0.688
171	47	CLT	IRPINIA EARTHQUAKE	23/11/1980	6.9	Normal	18.855	1.550	1.718	0.260	0.291	16.428	17.067	0.747	0.919
166	47	BGI	IRPINIA EARTHQUAKE	23/11/1980	6.9	Normal	21.803	1.268	1.832	0.225	0.344	7.785	4.403	1.096	0.774
171	47	CLT	IRPINIA EARTHQUAKE	23/11/1980	6.9	Normal	18.855	1.550	1.718	0.260	0.291	16.428	17.067	0.747	0.919
mean:					6.57		13.590	3.177	3.303	0.288	0.322	9.531	9.628	0.702	0.866

Figure 4.48 Main parameters of selected waveforms, directly obtained by Rexel (Iervolino et al. 2010)

4.3.4 Rocking analysis

Dynamic nonlinear analysis of the Mechanism E is carried out for each model configuration.

In case of Model 1 (no connections), given the absence of the connections, the masonry wall is basically in free-standing configuration. The influence of the lateral walls can be studied including (or not) the bed spring with stiffness equivalent to the size and the characteristics of the transversal walls. The mechanism under study is assumed to be the OOP of W_x_3b wall up to the end of the corner at the interface with lateral wall. Thus, the presence of the lateral wall should be properly taken into account when the wall rotates inward. The lateral stiffness can be assumed as $K_L = E_L s / L_{eff}$, where the masonry Young's modulus can be assumed $E\_L \ = 1187 \, MPa$ (in consistence with properties used in Section 4.1), $s \ = \ 55 \, cm$ is the average stiffness of the lateral wall, and $L_{eff} = \ 300 \, cm$ is the effected length of the transversal wall.

In order to better understand the influence of the lateral walls, both one-sided (presence of lateral walls) and two-sided (absence of lateral walls) configurations are studied, solely for Model 1. The coefficient of restitution is simply based on the analytical formulation proposed by Housner (1963), only function of the geometry of the block ($e = e_H = 1 - \frac{3}{2} sin^2 \, \alpha$).

Results are shown in terms of normalized rotation time-histories ($\theta(t)/\alpha$) in Figure 4.49 and are collected in Table 4.11 in terms of maximum horizontal displacement of the centre of gravity d_G. The maximum displacement capacity of the block (relative the LLS) corresponds to the rotation of the block that brings the centre of gravity vertically aligned with the pivot point (that is $d_G = d_0$). Furthermore, the averaged displacement is compared to $0.4 d_0$.

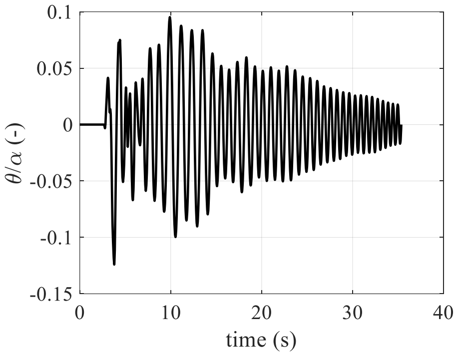

IT0014xa_record

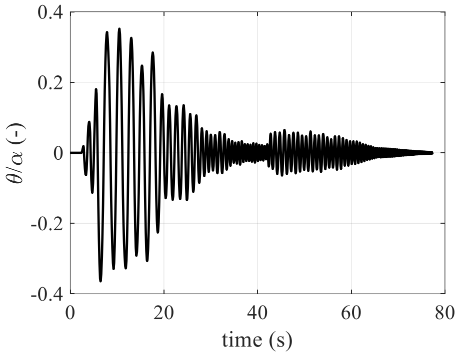

IT0166xa_record

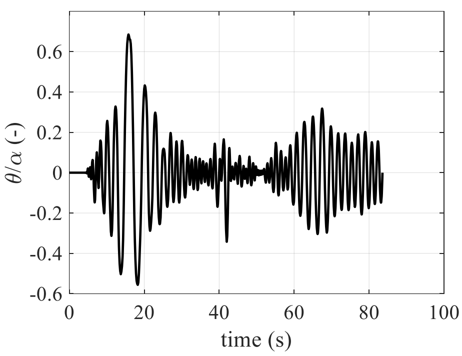

IT0171xa_record

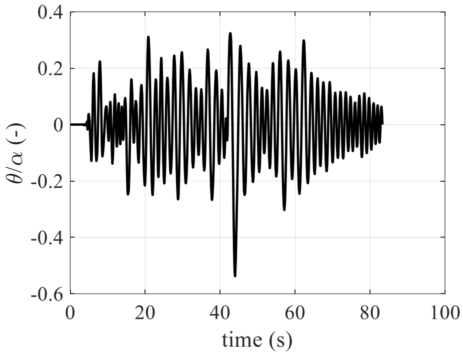

IT0171ya_record

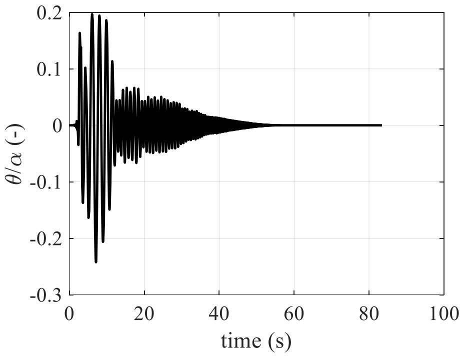

IT0789xa_record

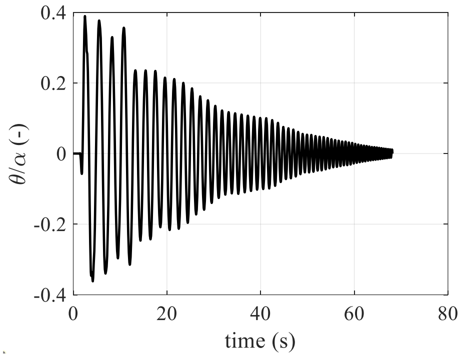

IT0790ya_record

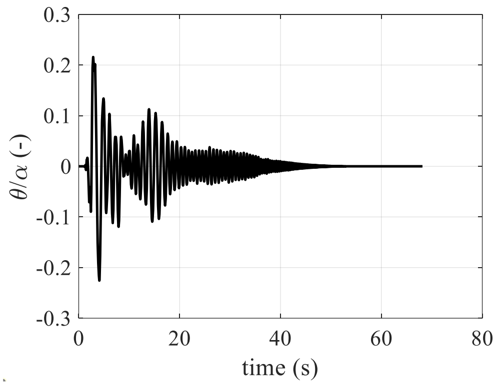

IT0792xa_record

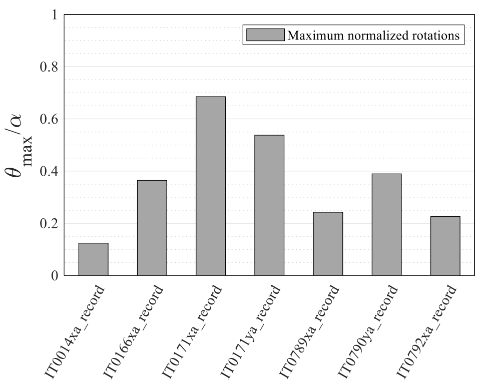

normalized rotations summary

Figure 4.49. Normalized rotation time-histories. Mechanism E, two-sided configuration, Model 1.

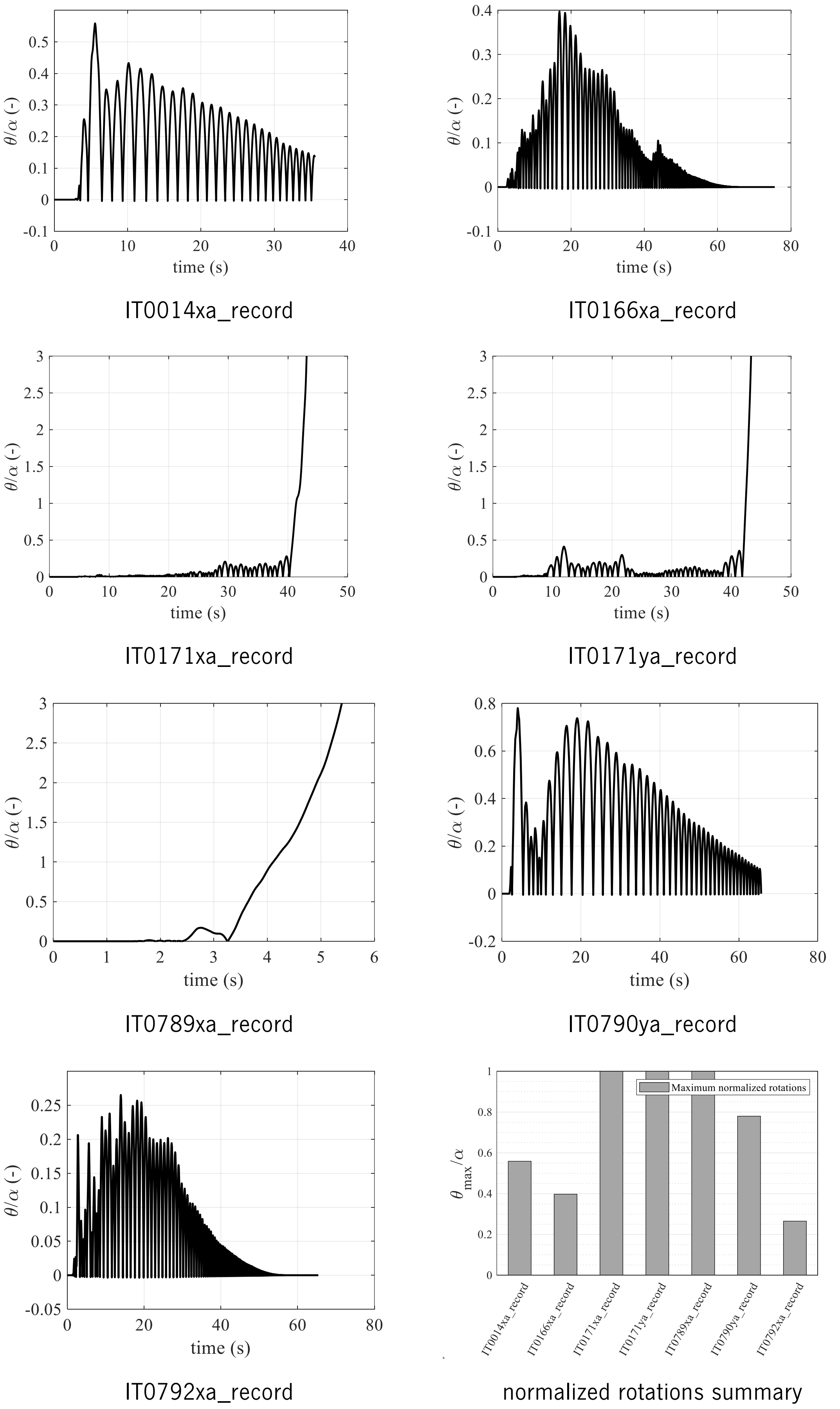

Figure 4.50. Normalized rotation time-histories. Mechanism E, one-sided configuration, Model 1.

Figure 4.50 reveals that not only the presence of the lateral walls leads to the increment of the maximum rotation of the wall, but it also causes the overturning of the wall (3 cases over a total of 7). Figure 4.51 shows the normalized rotation obtained for IT0014xa and IT0171xa records highlighting the detrimental effect of transversal walls comparing the response to one-sided configuration (presence of lateral walls) to that of two-sided configuration (free-standing wall). This is likely to be due to the rebound effect of the wall rotating inward and impacting to the transversal walls. Such an effect is only visible under dynamic analysis and impossible to result under static (linear or nonlinear) analysis.

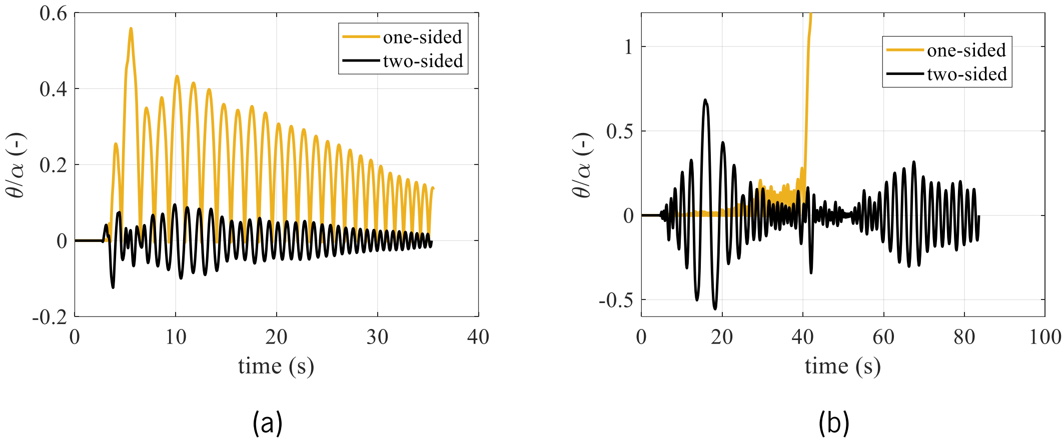

Figure 4.51. Influence of the presence of lateral walls in the dynamic analysis of free-standing walls. (a) IT0014xa record, (b) IT0171xa record. Mechanism E, Model 1. One-sided: presence of lateral walls; Two-sided: absence of lateral walls.

Given the above, the one-sided configuration is assumed for the remaining models as the one leading to more conservative results and more realistic, based on knowledge gained from previous seismic events.

Results in terms of maximum horizontal displacement of the centre of gravity $d_{G,max}$ are collected in Table 4.11 for Mechanism E in one-sided motion and for Model 1.

Table 4.11. Dynamic analysis of Mechanism E, Model 1 in terms of maximum horizontal displacement of the centre of gravity.

Event	$d_{G,max}$ (cm)	$d_0/d_{G,max}$ (-)
IT0014xa_record	16.75	1.79
IT0166xa_record	11.90	2.52
IT0171xa_record	300.00	overturning
IT0171ya_record	300.00	overturning
IT0789xa_record	300.00	overturning
IT0790ya_record	23.39	1.28
IT0792xa_record	7.94	3.78
		$(0.4\ d_0)/d_{G,mean}$
mean	15.00	0.80

The high vulnerability of masonry walls with no WD connections is confirmed by the dynamic analysis showing three overturning cases out of the total seven cases. Moreover, the mean value of the maximum displacement is less than $0.4d_0$, further demonstrating the condition below the safety.

Dynamic analysis of restrained rigid blocks requires the definition of a hysteretic constitutive model for the horizontal restraint. In consistence with nonlinear kinematic analysis (Section 0), WD connection is defined by elasto-plastic behavior properly representing the quality of the connection. Models 2 and 3 represent unstrengthened and strengthened connections, respectively, simulated according to simplified bilinear curves performed in Section 3.2. The unloading-reloading behavior is elastic, as defined in Section 4.3.2. Whereas Model 4 simulates a perfect connection, and its constitutive law is associated to the timber beam stiffness, strength, and failure. However, given the high value of the ultimate resisting force of the timber beam, it hardly fails, thus remaining within the elastic range. A detail of backbone parameters defining the WD hysteresis curve for each model can be found in Section 0.

The normalized rotation TH is shown in Figure 4.52 and Figure 4.53 for each model configuration, solely for IT0014xa and IT0792xa records, respectively while the whole set of responses is reported in Appendix 2. Here, the results are presented in two separate Figures comparing models 1 and 2 (Figure 4.52a), while models 3 and 4 are compared in Figure 4.52b, for the matter of clarity. Indeed, the increased quality of the connection given by models lead to strongly reduced rotations, thus a lower scale is necessary.

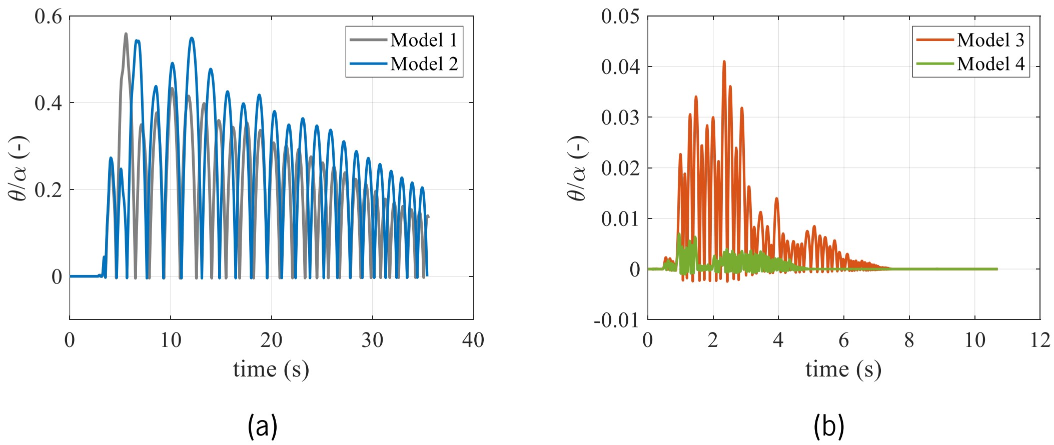

Figure 4.52. Influence of WD connection quality on the normalized rotation TH. (a) Model 1 vs. Model 2; (b) Model 3 vs. Model 4. Mechanism E, IT0014xa_record.

Similarly, normalized rotation TH are shown for IT0792xa record in two separate Figures for the sake of clarity. Although the overall beneficial effect of the connection is visible for models

3 and 4, this is not true for Model 2 with respect to Model1: when poor connection is present, the wall overturns, while the same block in free configuration is stable (Figure 4.53a). Thus, the influence of the WD connection on the dynamic behavior of the OOP masonry wall does not necessarily lead to safer results, especially if a poor strength and displacement capacity is considered.

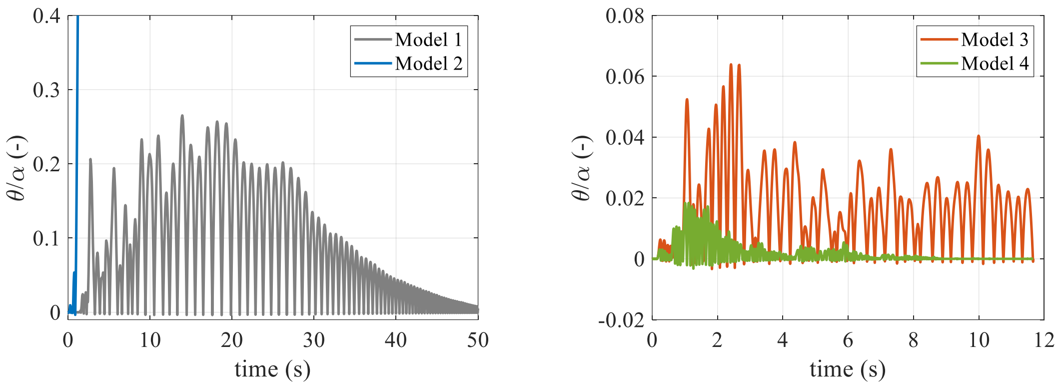

(a) (b)

Figure 4.53. Influence of WD connection quality on the normalized rotation TH. (a) Model 1 vs. Model 2; (b) Model 3 vs. Model 4. Mechanism E, IT0792xa_record.

Figure 4.54 shows the WD connection normalized force TH obtained for models 2,3,4, and for IT0792xa_record, whereas the corresponding connection hysteresis in terms of Force-Slip curve, is shown in Figure 4.55.

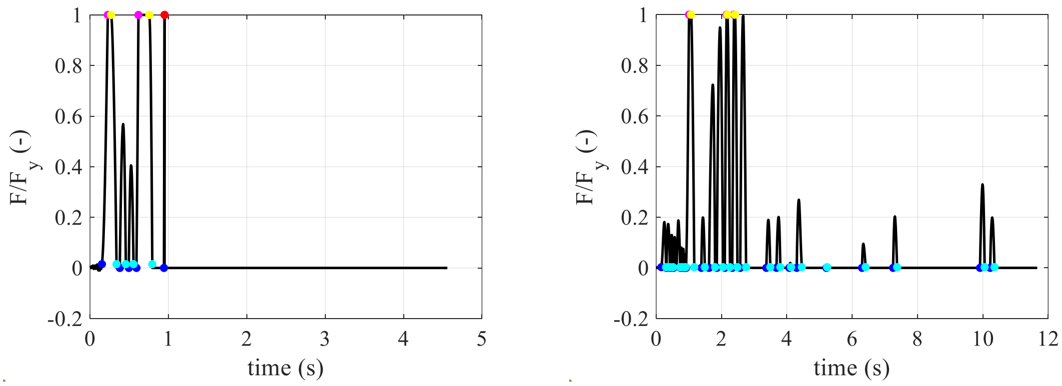

(a) (b)

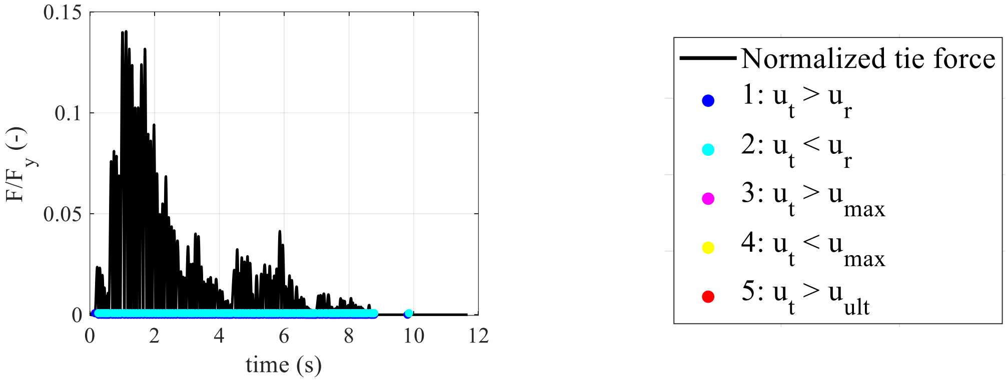

(c)

Figure 4.54. Influence of WD connection quality in terms of connection normalized force TH. (a) Model 2; (b) Model 3; (c) Model 4. Mechanism E, IT0792xa_record.

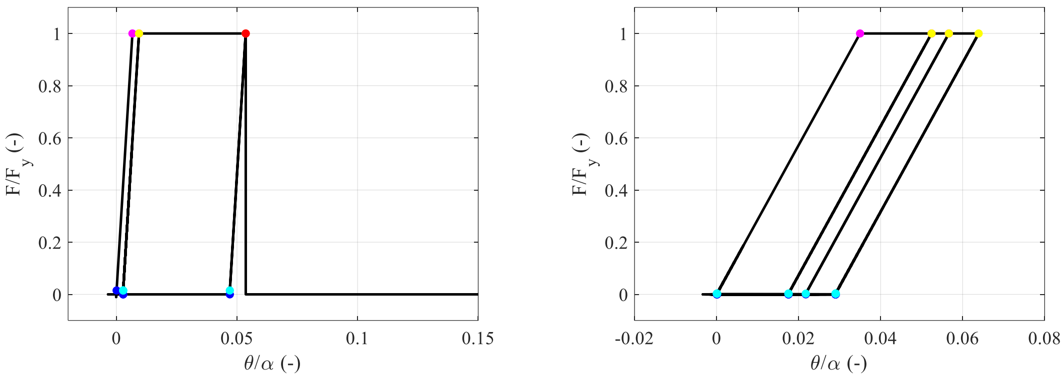

(a) (b)

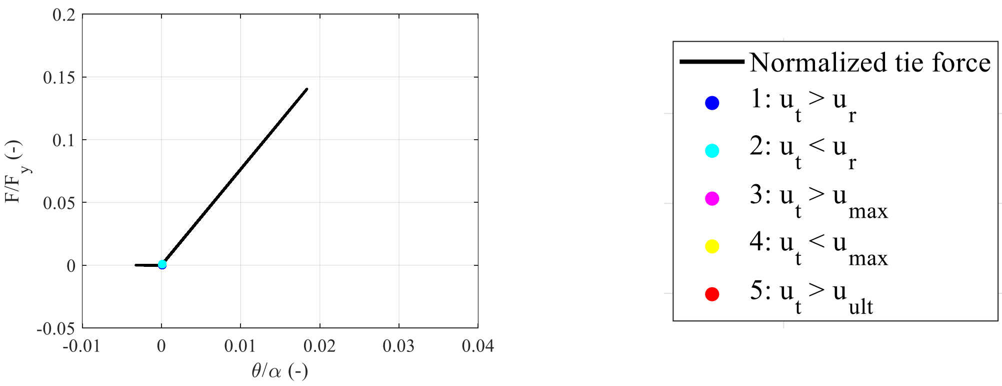

(c)

Figure 4.55. Influence of WD connection quality in terms of connection force-slip hysteresis. (a) Model 2; (b) Model 3; (c) Model 4. Mechanism E, IT0792xa_record.

The output shown in Figure 4.55 is quite useful as it is capable of showing the evolution of the nonlinear connection within the ground motion, highlighting the nonlinear events that define the phase transition (see Figure 4.44). The WD connection undergoes rupture in Model 2, while in Model 3 it goes over the elastic limit but does not fail. The strong restraining effect given by

Model 4 make the WD connection to remain elastic and far from the yielding limit (<15%, Figure 4.55c).

Furthermore, it must be noted that in reality the WD connection hardly behaves like Model 4, and such a retrofit model can be costly and invasive for the existing building. Moreover, if such a strong connection resistance is assumed, it is more likely that other failure modes occur given by the high level of stress in the area of the connection. Even though the connection in model 3 overcomes the elastic limit, this can still exploit its ductile capacities enabling a higher energy dissipation during the hysteresis.

Results are summarized in Table 4.12 in terms of maximum displacement values, compared to the corresponding LLS displacement capacity for seismic vulnerability assessment.

The overall behavior of the local mechanism under study increases if the quality of the connection increases. The results obtained for Model 3 (strengthened connections) demonstrates the benefit of the retrofitting solution reaching safety factors highly over the unity. Moreover, additional strengthening (Model 4) may result unnecessary.

Table 4.12. Seismic vulnerability assessment of Mechanism E through nonlinear dynamic analysis of rigid blocks.

	Model 1		Model 2	
Event	$d_{G,max}$ (cm)	$d_0/d_{G,max}$ (-)	$d_{G,max}$ (cm)	$d_0/d_{G,max}$ (-)
IT0014xa_record	16.75	1.79	16.45	1.82
IT0166xa_record	11.90	2.52	0.43	68.97
IT0171xa_record	300.00	overturning	0.34	87.80
IT0171ya_record	300.00	overturning	7.59	3.95
IT0789xa_record	300.00	overturning	11.57	2.59
IT0790ya_record	23.39	1.28	300.00	overturning
IT0792xa_record	7.94	3.78	300.00	overturning
		$(0.4\ d_0)/d_{G,mean}$		$(0.4\ d_0)/d_{G,mean}$
mean	15.00	0.80	7.28	1.65

	Model 3		Model 4	
Event	$d_{G,max}$ (cm)	$d_0/d_{G,max}$ (-)	$d_{G,max}$ (cm)	$d_0/d_{G,max}$ (-)
IT0014xa_record	1.23	24.44	0.21	143.75
IT0166xa_record	0.15	194.41	0.05	609.93
IT0171xa_record	0.13	233.02	0.04	739.65
IT0171ya_record	0.21	141.46	0.04	680.63
IT0789xa_record	5.03	5.97	0.39	76.85
IT0790ya_record	1.03	29.22	0.20	147.82
IT0792xa_record	1.91	15.68	0.55	54.55
		$(0.4\ d_0)/d_{G,mean}$		$(0.4\ d_0)/d_{G,mean}$
mean	1.38	8.67	0.21	56.53

4.4 Conclusive remarks

This chapter faced the seismic vulnerability of a benchmark 4-level building through global and local analyses. The influence of the wall-to-horizontal diaphragm (WD) connection was studied defining four different configurations: (Model 1) very poor; (Model 2) unstrengthened; (Model 3) strengthened; and (Model 4) perfect connections. The methodology adopted included the development of a finite element model capable of providing important information of the global building in terms of modal properties, strength and displacement capacity, as well as damage pattern. Model 1 is basically represented by a model with no floor stiffness and can be seen as the lower bound model. The actual behavior should be represented by models 2 and 3, while Model 4 is the reference upper bound model. Mass-proportional pushover analysis was carried out showing that the overall building capacity increases in terms of force. The main differences were obtained between Model 1 and 2 and between Model 3 and Model 4. Moreover, even if the building strength increases, the ductility decreases from Model 1 to 3. Similar results are confirmed by incremental dynamic analysis (IDA) performed for each configuration. The force displacement envelope based on maximum force was seen to be promising for the actual capacity of the building, closely similar to pushover curves. The dynamic effects were studied in this case in terms of force-slip hysteresis within the WD connections, allowing for the total energy computation. Only the unstrengthened connection (Model 2) undergoes into the plastic phase, while the strengthened connection basically remains elastic, thus allowing a lower energy dissipation within the ground motion.

The influence of WD connections was also studied through the local assessment of OOP masonry walls, mainly using two different approaches: (i) linear and nonlinear kinematic analysis; (ii) dynamic analysis of rigid block (that is rocking analysis). Linear kinematic analysis allowed for simple and quick force-based vulnerability assessment of the selected mechanisms. Indeed, one of the crucial aspects is the prior selection of all possible failure mechanisms likely to occur. The dynamic amplification and filtering effect of the seismic force, eventually occurring at certain floor level, was considered constructing proper floor spectra, as suggested by current Code Standards. URM buildings with poor connections resulted to be very sensitive to period of vibration assumed for the definition of the corresponding floor spectrum. As a result, the contribution of all significant modes of vibration should be taken into account

Results obtained both in terms of acceleration safety factor (ASF) and displacement safety factor (DSF) demonstrate the high vulnerability of Model 1, and the high safety of Model 4, actually at the extreme boundaries. Strengthening solution simulated through Model3 provided the necessary reinforcement level meeting the requested safety condition. On the other hand, poor WD connections hardly meet the safety standards, especially through nonlinear kinematic approach. This was mainly caused by the low displacement capacity constrained by the low ductility of the connection.

A more advanced method was also adopted capable of studying the dynamic stability of OOP masonry walls, possibly including nonlinear WD connections. The study revealed the importance of accounting for transversal walls as they can lead to higher displacement levels and overturning of the wall. This can be due the rebound effect possibly caused at the wall-to-wall interface. Besides the overall behavior improves when passing from Model 1 to Model 2, the latter poorly performed, mainly because of the failure of the connection. The reinforcement gained from Model 3 configuration was demonstrated in terms of maximum wall displacement and WD connection force, capable of resisting the seismic load without failing. The ductile capacities of the connection were fundamental for a proper energy dissipation.

CHAPTER 5
DESIGN PROCEDURE

Overview

In this final chapter, the main outcomes are used as the bases of the suggested design procedure for the assessment and the design of WD seismic connections in existing historical buildings.

The seismic assessment of wall-to-horizontal diaphragm (WD) connections in historical constructions is crucial for the evaluation of the current state of the building and the design of the potential retrofitting solutions. This can be carried out mainly through a force-based or displacement-based criteria. Besides the global analysis of the building is fundamental for the overall capacity, this may be complex leading to high computational costs and uncertain results. On the other hand, local analysis, based on the Virtual Work Principle, currently suggested by the Italian Code is quick and simple, capable of gaining the safety index after proper estimation of the capacity and of the demand. Such a procedure is currently spread among practitioners and well known. Both linear and nonlinear kinematic approaches were also validated by additional advanced nonlinear dynamic analysis of rigid blocks, leading to similar results.

Based on the above and given the results obtained after the sensitivity study carried out in Chapter 4 through different numerical approaches, a simple ready-to use design procedure is suggested herein capable of performing the seismic assessment of WD connections in the current state and in the possible retrofitted stage.

The procedure focuses on the axial pull-out capacity of masonry-to-timber beam connections, common in historical URM constructions but it can be easily applied to a wider category.

The suggested procedure can be summarized in the following steps (Figure 5.1):

- Inspection and diagnosis of the current state of structural connections;
- Estimation of the pull-out strength and displacement capacity of the connection;
- Preliminary assessment of the current state of the building through linear or nonlinear limit analysis;
- Preliminary design of the retrofitting solution;
- Estimation of the strengthened connection capacity;
- Assessment of the updated state through linear or nonlinear limit analysis;
- Optimization of the retrofitting solution;

Acquiring proper knowledge about the actual state of the structural connection is crucial for setting the bases of subsequent analysis. Visual inspections are strongly recommended as well as non-destructive or destructive tests, when possible. When in-situ tests are not possible, similar samples can be tested in laboratory. Whereas, if no experimental data can be acquired, information available in literature and simple analytical formulations can be useful for the estimation of the pull-out capacity of the connection. Depending on the type of the connection, it is possible to identify the failure modes that are most likely to occur, and the corresponding connection capacity can, than, be computed (see (Moreira 2015), Section 6.4.2).

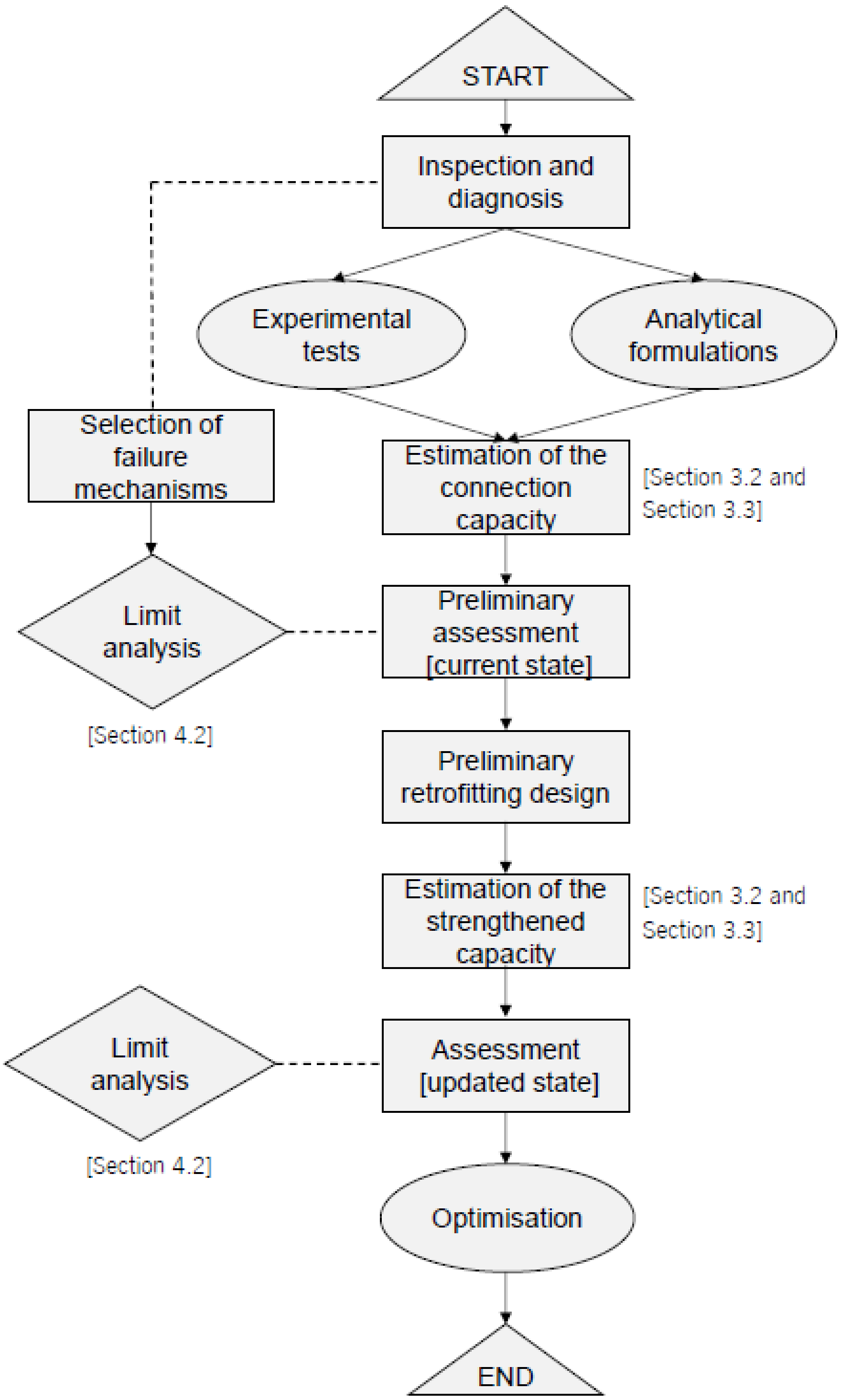

Figure 5.1. Suggested design procedure for the seismic vulnerability assessment of WD connections in historical constructions.

Preliminary inspection of the current damage level and crack pattern of the building can also give additional information about the wall failure modes that are most likely to occur. Once all these information are available, the preliminary assessment of the local mechanisms with WD connections in their current state can be caried out through linear kinematic analysis. If nonlinear parameters of the connections are available, nonlinear kinematic analysis is suggested, instead.

Therefore, the preliminary design of the WD connections strengthening solution can be performed through available technologies and traditional or innovative solutions. One of the most common solutions comprises the use of steel ties and anchors increasing the pull-out capacity of the connections. The capacity of the strengthened solution can either be estimated through simplified analytical formulations or based on literature, from data about similar connections. Depending on the current quality of the connections, the number of strengthened anchors may vary, being one anchor every 2, 3 or 4 joists, also depending on the timber joists spacing.

Next, the assessment of the local mechanisms through limit analysis can be carried out in the updated model. Again, if nonlinear properties of the connections can be evaluated, the seismic vulnerability assessment can be carried out in terms of displacement (nonlinear kinematic analysis) or acceleration (linear kinematic analysis).

Finally, an optimisation phase can be adopted in order to re-design the strengthened solution or the number of anchors to be applied, in such a way to obtain a well-balanced solution in terms of cost-benefit and avoid too conservative or too invasive retrofitting procedure.

CHAPTER 6
CONCLUSIONS

Overview

This Chapter summarizes the main outcomes of the research work considering the models proposed in Chapter 3 for the unstrengthened and strengthened connections. It also succinctly discusses the original contributions of this research to the existing literature.

In this thesis, the analysis of wall-to-horizontal diaphragm connections was carried out through a comprehensive numerical study accounting for simplified and advanced strategies. A thorough literature review about traditional and innovative wall-to-horizontal diaphragm (WD) connections was of primary importance to set the bases for the interpretation of the numerical campaign. Based on available experimental data on the axial pull-out capacity of WD connections, simplified bilinear curves were developed, useful for being applied on numerical models. A benchmark 4-storey building was analysed in terms of both global and local failure modes. Given the low masonry tensile strength, the study was performed through nonlinear static and nonlinear dynamic analyses.

The global capacity of the building is very sensitive to the quality of the connection. In particular, the strength capacity increases with respect to poor existing connections if the strengthened solution is applied. However, the ductility of the system may decrease, possibly by the increased lateral stiffness and force levels acting on different structural components, and reducing displacement capacity.

The global analysis of URM buildings accounting for WD connections was useful to obtain important information about possible failure modes and the overall construction capacity. However, it required high computational costs, and the results are highly sensitivity and expertise of the analyst. Uncertainties may also rise about the material properties definition or numerical issues.

Notwithstanding the increased global capacity of Model 4 (ideally perfect connections), its overall damage pattern comprises vertical cracks along the wall-to-wall interface, still highlighting the possible detachment of the main façade from the side-walls, and possibly causing high displacement levels and consequent damage.

In general, if proper structural connections are assumed, the building performs like a box, capable of transmitting seismic forces to lateral resisting walls. However, when the quality of the connections decreases the box-type behavior fails and local mechanisms may be activated. This effect is strongly influenced by long-spanning walls and by the irregularity of the building, in which even the assumption of perfect WD connections may not guarantee the correct seismic load distribution among the different structural elements. Proper strengthening solution aiming at increasing the WD connection quality, lead the opposite walls to be tight together, reducing relative displacements caused by the walls vibrating out of phase. Such a solution should always be combined with wall-to-wall strengthening, and, if necessary, additional in-plane resisting wall capable of reducing the OOP wall free span.

Local analysis based on virtual work principle was carried out over the main failure mechanisms of the reference building. The procedure allowed to calculate both acceleration safety factors (ASF) and displacement safety factors (DSF) for the seismic vulnerability of OOP walls including WD connections. Linear kinematic analysis was useful as preliminary assessment of the wall in the current state, while nonlinear kinematic analysis revealed to be a more accurate procedure capable of accounting for sound floor spectra in cases of mechanisms taking place at the floor level. Such a procedure is further supported by nonlinear dynamic analysis of rigid blocks (rocking analysis) useful for a better identification of the dynamic effect during the oscillation of the walls. One of the limits of such an approach is based on the prior definition of the mechanisms, but also on the rigid-like assumption of the walls. This can also be the advantage of the methodology, as no masonry properties are necessary to be defined for the analysis.

In summary, the OOP vulnerability of URM walls restrained by WD anchors highly decreases if the quality of the connection increases. In particular, care must be taken in case of poor existing connections, mainly based on friction, and engineered solutions should be accordingly designed. Modeling strategies where connections are assumed perfect or absent may lead to over- and under-estimated strength capacities, respectively, if compared to more realistic cases, thus should be considered at the two boundaries.

A simple strengthening solution such as steel ties coupled with steel plates, bolted to the timber joist/beam and anchored to the external wall seems to be a mini-invasive and well-balanced cost-benefit solution within the required seismic safety conditions.

Based on this study about the seismic assessment of WD connections, a simple design procedure was developed capable of assessing the actual state of the walls and the corresponding upgraded state including the designed retrofitted solution.

The outcomes of this study set forth the bases for extending the research about WD connections on different further scale levels and wider domains. A case-study application can serve as proof of the suggested methodology, highlighting all the necessary steps and possible issues. Automatic optimization procedures can be developed capable of auto-calibrate hysteretic roles of pull-out experimental data, useful for application on appropriate numerical models. Experimental campaign about pull-out and pull-in (compression), as well as shear behavior of WD connections can be useful for acquiring additional knowledge about the connection capacity on the remaining degrees of freedom.

LIST OF REFERENCES

Abdul Karim, Abdul Razak, Pierre Quenneville, Norazzlina M. Sa'don, and Jason Ingham. 2013. "Assessment Guidelines of Wall-Diaphragm Connections for Masonry Buildings." Pp. 1019–24 in *7th International Structural Engineering and Construction Conference*.

ACI. 2008. *Building Code Requirements and Specification for Masonry Structures*.

Aghagholizadeh, Mehrdad and Nicos Makris. 2018. "Earthquake Response Analysis of Yielding Structures Coupled with Vertically Restrained Rocking Walls." *Earthquake Engineering and Structural Dynamics*.

Alberti, L. B. 1452. *De Re Aedificatoria*. edited by C. Bartoli. Milano.

Alecci, Valerio, Silvia Briccoli Bati, and Giovanna Ranocchiai. 2009. "Numerical Homogenization Techniques for the Evaluation of Mechanical Behaviour of a Composite with SMA Inclusions." *Journal of Mechanics of Materials and Structures* 4(10):1675–88.

Alecci, Valerio, Silvia Briccoli Bati, and Giovanna Ranocchiai. 2014. "Concrete Columns Confined with CFRP Wraps." *Materials and Structures/Materiaux et Constructions*.

Alecci, Valerio, Mario De Stefano, Francesco Focacci, Raimondo Luciano, Luisa Rovero, and Gianfranco Stipo. 2017. "Strengthening Masonry Arches with Lime-Based Mortar Composite." *Buildings*.

AlShawa, Omar, Domenico Liberatore, and Luigi Sorrentino. 2019. "Dynamic One-Sided Out-Of-Plane Behavior of Unreinforced-Masonry Wall Restrained by Elasto-Plastic Tie-Rods." *International Journal of Architectural Heritage* 00(00):1–18.

Ambraseys, N., P. Smit, R. Sigbjornsson, P. Suhadolc, and B. Margaris. 2002. "Internet-Site for European Strong-Motion Data."

American Society of Civil Engineers (ASCE). 2013. *ASCE/SEI 41-13 : Seismic Evaluation and Retrofit of Existing Buildings*.

Andreini, Marco, Anna de Falco, Linda Giresini, and Mauro Sasso. 2013. "Structural Analysis and Consolidation Strategy of the Historic Mediceo Aqueduct in Pisa (Italy)." *Applied Mechanics and Materials* 352(Advances in Civil Structures):351–52.

Appleton, João. 2003. *Reabilitação de Edifícios Antigos - Patologias e Tecnologias de Intervenção*. edited by Orion. Amadora.

Araújo, Ana S. 2014. "Modelling of the Seismic Performance of Connections and Walls in Ancient Masonry Buildings."

ASCE. 2007. *Seismic Rehabilitation of Existing Buildings - ASCE/SEI 41-06*. Reston, Virginia.

ASCE. 2017. *Seismic Evaluation and Retrofit of Existing Buildings - ASCE/SEI 41-17*. Reston, Virginia: American Society of Civil Engineers.

Aşıkoğlu, Abide, Graça Vasconcelos, Paulo B. Lourenço, and Bartolomeo Pantò. 2020. "Pushover Analysis of Unreinforced Irregular Masonry Buildings : Lessons from Di Ff Erent Modeling Approaches." 218(March).

Aslam, Mohammad, William G. Godden, and D. Theodore Scalise. 1980. "Earthquake Rocking Response of Rigid Bodies." *Journal of the Structural Division* 106(2):377–92.

Blaikie, E. L. and D. D. Spurr. 1992. *Earthquake Vulnerability of Existing Unreinforced Masonry Buildings*. edited by Works Consultancy Services. Wellington, NZ.

Bothara, Jithendra and Svetlana Brzev. 2011. *A Tutorial: Improving the Seismic Performance of Stone Masonry Buildings*. First Edit. Oakland, California, United States of America: Earthquake Engineering Research Institute.

Bothara, Jithendra, Rajesh P. Dhakal, and John B. Mander. 2010. "Seismic Performance of an Unreinforced Masonry Building: An Experimental Investigation." *Earthquake Engineering and Structural Dynamics* (39):45–68.

Breymann, G. A. 1880. *Trattato Delle Costruzioni Civili*.

Brignola, Anna, Stefano Podestà, and Stefano Pampanin. 2008. "In-Plane Stiffness of Wooden Floor." *2008 NZSEE Conference, Paper 49* (49):1–19.

Bruneau, Michel. 1994. "State-of-the-Art Report on Seismic Performance of Unreinforced Masonry Buildings." *Journal of Structural Engineering* 120(1):230–51.

C. Casapulla; L. U. Argiento. 2018. "In-Plane Frictional Resistances in Dry Block Masonry Walls and Rocking-Sliding Failure Modes Revisited and Experimentally Validated." *Composites Part B: Engineering* 132:197–213.

C.S.LL.PP. 2009. "Circolare 02 Febbraio 2009 n. 617 Istruzioni per l'applicazione Delle 'Nuove Norme Tecniche per Le Costruzioni' Di Cui Al D. M. 14 Gennaio 2008. (in Italian)."

C.S.LL.PP. 2019. "Circolare 21 Gennaio 2019 n. 7 Istruzioni per l'applicazione Dell' 'Aggiornamento Delle Norme Tecniche per Le Costruzioni' Di Cui Al Decreto Ministeriale 17 Gennaio 2018. (in Italian)."

Calderini, C., R. Vecchiattini, C. Battini, and P. Piccardo. 2016. "Mechanical and Metallographic Characterization of Iron Tie-Rods in Masonry Buildings: An Experimental Study." Pp. 1293–1300 in *Structural Analysis of Historical Constructions: Anamnesis, diagnosis, therapy, controls - Proceedings of the 10th International Conference on Structural Analysis of Historical Constructions, SAHC 2016*, edited by Van Balen & Verstrynge. London: Taylor & Francis Group.

Campbell, Josiah, Dmytro Dizhur, Michael Hodgson, George Fergusson, and Jason M. Ingham. 2012. "Test Results for Extracted Wall-to-Diaphragm Anchors from Christchurch Unreinforced Masonry Buildings." *SESOC Journal* 25(1):57–67.

Casapulla, C. and L. U. Argiento. 2016. "The Comparative Role of Friction in Local Out-of-Plane Mechanisms of Masonry Buildings. Pushover Analysis and Experimental Investigation." *Engineering Structures* 126(August):158–73.

Casapulla, C., L. Giresini, and P. B. Lourenço. 2017. "Rocking and Kinematic Approaches for Rigid Block Analysis of Masonry Walls: State of the Art and Recent Developments." *Buildings* 7(3).

Casapulla, C., A. Maione, L. U. Argiento, and Elena Speranza. 2018. "Corner Failure in Masonry Buildings: An Updated Macro-Modeling Approach with Frictional Resistances." *European Journal of Mechanics, A/Solids* 70(March):213–25.

CEB-FIP. 1993. *Model Code 90*.

CEN. 2009. "UNI EN 338: Structural Timber — Strength Classes - British Standards Institute."

Cervera, Miguel, Javier Oliver, and Rui Faria. 1995. “Seismic Evaluation of Concrete Dams via Continuum Damage Models.” *Earthquake Engineering & Structural Dynamics*.

Cestari, Clara Bertolini and Antonella Di Lucchio. 2001. “Interventions on Historical Building Timber Floors : Retractable – Visible ? Invasive – Not Visible ? .... A Case Study.” 837–46.

Chevalley, G. 1924. “Elementi Di Tecnica Dell’architettura.” Torino: Pasta editore.

Clementi, F., V. Gazzani, M. Poiani, and S. Lenci. 2016. “Assessment of Seismic Behaviour of Heritage Masonry Buildings Using Numerical Modelling.” *Journal of Building Engineering* 8:29–47.

Clementi, Francesco, Valentina Gazzani, Marina Poiani, Pardo Antonio Mezzapelle, and Stefano Lenci. 2018. “Seismic Assessment of a Monumental Building through Nonlinear Analyses of a 3D Solid Model.” *Journal of Earthquake Engineering* 22(sup1):35–61.

Cóias, Vitor. 2007. *Reabilitação Estrutural de Edifícios Antigos - Alvenaria, Madeira - Técnicas Pouco Intrusivas*. Lisbon, Portugal: Ed. Argumentum & Gecorpa (In Portuguese).

Collins, M., B. Kasal, P. Paevere, and G. C. Foliente. 2005. “Three-Dimensional Model of Light Frame Wood Buildings. II: Experimental Investigation and Validation of Analytical Model.” *Journal of Structural Engineering* 131(4):684–92.

Company, International Text Book. 1923. “International Library of Technology.” Scranton.

Costa, Alexandre A. 2012. “Seismic Assessment of the Out of Plane Performance of Traditional Stone Masonry Walls.” (March 2012):233.

Costley, A. C. and D. P. Abrams. 1996. *Dynamic Response of Unreinforced Masonry Buildings with Flexible Diaphragms*. Buffalo, New York.

Cross, By W. Bradford, Nicholas P. Jones, and ASCE. 1994. “Seismic Performance of Joist-Pocket Connections. I: Modeling.” *Journal of Structural Engineering* 119(10):2986–3007.

D’Amico, Maria, Chiara Felicetta, Emiliano Russo, S. Sgobba, G. Lanzano, F. Pacor, and L. Luzi. 2020. “Italian Accelerometric Archive (ITACA).”

D’Ayala, D. and E. Speranza. 2003. “Definition of Collapse Mechanisms and Seismic Vulnerability of Historic Masonry Buildings.” *Earthquake Spectra* 19(3):479–509.

Dazio, A. 2008. “The Effect of the Boundary Conditions on the Out-of-Plane Behaviour of Unreinforced Masonry Walls.” in *Proceedings of the 14th World Conference on Earthquake Engineering*. Beijing, China.

Degli Abbati, Stefania, Serena Cattari, and Sergio Lagomarsino. 2018. “Theoretically-Based and Practice-Oriented Formulations for the Floor Spectra Evaluation.” *Earthquakes and Structures* 15(5):000–000.

Degli Abbati, Stefania and Sergio Lagomarsino. 2017. “Out-of-Plane Static and Dynamic Response of Masonry Panels.” *Engineering Structures* 150:803–20.

DeJong, Matthew J., Beatrice Belletti, Max A. N. Hendriks, and Jan G. Rots. 2009. “Shell Elements for Sequentially Linear Analysis: Lateral Failure of Masonry Structures.” *Engineering Structures*.

Dimitrakopoulos, Elias G. and Matthew J. DeJong. 2012. “Overturning of Retrofitted Rocking Structures under Pulse-Type Excitations.” *Journal of Engineering Mechanics* 138(8):963–

72.

Dizhur, Dmytro, Marta Giaretton, and Jason M. Ingham. 2018. “URM Wall-to-Diaphragm and Timber Joist Connection Testing.” in *10th International Masonry Conference - IMC*.

Dizhur, Dmytro, Arturo Schultz, and Jason M. Ingham. 2016. “Pull-out Behavior of Adhesive Connections in Unreinforced Masonry Walls.” *Earthquake Spectra* 32(4):2357–75.

DMI. 2008. “D.M. 14 Gennaio 2008. Approvazione Delle Nuove Norme Tecniche per Le Costruzioni (NTC 2008). (in Italian).”

DMI. 2018. “D.M. 17 Gennaio 2018. Aggiornamento Delle ‘Norme Tecniche per Le Costruzioni (NTC 2018)’ (in Italian).”

Doherty, K., M. C. Griffith, N. Lam, and J. Wilson. 2002. “Displacement-Based Seismic Analysis for out-of-Plane Bending of Unreinforced Masonry Walls.” *Earthquake Engineering and Structural Dynamics* 31(4):833–50.

Donà, Marco, Pietro Carpanese, Veronica Follador, Luca Sbrogiò, and Francesca da Porto. 2020. “Mechanics-Based Fragility Curves for Italian Residential URM Buildings.” *Bulletin of Earthquake Engineering*.

Donghi, D. 1923. “Manuale Dell’Architetto.” Torino: UTET.

Dvorkin, Eduardo N., Daniel Pantuso, and Eduardo A. Repetto. 1995. “A Formulation of the MITC4 Shell Element for Finite Strain Elasto-Plastic Analysis.” *Computer Methods in Applied Mechanics and Engineering* 125(1–4):17–40.

EC (Eurocode) 8. 2005. “Design of Structures for Earthquake Resistance - Part 3: Assessment and Retrofitting of Buildings.”

EC8-1. 2004. “Eurocode 8: Design of Structures for Earthquake Resistance—Part 1: General Rules, Seismic Actions and Rules for Buildings.”

Emi, A. R. 1856. *Trattato Dell’arte Del Carpentiere*.

EN 1998-3. 2005. *Eurocode 8: Design of Structures for Earthquake Resistance - Part 3: Assessment and Retrofitting of Buildings*.

Ewing, R. D. and J. C. Kariotis. 1981. “Methodology for Mitigation of Seismic Hazards in Existing Unreinforced Masonry Buildings: Wall Testing, out-of-Plane.” *Methodology for Mitigation of Seismic Hazards in Existing Unreinforced Masonry Buildings: Diaphragm Testing* Topical report 01.

de Falco, Anna, Linda Giresini, and Mauro Sassu. 2013. “Temporary Preventive Seismic Reinforcements on Historic Churches: Numerical Modeling of San Frediano in Pisa.” *Applied Mechanics and Materials*.

de Felice, Gianmarco, Stefano De Santis, Paulo B. Lourenço, and Nuno Mendes. 2017. “Methods and Challenges for the Seismic Assessment of Historic Masonry Structures.” *International Journal of Architectural Heritage* 11(1):143–60.

FEMA. 1992. “NEHRP Handbook of Techniques for the Seismic Rehabilitation of Existing Buildings (FEMA-172).” *Building Seismic Safety Council for FEMA, Washington, D.C.* (June).

FEMA. 2006a. “Next-Generation Performance-Based Seismic Design Guidelines (FEMA-445).” *Federal Emergency Management Agency* (August).

FEMA. 2006b. “Techniques for the Seismic Rehabilitation of Existing Buildings (FEMA-547).” *Federal Emergency Management Agency*.

FEMA. 2009. “NEHRP Recommended Seismic Provisions.” 383.

Ferreira Freitas Araújo, Ana Sofia. 2014. “Modelling of the Seismic Performance of Connections and Walls in Ancient Masonry Buildings.”

Ferreira, Tiago Miguel, Alexandre A. Costa, and Aníbal Costa. 2015. “Analysis of the Out-Of-Plane Seismic Behavior of Unreinforced Masonry: A Literature Review.” *International Journal of Architectural Heritage* 9(8):949–72.

Fmk and Mitra Nilinjan. 2003. “Pinching4 Material.”

Formenti, C. 1893. “La Pratica Del Fabbricare.”

Formisano, Antonio, Giuseppe Ciccone, and Annalisa Mele. 2017. “Large Scale Seismic Vulnerability and Risk Evaluation of a Masonry Churches Sample in the Historical Centre of Naples.” *AIP Conference Proceedings* 1906.

Formisano, Antonio, Generoso Vaiano, Francesco Fabbrocino, and Gabriele Milani. 2018. “Seismic Vulnerability of Italian Masonry Churches: The Case of the Nativity of Blessed Virgin Mary in Stellata of Bondeno.” *Journal of Building Engineering*.

Fuchs, Werner, Rolf Eligehausen, and John E. Breen. 1995. “Concrete Capacity Design (CCD) Approach for Fastening to Concrete.” *ACI Structural Journal*.

Galasco, Alessandro, Sergio Lagomarsino, and Andrea Penna. 2006. “On the Use of Pushover Analysis for Existing Masonry Buildings.” *First European Conference on Earthquake Engineering and Seismology* (September):3–8.

Giresini, Linda. 2016a. “Energy-Based Method for Identifying Vulnerable Macro-Elements in Historic Masonry Churches.” *Bulletin of Earthquake Engineering*.

Giresini, Linda. 2016b. “Rocking and Kinematic Analysis of Two Masonry Church Façades.” *Structural Analysis of Historical Constructions - Anamnesis, Diagnosis, Therapy, Controls* (October):1190–96.

Giresini, Linda, Claudia Casapulla, Roman Denysiuk, Jose Matos, and Mauro Sassu. 2018. “Fragility Curves for Free and Restrained Rocking Masonry Façades in One-Sided Motion.” *Engineering Structures* 164:195–213.

Giresini, Linda, Massimo Fragiacomo, and Mauro Sassu. 2016. “Rocking Analysis of Masonry Walls Interacting with Roofs.” *Engineering Structures* 116:107–20.

Giresini, Linda and Mauro Sassu. 2017. “Horizontally Restrained Rocking Blocks: Evaluation of the Role of Boundary Conditions with Static and Dynamic Approaches.” *Bulletin of Earthquake Engineering* 15(1):385–410.

Giresini, Linda, Mauro Sassu, Christoph Butenweg, Valerio Alecci, and Mario D. De Stefano. 2017. “Vault Macro-Element with Equivalent Trusses in Global Seismic Analyses.” *Earthquake and Structures*.

Giresini, Linda, Francesca Taddei, Fabio Solarino, G. Muller, and Pietro Croce. 2021. “Influence of Stiffness and Damping Parameters of Passive Seismic Control Device in One-Sided Rocking of Masonry Walls.” *Journal of Structural Engineering ASCE*.

Giuffrè, Antonino. 1994. “Seismic Safety and Strengthening of Historical Buildings and Urban

Fabrics." Pp. 6583–96 in *Earthquake Engineering, Tenth World Conference*. Balkema, Rotterdam.

Grillanda, Nicola, Marco Valente, and Gabriele Milani. 2020. "ANUB-Aggregates: A Fully Automatic NURBS-Based Software for Advanced Local Failure Analyses of Historical Masonry Aggregates." *Bulletin of Earthquake Engineering*.

Hilber, Hans M., Thomas J. R. Hughes, and Robert L. Taylor. 1977. "Improved Numerical Dissipation for Time Integration Algorithms in Structural Dynamics." *Earthquake Engineering and Structural Dynamics* 5(June 1976):283–92.

Housner, George W. 1963. "The Behavior of Inverted Pendulum Structures during Earthquakes." *Bulletin of the Seismological Society of America* 53(2):403–17.

Hsiao, K. J. and J. Tezcan. 2012. "Seismic Retrofitting for Chord Reinforcement for Unreinforced Masonry Historic Buildings with Flexible Diaphragms." *American Society of Civil Engineers* 17(August).

Iervolino, Iunio, Carmine Galasso, and Edoardo Cosenza. 2010. "REXEL: Computer Aided Record Selection for Code-Based Seismic Structural Analysis." *Bulletin of Earthquake Engineering*.

International Code Council. 2009. *International Building Code*. Country Club Hills, IL.

Ismail, Najif. 2016. "Performance of Wall to Diaphragm Anchors for Use in Seismic Upgrade of Heritage Masonry Buildings." *International Journal of Architectural Heritage* 10(7):829–40.

Ismail, Najif and Jason M. Ingham. 2016. "In-Plane and out-of-Plane Testing of Unreinforced Masonry Walls Strengthened Using Polymer Textile Reinforced Mortar." *Engineering Structures* 118:167–77.

Isoda, Hiroshi and Solomon Tesfamariam. 2016. "Connections for Timber–Concrete Hybrid Building: Experimental and Numerical Model Results." *Journal of Performance of Constructed Facilities* 30(5):04016024.

Istat. 2004. "Edifici Ed Abitazioni: Censimento 2001. Dati Definitivi (in Italian)."

Jaaranen, Joonas and Gerhard Fink. 2020. "Frictional Behaviour of Timber-Concrete Contact Pairs." *Construction and Building Materials*.

Jacks, D. H. and G. J. Beattie. 1990. "Dynamic Testing of Seismic Anchors in Unreinforced Brick Masonry Walls."

Kounadis, A. N. and G. J. Papadopoulos. 2016. "On the Rocking Instability of a Three-Rigid Block System under Ground Excitation." *Archive of Applied Mechanics* 86(5):957–77.

Lagomarsino, Sergio. 2014. "Seismic Assessment of Rocking Masonry Structures." *Bulletin of Earthquake Engineering* 13(1):97–128.

Lagomarsino, Sergio, Andrea Penna, Alessandro Galasco, and Serena Cattari. 2013. "TREMURI Program: An Equivalent Frame Model for the Nonlinear Seismic Analysis of Masonry Buildings." *Engineering Structures*.

Landi, Luca, Rocco Gabellieri, and Pier Paolo Diotallevi. 2015. "A Model for the Out-of-Plane Dynamic Analysis of Unreinforced Masonry Walls in Buildings with Flexible Diaphragms." *Soil Dynamics and Earthquake Engineering* 79:211–22.

Lang, K. and H. Bachmann. 2003. "On the Seismic Vulnerability of Existing Unreinforced Masonry Buildings." *Journal of Earthquake Engineering* 7(3):407–26.

Lawrence, S. and R. Marshall. 2000. "Virtual Work Design Method for Masonry Panels under Lateral Load." *12th International Brick/Block Masonry Conference* 1063–73.

LECA. 2021. "Laterlite S.P.A. Via Vittorio Veneto 30 - 43046 Rubbiano Di Solignano (PR)." Retrieved August 27, 2018 (www.leca.it).

Lemos, José V. 2007. "Discrete Element Modeling of Masonry Structures." *International Journal of Architectural Heritage*.

Lin, Tsu Jung and James M. LaFave. 2012. "Experimental Structural Behavior of Wall-Diaphragm Connections for Older Masonry Buildings." *Construction and Building Materials* 26(1):180–89.

Lipscombe, P. R. and S. Pellegrino. 1993. "Free Rocking of Prismatic Blocks." *Journal of Engineering Mechanics* 119(7):1387–1410.

Lourenço, P. B. 2009. "Recent Advances in Masonry Modelling: Micromodelling and Homogenisation." *Multiscale Modeling in Solid Mechanics*.

Lu, Xinzheng, Linlin Xie, Hong Guan, Yuli Huang, and Xiao Lu. 2015. "A Shear Wall Element for Nonlinear Seismic Analysis of Super-Tall Buildings Using OpenSees." *Finite Elements in Analysis and Design*.

Lubliner, J., J. Oliver, S. Oller, and E. Onate. 1989. "A Plastic-Damage Model for Concrete." *International Journal of Solids and Structures* 25(3):299–326.

Luzi, L., G. Lanzano, C. Felicetta, M. C. D'Amico, E. Russo, S. Sgobba, F. Pacor, and ORFEUS Working Group 5. 2020. "Engineering Strong Motion Database (ESM) (Version 2.0)." *Istituto Nazionale Di Geofisica e Vulcanologia (INGV)*.

Magenes, Guido, Andrea Penna, and Alessandro Galasco. 2010. "A Full-Scale Shaking Table Test on a Two-Storey Stone Masonry Building." P. 384 in *14th European Conference on Earthquake Engineering*. Ohrid, Republic of Macedonia: Curran.

Magenes, Guido, Andrea Penna, Ilaria Enrica Senaldi, Maria Rota, and Alessandro Galasco. 2014. "Shaking Table Test of a Strengthened Full-Scale Stone Masonry Building with Flexible Diaphragms." *International Journal of Architectural Heritage* 8(3):349–75.

Makris, Nicos and Dimitrios Konstantinidis. 2003. "The Rocking Spectrum and the Limitations of Practical Design Methodologies." *Earthquake Engineering and Structural Dynamics* 32(2):265–89.

Maresta, Werner. 2018. "Construction 102: Mezzanine Wooden Frame (1) - Beams and Joists." *DOMUS Project*.

MathWorks. 2016. "Matlab R2016b." Retrieved (https://it.mathworks.com/products/matlab.html).

Mauro, Alberto, Gianmarco de Felice, and Matthew J. DeJong. 2015. "The Relative Dynamic Resilience of Masonry Collapse Mechanisms." *Engineering Structures* 85:182–94.

McKenna, Frank, Gregory L. Fenves, Filip C. Filippou, and Michael Scott. 2000. "Open System for Earthquake Engineering Simulation (OpenSees)."

Mendes, Nuno. 2012. "Seismic Assessment of Ancient Masonry Buildings: Shaking Table Tests and Numerical Analysis."

Mendes, Nuno and Paulo B. Lourenço. 2010. "Seismic Assessment of Masonry Gaioleiro Buildings in Lisbon, Portugal." *Journal of Earthquake Engineering* 14(1):80–101.

Menon, Arun and Guido Magenes. 2008. *Out-of-Plane Seismic Response of Unreinforced Masonry: Definition of Seismic Input*. edited by Fondazione EUCENTRE. Pavia: IUSS Press.

Milano, L., a Mannella, C. Morisi, and a Martinelli. 2009. "Schede Illustrative Dei Principali Meccanismi Di Collasso Locali Negli Edifici Esistenti in Muratura e Dei Relativi Modelli Cinematici Di Analisi."

Milizia, F. 1785. *Principi Di Architettura Civile*.

Moreira, Susana. 2015. "Seismic Retrofit of Masonry-to-Timber Connections in Historical Constructions." PhD Thesis, University of Minho, Guimarães, Portugal.

NIKER. 2010. *New Integrated Knowledge-Based Approaches to the Protection of Curtural Heritage from Earthquake-Induced Risk: Workpackage 3 and 10*. Padova.

NZSEE. 2015. "Assessment and Improvement of the Structural Performance Ofbuildings in Earthquakes: Recommendations of ANZSEE Study Group on Earthquake Risk Buildings."

NZSEE. 2016. "The Seismic Assessment of Existing Buildings Technical Guidelines for Engineering Assessments Part B – Initial Seismic Assessment." (October).

Oliveira, Carlos Sousa, José V. Lemos, and Gabriela E. Sincraian. 2002. "Modelling Large Displacements of Structures Damaged by Earthquake Motions." *European Earthquake Engineering* 3:56–71.

Ortega, Javier, Graça Vasconcelos, Hugo Rodrigues, and Mariana Correia. 2018. "Assessment of the Influence of Horizontal Diaphragms on the Seismic Performance of Vernacular Buildings." *Bulletin of Earthquake Engineering*, 1–34.

Pacific Earthquake Engineering Research Center (PEER). 2016. "OpenSees : Open System For Earthquake Engineering Simulation." Retrieved (http://opensees.berkeley.edu).

Paganoni, Sara, Dina D'Ayala, and Dina D'Ayala. 2010. "Experimental and Computational Validation of Dissipative Prototype for the Seismic Protection of Heritage Buildings." *Advanced Materials Research* 133–134(April 2009):831–36.

Pantò, B., F. Cannizzaro, S. Caddemi, and I. Caliò. 2016. "3D Macro-Element Modelling Approach for Seismic Assessment of Historical Masonry Churches." *Advances in Engineering Software* 97:40–59.

Pantò, Bartolomeo, Linda Giresini, Mauro Sassu, and Ivo Caliò. 2017. "Non-Linear Modeling of Masonry Churches through a Discrete Macro-Element Approach." *Earthquake and Structures*.

Pareto, R. and G. Sacheri. 1889. *Enciclopedia Delle Arti e Delle Industrie*. Vol. IV. Torino: UTET.

Penna, A. 2015. "Seismic Assessment of Existing and Strengthened Stone-Masonry Buildings: Critical Issues and Possible Strategies." *Bulletin of Earthquake Engineering* 13(4):1051–71.

Peralta, David F., Joseph M. Bracci, and Mary Beth D. Hueste. 2004. "Seismic Behavior of

Wood Diaphragms in Pre-1950s Unreinforced Masonry Buildings." *Journal of Structural Engineering* 130(12):2040–50.

Petracca, Massimo and Guido Camata. 2019. "A Mixed Implicit-Explicit Tension-Compression Plastic-Damage Model."

Petracca, Massimo, M. Candeloro, and Guido Camata. 2017. "STKO User Manual."

Petracca, Massimo, Luca Pelà, Riccardo Rossi, Stefano Zaghi, Guido Camata, and Enrico Spacone. 2017. "Micro-Scale Continuous and Discrete Numerical Models for Nonlinear Analysis of Masonry Shear Walls." *Construction and Building Materials* 149(December):296–314.

Van Der Pluijm, R. 1992. "Material Properties of Masonry and Its Components under Tension and Shear." *Proc. 6th Canadian Masonry Symposium* 675–86.

Polidoro, B. 2010. "La Valutazione Della Vulnerabilità Sismica: Il Caso Di Pettino (AQ)." University of Naples, Federico II.

Presidenza del Consiglio dei Ministri. 2011. "Linee Guida per La Valutazione e Riduzione Del Rischio Sismico Del Patrimonio Culturale Con Riferimento Alle Norme Tecniche per Le Costruzioni." *Gazzetta Ufficiale*.

Priestley, M. J. N., R. J. Evision, A. J. Carr, R. J. Evison, and A. J. Carr. 1978. "Seismic Response of Structures Free to Rock on Their Foundations." *Bulletin of the New Zealand National Society for Earthquake Engineering* 11(3):141–50.

Priestly, M. J. N. 1985. "Seismic Behaviour of Unreinforced Masonry Walls." *Bulletin of the New Zealand National Society for Earthquake Engineering* 18(2):191–205.

Psycharis, Ioannis N. 1990. "Dynamic Behaviour of Rocking Two-Block Assemblies." *Earthquake Engineering & Structural Dynamics* 19(4):555–75.

Quagliarini, E., S. Lenci, F. Monni, and S. Vallucci. 2014. "La Conoscenza Della Fabbrica Come Strumento Di Recupero Sostenibile. La Chiesa Di S.M. Della Carità (Ascoli Piceno) (in Italian)." *Il Progetto Sostenibile* 2(May 2017):78–85.

Quagliarini, E., G. Maracchini, and F. Clementi. 2017. "Uses and Limits of the Equivalent Frame Model on Existing Unreinforced Masonry Buildings for Assessing Their Seismic Risk: A Review." *Journal of Building Engineering* 10:166–82.

Ramsey, C. G. and H. G. Sleeper. 1932. *Architectural Graphic Standards*. New York, United States of America.

Rinaldin, Giovanni, Claudio Amadio, and Massimo Fragiacomo. 2013. "A Component Approach for the Hysteretic Behaviour of Connections in Cross-Laminated Wooden Structures." *Earthquake Engineering & Structural Dynamics* 42(13):2023–42.

Rondelet, J. Par. 1802. "Traité Théorique et Pratique de l'art Du Batir." in *Vol. 5*. Paris, France: Chez l'Auteur.

Russell, A. P., Jason M. Ingham, and Michael C. Griffith. 2006. "Comparing New Zealand's Unreinforced Masonry Details with Those of Other Seismically Active Countries." Pp. 2–9 in *International Masonry Conference*.

Scacco, Jacopo, Nicoletta Bianchini, Nuno Mendes, Cassie Cullimore, and Lavina Jain. 2019. "Seismic Assessment of the Church of Carmo Convent." *Congresso de Métodos*

Numéricos Em Engenharia (July).

Scali, L. 2011. "Il Muratore." *Murocultura n.5/2011*. Retrieved September 27, 2018 (http://www.murlocultura.com/old_site/MurloCultura_5_2011/MurloCultura_5_2011_pag8.html).

Scamozzi, Vincenzo. 1615. *L'idea Dell'Architettura Universale*. Venezia.

Scotta, Roberto, Davide Trutalli, Luca Marchi, and Luca Pozza. 2018. "Seismic Performance of URM Buildings with In-Plane Non-Stiffened and Stiffened Timber Floors." *Engineering Structures* 167:683–94.

Seismosoft. 2001. "SeismoSignal - A Computer Program for Signal Processing of Strong-Motion Data."

Senaldi, Ilaria Enrica, Guido Magenes, Andrea Penna, Alessandro Galasco, and Maria Rota. 2014. "The Effect of Stiffened Floor and Roof Diaphragms on the Experimental Seismic Response of a Full-Scale Unreinforced Stone Masonry Building." *Journal of Earthquake Engineering* 18(3):407–43.

Shabani, Amirhosein, Mahdi Kioumarsi, and Maria Zucconi. 2021. "State of the Art of Simplified Analytical Methods for Seismic Vulnerability Assessment of Unreinforced Masonry Buildings." *Engineering Structures* 239(March):112280.

Simsir, Can C., Mark A. Aschheim, and Daniel P. Abrams. 2004. "Out-of-Plane Dynamic Response of Unreinforced Bearing Walls Attached to Flexible Diaphragms." P. 15 in *Proceedings of 13th World Conference on Earthquake Engineering*.

sismica s.r.l., Gruppo. 2018. "3D MACRO."

Smerzini, C. and R. Paolucci. 2013. *SIMBAD: A Database with Selected Input Motions for Displacement_Based Assessment and Design – 3rd Release*. Milano, Italy.

Software, ACCA. 2021. "EdiLus-MU."

Solarino, Fabio, Linda Giresini, and Daniel V Oliveira. 2020. "Mitigation of Amplified Response of Restrained Rocking Walls through Horizontal Dampers." in *EURODYN 2020 - XI International Conference on Structural Dynamics*, edited by M. Papadrakakis, M. Fragiadakis, and C. Papadimitiou. Athens, Greece.

Sorrentino, Luigi, Omar AlShawa, and Luis D. Decanini. 2011. "The Relevance of Energy Damping in Unreinforced Masonry Rocking Mechanisms. Experimental and Analytic Investigations." *Bulletin of Earthquake Engineering* 9(5):1617–42.

Sorrentino, Luigi, Dina D'Ayala, Gianmarco de Felice, Michael C. Griffith, Sergio Lagomarsino, and Guido Magenes. 2017. "Review of Out-of-Plane Seismic Assessment Techniques Applied To Existing Masonry Buildings." *International Journal of Architectural Heritage* 11(1):2–21.

Spina, G., F. Ramundo, and A. Mandara. 2005. "Masonry Strengthening by Metal Tie-Bars , a Case Study." *Structural Analysis of Historical Constructions - Modena, Lourenço & Roca (Eds)* 1207–14.

Tena-Colunga, A. and DP Abrams. 1996. "Seismic Behavior of Structures with Flexible Diaphragms." *Journal of Structural Engineering* 122(4):439–45.

Tomaževič, Miha. 1999. *Earthquake-Resistant Design of Masonry Buildings*. Vol. 1. edited by A.

S. Elnashai & P. J. Dowling Eds. London, UK: Imperial College Press.

Tomaževič, Miha. 2011. "Seismic Resistance of Masonry Buildings in Historic Urban and Rural Nuclei: Lessons Learned in Slovenia." *International Journal of Architectural Heritage* 5(4–5):436–65.

Tomaževič, Miha, Iztok Klemenc, and Polona Weiss. 2009. "Seismic Upgrading of Old Masonry Buildings by Seismic Isolation and CFRP Laminates: A Shaking-Table Study of Reduced Scale Models." *Bulletin of Earthquake Engineering* 7(1):293–321.

Tomaževič, Miha, Marjana Lutman, and Polona Weiss. 1996. "Seismic Upgrading of Old Brick-Masonry Urban Houses: Tying of Walls with Steel Ties." *Earthquake Spectra* 12(3):599–622.

Trifunac, M. D. and A. G. Brady. 1975. "A Study on the Duration of Strong Earthquake Ground Motion." *Bulletin of the Seismological Society of America* 65(3):581–626.

Valadier, Giuseppe. 1831. *L'architettura Pratica*.

Valluzzi, Maria Rosa, Enrico Garbin, Massimo dalla Benetta, and Claudio Modena. 2013. "Experimental Characterization of Timber Floors Strengthened by In-Plane Improvement Techniques." *Advanced Materials Research*.

Vintzileou, Elizabeth, Charalambos Mouzakis, Chrissy Elpida Adami, and Lucia Karapitta. 2015. "Seismic Behavior of Three-Leaf Stone Masonry Buildings before and after Interventions: Shaking Table Tests on a Two-Storey Masonry Model." *Bulletin of Earthquake Engineering* 13(10):3107–33.

APPENDIX

Appendix 1 WD pinching4 model parameters

Table A 1 Pinching4 model parameters defining WD unstrengthened connection model.

Parameter	**Unit**	**Values**
Backbone coordinates		
ePf1, ePf2, ePf3, ePf4	kN	[0.04, 4.3, 4.301, 0.043]
ePd1, ePd2, ePd3, ePd4	mm	[0.01, 4.0, 32.2, 33.2]
eNf1, eNf2, eNf3, eNf4	kN	[-2.5, -100.0, -150.0, -200.0]
eNd1, eNd2, eNd3, eNd4	mm	[-0.02, -0.74, -1.11, -1.48]
Hysteretic rules parameters		
rDispP, rDispN	-	[0.1, 0.5]
rForceP, rForceN	-	[0.1, 0.1]
uForceP, uForceN	-	[0.01, 0.03]
Degradation parameters		
gK1, gK2, gK3, gK4, gKLim	-	[0.0, 0.0, 0.0, 0.0, 0.0]
gD1, gD2, gD3, gD4, gDLim	-	[0.0, 0.0, 0.0, 0.0, 0.0]
gF1, gF2, gF3, gF4, gFLim	-	[0.0, 0.0, 0.0, 0.0, 0.0]
gE	-	10
dmgType	-	“energy”

Table A 2 Pinching4 model parameters defining WD strengthened connection model.

Parameter	**Unit**	**Values**
Backbone coordinates		
ePf1, ePf2, ePf3, ePf4	kN	[0.728, 728, 728.01, 0.728]
ePd1, ePd2, ePd3, ePd4	mm	[0.052, 20.8, 76.77, 77.7]
eNf1, eNf2, eNf3, eNf4	kN	[-2.5, -100.0, -150.0, -200.0]
eNd1, eNd2, eNd3, eNd4	mm	[-0.02, -0.74, -1.11, -1.48]
Hysteretic rules parameters		
rDispP, rDispN	-	[0.77, 0.5]
rForceP, rForceN	-	[0.067, 0.5]
uForceP, uForceN	-	[0.0001, 0.0001]
Degradation parameters		
gK1, gK2, gK3, gK4, gKLim	-	[0.0, 0.0, 0.0, 0.0, 0.0]
gD1, gD2, gD3, gD4, gDLim	-	[0.0, 0.0, 0.0, 0.0, 0.0]
gF1, gF2, gF3, gF4, gFLim	-	[0.0, 0.0, 0.0, 0.0, 0.0]
Ge	-	10
dmgType	-	“energy”

Appendix 2 Dynamic analysis of local mechanism

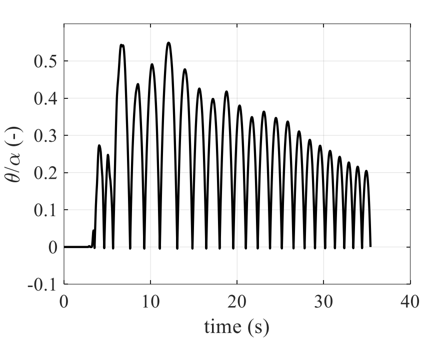

IT0014xa_record

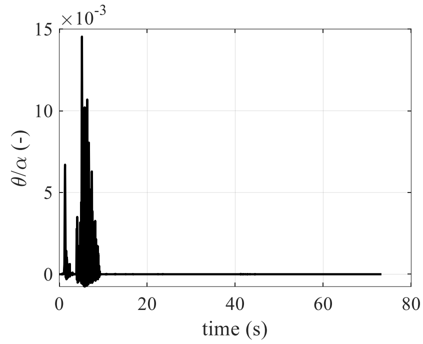

IT0166xa_record

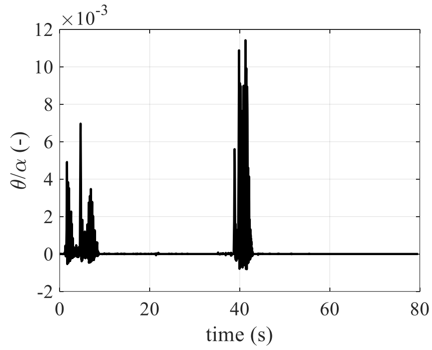

IT0171xa_record

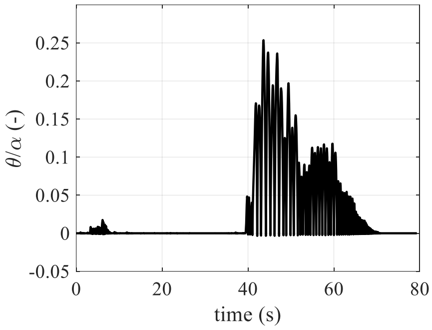

IT0171ya_record

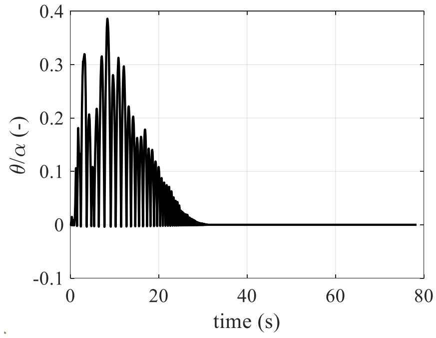

IT0789xa_record

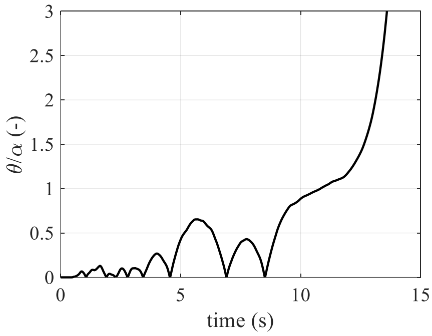

IT0790ya_record

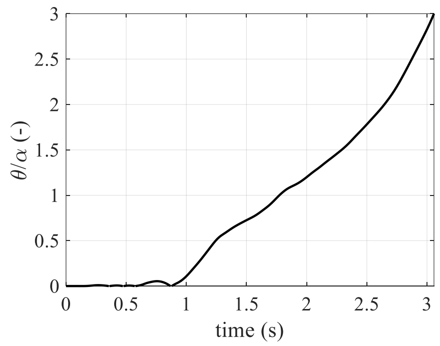

IT0792xa_record

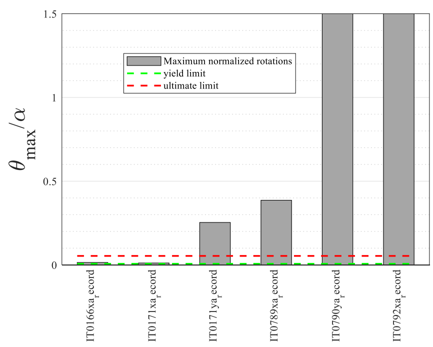

normalized rotations summary

Figure 6.1. Normalized rotation time-histories of Mechanism E, Model 2 (unstrengthened WD connections).

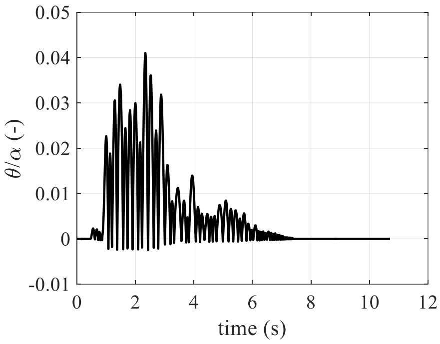

IT0014xa_record

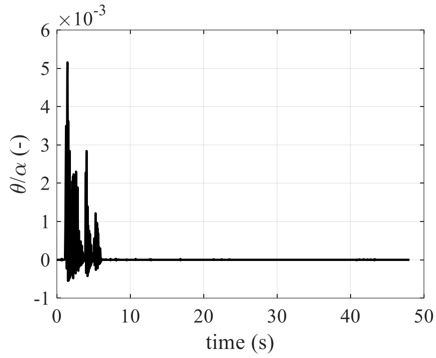

IT0166xa_record

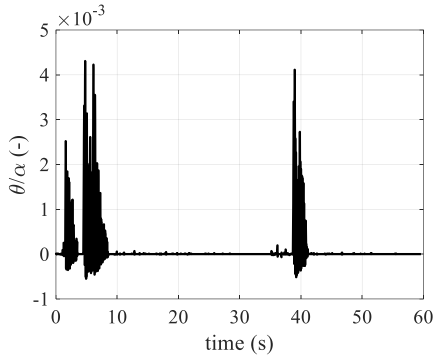

IT0171xa_record

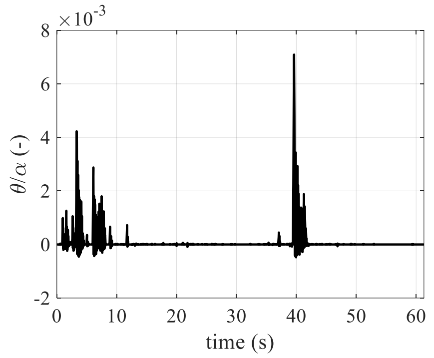

IT0171ya_record

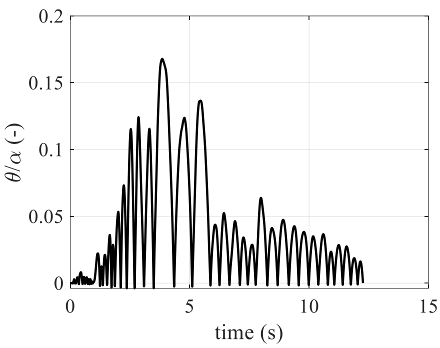

IT0789xa_record

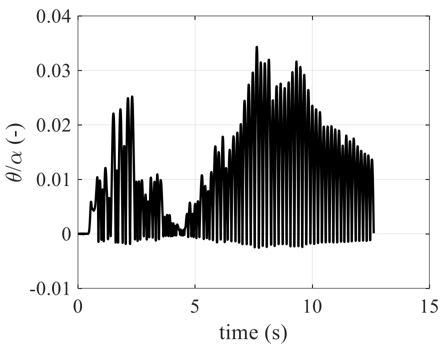

IT0790ya_record

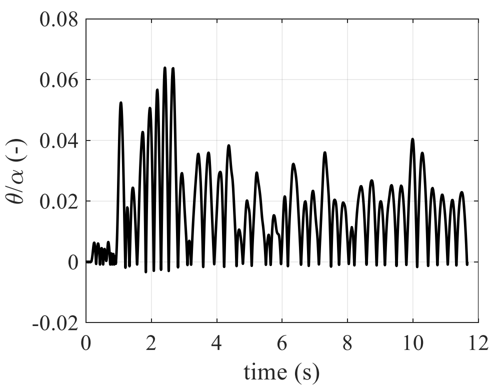

IT0792xa_record

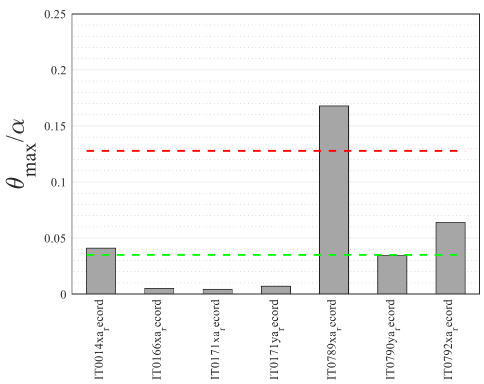

normalized rotations summary

Figure 6.2. Normalized rotation time-histories of Mechanism E, Model 3 (strengthened WD connections).

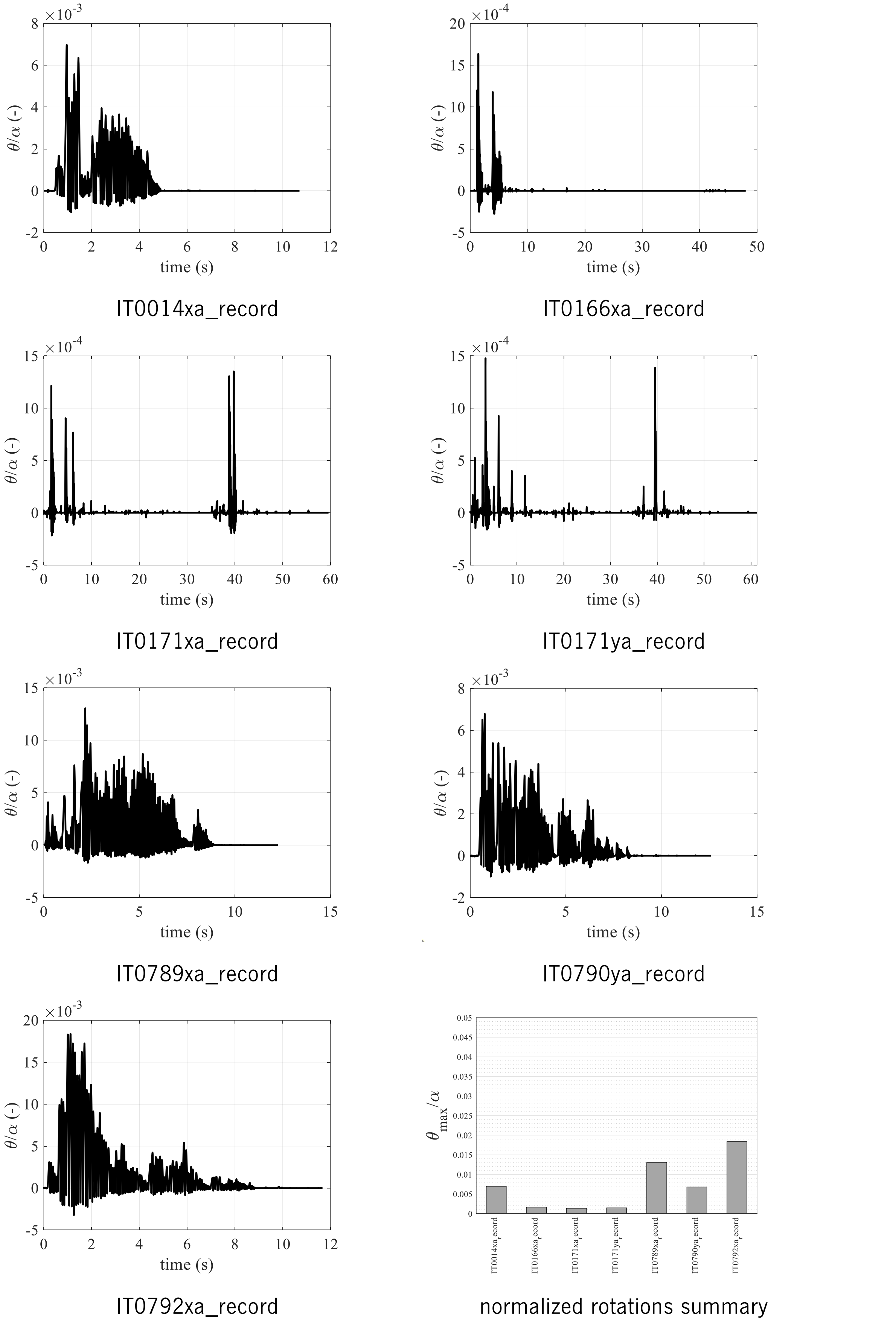

Figure 6.3. Normalized rotation time-histories of Mechanism E, Model 4 (perfect WD connections).